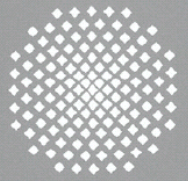
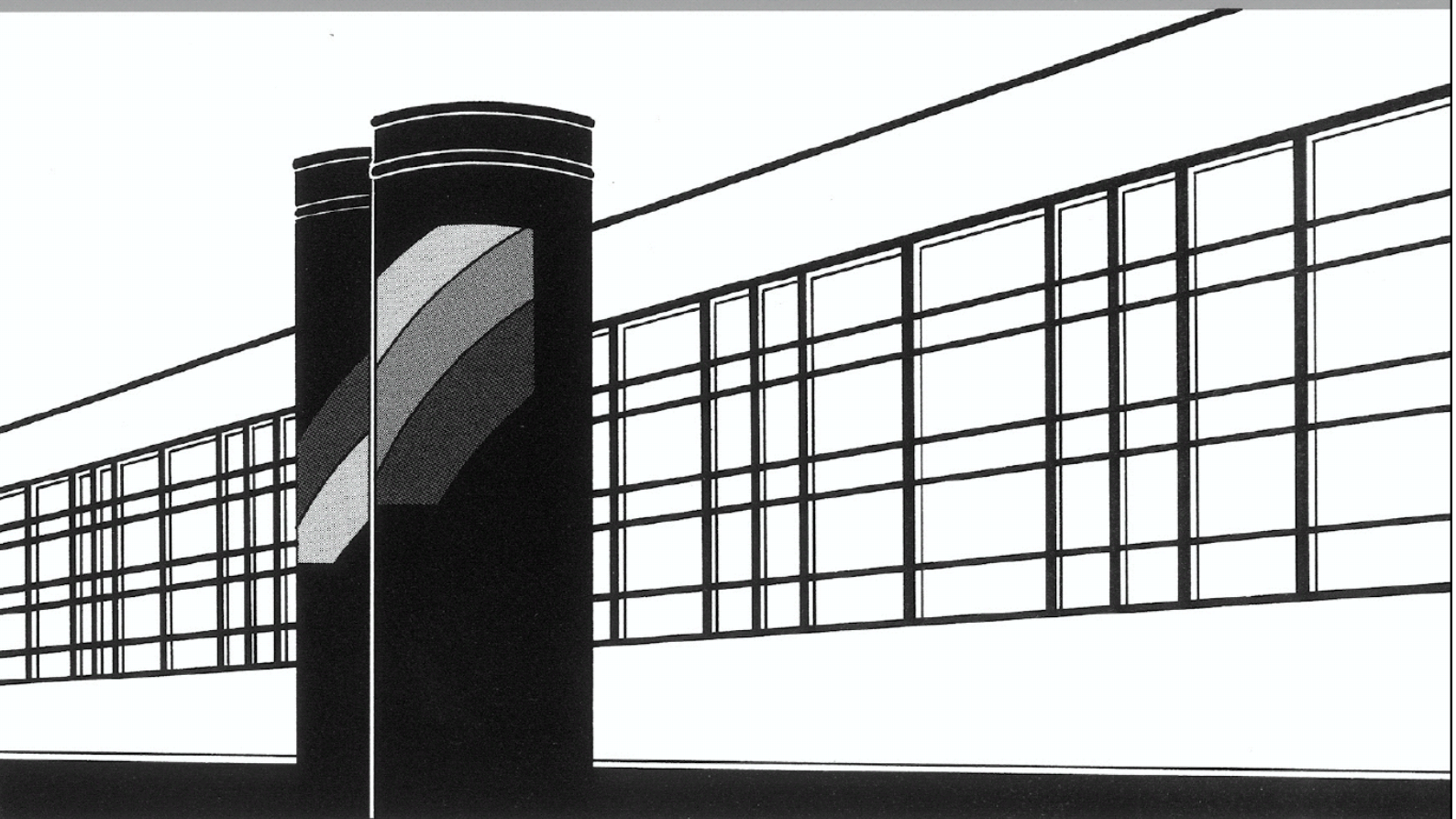


Universität Stuttgart



Institut für Wasser- und Umweltsystemmodellierung

# *Mitteilungen*



Heft 274 Timo Koch

Mixed-dimension models for flow and transport processes in porous media with embedded tubular network systems



# **Mixed-dimension models for flow and transport processes in porous media with embedded tubular network systems**

von der Fakultät Bau- und Umweltingenieurwissenschaften  
und dem Stuttgart Research Centre for Simulation Technology der  
Universität Stuttgart zur Erlangung der Würde eines  
Doktor-Ingenieurs (Dr.-Ing.) genehmigte Abhandlung

vorgelegt von  
**Timo Koch**  
aus Nagold, Deutschland

Hauptberichter: apl. Prof. Dr. rer. nat. Bernd Flemisch  
Mitberichter: Prof. Dr.-Ing. Rainer Helmig  
Prof. Dr. Patrick Jenny  
Prof. Dr. Dominik Obrist

Tag der mündlichen Prüfung: 19. Februar 2020

Institut für Wasser- und Umweltsystemmodellierung  
der Universität Stuttgart  
2020



Heft 274    **Mixed-dimension models for  
flow and transport processes  
in porous media with  
embedded tubular network  
systems**

von  
Dr.-Ing.  
Timo Koch

Eigenverlag des Instituts für Wasser- und Umweltsystemmodellierung  
der Universität Stuttgart

**D93 Mixed-dimension models for flow and transport processes in porous media with embedded tubular network systems**

**Bibliografische Information der Deutschen Nationalbibliothek**

Die Deutsche Nationalbibliothek verzeichnet diese Publikation in der Deutschen Nationalbibliografie; detaillierte bibliografische Daten sind im Internet über <http://www.d-nb.de> abrufbar

Koch, Timo:

Mixed-dimension models for flow and transport processes in porous media with embedded tubular network systems, Universität Stuttgart. - Stuttgart: Institut für Wasser- und Umweltsystemmodellierung, 2020

(Mitteilungen Institut für Wasser- und Umweltsystemmodellierung, Universität Stuttgart: H. 274)

Zugl.: Stuttgart, Univ., Diss., 2020

ISBN 978-3-942036-78-8

NE: Institut für Wasser- und Umweltsystemmodellierung <Stuttgart>: Mitteilungen

Gegen Vervielfältigung und Übersetzung bestehen keine Einwände, es wird lediglich um Quellenangabe gebeten.

Herausgegeben 2020 vom Eigenverlag des Instituts für Wasser- und Umweltsystemmodellierung

Druck: DCC Kästl e.K., Ostfildern

## Danksagung

Ich möchte hiermit allen danken, die mich den letzten Jahren unterstützt haben und maßgeblich zum Gelingen dieser Arbeit beigetragen haben.

Zuallererst danke ich Naeme, ohne die das Projekt sicher nicht möglich gewesen wäre, die mir stets mit der nötigen Geduld, Motivation, Humor und Leichtigkeit zur Seite steht und sich dafür einsetzt, dass ich neben dem zeitintensiven Arbeitsalltag auch Zeit für Familie und Freunde finde.

Ich danke meinen Eltern für die großartige und anhaltende Unterstützung, aufmunternde Worte und Ratschläge fürs Leben.

Ein besonderer Dank gilt Rainer Helmig, Bernd Flemisch und Holger Class, die für eine einzigartige Arbeitsatmosphäre und ein Klima im Team sorgen, bei dem es genauso viel Platz für Sachliches wie für Menschliches gibt. Deren unkomplizierte Herangehensweise, Begeisterung fürs wissenschaftliche Arbeiten, hoch motivierende Art und Erfahrung spielten eine entscheidende Rolle für das Gelingen dieser Arbeit.

Ich danke allen Kollegen am LH<sup>2</sup>. Es ist wirklich ein tolles Team, indem man sich gegenseitig hilft und schätzt. Ein besonderer Dank geht an meine langjährigen Kollegen und Freunde Dennis, Martin und Kilian für die zahlreichen Diskussionen und gemeinsamen Projekte, in denen auch viele der Ideen für diese Arbeit ihren Ursprung haben und für jede Menge Spaß bei langen Kaffeepausen, philosophischen Debatten oder beim Feierabendbier. Mit organisatorischen Fragen und Formularen konnte ich mich immer auf die freundliche Hilfe von Pru und Steffi verlassen und für EDV Kenntnisse war stets auf David und Michelle Verlass.

Ich danke Dominik Obrist, der mir einen dreimonatigen Forschungsaufenthalt am ARTORG Center for Biomedical Engineering Research in Bern ermöglicht hat und als Gutachter zur Verfügung stand. Durch die höchst interessante Forschung und die Diskussionen und Vorträge während meiner Zeit in Bern hat er mein Interesse und meine Begeisterung für biomedizinische Anwendungen maßgeblich befeuert. In Bern lernte ich auch Roland Wiest kennen, dem ich besonders für seine Offenheit und motivierende Neugier bei unserer interdisziplinären Zusammenarbeit an der Schnittstelle von Wissenschaftlichem Rechnen und Neuroradiologie danken möchte.

Ich danke Patrick Jenny, der sich als Gutachter zur Verfügung gestellt hat, die initiale Idee beigetragen hat, die zu unserer gemeinsamen Publikation geführt hat und mit stets exzellenten Fragen die Diskussion in die richtige Richtung gelenkt hat.

Ich möchte Valerij Kiselev danken, der sich kurzfristig einen Nachmittag Zeit genommen hat, um mit mir über mesoskalige Effekte in der Magnetresonanztomografie zu diskutieren, obwohl wir uns davor noch nicht kannten.

Ich danke der Deutschen Forschungsgemeinschaft (DFG) für die Förderung dieses Projekts im Rahmen des Exzellenzclusters Simulation Technology (SimTech) und allen an SimTech Beteiligten, für die tolle Atmosphäre und den guten wissenschaftlichen Austausch. Insbesondere danke an Michael Sinsbeck, Wolfgang Nowak und Sergey Oladyshkin für die Beantwortung meiner Fragen und Empfehlungen zur Stochastik.



# Contents

List of Figures	XIII
List of Tables	XV
Nomenclature	XVII
Abstract	XXIII
Kurzfassung	XXV
<b>1 Introduction</b>	<b>1</b>
1.1 Biological tissue perfusion models . . . . .	2
1.2 Root-soil interaction in the vadose zone . . . . .	4
1.3 Well modeling in geological formations . . . . .	6
1.4 Modeling concept . . . . .	8
1.5 Overview and structure . . . . .	8
<b>2 Flow and transport in porous media</b>	<b>11</b>
<b>3 Modeling tissue perfusion</b>	<b>15</b>
3.1 Blood flow and drug transport in capillaries . . . . .	16
3.2 Transmural fluid exchange . . . . .	19
3.3 Extra-vascular compartment . . . . .	21
3.4 Mixed-dimension tissue perfusion model . . . . .	22
<b>4 Modeling root-soil interaction</b>	<b>25</b>
4.1 Flow and transport in unsaturated soil . . . . .	26
4.2 Flow and transport in the root xylem . . . . .	28
4.3 Root water uptake (transmural exchange) . . . . .	29
4.4 Mixed-dimension root water uptake model . . . . .	31
4.5 Transpiration . . . . .	32
4.6 Evaporation from soil . . . . .	33
4.7 Root growth . . . . .	35

<b>5</b>	<b>Modeling wells</b>	<b>39</b>
5.1	Flow in the rock matrix . . . . .	40
5.2	Flow in the well . . . . .	40
5.3	Fluid exchange with the rock matrix . . . . .	41
5.4	Well index and Peaceman well model . . . . .	42
<b>6</b>	<b>Mixed-dimension embedded methods and applications</b>	<b>45</b>
6.1	Generalized mixed-dimension embedded problem . . . . .	51
6.2	Dimensional analysis . . . . .	52
6.2.1	Tissue perfusion . . . . .	53
6.2.2	Root water uptake . . . . .	54
6.2.3	Well modeling . . . . .	57
6.2.4	Conclusion . . . . .	58
<b>7</b>	<b>A new method for the simulation of tissue perfusion</b>	<b>61</b>
7.1	Mixed-dimension problem with distributed sources . . . . .	61
7.1.1	Flux scaling factor $\Xi$ (single straight vessel) . . . . .	62
7.1.2	Kernel support radius $\varrho$ . . . . .	65
7.1.3	Multiple vessels . . . . .	65
7.2	Discretization . . . . .	67
7.2.1	Numerical fluxes $F_{K_\Omega, \sigma}$ . . . . .	69
7.2.2	Numerical fluxes $F_{K_\Lambda, \sigma}$ . . . . .	69
7.2.3	Numerical source term $Q_\Gamma$ . . . . .	70
7.2.4	Kernel integration . . . . .	72
7.3	Numerical experiments . . . . .	73
7.3.1	Implementation and linear solver . . . . .	73
7.3.2	Single vessel . . . . .	74
7.3.3	Multiple parallel vessels . . . . .	78
7.3.4	Multiple arbitrarily-oriented vessel . . . . .	82
7.3.5	Vessel network . . . . .	84
7.4	Summary and conclusion . . . . .	87
<b>8</b>	<b>A new well model using distributed sources</b>	<b>91</b>
8.1	The distributed source method for isotropic media . . . . .	92

8.2	Extension to anisotropic media . . . . .	93
8.2.1	Analytical solution . . . . .	93
8.2.2	A kernel function for anisotropic media . . . . .	96
8.3	Numerical method . . . . .	99
8.3.1	Kernel integration . . . . .	101
8.4	Numerical experiments and discussion . . . . .	101
8.4.1	Grid convergence for different anisotropy ratios . . . . .	102
8.4.2	Influence of the outer kernel radius $\varrho_o$ . . . . .	103
8.4.3	Robustness with respect to rotation . . . . .	105
8.4.4	Comparison with a Peaceman-type well model . . . . .	106
8.5	Summary . . . . .	109
<b>9</b>	<b>A multi-scale sub-voxel perfusion model for perfusion MRI</b>	<b>111</b>
9.1	Flow and transport model and model parameters . . . . .	114
9.2	NMR signal model . . . . .	115
9.3	Numerical treatment . . . . .	120
9.4	Inverse modeling using clinical MRI data . . . . .	121
9.4.1	Parameter estimation . . . . .	123
9.4.2	Parameter sensitivity . . . . .	125
9.4.3	Bayesian parameter inference . . . . .	129
9.5	Model limitations and outlook . . . . .	135
9.6	Summary and conclusion . . . . .	136
<b>10</b>	<b>Simulation of root water uptake and root growth</b>	<b>139</b>
10.1	Root water uptake benchmark . . . . .	139
10.2	Application I: Root water uptake with tracer . . . . .	141
10.3	Application II: Grid growth . . . . .	143
10.4	Application III: Evapotranspiration . . . . .	145
10.5	Conclusion and outlook . . . . .	147
<b>11</b>	<b>Software and implementation</b>	<b>151</b>
11.1	Network grids . . . . .	153
11.2	Coupling different domains . . . . .	157
11.3	Intersecting grids . . . . .	158
11.4	Assembly and linear solver . . . . .	161

11.5 Sustainable development and quality assurance . . . . .	162
<b>12 Summary and outlook</b>	<b>165</b>
12.1 Summary . . . . .	165
12.2 Outlook . . . . .	166
<b>A Appendices</b>	<b>169</b>
A.1 Dimensional analysis of a simplified tissue system . . . . .	169
A.2 Dimensional analysis of a simplified root system . . . . .	170
A.3 Additional vessel network data . . . . .	171
A.4 Rotation of coordinates in well-bore ellipse axes . . . . .	172
A.5 Rodrigues' rotation formula . . . . .	173
A.6 Properties of the conformal mapping . . . . .	174
A.7 Transformation of the Laplace operator . . . . .	176
A.8 Source scaling factor in $w$ -coordinates . . . . .	178
A.9 Determinant of the Joukowski transformation . . . . .	179
A.10 Convergence rates for different anisotropy ratios . . . . .	179
A.11 Convergence study in space and time . . . . .	180
A.12 Prior distributions for MCMC . . . . .	183
A.13 Ensemble sampler for MCMC . . . . .	183
A.14 MCMC results for $\sigma = 0.095$ . . . . .	184
<b>Bibliography</b>	<b>187</b>

# List of Figures

1.1	Tissue perfusion (image compilation) . . . . .	2
1.2	Root water uptake (image compilation) . . . . .	4
3.1	Model reduction for flow in capillaries . . . . .	15
4.1	Typical processes in the vadose zone . . . . .	25
4.2	Cross-sectional anatomy of a dicot root . . . . .	28
5.1	Schematic representation of two types of wells . . . . .	39
5.2	Setup for the derivation of the Peaceman well model . . . . .	42
6.1	Bifurcating tubular network—schematic representation . . . . .	46
6.2	Mixed-dimension coupling methods . . . . .	50
6.3	Root conductivity and 8-day-old lupin root system . . . . .	55
6.4	Relative permeabilities for different soil types . . . . .	56
7.1	Pressure solution near vessel . . . . .	62
7.2	Visualization of the discretization . . . . .	68
7.3	Kernel integration . . . . .	72
7.4	Numerical solution $p_t^{ps}$ for $r_v = 0.03$ and $\varrho = r_v$ . . . . .	74
7.5	Discretization errors in $p_t$ , $p_v$ , and $\hat{q}_m$ ( $r_v = 0.1$ ) . . . . .	77
7.6	Discretization errors in $p_t$ , $p_v$ , and $\hat{q}_m$ ( $r_v = 0.05$ ) . . . . .	77
7.7	Numerical solution of hydraulic pressure . . . . .	78
7.8	Analytical and numerical solutions for three methods . . . . .	80
7.9	Discretization errors for different methods . . . . .	81
7.10	Discretization errors for different kernel support radii . . . . .	81
7.11	Computational domain—multiple arbitrarily-oriented vessels . . . . .	82
7.12	Difference in the source term with respect to the reference solution . . . . .	83
7.13	Vessel network, rat brain superficial cortex . . . . .	85
7.14	Differences to reference solution, network with bifurcations . . . . .	86
7.15	Local error distribution—network with bifurcations . . . . .	86
8.1	Well model with distributed sources: schematic representation . . . . .	92

8.2	Analytical pressure solution for a slanted well . . . . .	96
8.3	Visualization of coordinate transformation . . . . .	98
8.4	Visualization of the discretization process . . . . .	99
8.5	Grid convergence for different anisotropy ratios . . . . .	103
8.6	Grid convergence for different kernel support radii . . . . .	104
8.7	Source error for different $K$ and well orientations . . . . .	105
8.8	Reference solution for comparison with PM well model . . . . .	107
8.9	Relative integral source error for PM and DS model . . . . .	108
8.10	Plot of numerical pressure for PM and DS model . . . . .	109
9.1	Signal intensity-time curves for lesion and NAWM tissue . . . . .	112
9.2	Simulated normalized NMR signals compared with MRI data . . . . .	124
9.3	Contrast agent leakage for different $D_\omega$ . . . . .	125
9.4	Sensitivity analysis: lesion tissue sample . . . . .	127
9.5	Sensitivity analysis: NAWM tissue sample . . . . .	128
9.6	Parameter distributions after learning from lesion data ( $\sigma = 0.009$ ) . . . . .	132
9.7	Parameter distributions after learning from NAWM data ( $\sigma = 0.009$ ) . . . . .	133
9.8	$D_\omega$ distributions after learning from clinical MRI data . . . . .	134
10.1	Locally refined tetrahedral grid . . . . .	140
10.2	Simulated transpiration rates for drying soil . . . . .	140
10.3	Simulation of root-water uptake and tracer transport . . . . .	142
10.4	Root water uptake of two growing root systems . . . . .	144
10.5	Evaporation, transpiration, and evapotranspiration rates . . . . .	146
10.6	Root water uptake and hydraulic redistribution . . . . .	147
11.1	Different types of model coupling in DuMu <sup>x</sup> multi-domain simulations . . . . .	152
11.2	Axis-aligned bounding box volume hierarchy . . . . .	159
A.1	Visualization of the (inverse) Joukowski transformation . . . . .	174
A.2	Determinant of the Jacobian of the transformation . . . . .	176
A.3	Convergence study in space and time . . . . .	182
A.4	Parameter distributions after learning from lesion data ( $\sigma = 0.095$ ) . . . . .	185
A.5	Parameter distributions after learning from NAWM data ( $\sigma = 0.095$ ) . . . . .	186

# List of Tables

6.1	Tissue perfusion problem in generalized form . . . . .	52
9.1	Parameter values from global optimization best fit . . . . .	123
10.1	Parameter values for root water uptake simulation . . . . .	143
10.2	Different scenarios for the evapotranspiration simulation . . . . .	146
A.1	Vessel specifications for numerical experiment in Section 7.3.4 . . . . .	172
A.2	Convergence rates for different anisotropy ratios . . . . .	179
A.3	Errors and convergence rates in space for $p_t$ and $x_t$ . . . . .	181
A.4	Prior distribution for parameters for Bayesian parameter inference . . . . .	183





# Nomenclature

The following nomenclature introduces the most significant symbols and abbreviations used in this work. Local notations and extension, such as subscripts and superscripts to distinguish symbols of the same type, are explained where introduced in the text. Vectors and vector fields are typeset in bold with small letters ( $\boldsymbol{v}$ ) and second-order tensor fields are typeset in bold with capital letters ( $\boldsymbol{K}$ ). Units are given if applicable and unambiguous.

## Abbreviations

BBB	blood-brain barrier
DSC-MRI	dynamic susceptibility contrast MRI
ECM	extra-cellular matrix
MRI	magnetic resonance imaging
MR	magnetic resonance
MS	multiple sclerosis
PDE	partial differential equation
RBC	red blood cell / erythrocyte
REV	representative elementary volume

## Coordinate system

$r, \theta, z$	radial, angular, axial coordinate in a cylindrical coordinate system
$\boldsymbol{e}_1, \boldsymbol{e}_2, \boldsymbol{e}_3$	unit normal vectors forming a basis of a coordinate system
$s$	local coordinate for the parametrization of lines
$\boldsymbol{x}$	position in Cartesian coordinates
$x_1, x_2, x_3$	coordinates in a Cartesian coordinate systems, comp. of $\boldsymbol{x}$

## Discretization framework

$F_{K,\sigma}$	discrete flux from cell $K$ over face $\sigma$
$K$	cell
$L$	(neighboring) other cell

$\Lambda_b$	discrete embedded domain
$\mathbf{n}_{K,\sigma}$	center unit outer normal vector on face $\sigma \subset \partial K$
$\Omega_b$	discrete bulk domain
$\sigma$	cell face

### Continuum mechanics

$A$	cross-sectional area	$\text{m}^2$
$c_{p,s}$	specific heat capacity of the solid phase	$\text{J kg}^{-1} \text{K}^{-1}$
$C_F$	Forchheimer coefficient	-
$C_\lambda$	friction coefficient	-
$c_\alpha^\kappa$	molar concentration of component $\kappa$ in phase $\alpha$	$\text{mol m}^{-3}$
$\delta_{\text{BL}}$	thickness of the boundary layer	$\text{m}$
$d$	diameter	$\text{m}$
$D_\alpha^\kappa$	binary diffusion coeff. of comp. $\kappa$ and the main comp. of phase $\alpha$	$\text{m}^2 \text{s}^{-1}$
$D_{\alpha,e}^\kappa$	effective binary diffusion coefficient	$\text{m}^2 \text{s}^{-1}$
$D_\omega$	effective diffusive wall conductivity	$\text{m s}^{-1}$
$g$	gravitational acceleration	$\text{m s}^{-2}$
$\mathbf{g}$	gravitational vector field	$\text{m s}^{-2}$
$H_\pi^\kappa$	Henry coefficient for the dissolution of comp. $\kappa$ in comp. $\pi$	$\text{Pa}$
$h_\alpha$	specific enthalpy of phase $\alpha$	$\text{J kg}^{-1}$
$K$	intrinsic permeability tensor	$\text{m}^2$
$k$	intrinsic isotropic permeability	$\text{m}^2$
$k_{\text{ax}}$	axial root conductivity	$\text{m}^4 \text{Pa}^{-1} \text{s}^{-1}$
$k_{r\alpha}$	relative permeability of phase $\alpha$	-
$k_{\text{rad}}$	radial root conductivity	$\text{m s}^{-1} \text{Pa}^{-1}$
$\lambda_\alpha$	thermal conductivity of phase $\alpha$	$\text{W m}^{-1} \text{K}^{-1}$
$\lambda_e$	effective thermal conductivity	$\text{W m}^{-1} \text{K}^{-1}$
$L_p$	filtration coefficient	$\text{m Pa}^{-1} \text{s}^{-1}$
$M^\kappa$	molar mass of component $\kappa$	$\text{kg mol}^{-1}$

$M_\alpha$	average molar mass of phase $\alpha$	$\text{kg mol}^{-1}$
$\mu$	dynamic viscosity	$\text{Pa s}$
$\mu_\alpha$	dynamic viscosity of phase $\alpha$	$\text{Pa s}$
$\mathbf{n}$	unit normal vector	-
$\pi$	osmotic or oncotic pressure	$\text{Pa}$
$p$	pressure	$\text{Pa}$
$p_\alpha$	phase pressure of phase $\alpha$	$\text{Pa}$
$p_c$	capillary pressure	$\text{Pa}$
Pe	Péclet number	-
$P$	cross-sectional tube perimeter	$\text{m}$
$\phi$	porosity	-
$p_\alpha^\kappa$	partial pressure of component $\kappa$ in phase $\alpha$	$\text{Pa}$
$p_{\text{sat}}^\kappa$	saturation vapor pressure of component $\kappa$	$\text{Pa}$
$q_m$	mass source	$\text{kg s}^{-1} \text{m}^{-3}$
$\hat{q}_m$	mass (line) source in a tube	$\text{kg s}^{-1} \text{m}^{-1}$
$q_c$	molar source	$\text{mol s}^{-1} \text{m}^{-3}$
$\hat{q}_c$	molar (line) source in a tube	$\text{mol s}^{-1} \text{m}^{-1}$
$q_h$	heat source	$\text{J s}^{-1} \text{m}^{-3}$
$q_v$	volumetric source	$\text{m}^3 \text{s}^{-1} \text{m}^{-3}$
$\hat{q}_v$	volumetric (line) source in a tube	$\text{m}^3 \text{s}^{-1} \text{m}^{-1}$
$r$	radius	$\text{m}$
Re	Reynolds number	-
$\mathcal{R}$	universal gas constant	$\text{J K}^{-1} \text{mol}^{-1}$
$\rho$	density	$\text{kg m}^{-3}$
$\rho_\alpha$	phase density of phase $\alpha$	$\text{kg m}^{-3}$
$S_\alpha$	phase saturation of phase $\alpha$	-
$S_{\alpha e}$	effective phase saturation of phase $\alpha$	-
$S_{\alpha r}$	residual phase saturation of phase $\alpha$	-

$\sigma$	osmotic reflection coefficient (or cell face in discretization context)	-
$\sigma_c$	solvent-drag reflection coefficient	-
$\tau$	tortuosity	-
$T$	temperature	K
$u_\alpha$	specific internal energy of phase $\alpha$	$\text{J kg}^{-1}$
$v$	cross-section averaged velocity	$\text{m s}^{-1}$
$\boldsymbol{v}$	fluid velocity	$\text{m s}^{-1}$
$\boldsymbol{v}_\alpha$	fluid velocity of phase $\alpha$	$\text{m s}^{-1}$
$D(\boldsymbol{v})$	symmetric velocity gradient	$\text{s}^{-1}$
$\alpha_{\text{VG}}$	van Genuchten–Mualem model parameter	$\text{Pa}^{-1}$
$l_{\text{VG}}$	van Genuchten–Mualem model parameter	-
$m_{\text{VG}}$	van Genuchten–Mualem model parameter	-
$n_{\text{VG}}$	van Genuchten–Mualem model parameter	-
$V$	sample volume	$\text{m}^3$
$V_\alpha$	volume of phase $\alpha$	$\text{m}^3$
$V_p$	sample pore volume	$\text{m}^3$
Wo	Womersley number	-
$x_\alpha^\kappa$	mole fraction of component $\kappa$ in phase $\alpha$	-

### Mixed-dimension embedded framework

1D/2D/3D one-/two-/three-dimensional

$c$	conserved quantities in the porous domain	
$\hat{c}$	conserved quantities in the network domain	
$\delta_\Lambda$	Dirac delta distribution	$\text{m}^{-2}$
$F$	fluxes in the porous domain	
$f$	fluxes in the tube domain	
$\Gamma$	intersection between two objects	
$\Lambda$	continuous embedded / network domain, vascular domain	
$\Omega$	continuous bulk / porous domain, extra-vascular domain	

$\Phi_\Lambda$	kernel function	$m^{-2}$
$q$	sources in the porous domain	
$\hat{q}$	(line) sources	
$\bar{u}$	average of a variable $u$ over perimeter of a tube cross-section	
$r$	local radius of a network segment	$m$
$\varrho$	radial kernel extent	$m$
$\mathcal{S}$	kernel support	
$u$	primary variables in the network domain	
$w$	primary variables in the porous domain	

#### Sub- and superscripts

$\alpha$	phase
BL	boundary layer
B	blood
$\kappa$	component
I	interstitial fluid
n	non-wetting fluid phase
m	embedding porous medium / domain
r	root compartment / domain
s	soil compartment / domain
t	extra-vascular compartment / domain
up	upwind
v	embedded network compartment / domain
v	vascular compartment / domain
$\omega$	wall / membrane of a tube segment
w	wetting fluid phase



# Abstract

Flow in vascularized biological tissue, root water uptake, or flow around injection or extraction wells can be modeled by coupled mixed-dimensional PDE systems. Conceptually, such systems can be described as porous media with embedded tubular transport networks. We describe numerical methods for the simulation of such systems. The compartments are spatially discretized by non-matching computational grids: a three-dimensional mesh for the porous medium domain, and a geometrically embedded mesh of connected line segments for the network domain. A generalized abstract form of mixed-dimension embedded models is presented which summarizes several existing methods. A particularity of solutions to mixed-dimensional PDEs with dimensional gap two (0D-2D or 1D-3D) is the occurrence of singularities where the network center-lines intersect the porous domain. We introduce a new numerical scheme which removes these singularities by smoothing kernels, and exhibits improved convergence behavior and accuracy for coarse grid resolutions. The method is developed for isotropic, as well as anisotropic porous media. Furthermore, a new mixed-dimension embedded model for tissue perfusion and NMR signal generation is presented. Detailed perfusion simulations on the capillary scale are shown to reproduce image contrast of clinical (organ-scale) MRI data from multiple sclerosis patients. Similar modeling techniques and methods are then used to simulate root water uptake. For the implementation of such applications, a common software framework is developed by use of the open-source simulator DuMu<sup>x</sup>. The framework allows the implementation of coupled mixed- and equidimensional models in a unified way, using software abstractions. Possible framework applications go beyond the methods presented in this work.





# Deutsche Zusammenfassung

Poröse Medien weisen durch ihren kleinskaligen, stark gewundenen Porenraum große Fließwiderstände auf. In einigen biologischen und technischen Anwendungen ermöglichen eingebettete hohle Netzwerkstrukturen effizienten Massen- und Energietransport. Zum Beispiel besteht das Herz-Kreislauf-System zum größten Teil aus einem Netzwerk an Blutgefäßen, welches Funktionalgewebe mit Flüssigkeit, Nährstoffen, Sauerstoff und anderen lebensnotwendigen Substanzen versorgt und von metabolischen Abfallprodukten befreit. Die kleinsten Blutgefäße (Kapillaren) bilden ein dichtes Netzwerk welches Transportwege minimiert. Durch den hierarchischen Netzwerkaufbau können Gewebe und Zellen gleichmäßig und effizient versorgt werden. Pflanzen weisen ganz ähnliche Strukturen auf. Ein hierarchisches Wurzelsystem ermöglicht den Pflanzen Wasser aus selbst trockensten Böden aufzunehmen oder zu verteilen. Moderne Bohrtechniken ermöglichen die Bohrung von Netzwerksystem aus Brunnen in extrem undurchlässigen geologischen Formationen wie Ölschiefer. Solche Bohrlöcher werden zur Öl- und Gasförderung, aber auch für geothermische Energieerzeugung und Energiespeicherung im Untergrund eingesetzt.

Mathematische Modelle fluidmechanischer Prozesse und deren Rolle in biologischen Geweben sind wichtig, um die Gewebestruktur zu verstehen. Zum Beispiel ist es im Kapillarnetzwerk schwer Experimente im lebenden Organismus durchzuführen, ohne die natürliche Umgebung zu stören. Oft sind Experimente ethisch nicht vertretbar. Nichtinvasive Bildgebungsverfahren, wie die Magnetresonanztomographie (MRT), können die Mikrostruktur des Gewebes und der Blutgefäße nicht auflösen. Interessanterweise sind jedoch die Signale, die in der MRT gemessen werden, direkt von der Gewebestruktur und -durchströmung beeinflusst. Solche Effekte können in Simulationen und durch mathematische Modelle analysiert werden. Darum entwickeln wir in dieser Arbeit ein MRT Modell, das auf Prozessen der Kapillarskala beruht, aber Bildpunkte aus klinischen Daten auf der MRT-Skala reproduzieren kann. Mittelfristig könnte die Analysen durch solche Modelle zur besseren Interpretierbarkeit solcher Bildgebungsverfahren führen.

Effiziente numerische Simulation solcher System basieren auf Modellreduktionstechniken. Diese sind notwendig, da die Netzwerke oft aus zahlreichen Segmenten bestehen. Die Durchströmung der Netzwerke kann oft hinreichend genau durch querschnittsgemittelte

Größen beschrieben werden. Dies bedeutet eine Modellreduktion um zwei Raumdimensionen. Strömungen im porösen Medium weisen jedoch dreidimensionale Strukturen auf. Die resultierenden gekoppelten partiellen Differentialgleichungen werden als gemischt- bzw. hybrid-dimensional bezeichnet. Zur numerische Berechnung von Lösungen solcher Gleichungssysteme, sind spezielle nicht-lokale Methoden notwendig. Diese Arbeit gibt einen Überblick über solche Methoden.

Insgesamt leistet diese Dissertation ein Beitrag zur Beschreibung und zum Verständnis hybrid-dimensionaler Modelle von porösen Medien mit eingebetteten Netzwerken. Die Arbeit umfasst die mathematische Modellierung und die Diskussion numerischer Methoden anhand von drei Anwendungen: Durchströmung von biologischem Gewebe, Wasseraufnahme durch Wurzeln und Brunnenmodellierung. Die Modellgebiete für diese Anwendungen bestehen hauptsächlich aus zwei Teilen: Einem porösen Medium, welches diskret durch ein dreidimensionales Rechengitter dargestellt wird und ein eingebettetes Netzwerk von geraden Liniensegmenten, die geometrisch nicht zwingend mit den dreidimensionalen Gitterzellen übereinstimmen. In jedem Gebiet werden zunächst unabhängig Bilanzgleichungen formuliert, die dann über geeignete Bedingungen gekoppelt werden. Wir präsentieren einen generalisierten, abstrakten Ansatz für die konsistente Beschreibung solcher System, der mehrere existierende Methoden beinhaltet. Eine Besonderheit von Lösungen solch hybrid-dimensionaler gekoppelter Gleichungssysteme (0D-2D oder 1D-3D) sind Singularitäten an den Schnittpunkten der Gebiete. In dieser Arbeit entwickeln wir eine neue numerische Methode, die diese Singularitäten durch Glättungskernel kontrolliert und zu besserem Konvergenzverhalten und erhöhter Präzision auf groben Rechengittern führt. Die Methode wird für sowohl für isotrope als auch anisotrope poröse Medien entwickelt. In der zweiten Hälfte der Arbeit werden hybrid-dimensionale Modelle für die Nachbearbeitung von klinischen MRT Daten und die Modellierung der Wasseraufnahme von Wurzeln angewendet. Außerdem wird ein abstraktes Softwareframework entwickelt, das es erlaubt, die beschriebenen Modelle vereinheitlicht zu programmieren. Das entwickelte Framework erlaubt auch Simulation von allgemeineren gekoppelten Simulationen, außerhalb des Rahmens der in dieser Arbeit behandelten Problemklassen.

# 1 Introduction

Porous media often exhibit high flow resistance due to narrow and tortuous pore structures. In several biological and technical applications, embedded hollow network structures enhance transport of mass or energy through such media. For example, the cardiovascular system comprises a network of blood vessels which supplies functional tissue with fluids, nutrients, oxygen and other substances, and clears metabolic waste products. The smallest blood vessels (capillaries) form a dense network to minimize transport pathways through the extra-cellular space—a porous structure. By hierarchical organization of the network, tissue and cells can be supplied evenly and efficiently with vital substances. Similarly, plants form hierarchical root systems to extract and distribute water in the vadose zone. Modern drilling techniques allow creating networks of wells inside ultra-low-permeable geological layers, such as shale for oil and gas production, as well as for geothermal energy production and subsurface energy storage. In all mentioned applications, the exchange of mass and energy between the network system and the supplied porous structure is essential for fluid transport through the porous system.

Mathematical models of the fluid-mechanical processes and their role in biological porous media with embedded transport networks are essential to understand the functional concepts behind their design. In particular for the microvasculature, in-vivo experiments are difficult to conduct without disturbing the natural environment and are often ethically not justifiable. Moreover, for non-invasive imaging techniques such as magnetic resonance imaging (MRI), image resolutions are insufficient to resolve the microvasculature. However, the signal measured in MRI scanners is directly affected by the tissue microstructure and perfusion. Such effects can be analyzed in-silico using mathematical models, which may ultimately lead to the improvement or better interpretability of such methods. Therefore, we develop a mathematical model based on processes on the capillary scale which can reproduce MRI signals from clinical data on the organ scale (see Chapter 9).

Efficient numerical simulations require model reduction techniques since the number of segments in a network can get very large. The network flow can usually be described by cross-section averaged quantities, which reduces the model spatially by two dimensions. However, flow patterns in the embedding porous medium are usually three-dimensional. The resulting

coupled partial differential equation systems can be described as mixed-dimensional. In the numerical approximation of solutions to such equations, non-standard and non-local methods arise. This work gives an overview over such methods. Moreover, several existing methods are summarized in a common mathematical framework. A new method for the numerical approximation of mass exchange between porous media and embedded networks is presented in Chapters 7 and 8.

This dissertation is a contribution to the description and understanding of mixed-dimension embedded models, covering mathematical modeling as well as numerical methods at the example of three applications: biological tissue perfusion, root water uptake, and well modeling. In the remaining part of this introduction, Sections 1.2 to 1.3 discuss the three applications individually and briefly summarize the state-of-the-art modeling techniques for each application domain. The content of Sections 1.2 to 1.3 is based on Koch et al. (2018b, 2020d,c). Section 1.4 outlines the mixed-dimension embedded model concept used in this work for the mathematical description of all systems. Section 1.5 concludes with a structural overview of the rest of this work.

## 1.1 Biological tissue perfusion models

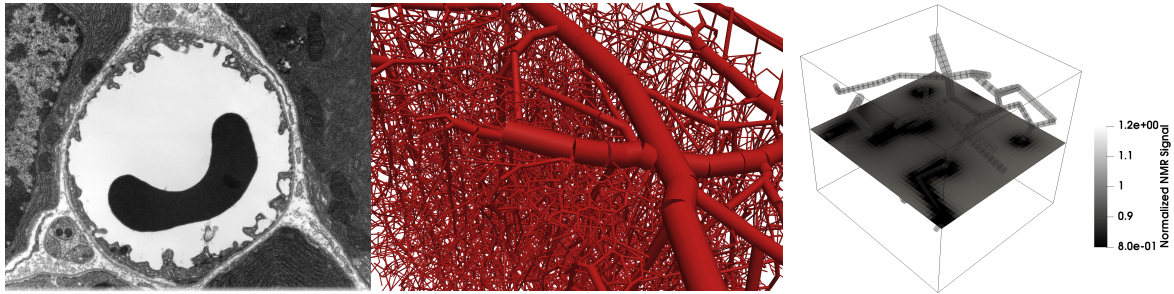


**Figure 1.1 – Tissue perfusion.** Left, capillary cross-section with red blood cell and surrounding tissue, transmission electron microscopy image (license: public domain), Middle, rendering of segmented blood vessel network sample from mouse cortex, from data by Blinder et al. (2013). Right, simulation of NMR signal in a small capillary network using DuMu<sup>x</sup>, see Chapter 9.

Due to the large number of vessels in the microvasculature (see Fig. 1.1), fully three-dimensionally resolved computational models are only feasible for small tissue samples. A class of simplified models uses homogenization techniques to obtain a porous medium, including both the extra-vascular space and the vascular system in the homogenization

process (Chapman et al., 2008; Shipley and Chapman, 2010; Penta et al., 2015; Schröder et al., 2018; Ehlers and Wagner, 2015; Wagner and Ehlers, 2010; Wagner et al., 2018; Roose and Swartz, 2012). However, such models are difficult to parameterize and often neglect the hierarchical nature of the vascular network. The latter shortcoming is addressed by Michler et al. (2013) and Hyde et al. (2013) by using a hierarchical multi-continuum porous medium model. A further improvement are hybrid models, for which only the microvasculature is homogenized and larger vessels, such as the pial and the major penetrating vessels in the brain cortex, are discretely resolved with one-dimensional models (El-Bouri and Payne, 2015; Peyrounette et al., 2018; Shipley et al., 2019; El-Bouri and Payne, 2018; Vidotto et al., 2019). The referenced models neglect the effect of the extra-vascular compartment, which is included in a recent study by Vidotto et al. (2019). The study compares a hybrid model to a mixed-dimension model with discretely resolved microvasculature. However it shows that it remains difficult to parameterize continuum models to reproduce the flow characteristics estimated with a discrete vascular graph model.

Another approach considers stationary solutions for homogeneous extra-vascular compartments. The pressure or concentration maps in the extra-vascular compartment are approximated by an analytical solution obtained by the superposition of point sources along the vascular graph (Beard and Bassingthwaite, 2001; Secomb et al., 1993, 2004; Sun and Wu, 2013; Goldman, 2008). The method, introduced by Hsu and Secomb (1989) as the Green's function method for the study of oxygen transport (Secomb et al., 2000, 2004), has been recently adapted to study tumor perfusion (Robert et al., 2016; d'Esposito et al., 2018; Sweeney et al., 2019). These models cannot capture transient effects.

Herein, we consider a class of models, for which the microvasculature is represented by a network of vessel segments embedded in the extra-vascular space. The flow in the vessels is modeled by partial differential equations (PDEs) with spatial dimension one, whereas the extra-vascular space is modeled as a homogenized porous medium described by PDEs with spatial dimension three. The PDEs are coupled via source terms. The three-dimensional domain and the one-dimensional domain are independently discretized by computational grids. Such embedded mixed-dimension models have been used to study the proliferation of cancer drugs (D'Angelo, 2007; Cattaneo and Zunino, 2014), nano particle transport for hyperthermia therapy (Nabil et al., 2015), oxygen transport (Fang et al., 2008; Reichold et al., 2009; Linninger et al., 2013), and contrast agent perfusion (Holter et al., 2019). These methods allow to efficiently describe flow and transport in vascularized tissues. Another advantage of such methods, is the description of growing networks without re-meshing.

This is of particular interest for modeling angiogenesis (Secomb et al., 2013), which is, for example, an important factor of tumor growth (Hanahan and Weinberg, 2011).

In this work, we discuss a new consistent mixed-dimension embedded method which allows to approximate the fluid exchange rates between the vascular and the extra-vascular space more accurately for coarse grid resolutions. Furthermore, we use mixed-dimension embedded methods to develop a sub-voxel brain tissue perfusion model to simulate perfusion MRI (magnetic resonance imaging) experiments in-silico. The model is compared with clinical MRI data from multiple sclerosis patients.

## 1.2 Root-soil interaction in the vadose zone\*



**Figure 1.2 – Root water uptake.** Left, liliun root cross-section (license: public domain), Middle, unearthed young root system (license: CC0). Right, simulation of root water uptake using DuMu<sup>x</sup>, see Chapter 10.

Natural vegetation as well as cultivated crops play an important role in the global water budget, above and below the surface. Therefore, understanding transpiration from vegetation is essential and has to be considered in land-atmosphere models used in climatology and hydrology. The interactions of water and plants need to be analyzed on a broad range of temporal and spatial scales (Fatichi et al., 2016), one of them focusing on the interaction of the root system of a single plant with the surrounding soil. Mathematical models and simulation of the relevant processes can help with the fundamental understanding of the plants' reactions to their environment, how plant roots contribute to soil water distribution and flow, adapt to drought, or how they are influenced by soil water contamination or salinization (Shani and

---

\*This introductory section is based on Koch, Heck, Schröder, Class, and Helmig (2018b).

Ben-Gal, 2005). Although in-situ monitoring methods of the physical processes at the soil-root interface are continuously improved, measurements remain difficult (Zarebanadkouki et al., 2013).

Mathematical models of coupled soil-root systems have been developed to study the transfer processes between the soil and the root systems. Such models can also help to analyze and interpret measurements, and support the design of future experimental setups. Challenges include large differences in spatial and temporal scales and the combination of physical, chemical and biological processes in a single model. Existing soil-root models range from single root segment models (Roose and Schnepf, 2008) for local soil-root interface studies, crop models used to predict yields (Malézieux et al., 2009), models with empirical root uptake functions (Somma et al., 1998), to plant-scale models (Javaux et al., 2008) using an explicit description of the three-dimensional root system and root system growth. Dunbabin et al. (2013) recently compiled a detailed overview of plant-scale models. This kind of model is also the focus in this work. Plant-scale models include an explicit description of one or more plant root system architectures embedded in the surrounding soil. The root system (see Fig. 1.2) is usually represented by a network of discrete cylindrical segments, while physical quantities, such as water pressure, are averaged over the cross-section of the cylinder (Clausnitzer and Hopmans, 1994; Doussan et al., 1998). This simplification of the root system architecture increases the computational efficiency in comparison with a three-dimensional resolution of the processes in the roots. As a consequence, the mathematical model is reduced to a PDE system formulated on the center-lines of a tubular network domain. The root network is geometrically embedded into the three-dimensional soil domain (a porous medium). The explicit geometrical description of the root system inside the soil allows modeling transfer processes at the soil-root interface, as well as a natural description of sap and nutrient transport within the root system.

Many algorithms have been developed to model soil-root interaction and root architecture. We only mention here a selection that features three-dimensional root architecture models including at least some interaction with the soil: Diggle (1988); Clausnitzer and Hopmans (1994); Lynch et al. (1997); Pagès et al. (2004); Javaux et al. (2008); Leitner et al. (2010); Schneider et al. (2010); Postma et al. (2017). However, these models are either restricted to the Richards flow model or more simplified soil flow models, or lack the description of soil flow and transport entirely, and are restricted to specific models for the description of xylem flow and water and nutrient uptake, see Dunbabin et al. (2013) for a review. The numerical schemes of the available models are not generally locally mass-conservative which can be an

issue if quantification of tracers and root water uptake is of interest. Only one of the models mentioned by Dunbabin et al. (2013) is publicly available under an open-source license. The root system architecture model SimRoot (Lynch et al., 1997) has been recently extended by a hydrology module, and is now available under an open-source license (Postma et al., 2017). Although such models have been developed since the late 1980s, the literature focusing on the numerical aspects of such models is surprisingly sparse. To the best of our knowledge, the only studies focusing on the effects of grid refinement are by Schröder et al. (2008, 2009a). Schröder et al. (2008) compare numerical solutions to an analytical approximation in a simplified setting and conclude that fine grid resolutions are necessary to yield accurate results. Furthermore, they note in their introduction that their numerical model, which is state-of-the-art in the root-soil modeling community (Dunbabin et al., 2013), does not behave well when refining the soil grid.

In this work, we propose a simulation framework with strong emphasis on a consistent and generalized formulation of the fluid mechanical processes. The interaction between root and soil is described by a mathematically sound mixed-dimension embedded model. The interaction between different transport processes in the vadose zone is investigated by numerical experiments in Chapter 10.

### 1.3 Well modeling in geological formations

The accurate description of the flow around wells is essential for various engineering applications, as for example reservoir simulation, geothermal energy production or energy storage, where injection or extraction processes strongly influence the flow behavior. In the majority of models, the well geometry is not explicitly resolved in the mesh but instead modeled as a line source with given extraction or injection rate. However, this simplified approach introduces singularities, meaning that the logarithmic solution profiles are undefined at the center-line of the well. This leads to a significant deviation between numerical and analytical solution in the near-well region. For a better approximation, locally refined meshes around the wells are needed, which however deteriorate efficiency and are therefore often not suitable for field-scale simulations, especially when multiple wells are present.

A common approach is the use of well-index-based well models. Such well models aim to find a relation between well rate, bottom hole pressure and numerically calculated



pressure (well-block pressure) for each cell (grid-block) that contains the well. In reservoir engineering such a relation is denoted as well index. The first theoretical derivation of a well index for two-dimensional structured uniform grids with isotropic permeability has been presented by Peaceman (1978). A discussion of possible extensions and generalization to other discretization schemes can be found in the review by Chen and Zhang (2009), with the restriction of two-dimensional grids. An extension to three-dimensional slanted wells is presented in Alvestad et al. (1994); Aavatsmark and Klausen (2003). Babu and Odeh (1989); Babu et al. (1991); Wolfsteiner et al. (2003) use Green's functions for the computation of well indices. Hales (1997); Gjerde et al. (2019) use a singularity subtraction method to obtain smooth solutions in the near-well region.

Dogan (2011) discusses coupled models of one-dimensional tube flow with three-dimensional porous medium flow in terms of a dual-continuum model. The tube center-lines conform with the edges of the computational grid of the three-dimensional domain. The mass exchange between the two compartments is modeled by linear mass transfer function derived from a dual-continuum approach although the network domain is discretely represented and not homogenized as to obtain a continuum on a coarser scale. This means that models derived for different scales are coupled. Furthermore, the transfer coefficient is scale-dependent. Surprisingly, Dogan (2011) assesses in a numerical test that his numerical method is very robust with respect to grid refinement and concludes that 1D-3D mixed-dimension approaches are less grid sensitive than 2D-3D mixed-dimension approaches (for example discrete fracture models). We question his conclusion. Due to the dimensional gap of two, pressure solutions in 1D-3D mixed-dimension flow problems exhibit large and nonlinearly increasing gradients in vicinity of the tubes, even for single phase flow problems. Typical errors of the pressure solution observed in grid convergence studies against analytical solutions are relatively low even for coarse 3D grid resolutions in comparison with the fracture aperture for the 2D-3D case (Ahmed et al., 2015; Gläser et al., 2017a). For the 1D-3D case, similar error magnitudes can only be obtained by using 3D grid resolutions in the order of the tube radius and smaller (D'Angelo, 2007; Köppl et al., 2016, 2018); see also Chapter 7 in this work.

In Cerroni et al. (2019), well modeling is (to the best of our knowledge) first discussed in terms of fully coupled PDE systems of one-dimensional PDEs for the well flow, and three-dimensional PDEs for describing the flow in the embedding rock. However, due to the employed numerical method they require fine grids for the rock domain. In this work, we contribute to the development of more accurate well models by presenting an embedded mixed-dimension method for porous media with anisotropic permeability tensor fields,

which achieves a higher accuracy in modeling the flow field in some distance to the well for coarse grid resolutions than conventional approaches.

## 1.4 Modeling concept

All introduced applications make use of the same modeling concept. They have in common that tubular network systems supply fluids to, or extract fluids from an embedding porous domain. Specifically, in the first application, the porous domain is the biological soft tissue which is supplied with fluids, nutrients, and oxygen by a hierarchical network of blood vessels. In the second applications water and nutrients are extracted from (or redistributed in) the top layer of the soil by a network of roots. In the last application, water, fracking fluid, or oil is injected to or produced from the rock matrix in a geological formation, or from an aquifer. The network tube radius is small in comparison with the domain size. This allows using model reduction techniques which render conservation equations in the network domain one-dimensional in space. Due to these similarities, we treat these applications in a common mathematical and numerical framework. In particular, we want to emphasize that although the individual chapters in this work mostly focus on a single application, the presented concepts, methods and results are directly relevant for the respective other applications.

The numerical implementation of mixed-dimension methods is rather difficult in comparison with standard methods. For the sake of improved software sustainability, faster prototyping of new methods, and flexibility with respect to the considered physical processes, we develop an open-source software framework dedicated to problems such as the implementation of mixed-dimension embedded models. The software framework goes even further, and discusses mixed-dimension embedded models as a sub-class of coupled problems of different physical processes, on possibly different spatial domains, discretized with possibly different numerical methods.

## 1.5 Overview and structure

In Chapter 2, we briefly introduce the common concept and terminology for modeling flow and transport in porous media. In the following Chapters 3 to 5, we derive math-

---

emtical models for three different fluid-mechanical problems. In Chapter 3, we derive a fluid-mechanical model for drug proliferation in brain tissue including flow in the microvasculature and the extra-vascular extra-cellular space. Chapter 4 presents a model for thermo-fluid-mechanical processes in the vadose zone including root water uptake, solute transport, plant transpiration and soil evaporation. Finally, in Chapter 5 we discuss mathematical models used for well modeling in the petroleum industry, for geothermal energy systems, or groundwater wells. The chapters emphasize how the same modeling concept emerges for all three applications, such that they can be treated in a common mathematical and numerical framework. We discuss state-of-the-art techniques in relation to the presented model, and investigate the most important modeling assumptions to arrive at the presented models. A general framework and the corresponding terminology to describe embedded mixed-dimension problems of tubular networks in porous media is presented in Chapter 6. In Chapter 7, we present a new numerical method for embedded mixed-dimension problems using distributed sources on the example of the simulation of tissue perfusion. The method is extended for porous media with anisotropic permeability in Chapter 8, for the example of well modeling in the context of single phase flow in porous media. In Chapter 9, a mixed-dimensional model is used to develop a sub-voxel tissue perfusion model for the analysis of perfusion MRI data. The resulting model is compared to clinical MRI data. In Chapter 10, we present simulations of root water uptake and root growth in unsaturated soil. Chapter 11 discusses implementation aspects of the presented models. Finally, summary and outlook are presented in Chapter 12.



## 2 Flow and transport in porous media

This chapter briefly introduces some basic concepts and terminology for modeling flow and transport in porous media. Porous media are materials with an internal pore structure, such as sponges, soil, rocks, or biological tissue. Herein, we describe flow through porous media using continuum theory (Bear, 2013). The physical processes are not described on the scale of the individual pores and grains of the soil but rather in terms of continuum-scale quantities, volume fractions, using mixture theory (Truesdell, 1984). The relevant scale is defined by the size of a representative elementary volume (REV), which is the minimal volume for which characteristic macro-scale quantities are representative of a much larger volume of a porous medium (Hill, 1963). The REV size can range from micrometers (e.g. for biological tissues) to millimeters (e.g. for sand) to kilometers (e.g. for a fractured rock system). For a porous medium sample with total volume  $V$ , we define the porosity

$$\phi = \frac{V_p}{V}, \quad 0 < \phi < 1, \quad (2.1)$$

where  $V_p$  is the total pore volume (or void volume) of the sample. We neglect mechanical deformation of the matrix (the solid skeleton), as well as swelling, dissolution, and precipitation processes, so that the porosity is usually constant over time, but may be spatially varying. The pore space is filled by one or more fluid phases. The saturation of a phase  $\alpha$  is defined by

$$S_\alpha = \frac{V_\alpha}{V_p}, \quad \text{with } \sum_\alpha S_\alpha = 1, \quad (2.2)$$

where  $V_\alpha$  denotes the volume occupied by the phase  $\alpha$  in the given sample.

In the following, we consider systems with a maximum of two fluid phases occupying the pore space. The interface between two phases is normally curved, since one phase usually has a lower contact angle (wetting phase) when wetting the matrix than the other phase (non-wetting phase). Due to low fluid velocities in porous media, a common assumption is that of local thermodynamic equilibrium, see for example Class et al. (2002). In equilibrium, there is a pressure difference between two fluid phases called capillary pressure

$$p_c = p_n - p_w, \quad (2.3)$$

where  $p_n$  and  $p_w$  are the pressures of the non-wetting and the wetting phase fluid, respectively. The capillary pressure between two fluids in a narrow tube can be described by the Young-Laplace equation depending on the contact angle, surface tension, and the radius of the tube. On the continuum scale, capillary pressure is usually formulated as a function of the wetting fluid saturation with empirically determined parameters. A common parametrization for two-phase systems in soils is the Van Genuchten model (Van Genuchten, 1980)

$$S_{we} = [1 + (\alpha_{vg} p_c)^{n_{vg}}]^{-m_{vg}}, \quad m_{vg} = 1 - \frac{1}{n_{vg}}, \quad S_{we} = \frac{S_w - S_{wr}}{1 - S_{wr} - S_{nr}} \quad (2.4)$$

where  $\alpha_{vg}$  and  $n_{vg}$  are empirical shape parameters depending on soil properties, such as the grain size distribution. The residual saturation,  $S_{\alpha r}$ , is an empirical parameter describing a saturation threshold below which the phase  $\alpha$  is immobile, and  $S_{we}$  is the effective wetting saturation. In the soil sciences, Eq. (2.4) is usually formulated in terms of the water content  $\theta := \phi S_w$ , the residual water content  $\theta_r := \phi S_{wr}$ , and the water content at saturation,  $\theta_{sat} := \phi$ .

The fluid flow through the rigid matrix is characterized by the filter velocity\*

$$\mathbf{v}_\alpha = -\frac{k_{r\alpha}}{\mu_\alpha} \mathbf{K} (\nabla p_\alpha - \rho_\alpha \mathbf{g}) \quad (2.5)$$

for each phase  $\alpha$  (Helmig, 1997), where  $\mu_\alpha$  is the dynamic viscosity,  $\rho_\alpha$  the density, and  $p_\alpha$  the fluid pressure of phase  $\alpha$ . The intrinsic permeability tensor field  $\mathbf{K}$  is a friction coefficient of the solid matrix, and  $\mathbf{g}$  the gravitational field. The dimensionless relative permeability  $k_{r\alpha}$  describes the apparent reduction in permeability for one phase due to the presence of other phases. It is commonly modeled by an empirical relationship. For instance, for the Van Genuchten–Mualem model for two-phase flow (Van Genuchten, 1980; Mualem, 1976; Luckner et al., 1989),

$$k_{rw} = (S_{we})^{l_{vg}} \left[ 1 - \left( 1 - S_{we}^{\frac{1}{m_{vg}}} \right)^{m_{vg}} \right]^2, \quad k_{rn} = (1 - S_{we})^{l_{vg}} \left[ 1 - S_{we}^{\frac{1}{m_{vg}}} \right]^{2m_{vg}}. \quad (2.6)$$

The pore-connectivity parameter  $l_{vg}$  is commonly chosen as 0.5 due to Mualem (1976) (the parameter has the symbol  $n$  in the original paper), who showed good agreement for a wide range of soils. Sometimes,  $l_{vg}$  is used as additional empirical fitting parameter, e.g. by Wösten et al. (2001). For single-phase flow of phase  $\alpha$ ,  $k_{r\alpha} = 1$  and  $S_\alpha = 1$ .

\*also “seepage velocity” or “Darcy velocity”, due to Darcy (1856)

A fluid phase can consist of several components,  $\kappa$ . For multi-component systems, diffusion is often an important transport process. For components with low concentrations (solute) dissolved in a phase mostly consisting of a single main component (solvent), diffusion fluxes can be described by Fick's law with binary diffusion coefficients,  $D_\alpha^\kappa$ . In a multi-phase porous medium system modeled on the continuum scale, the effective diffusion coefficients are lower than diffusion coefficients in pure fluids due to the tortuous nature of the pore network and the local phase distribution. An effective diffusion coefficient can be estimated by (Bear, 2013)

$$D_{\alpha,e}^\kappa = \tau S_\alpha \phi D_\alpha^\kappa, \quad (2.7)$$

where  $\tau$  is the tortuosity of the pore space.

Moreover, the phases may be considered miscible, that is that components of one phase can dissolve in another phase. In local thermodynamic equilibrium, all components in a given small control volume have equal chemical activity. Hence, the phase composition in this control volume can be computed from pressure and temperature (Class, 2007) and the constraint

$$\sum_\kappa x_\alpha^\kappa = 1, \quad (2.8)$$

where  $x_\alpha^\kappa$  denotes the mole fraction of component  $\kappa$  in phase  $\alpha$ . For example, in a water-air system  $\kappa \in \{w, a\}$ ,  $\alpha \in \{l, g\}$ , the equilibrium mole fraction of water in the gas phase g can be computed with Dalton's law, and assuming that water vapor is in equilibrium with liquid water,

$$x_g^w = \frac{p_{\text{sat}}^w}{p_g}, \quad (2.9)$$

where  $p_{\text{sat}}^w = p_{\text{sat}}^w(T)$  is the saturation vapor pressure of water. The mole fraction of air in the liquid phase l can be approximated with Henry's law

$$x_l^a = \frac{p_g^a}{H_w^a}, \quad (2.10)$$

with the partial air pressure  $p_g^a = x_g^a p_g$ , and the Henry coefficient for the dissolution of air in water  $H_w^a = H_w^a(T)$ , see e.g. Helmig (1997).

For non-isothermal systems, we need to describe heat conduction. Again, we use the assumption of local thermodynamic equilibrium. This means that a single temperature is assigned to all fluid phases and the solid matrix within a small control volume. Heat

conduction is then described with an effective thermal conductivity  $\lambda_e$ , depending on the local volume fractions and the thermal conductivities of all fluid phases and the solid phase. A suitable model for estimating the effective thermal conductivity is, for instance, given by Somerton et al. (1974)

$$\lambda_e = \lambda_{\text{dry}} + \sqrt{S_w} (\lambda_{\text{wet}} - \lambda_{\text{dry}}), \quad (2.11a)$$

$$\lambda_{\text{wet}} := \lambda_s^{(1-\phi)} \lambda_w^\phi, \quad (2.11b)$$

$$\lambda_{\text{dry}} := \lambda_s^{(1-\phi)} \lambda_n^\phi, \quad (2.11c)$$

where  $\lambda_s$  is the thermal conductivity of the solid matrix and  $\lambda_\alpha$ ,  $\alpha \in \{w, n\}$ , the thermal conductivity of the wetting and non-wetting fluid phases, respectively. The geometric mean in Eqs. (2.11b) and (2.11c) is suggested by Somerton (1992) due to a good match with experimental data.

For a more detailed description on modeling multi-phase flow and transport in porous media, we refer to Helmig (1997) and Class (2007).



### 3 Modeling tissue perfusion\*

In the following chapter, we describe the brain tissue perfusion model used in this work in the context of perfusion magnetic resonance imaging (MRI). Many of the presented concepts and assumptions also apply for other vascularized tissues. Of particular interest is the exchange of substances over the endothelium, which takes place primarily in the smallest blood vessel, the capillaries, characterized by diameters (in humans) of about 5 to 10  $\mu\text{m}$ .

The tissue is decomposed into two domains. The vascular compartment comprises blood vessels, including the capillary lumen, the endothelial surface layer, the basement membrane, and blood. The extra-vascular compartment includes cells, the extra-cellular matrix (ECM), and the interstitial fluid. The compartments communicate by the exchange of substances over the capillary wall (transmural exchange). In the following three sections, the modeling assumptions are discussed separately for both compartments and the transmural exchange. These sub-domain models are then combined, to obtain a mixed-dimension tissue perfusion model. The model reduction process from a three-dimensional vessel model to a one-dimensional vessel model including transmural exchange is summarized schematically in Fig. 3.1.

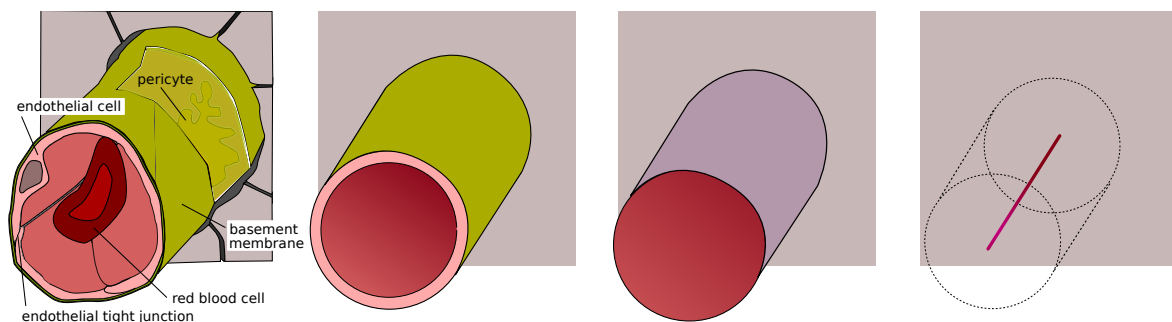


**Figure 3.1 – Modeling of blood flow in capillaries by step-wise abstraction and model reduction.** The capillary is modeled as a leaky tube, with a selectively permeable membrane wall. The wall is reduced to a two-dimensional surface. Finally, the three-dimensional flow model is reduced to a one-dimensional cross-section averaged flow model. For the anatomical structure of continuous and other capillary types, see e.g. Junqueira et al. (2002).

---

\*This chapter is based on Koch, Flemisch, Helmig, Wiest, and Obrist (2020a).

### 3.1 Blood flow and drug transport in capillaries

Blood plasma can be modeled as an incompressible Newtonian fluid and its flow through the vessel lumen is described by the Navier-Stokes equations, similar to water flow through a pipe,

$$\rho \left[ \frac{\partial \mathbf{v}}{\partial t} + \nabla \cdot (\mathbf{v} \mathbf{v}^T) \right] = 2\mu \nabla \cdot \mathbf{D}(\mathbf{v}) - \nabla p + \rho \mathbf{g}, \quad (3.1a)$$

$$\nabla \cdot \mathbf{v} = 0, \quad (3.1b)$$

where  $\mathbf{v}$  denotes fluid velocity,  $\rho$  fluid density,  $\mu$  fluid viscosity,  $p$  fluid pressure, and  $\mathbf{D}(\mathbf{v}) = \frac{1}{2}(\nabla \mathbf{v} + \nabla^T \mathbf{v})$  is the symmetric velocity gradient. The gravitational vector field is denoted by  $\mathbf{g}$ . For small vessels, we assume that there is no significant vessel dilation due to pressure fluctuations. Blood flow is predominantly laminar, especially within the smaller vessels. Typical Reynolds numbers in capillaries are as small as

$$\text{Re} = \frac{\rho v_c d_c}{\mu} \approx 0.002 \text{ to } 0.006, \quad (3.2)$$

cf. Formaggia et al. (2009), where  $v_c$  denotes a characteristic velocity, and  $d_c$  a characteristic vessel diameter. Flow velocities in capillaries are on the order of than  $1 \text{ mm s}^{-1}$  (Quarteroni and Formaggia, 2004). For creeping flow ( $\text{Re} \ll 1$ ), the non-linear inertial term on the left-hand side can be neglected. We neglect gravitational forces due to the small spatial scale of interest. The Womersley number relates pulsatile flow frequency to viscous effects and can be estimated for capillaries by

$$\text{Wo} = d_c \left( \frac{\omega \rho}{\mu} \right)^{\frac{1}{2}} \approx 0.004 \text{ to } 0.011, \quad (3.3)$$

where  $\omega \approx 1 \text{ Hz}$  is the heartbeat frequency. Therefore, we assume a quasi-stationary flow regime. Under these conditions, Eq. (3.1) can be simplified to the stationary incompressible Stokes equations

$$-2\mu \nabla \cdot \mathbf{D}(\mathbf{v}) + \nabla p = 0, \quad (3.4a)$$

$$\nabla \cdot \mathbf{v} = 0. \quad (3.4b)$$

As radial velocities in long vessels (compared to their radius) are negligibly small in comparison with the axial velocities, the three-dimensional Stokes equations can be further simplified to a one-dimensional description by introducing a cross-section-averaged pressure and assuming a specific axial velocity profile (Formaggia et al., 2003), so that

$$\frac{\partial(\rho A_v v)}{\partial s} = -\frac{\partial}{\partial s} \left( \rho \frac{A_v r_v^2}{2(2+\gamma)\mu} \frac{\partial p_v}{\partial s} \right) = -\hat{q}_m, \quad (3.5)$$

with the equivalent vessel radius  $r_v$ , the vessel cross-section area  $A_v = \pi r_v^2$ , the mean velocity  $v$ , the cross-section averaged pressure  $p_v$ , and the local axial coordinate  $s$ . The rate of mass exchange with the extra-vascular compartment is denoted by  $\hat{q}_m$  (units of  $\text{kg s}^{-1} \text{m}$ ). A model for  $\hat{q}_m$  is discussed in Section 3.2. The shape parameter  $\gamma$  parameterizes the assumed axial velocity profile,

$$\mathbf{v} \cdot \mathbf{n}_z = \frac{1}{\gamma}(2+\gamma) \left[ 1 - \left( \frac{r}{r_v} \right)^\gamma \right] v, \quad (3.6)$$

where  $\mathbf{n}_z$  denotes a normalized vector in local axial direction. A parabolic profile is obtained for  $\gamma = 2$ . Higher values yield plug flow velocity profiles (flat in tube center, large gradients at the wall). Modeling blood flow by models using one-dimensional descriptions is very common (also for larger vessels and pulsatile flow) due to the large reduction in model complexity (cf. Olufsen et al., 2000; Sherwin et al., 2003; Formaggia et al., 2003, 2009; Blanco et al., 2015; Köppl, 2015; Perdikaris et al., 2016; Quarteroni et al., 2017). For many situations one-dimensional models have shown to accurately describe physiological flow characteristics.

Until here, we only considered blood plasma or blood as a single continuum phase. However, blood is a mixture of several components. Most prominently, it consists of red blood cells (RBC), white blood cells, blood platelets, plasma and plasma proteins (Formaggia et al., 2009). The shear stress behavior of the mixture is usually considered non-Newtonian (Misra et al., 1993). RBCs are typically non-uniformly distributed in blood vessels and affect the local flow resistance. Several well-known effects influencing the local RBC distribution are the Fåhræus effect, the Fåhræus-Lindqvist effect, and the phase-separation effect at diverging bifurcations (Schmid, 2017). For capillaries with diameters below  $10 \mu\text{m}$ , RBCs ( $\varnothing 6.2$  to  $8.2 \mu\text{m}$  (Turgeon, 2005) in humans) can only move in single file flow through the lumen. To pass through the smallest vessels, RBCs need to deform (Fung and Zweifach, 1971; Popel and Johnson, 2005). In this work, we consider empirical relations describing the influence of the local RBC distribution in terms of an effective viscosity  $\mu_B$  in Pa s, due

to Pries et al. (1996),

$$\mu_B = 0.001 \cdot [220 \cdot \exp(-2.6r_v) - 2.44 \cdot \exp(-0.06 \cdot (2r_v)^{0.645}) + 3.2], \quad (3.7)$$

where we followed Guibert et al. (2012), Linninger et al. (2013), and Gagnon et al. (2015) and assume a constant tube hematocrit of 0.45 for all vessels. The effective or apparent viscosity  $\mu_B$  replaces  $\mu$  in Eq. (3.5). Guibert et al. (2010) suggest that the variance of tube hematocrit is of little importance when analyzing flow through larger networks. For completeness, we mention that recent works considering the tracking of individual RBCs (Obrist et al., 2010; Schmid et al., 2015) suggest that the variability of the local RBC concentration has important regulatory effects on the flow field in microvascular networks (Schmid et al., 2017). Recent continuum model approaches consider temporally constant but spatially varying hematocrit depending on the network topology (Lorthois et al., 2011; Possenti et al., 2019). In this work, we do not consider the phase-separation effect at bifurcations by means of bifurcations rules (Fung, 1973; Pries et al., 1989).

Blood flow models are usually derived at the example of single straight or curved vessel segments. However, in a vessel network, vessels branch and join. We apply Eq. (3.5) for every segment and at such vessel bifurcations, we enforce continuity of pressure and conservation of mass to couple the equations of multiple segments.

The transport of a drug, such as a contrast agent, can be described by an advection-diffusion equation. Again, by integration of the three-dimensional equations over the vessel cross-section, the model can be reduced to a one-dimensional equation for the cross-section-averaged molar concentration  $c_v$  (Formaggia et al., 2003),

$$\frac{\partial (A_v c_v^\kappa)}{\partial t} + \frac{\partial}{\partial s} \left( A_v \omega v c_v^\kappa - A_v D_B^\kappa \frac{\partial c_v^\kappa}{\partial s} \right) = -\frac{\hat{q}_m^\kappa}{M^\kappa}, \quad (3.8)$$

where  $M^\kappa$  is the molar mass of the contrast agent,  $v$  is the mean velocity introduced in Eq. (3.5), and  $D_B^\kappa$  the binary diffusion coefficient of the contrast agent in blood. The exchange with the extra-vascular compartment is modeled by the flux  $\hat{q}_m^\kappa$  (units of  $\text{kg s}^{-1} \text{ m}$ ) as discussed in Section 3.2. The shape factor  $\omega > 0$  reflects the variation of axial velocity

profiles in vessel cross-sections (Formaggia et al., 2003),

$$\omega = \frac{1}{A_v} \int_0^{2\pi} \int_0^{r_v} \chi(r) \phi(r) r \, dr \, d\theta, \quad (3.9)$$

$$\text{with } \frac{1}{A_v} \int_0^{2\pi} \int_0^{r_v} f(r) r \, dr \, d\theta = 1 \quad \text{for } f \in \{\chi, \phi\}, \quad (3.10)$$

where  $\chi(r)$ ,  $\phi(r)$  are the dimensionless velocity profile and the dimensionless concentration profile, respectively. As it has been observed that small nano particles are likely to be distributed evenly in the capillary lumen (Lee et al., 2013), we choose  $\omega = 1$ . Typical Péclet numbers for small nano particle transport in capillaries are in the range of

$$\text{Pe} = \frac{v d_c}{D_B^\kappa} \approx 1 \text{ to } 50, \quad (3.11)$$

such that advective transport is usually slightly more important than diffusive transport. For instance, for the contrast agent Gadobutrol at body temperature,  $D_B^\kappa$  can be estimated by means of the Stokes-Einstein radius,  $r_{\text{hy}} = 0.9 \text{ nm}$  (Guthausen et al., 2015), as

$$D_B^\kappa \approx \frac{k_B T}{6\pi \mu_p r_{\text{hy}}} \approx 1.9 \cdot 10^{-10} \text{ m}^2 \text{ s}^{-1}, \quad (3.12)$$

where  $\mu_p = 1.32 \text{ Pas}$  (Pedersen et al., 2014) denotes the blood plasma viscosity,  $T$  the temperature in K, and  $k_B$  the Boltzmann constant.

## 3.2 Transmural fluid exchange

The wall of continuous capillaries consists of an endothelial surface layer, a basal membrane, and a layer of charged proteins, called glycocalyx (Sugihara-Seki and Fu, 2005). Mass exchange can occur passively through the endothelial tight junctions, or through trans-cellular pathways. Here, we consider only transport by advection and diffusion, following (Formaggia et al., 2009). Given a blood vessel volume fraction of 3 %, an average thickness of the endothelial surface layer of  $1 \mu\text{m}$  (Pries and Kuebler, 2006), and an average vessel radius of  $10 \mu\text{m}$ , the volume fraction of the capillary wall is less than 1 % of the tissue volume. The capillary wall can be conceptually reduced to a two-dimensional interface,

denoted by  $\Gamma$ , separating the vascular from the extra-vascular compartment. Note that this results in a pressure jump across  $\Gamma$ , which is inversely proportional to wall permeability and wall thickness. In the following, the subscripts v and t are used to distinguish between quantities in the vascular and the extra-vascular compartment. According to Starling's hypothesis (Starling, 1896; Kedem and Katchalsky, 1958), the transmural flux of a fluid is proportional to the sum of the hydraulic and the colloid osmotic pressure gradient between capillary lumen and interstitial space

$$\hat{q}_m = \rho_I L_p P_v [(p_v - \bar{p}_t) - \sigma(\pi_v - \bar{\pi}_t)], \quad (3.13)$$

where  $L_p$  is the filtration coefficient, with units of  $\text{mPa}^{-1} \text{s}^{-1}$ ,  $\rho_I$  the density of interstitial fluid,  $P_v = 2\pi r_v$  is the perimeter of a vessel cross-section,

$$\bar{p}_t = \frac{1}{P_v} \int_0^{2\pi} p_t \Big|_{r_v} r_v d\theta \quad (3.14)$$

is the average hydraulic pressure on the perimeter of a vessel cross-section,  $\pi_v, \bar{\pi}_t$ , denote the osmotic pressure in capillary lumen and interstitial space (averaged on the perimeter of a vessel cross-section), respectively, and  $0 \leq \sigma \leq 1$  is the osmotic reflection coefficient. It is close to 1 for macro-molecules and close to 0 for micro-molecules (Jain, 1987). The difference in osmotic pressure results from large plasma proteins in the blood stream (such as albumin), and effectively draws fluid into the vessels. Herein, we approximate the osmotic pressures as constants, so that  $\Delta\pi = \pi_v - \bar{\pi}_t = 2633 \text{ Pa}$  (Levick, 1991). Furthermore, we choose  $\sigma = 1$ .

The filtration coefficient in Starling's law can also be interpreted in terms of a porous medium model of the membrane (Quarteroni and Formaggia, 2004). However, it is questionable whether an REV really exists because of its small dimensions (Baber, 2014). Considering only normal flow across the membrane, the filtration coefficient can be analogously described as

$$L_p = \frac{K_\omega}{\mu_I d_\omega}, \quad (3.15)$$

where  $K_\omega$  is the intrinsic permeability (in normal direction,  $\text{m}^2$ ) of the membrane,  $d_\omega$  the membrane thickness and  $\mu_I$  the interstitial fluid viscosity.

A drug, such as a contrast agent, may be transported by advection and molecular diffusion. Some molecules might be transported across the capillary wall by active transport mechanisms. These effects are hard to quantify and not considered here. Instead, we assume that such processes depend on the concentration difference between vessel lumen and interstitial space and can be modeled by an increased diffusion coefficient. The conceptual reduction of the vessel wall to a surface leads to a concentration jump across the vessel wall, which is inversely proportional to diffusive wall conductivity and wall thickness. The transmural transport can be described as

$$\hat{q}_m^\kappa = D_\omega M^\kappa P_v (c_v^\kappa - \bar{c}_t^\kappa) + \frac{\hat{q}_m}{\rho_I} (1 - \sigma_c) M^\kappa c_{\text{up}}^\kappa \quad \forall \kappa, \quad (3.16)$$

due to Kedem and Katchalsky (1958), where  $D_\omega$  is the effective diffusive wall conductivity, with units of  $\text{m s}^{-1}$ ,

$$\bar{c}_t^\kappa = \frac{1}{P_v} \int_0^{2\pi} c_t^\kappa \Big|_{r_v} r_v d\theta \quad (3.17)$$

is the average contrast agent mole fraction on the perimeter of a vessel cross-section,

$$c_{\text{up}}^\kappa = \begin{cases} c_v^\kappa & \text{if } \hat{q}_m \leq 0 \\ \bar{c}_t^\kappa & \text{if } \hat{q}_m > 0 \end{cases} \quad (3.18)$$

denotes the concentration in upwind direction, and  $0 \leq \sigma_c \leq 1$  denotes the solvent-drag reflection coefficient. For a small contrast agent molecule and especially for cases where endothelial tight junctions are damaged (e.g. in inflamed lesion tissue due to multiple sclerosis), we set  $\sigma_c = 0$ , neglecting reflection. Determining  $D_\omega$  from MRI data is the major objective of the investigations presented in Chapter 9.

### 3.3 Extra-vascular compartment

The extra-vascular compartment is modeled as a porous medium with a rigid solid skeleton, consisting of cells, fibers, and extra-cellular matrix. Flow of a single fluid phase, the interstitial fluid, through a porous medium can be described by Darcy's law (Darcy, 1856)

$$\rho_I \nabla \cdot \boldsymbol{v} = -\frac{\rho_I}{\mu_I} \nabla \cdot (\boldsymbol{K} \nabla p_t) = q, \quad (3.19)$$

where  $\rho_I, \mu_I$  are density and viscosity of the interstitial fluid,  $\boldsymbol{v}$  is the filter velocity,  $\boldsymbol{K}$  is the intrinsic permeability of the extra-vascular compartment, and  $q$  ( $\text{kg s}^{-1} \text{m}^3$ ) denotes the mass exchange with the vascular compartment. For a more detailed description of porous media models for biological soft tissue, we refer to Ehlers and Blum (2002); Wagner and Ehlers (2010); Ehlers and Wagner (2015).

The transport of substances,  $\kappa$ , is modeled by advection-diffusion equations,

$$\phi \frac{\partial c_t^\kappa}{\partial t} + \nabla \cdot (\boldsymbol{v} c_t^\kappa - D_e^\kappa \nabla c_t^\kappa) = \frac{q_m^\kappa}{M^\kappa}, \quad (3.20)$$

where  $\phi$  denotes the porosity of the extra-vascular space,  $D_e^\kappa$  is the effective diffusion coefficient, and  $q_m^\kappa$  ( $\text{kg s}^{-1} \text{m}^3$ ) is the mass exchange with the vascular compartment. We assume that the interstitial space in the extracellular matrix, with pore throat diameters of around 50 nm (Syková and Nicholson, 2008), still allows for a viscous flow regime. Following the literature for tortuosity and porosity values (Syková and Nicholson, 2008), we choose  $\tau = 0.4$  and  $\phi = 0.2$ , and estimate the effective diffusion coefficient with Eq. (2.7).

### 3.4 Mixed-dimension tissue perfusion model

The mass balance equations, Eqs. (3.5), (3.8), (3.19) and (3.20), are coupled by Eqs. (3.13) and (3.16), where Eqs. (3.19) and (3.20) are described in the three-dimensional extra-vascular domain  $\Omega$ , and Eqs. (3.5) and (3.8) are associated with the one-dimensional vascular domain  $\Lambda$ . Mass leaving the vascular compartment has to enter the extra-vascular compartment and vice versa. To enforce this constraint, we introduce the coupling conditions

$$\int_{\Omega} \hat{q}_m \Phi_\Lambda dx = \int_{\Lambda} \hat{q}_m ds, \quad \text{and} \quad \int_{\Omega} \hat{q}_m^\kappa \Phi_\Lambda dx = \int_{\Lambda} \hat{q}_m^\kappa ds, \quad (3.21)$$



with the kernel function  $\Phi_\Lambda$  which will be motivated and defined in Chapter 6. Then, the coupled fluid-mechanical model of tissue perfusion is to find  $p_t$  and  $p_v$  such that

$$\begin{aligned} -\frac{\partial}{\partial s} \left( \frac{\rho_B}{\mu_B} \frac{A_v r_v^2}{2(2+\gamma)} \frac{\partial p_v}{\partial s} \right) &= -\hat{q}_m && \text{in } \Lambda, \\ -\nabla \cdot \left( \frac{\rho_I}{\mu_I} \mathbf{K} \nabla p_t \right) &= \hat{q}_m \Phi_\Lambda && \text{in } \Omega, \\ \rho_I L_p P_v [(p_v - \bar{p}_t) - \sigma(\pi_v - \bar{\pi}_t)] &= \hat{q}_m. \end{aligned} \quad (3.22)$$

Then find  $c_t$  and  $c_v$  such that

$$\begin{aligned} \frac{\partial (A_v c_v^\kappa)}{\partial t} + \frac{\partial}{\partial s} \left( A_v v c_v^\kappa - A_v D_B^\kappa \frac{\partial c_v^\kappa}{\partial s} \right) &= -\frac{\hat{q}_m^\kappa}{M^\kappa} && \text{in } \Lambda, \\ \phi \frac{\partial c_t^\kappa}{\partial t} + \nabla \cdot (v c_t^\kappa - D_e \nabla c_t^\kappa) &= \frac{\hat{q}_m^\kappa}{M^\kappa} \Phi_\Lambda && \text{in } \Omega, \\ D_\omega M^\kappa P_v (c_v^\kappa - \bar{c}_t^\kappa) + \frac{\hat{q}_m^\kappa}{\rho_I} (1 - \sigma_c) M^\kappa c_{\text{up}}^\kappa &= \hat{q}_m^\kappa, \end{aligned} \quad (3.23)$$

subject to appropriate boundary conditions on the boundaries,  $\partial\Lambda$  and  $\partial\Omega$ , of the vascular and the extra-vascular domains,  $\Lambda$  and  $\Omega$ .



## 4 Modeling root-soil interaction\*

This chapter introduces the modeling concepts and assumptions to model non-isothermal, miscible two-phase, two-component subsurface flow in the vadose zone including embedded root systems. Furthermore, we discuss how root growth and water uptake can be simulated simultaneously in a coupled model with improved numerical properties compared to existing growth algorithms, concerning mass conservation.

Looking at the processes in the unsaturated soil (vadose zone) around a plant's root system, we can identify typical processes involving flow and transport of water and nutrients. An overview is schematically presented in Fig. 4.1. Important processes involving the root system architecture are root water uptake, xylem flow and transport of minerals, and root growth. For the water management in the upper layer of the soil, root water uptake is a driver for water movement. However, there are competing driving forces like gravity, soil water evaporation into the atmosphere and water precipitation during rainfall events or irrigation.

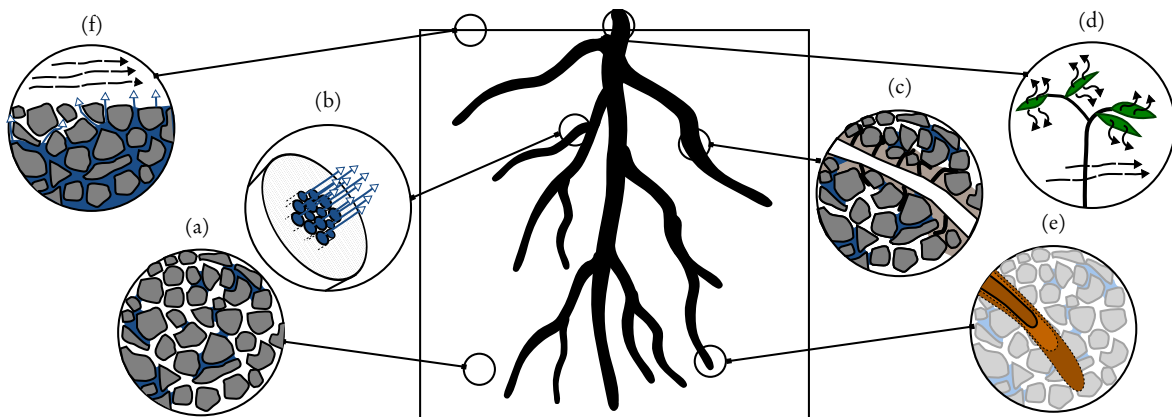


**Figure 4.1 – Typical processes in the vadose zone.** (a) flow and transport in unsaturated soil (see Section 4.1), (b) xylem flow and transport (see Section 4.2), (c) root water uptake (see Section 4.3), (d) transpiration (see Section 4.5), (e) root growth (see Section 4.7), (f) soil evaporation, water precipitation (see Section 4.6). Figure from Koch et al. (2018b).

We conceptually decompose the vadose zone into two domains. The root compartment consists of all embedded root systems and the soil compartment comprises the embedding

---

\*This chapter is based on Koch, Heck, Schröder, Class, and Helmig (2018b).

porous soil matrix. The compartments communicate by the exchange of substances over the root wall (transmural exchange). To model soil evaporation, an additional compartment (atmosphere) comprises a free-flow layer of air in the atmosphere just above the soil surface.

## 4.1 Flow and transport in unsaturated soil

The unsaturated soil (excluding roots) can be described as a two-(fluid)-phase, multi-component, non-isothermal porous media system, with a liquid phase (subscript l) and a gaseous phase (subscript g) that are partly miscible, and the components water (superscript w) and air (superscript a). The governing equations of such a system are given by the conservation equations for mass, energy, and momentum, with the definitions and assumptions made in Chapter 2,

$$\frac{\partial}{\partial t} \left[ \sum_{\alpha} \phi S_{\alpha} c_{\alpha}^{\kappa} \right] + \nabla \cdot \left[ \sum_{\alpha} (c_{\alpha}^{\kappa} \mathbf{v}_{\alpha} - D_{e,\alpha}^{\kappa} \nabla c_{\alpha}^{\kappa}) \right] = \sum_{\alpha} \frac{q_{\alpha}^{\kappa}}{M^{\kappa}}, \quad \forall \kappa \in \{\text{w}, \text{a}\}, \quad (4.1a)$$

$$\frac{\partial}{\partial t} \left[ \sum_{\alpha} (\phi \rho_{\alpha} u_{\alpha} S_{\alpha}) + (1 - \phi) \rho_s c_{p,s} T \right] + \nabla \cdot \left[ \sum_{\alpha} (\rho_{\alpha} h_{\alpha} \mathbf{v}_{\alpha}) - \lambda_e \nabla T \right] = q_h, \quad (4.1b)$$

where the momentum balance is given by the definition of the filter velocity  $\mathbf{v}_{\alpha}$  in Eq. (2.5) for each phase  $\alpha \in \{\text{l}, \text{g}\}$ . In Eq. (4.1a),  $c_{\alpha}^{\kappa} = \rho_{m,\alpha} x_{\alpha}^{\kappa}$  is the molar concentration of component  $\kappa$  in phase  $\alpha$ , with the molar density of the phase  $\rho_{m,\alpha}$  and the mole fraction  $x_{\alpha}^{\kappa}$  of component  $\kappa$  in phase  $\alpha$ , and  $M^{\kappa}$  is the molar mass of  $\kappa$ . In Eq. (4.1b),  $u_{\alpha}$  denotes the internal energy of phase  $\alpha$ ,  $h_{\alpha}$  its enthalpy,  $T$  is the temperature,  $c_{p,s}$  is the specific heat capacity,  $\rho_s$  is the density of the solid matrix,  $\lambda_e$  is the effective heat conductivity introduced in Eq. (2.11), and  $q_h$  summarizes all external energy sources. We assume binary diffusion with one molecule of water replacing one pseudo-molecule of air, so that e.g.  $D_{e,l}^w$  is identical to  $D_{e,l}^a$ , and thus  $D_{e,l}^w \nabla c_l^w = -D_{e,l}^a \nabla c_l^a$ , using Eq. (2.8).

Using the definitions from Chapter 2, Eq. (4.1) and Eq. (2.5) can be formulated in the primary variables  $p_w$ ,  $S_g$ , and  $T$ . Unfortunately, the constitutive equations for computing the phase composition are no longer applicable in case the two-phase system reduces to one-phase flow in parts of the domain. We use the primary variable switching concept as described by Class et al. (2002). For single phase liquid flow, the primary variables are

switched to  $p_w$ ,  $x_1^a$ , and  $T$ , while for single phase gas flow, the primary variables are switched to  $p_w$ ,  $x_g^w$ , and  $T$ . We note that the switching model is based on the practical assumption that the capillary pressure saturation curve, Eq. (2.4), is regularized for low water saturation so that  $p_w$  is finite, even if the liquid phase vanishes.

For most situations in the vadose zone, we can exploit the fact that the viscosity of the gas phase  $\mu_g$  is much smaller than the viscosity of the liquid phase. Therefore, the gas phase can be assumed infinitely mobile,  $m_g = k_{rg} \mu_g^{-1} \rightarrow \infty$ , where  $m_\alpha$  denotes the mobility of phase  $\alpha$ . Furthermore, the dissolution of air in water is often neglected. As a consequence, the pressure of air inside the soil pores is constant and equivalent to the atmospheric pressure, and the conservation equations need to be computed for the water phase only. The resulting liquid phase mass balance replaces Eq. (4.1a),

$$\frac{\partial (\phi S_l \rho_l)}{\partial t} - \nabla \cdot \left[ \rho_l \frac{k_{rl}}{\mu_l} \mathbf{K} (\nabla p_l - \rho_w \mathbf{g}) \right] = q_l^w. \quad (4.2)$$

It still contains the influence of air in the storage term and the constitutive relationship for the relative permeability  $k_{rl}$ , given by Eq. (2.6). Assuming an incompressible liquid phase ( $\rho_l = \text{const.}$ ) and a constant water viscosity  $\mu_l$ , this model is known as the Richards equation, due to Richards (1931).

The Richards equation is the most commonly applied model in the unsaturated zone. However, the model's applicability is limited if one of the assumptions is violated or the application has a focus on air flow, e.g. volatile components transported in air (Szymkiewicz, 2013). For example, when soil dries by evaporation, water vapor transport in the pore space is particularly important as soon as a dry zone established inside the porous medium. Szymkiewicz (2013) lists several cases where the Richards equation inaccurately describes the problem, even when the focus is on water flow. The mobility ratio  $m_g/m_l$  can become small for small air saturation as the relative permeability  $k_{rg}$  decreases, while  $k_{rl}$  is high. This violates the Richards assumption of infinite mobility and introduces significant errors (Forsyth, 1988). Szymkiewicz (2013) mentions that the Richards equation produces inaccurate results, if obstacles (e.g. highly water saturated layer) hinder the air contact with the atmosphere. All three cases may occur in applications with root systems in the vadose zone.

We can describe the transport of components other than the main components (water and air) in the soil by additional advection-diffusion-reaction equations. In combination with the

Richards equation it is usually assumed that the component only exists in the liquid phase. As an extension of the Richards equation, water vapor in the air phase can be described by an additional diffusion equation and assuming a negligible gas phase velocity  $v_g \rightarrow 0$  and local thermodynamic equilibrium, see for example (Vanderborght et al., 2017). This formulation is often considered when describing evaporation from soil, also see Section 4.6.

## 4.2 Flow and transport in the root xylem

Roots have two different tube systems, the xylem transporting the liquid xylem sap, and the phloem transporting nutrients. These are surrounded by a cell layer called the cortex. The surface of a root usually contains root hairs, which have been suggested to enhance fluid transport into the roots (Libault et al., 2010). A schematic drawing of the anatomy of a dicot<sup>†</sup> root cross-section is shown in Fig. 4.2. Water (or xylem sap) flows through the

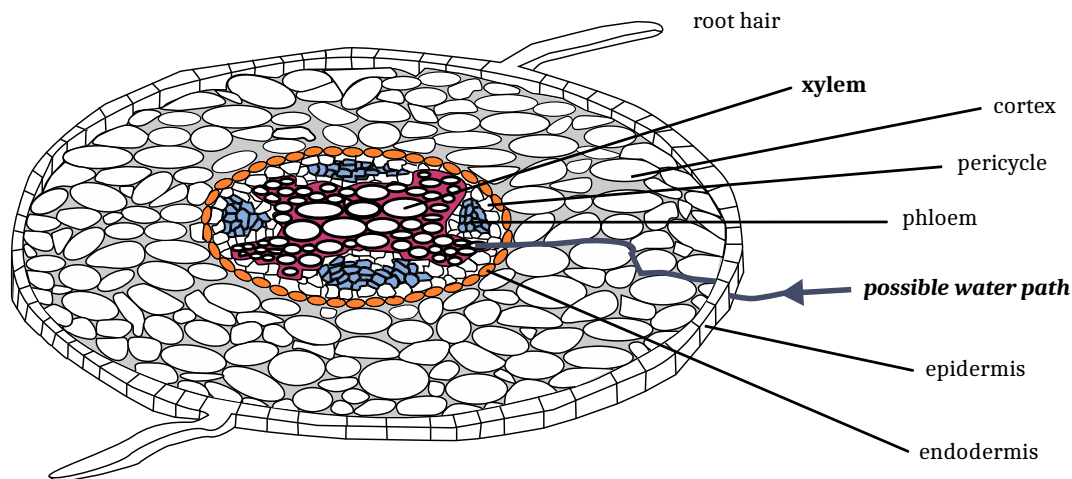


**Figure 4.2 – Cross-sectional anatomy of a dicot root.** Schematic representation. Water from the soil has to penetrate the epidermis, and flow through the interstitial space of the cortex to end up in the xylem. The xylem transports the water upwards.

root xylem, a bundle of tubes composed of cell walls. According to the cohesion-tension theory (Tyree, 1997), the driving force for xylem flow is the pressure gradient caused by the transpiration in the stomata of the leaves.

The single-phase flow of the liquid in each tube can be described by Poiseuille’s law. Homogenization leads to a Darcy’s law analogy (bundle-of-tubes model) for xylem flow (Doussan

<sup>†</sup>short for dicotyledon, a group of flowering plants, such as the lupin investigated in this work

et al., 1998), with the axial conductivity  $k_{\text{ax}}$  in  $\text{m}^4 \text{Pa}^{-1} \text{s}^{-1}$ ,

$$\frac{\partial(\rho_l A_r \phi_r)}{\partial t} + \frac{\partial(\rho_l A_r v)}{\partial s} = -\hat{q}, \quad v = -\frac{k_{\text{ax}}}{A_r} \left( \frac{\partial p}{\partial s} + \rho_l g \frac{\partial x_3}{\partial s} \right) \quad (4.3)$$

wherein  $A_r = 2\pi r_r$  is the root cross-sectional area with the equivalent radius  $r_r$ , and  $\phi_r = V_x V^{-1}$  is the root porosity, where  $V_x$  is the xylem volume in a sample of size  $V$ . The vertical coordinate of a Cartesian coordinate system with coordinates  $x_i$  is denoted by  $x_3$ . The axial root conductivity  $k_{\text{ax}}$  is a parameter obtained from measurements and changes with root age (Steudle and Peterson, 1998), root radius (Vercambre et al., 2002), or environmental conditions (Lovisolo and Schubert, 1998).

The transport of, for example, minerals in the xylem sap can be modeled by one or more additional advection-diffusion-reaction equations. Such an equation is derived by integrating the three-dimensional equations over a cross-section of a segment, and introducing a cross-section-averaged molar concentration  $c^\kappa$ ,

$$\frac{\partial(A_r \phi_r c^\kappa)}{\partial t} + \frac{\partial}{\partial s} \left( A_r v c^\kappa - A_r D_e^\kappa \frac{\partial c^\kappa}{\partial s} \right) = -\frac{\hat{q}^\kappa}{M^\kappa}, \quad (4.4)$$

where  $D_e^\kappa$  is effective diffusion coefficient, and  $\hat{q}^\kappa$  a source term.

To the end of modeling a hierarchical network of root segments, the segment equations have to be coupled at branching points by appropriate coupling conditions, cf. Chapter 3. We enforce continuity of pressure and mole fractions at the junctions.

### 4.3 Root water uptake (transmural exchange)

At the soil-root interface, water and solutes are exchanged between the root system and the embedding soil. Water flow from soil into the root is mainly driven by pressure differences between the soil close to the root and the pressure inside the roots (Steudle and Peterson, 1998), and can be described by

$$\hat{q} = P_r k_\Gamma k_{\text{rad}} (p_{w,r} - \bar{p}_{w,s}) \rho_l, \quad (4.5)$$

where  $P_r = 2\pi r_r$  is cross-section perimeter, and  $k_{rad}$  in  $\text{ms}^{-1}\text{Pa}^{-1}$  denotes the radial conductivity, an effective parameter including effects of all possible transport paths through outer root layers to the xylem tubes. A possible water pathway is shown in Fig. 4.2. Finally,

$$\bar{p}_{w,s} = \frac{1}{S_r} \int_0^{2\pi} p_{w,s} \Big|_{r_r} r_r d\theta \quad (4.6)$$

denotes the average water pressure in the surrounding soil evaluated on the root surface and  $p_{w,r}$  the fluid pressure in the xylem.

In addition to Steudle and Peterson (1998), we introduce  $k_r$ , to account for the reduction in water mobility in the drying soil around the root. Assuming that the entire root surface is always in contact with water, the upper limit for  $k_r$  is 1, which is mostly assumed in the literature (Steudle and Peterson, 1998; Doussan et al., 1998; Javaux et al., 2008). In Koch et al. (2020a), we choose  $k_r$  as  $k_{r1}$  if the root is taking up water, so that when the residual liquid saturation  $S_{lr}$  of the soil around the root is approached, the relative permeability tends to zero, with the effect that the root segment cannot take up water anymore. The approach is based on the idea that the water mobility is limited by the upstream mobility. This approach corresponds to the lower limit and likely underestimates the radial conductivity. Schröder et al. (2009b) study grid refinement and conclude that the root water uptake locally dries out the vicinity of the root (rhizosphere), thus limiting water mobility. Schröder et al. (2009a) suggest including an additional analytical model for the conductivity drop in the rhizosphere. Mai et al. (2019) solve additional one-dimensional radial-symmetric problems in the rhizosphere to simulate nutrient uptake. Another approach is obtained by choosing  $k_r = \phi S_w$ , which models a partially wet root surface. The choice of  $k_r$  may affect the locality of the water uptake and the soil water pressure distribution. We note that modeling the full physiological response to drought and the resulting reduction of the transpiration rate, hydraulic conductivities in stem and leaves, and wilting (Bartlett et al., 2016), are beyond the scope of this work.

If component transport is considered, for example, to describe the root uptake of nutrients, salts, pesticides or fertilizers, the uptake mechanisms are specific to the considered solute molecule. Concentration gradients, solubility, and plant type further influence the transmural transfer. Varying demand of nutrients by the plant alters active uptake rates. Solute uptake may be described by a Michaelis-Menten-type kinetic (e.g. Buysse et al., 1996) or by an advection-diffusion model for solutes transported passively with water.



During day-time, the pressure difference between the soil and the root system  $\Delta p = p_{w,r} - \bar{p}_{w,s}$  is usually negative, resulting in a positive source at the root subsystem and a negative source (sink) at the soil subsystem. In this case, water is transferred from the soil into the root. During night-time or during local water scarcity this flux can also be negative. The root gives back water to the soil, an effect known as hydraulic redistribution (or hydraulic lift, however redistribution can be observed in any direction) (Richards and Caldwell, 1987; Smart et al., 2005). Hydraulic redistribution is a phenomenon seen in many plant species and hydraulic regimes. For further information, we refer to Caldwell and Richards (1989); Caldwell et al. (1998); Neumann and Cardon (2012); Manoli et al. (2017).

## 4.4 Mixed-dimension root water uptake model

Finally, we summarize the presented root and soil models in a single coupled PDE system. For brevity, the coupled PDE is only presented for water uptake and the Richards soil model. Nutrient uptake, as well as uptake for the two-phase soil model can be formulated analogously. We denote the soil domain as  $\Omega$  and the root network center-lines as  $\Lambda$ . The coupling conditions, based on conservation of mass, read

$$\int_{\Omega} \hat{q} \Phi_{\Lambda} dx = \int_{\Lambda} \hat{q} ds, \quad (4.7)$$

with the kernel function  $\Phi_{\Lambda}$  which will be properly introduced in Chapter 6. The root water uptake model can be formulated as follows. Find  $p_{w,s}$  and  $p_{w,r}$  such that

$$\frac{\partial (A_r \phi_r \rho_w)}{\partial t} - \nabla \cdot \left[ \rho_w k_{ax} \left( \frac{\partial p_{w,r}}{\partial s} + \rho_w g \frac{\partial x_3}{\partial s} \right) \right] = -\hat{q} \quad \text{in } \Lambda, \quad (4.8a)$$

$$\frac{\partial (\phi_s S_w \rho_w)}{\partial t} - \nabla \cdot \left[ \rho_w \frac{k_{rw}}{\mu_w} \mathbf{K} (\nabla p_{w,s} + \rho_w g \nabla x_3) \right] = \hat{q} \Phi_{\Lambda} \quad \text{in } \Omega, \quad (4.8b)$$

$$P_r k_r k_{rad} (p_{w,r} - \bar{p}_{w,s}) = \hat{q}, \quad (4.8c)$$

subject to appropriate boundary conditions. For the root, the uptake is already considered by Eq. (4.5), so that at root tips, we formally assume no-flow boundaries. Suitable boundary conditions for the root collar are discussed in Section 4.5, and boundary conditions at the top of the soil are discussed in Section 4.6.

## 4.5 Transpiration

Transpiration occurs due to the difference in vapor pressure in the stomata of the leaves and the atmosphere and is the driving force of root water uptake and sap flow (cohesion-tension theory). Rates depend on wind speed and temperature of the atmosphere as well as net radiation receipt of the leaves, which triggers stomata opening to take up carbon dioxide (Bierhuizen and Slatyer, 1965; Jarvis and McNaughton, 1986) and increases water losses due to evaporation. During night-time, the stomata usually close which leads to a decline in transpiration, although night-time transpiration has been observed in several species to be up to 10 % of day-time transpiration (Snyder et al., 2003).

Transpiration rates are typically imposed as Neumann boundary conditions at the root collar (Javaux et al., 2008; Clausnitzer and Hopmans, 1994). It is possible to simulate diurnal variations of the transpiration rate as a time-dependent Neumann boundary condition. In experimental setups, transpiration rates can often be measured. As noted by Javaux et al. (2008), such imposed flux conditions can lead to water stress, when the plant is not able to extract enough water from the soil to meet the transpirational demand. Following Javaux et al. (2008), we switch to a Dirichlet condition enforcing the permanent wilting point pressure ( $p_w = -1.4\text{MPa}$ ) after this pressure is reached at the root collar. This boundary condition assumes that the root collar pressure is kept constant by stomatal response of the plant to water stress. The transpiration rate subsequently decreases. We switch back to prescribing a transpiration rate if the transpiration rate predicted with the Dirichlet boundary condition would exceed the transpiration rate predicted by the usual diurnal cycle.

For growing root systems, we follow Clausnitzer and Hopmans (1994) and estimate the transpiration rate as a function of the root volume,  $V_{\text{root}}$ , with the following ratios,

$$\rho_r = \frac{m_r}{V_r}, \quad \varphi_{r:s} = \frac{m_r}{m_{\text{sh}}}, \quad \varphi_{A_L:s} = \frac{A_L}{m_{\text{sh}}}, \quad \varphi_{r_T:A_L} = \frac{r_T}{A_L}, \quad (4.9)$$

with the root (mass) density,  $\rho_r$ , the ratio  $\varphi_{r:s}$  between the root biomass,  $m_r$  (below the surface) and the shoot biomass,  $m_{\text{sh}}$  (above the surface), the ratio  $\varphi_{A_L:s}$  between leaf area,  $A_L$ , and shoot biomass, and the ratio  $\varphi_{r_T:A_L}$  between the transpiration rate,  $r_T$ , and the leaf area, respectively. These ratios are generally varying over time and through environmental factors, and can be estimated by experimental measurements, or literature values for a

given plant species. Clausnitzer and Hopmans (1994) estimate  $\rho_r = 750 \text{ kg m}^{-3}$ ,  $\varphi_{r:s} = 0.5$ ,  $\varphi_{A_L:s} = 20 \text{ m}^2 \text{ kg}^{-1}$ ,  $\varphi_{r_T:A_L} = 2.78 \cdot 10^{-8} \text{ m}^3 \text{ s}^{-1} \text{ m}^{-2}$ . For instance, for a root mass of 10 g this results in a transpiration rate of  $r_T = \rho_r V_r \varphi_{A_L:s} \varphi_{r_T:A_L} \varphi_{r:s}^{-1} \approx 1 \text{ g d}^{-1}$ .

## 4.6 Evaporation from soil

Evaporation is a process driven by the difference in water vapor pressure in the soil and the atmosphere. Using the standard Richards model, it is not possible to describe evaporation consistently, as water vapor transport is not accounted for. As noted in Section 4.1, it is possible to adapt the Richards equation to account for additional diffusive vapor transport in the air phase (Vanderborght et al., 2017). However, we will focus on the description of evaporation using a full two-phase two-component model where vapor transport is inherently considered and does not require additional model constraints. Consistent approaches to model soil evaporation are, to our knowledge, mostly neglected in state-of-the-art root architecture models, although soil evaporation plays a crucial role in soil-root-atmosphere interactions. For the description of evaporation, we can distinguish two distinct stages. In the atmosphere-driven stage I, the liquid water phase is continuously connected to the soil surface where water evaporates at the interface to the atmosphere. Stage II evaporation begins with the successive disconnection of the liquid water phase from the surface. The evaporation front sinks into the porous soil medium and the evaporation rate is limited by vapor diffusion in the porous medium resulting in much lower evaporation rates than in stage I. This phenomenon is described in various works, for example by Scherer (1990), or Lehmann et al. (2008).

There are different approaches to model interactions between free flow and porous medium flow. One approach is to use a two-domain model with a sharp interface separating the domains (Vanderborght et al., 2017; Mosthaf et al., 2011; Fetzer et al., 2016). The two domains are coupled at the interface. Coupling conditions need to be formulated for balance of mass, momentum and energy. In this section, a simplified version is described where no free flow equation system is explicitly solved.

Turbulent free flow leads to the formation of a viscous sub-layer, referred to as boundary layer. Assuming that the evaporation rate is mainly influenced by water vapor diffusion through that boundary layer (Haghighi et al., 2013), the coupling conditions can be simplified by

neglecting the momentum transfer between the porous medium and the free flow domain. Moreover, heat conduction is assumed to dominate the energy transfer (Fetzer et al., 2016). Assuming that the boundary layer mole fraction of water vapor in the gas phase,  $x_g^{w, \text{BL}}$ , the boundary layer thickness,  $\delta_{\text{BL}}$ , and the boundary layer temperature,  $T^{\text{BL}}$ , are constant, the evaporation model reduces to a Robin-type boundary condition for the soil domain. The evaporation rate driven by diffusion is calculated as in Mosthaf et al. (2014); Fetzer et al. (2016). The mass flux of the water component at the interface can be computed as

$$f^w = D_g^w \rho_n M^w \frac{x_g^{w, \text{BL}} - x_g^{w, \Gamma}}{\delta_{\text{BL}}}, \quad (4.10)$$

with  $x_g^{w, \Gamma}$  denoting the mole fraction of the water component in the gas phase at the interface (here: the top of the soil), and  $D_g^w$  being the binary diffusion coefficient of water in the gas phase.

When assuming chemical equilibrium, the mole fraction of water in the gas phase can be computed using Raoult's law. However, it is known that for very dry soil and thus high capillary pressure, stronger adhesion of water to the solid matrix reduces evaporation and shifts the liquid-vapor equilibrium in favor of the liquid phase. This relationship between the capillary pressure and the water vapor pressure  $p_n^w$  is expressed by the Kelvin equation (Edlefsen and Anderson, 1943),

$$p_g^w = p_{\text{sat}}^w \exp \left[ -\frac{p_c M^w}{\rho_l \mathcal{R} T} \right], \quad (4.11)$$

where  $\mathcal{R}$  is the universal gas constant.

The heat flux,  $f_h$ , due to heat conduction driven by the temperature differences of the soil surface and the boundary layer are accounted for by Fourier's law inside the boundary layer,

$$f_h = \lambda_g \frac{T^{\text{BL}} - T^\Gamma}{\delta_{\text{BL}}}, \quad (4.12)$$

where  $\lambda_g$  denotes the thermal conductivity of the gas phase, and  $T^\Gamma$  the soil surface temperature. The boundary layer model can be extended to include velocity-dependent boundary layer thickness or surface roughness. For further information on the theory of boundary layers and evaporation processes, we refer to the works of Fetzer et al. (2017) and Vanderborght et al. (2017).

## 4.7 Root growth

For some applications (evaluating agricultural irrigation plans, soil stabilization by plant roots) it is important to focus closely on the water management in the soil during root growth. Root growth depends on soil properties (Hewitt, 2004; Jakobsen and Dexter, 1987; Dunbabin et al., 2011) and root water uptake on the root architecture (Tron et al., 2015; Lynch, 1995). Models of root growth, with explicit description of the root system architecture, coupled with root water uptake and subsurface nutrient transport processes are important to analyze the interaction of the evolving root system with the embedding soil. Various algorithms have been developed for the description of root growth (Diggle, 1988; Clausnitzer and Hopmans, 1994; Lynch et al., 1997; Pagès et al., 2004), see Dunbabin et al. (2013) for an overview .

We herein want to discuss some details of modeling root growth and water flow simultaneously, on the example of the RootBox algorithm (Leitner et al., 2010; Leitner and Schnepf, 2016; Schnepf et al., 2018), an algorithm based on a recursively applied branch growth procedure; cf. L-systems, e.g. Prusinkiewicz (2004). The root extends with a certain growth rate. The direction has a random component emulating a finite number of possibilities for growth paths in the porous soil. The cost function of a certain direction choice is modeled by a so-called tropism. Tropisms usually result from external stimuli like gravity (gravitropism), soil water content (hydrotropism) or the plant's tendency to continue growing in an already established direction (exotropism). When reaching a certain length, root branches create daughter branches and the same growth procedure is applied to those branches. The algorithm results in hierarchical tree structures and can simulate growth of different plant species. To this end, all parameters assigned to branches are stochastically distributed parameters following experimental observations (Leitner et al., 2010).

The aspect of local mass conservation is usually overlooked in the current root growth literature. In addition to locally mass conservative discretization methods for the governing equations, growing root systems introduce mass into the system. On the one hand, this is the biomass of a new root segment that reduces the soil pore space, effectively reducing the soil porosity. Due to the discrete description of the root network, the volume fraction taken up by the root segments contained in a discrete soil cell can be easily computed by dividing the root volume in that cell by the cell volume. On the other hand, new pore space gets created in the form of the root xylem that needs to be filled with water. This is accounted

for in the xylem flow balance's storage term. Looking at the Reynolds transport theorem for the change of water mass in the root,  $m_{w,\text{root}}$ ,

$$\frac{dm_{w,\text{root}}}{dt} = \frac{\partial}{\partial t} \int_{K_\Lambda(t)} \phi_r \rho_w dV + \int_{\partial K_\Lambda(t)} \rho_w (\mathbf{v}_r \cdot \mathbf{n}) dA, \quad (4.13)$$

for a growing control volume  $K_\Lambda(t)$ , e.g. at the root tip, where  $\mathbf{v}_r$  denotes the fluid velocity relative to the moving control volume boundary  $\partial K_\Lambda(t)$ , we see that the storage integral is not constant in time. Assuming that a newly growing root segment is instantaneously filled with water during the growth, we can replace the relative velocity on the root segment boundary with the fluid velocity  $\mathbf{v}_r \approx \mathbf{v}$ . Using a finite difference approximation of the time derivative yields

$$\frac{\partial}{\partial t} \int_{K_\Lambda(t)} \phi_r \rho_w dV \approx \frac{[V \phi_r \rho_w]_{k+1} - [V \phi_r \rho_w]_k}{t_{k+1} - t_k}, \quad (4.14)$$

i.e. the control volume size  $V = |K_\Lambda|$  has to be evaluated at the next ( $t_{k+1}$ ) and current time discretization point ( $t_k$ ), effectively increasing the storage term by a contribution from the volume change.

Another issue concerns the discrete approximation of continuous growth. For small time steps tiny root segments may occur during growth that can cause ill-conditioned linear systems. For large time step sizes, root growth algorithms seek a uniform discrete representation of the created root segments and branches by a maximum segment length. This is necessary to achieve realistically-looking root architectures with smooth root progression. However, if the branching point positions are determined by a random process at the creation of the branch, such as for example for RootBox, respecting these positions can lead to small discrete root segments. For small time step sizes, the RootBox algorithm ignores tiny segments which leads to discontinuous growth in time. The branch would not grow in one time step and then, for example, grow twice as much in the following time step. These small elements can be avoided by allowing to move the vertex of existing elements at the root tip in order to increase the segment's length instead of creating a new small segment. This leads to a better distribution of element sizes with small elements only occurring at the tip of a growing branch. Such considerations have been made in the latest version of CRootBox (Schnepf et al., 2018). Moreover, this allows segments to continuously grow and

thus avoids additional mass balance errors destabilizing the numerical scheme. However, the volume change due to the movement of vertices has to be accounted for, see Eq. (4.14).





## 5 Modeling wells\*

This chapter briefly discusses the mathematical modeling of injection or extraction wells in subsurface hydraulic or petroleum reservoirs, in terms of mixed-dimension embedded models. First, we derive a more general model for a coupled flow problem where the well is represented by its one-dimensional center-line embedded in a three-dimensional porous rock matrix. Then, we discuss typical simplifications of reservoir engineering models. In this work, we restrict ourselves to single-phase flow. Some typical application scenarios with wells are shown schematically in Fig. 5.1. Typical bore hole diameters are in the range of 50 cm (towards the surface) to 10 cm (towards the tip). The target geological layer formations are ten to hundreds of meters in height and often kilometers in lateral extent. The depth of the target layers varies depending on the application from several meters for near surface groundwater extraction to several kilometers for some geothermal systems or petroleum extraction.

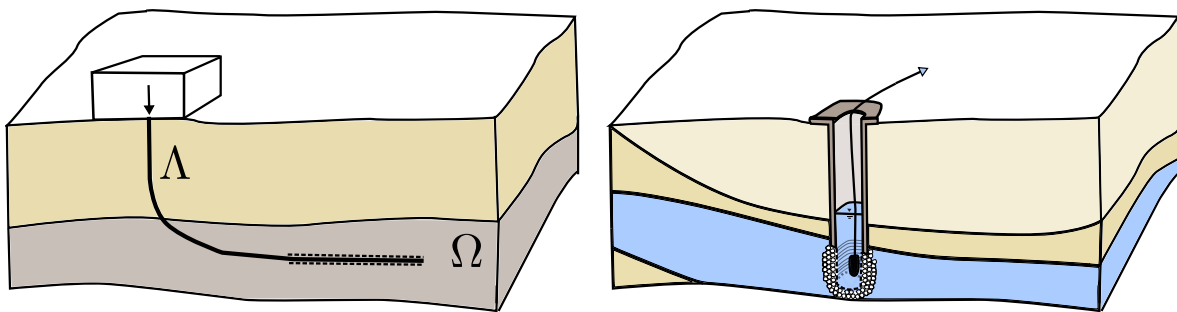


**Figure 5.1 – Schematic and idealized representation of two types of wells.** On the left, a horizontally drilled injection well for a fracking operation. The perforated, permeable segment is shown by the dotted lines. On the right, components of a ground water extraction well in a confined aquifer. A submersed pump extracts water from the bore hole. The bore hole is permeable inside the confined aquifer, covered by a screen and surrounded by a layer of gravel. The schematic representations are *not* to scale.

We conceptually decompose the subsurface into two domains. The well compartment includes the well and the possible casing or other technical structures, and the rock matrix compartment is the embedding porous soil matrix. The bore hole surface is only permeable in designated segments, where fluid is exchanged with the rock matrix, and otherwise sealed.

\*Sections 5.2 and 5.3 are based on Koch, Helmig, and Schneider (2020c), © 2020 Elsevier Inc.

## 5.1 Flow in the rock matrix

The mass balance for single-phase fluid flow through a rock matrix is given by

$$\frac{\partial(\phi\rho)}{\partial t} + \rho\nabla \cdot \mathbf{v} = q, \quad (5.1)$$

where the filter velocity  $\mathbf{v}$  can be modeled by Darcy's law, see Eq. (2.5). For higher Reynolds numbers that can occur in the near-well region in oil or gas production (Ewing et al., 1999), or for geothermal wells (Zhang and Xing, 2012), inertial forces cannot be entirely neglected. Then, for isotropic porous media,  $\mathbf{K} = k\mathbf{I}$ , Darcy's law is often substituted by the Forchheimer equation (Forchheimer, 1901; Ruth and Ma, 1992; Whitaker, 1996)

$$\mathbf{v} = -\frac{k}{\mu}(\nabla p - \rho\mathbf{g}) + \frac{\rho\sqrt{k}}{\mu C_F}\|\mathbf{v}\|\mathbf{v}, \quad (5.2)$$

with the coefficient  $C_F$ , often chosen as  $C_F = 0.55$  (Nield and Bejan, 2013). The nonlinear Forchheimer correction accounts for the increase in friction between matrix and fluid for high velocities. Adaptions for anisotropic media have been suggested (Wang et al., 1999). However, there is currently no commonly accepted approach for anisotropic media. For low flow velocities, the Forchheimer equation reduces to Eq. (2.5). In this work, we consider anisotropic media and restrict ourselves to the Darcy flow regime, that is low Reynolds numbers on the pore scale,  $\text{Re}_p = \rho v_c d_{p,c} \mu^{-1} \ll 1$ , with the characteristic pore throat diameter  $d_{p,c}$ .

## 5.2 Flow in the well

Single-phase flow through a tube can be modeled by the Navier-Stokes equations. For fully developed laminar flow of an incompressible fluid through a straight tube segment with impermeable wall, the model can be reduced to a one-dimensional mass balance equation,

$$\frac{\partial(\rho A_\omega v)}{\partial s} = -\frac{\partial}{\partial s} \left[ \frac{\rho A_\omega r_\omega^2}{8\mu} \left( \frac{\partial p_\omega}{\partial s} + \rho g \frac{\partial x_3}{\partial s} \right) \right] = 0, \quad (5.3)$$

where  $A_\omega = \pi r_\omega^2$  is the area of a well cross-section, and the expression for the velocity  $v$  is also known as Hagen-Poiseuille equation. By introducing the friction coefficient  $C_\lambda = \frac{64\mu}{2r_\omega v \rho} = \frac{64}{\text{Re}}$ ,

the expression for  $v$  can be reformulated to the Darcy-Weisbach equation (Brown, 2003)

$$\frac{\partial p_\omega}{\partial s} + \rho g \frac{\partial x_3}{\partial s} = -\frac{C_\lambda v^2}{4r_\omega}. \quad (5.4)$$

For the turbulent flow regime, the friction coefficient  $C_\lambda$  can be empirically determined or estimated. For instance, for hydraulically smooth tubes, the Blasius correlation estimates  $C_\lambda \approx \frac{0.316}{\sqrt{\text{Re}}}$  (Massey and Ward-Smith, 2005). Turbulent flow occurs in wells with high flow rates.

For modeling of injection and extraction scenarios, we assume that the pressure drop along the permeable well segment towards the end of the well bore hole is negligible in comparison with the pressure drop in the rock matrix, see Section 6.2.3. Consequently, if either the bottom hole pressure (the pressure in the permeable end segment of the bore hole), or the injection rate is known, no additional equation has to be solved in the well. However, Eq. (5.3) provides a relation to estimate the bottom hole pressure if, for instance, only the well pressure close to the surface is known.

### 5.3 Fluid exchange with the rock matrix

If the well bore has a permeable casing, the flow over this casing can be estimated by Darcy's law

$$\hat{q} = 2\pi r_\omega \frac{\rho k_c}{\mu} \frac{(p_\omega - \bar{p})}{d_c}, \quad (5.5)$$

where  $k_c$  is an estimate of the intrinsic permeability of the casing,  $d_c$  the casing thickness, and

$$\bar{p} = \frac{1}{2\pi} \int_0^{2\pi} p \Big|_{r_\omega} d\theta \quad (5.6)$$

is the average soil matrix pressure evaluated at the well-matrix interface. In the absence of a casing, or if it can be assumed that pressure drop across the casing is negligible (high permeability), we assume that the flow field is radially symmetric in a small neighborhood of the well (distance  $\delta = r_\omega + \epsilon$  from center-line). In the following, we consider a long straight well borehole segment. Let  $\bar{p}_\delta$  denote the average pressure at distance  $\delta$  from the well center-line. Furthermore, we assume constant fluid density, viscosity, and an isotropic

permeability,  $k$ , close to the well. Then, in the rock matrix, the fluid pressure for  $r_\omega < r < \delta$  is described by the analytical solution

$$p(r) = -\frac{\mu}{k\rho} \frac{\hat{q}}{2\pi} \ln r + C, \quad (5.7)$$

where  $\hat{q}$  in  $\text{kg s}^{-1} \text{m}^{-1}$  is the exchange flux with the matrix for a well cross-section with radius  $r_\omega$ . The constant  $C$  is determined by the well pressure,  $p_\omega$ ,

$$p_\omega = p(r_\omega) = -\frac{\mu}{k\rho} \frac{q}{2\pi} \ln r_\omega + C \Rightarrow C = p_\omega + \frac{\mu}{k\rho} \frac{q}{2\pi} \ln r_\omega,$$

so that

$$p(r) = p_\omega - \frac{\mu}{k\rho} \frac{q}{2\pi} \ln \left( \frac{r}{r_\omega} \right). \quad (5.8)$$

Consequently, the fluid exchange flux can be expressed in terms of  $p_\omega$  and  $\bar{p}_\delta$  as

$$\hat{q} = 2\pi r_\omega \frac{\rho k (p_\omega - \bar{p}_\delta)}{\mu r_\omega \ln \left( \frac{\delta}{r_\omega} \right)}. \quad (5.9)$$

In a dedicated chapter, Chapter 8, an analytical solution and a well model for a rock matrix with anisotropic permeability is derived.

## 5.4 Well index and Peaceman well model

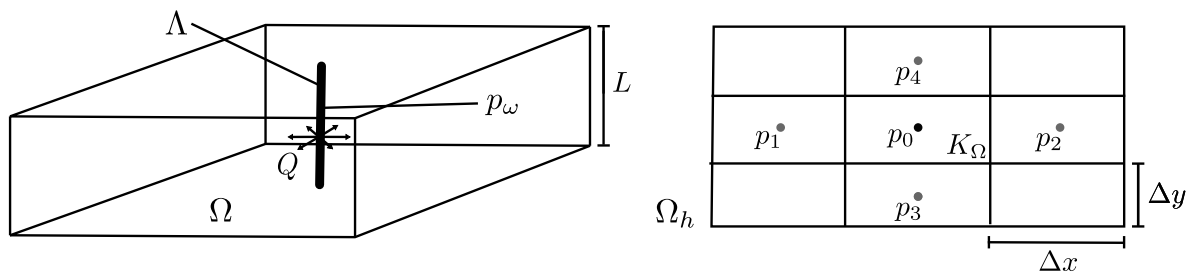


**Figure 5.2 – Setting for the derivation of a Peaceman well model.** The continuous domain, on the left, shows the location of the well center-line  $\Lambda$  in a rock matrix domain  $\Omega$  with height uniform  $L$ . The well is injecting a fluid with a mass flow rate of  $Q$  into  $\Omega$ . The domain is discretely approximated by  $\Omega_h$  (on the right). A pressure degree of freedom is located at the centroid of each cell. The cell  $K_\Omega$  contains the well. Its pressure value is denoted by  $p_0$ .

In particular for petroleum engineering applications, commercial codes typically use well-index based well models (ECLIPSE, 2014; IMEX, 2014) to numerically compute injection and extraction rates for given bottom hole well pressures. Such models are briefly described in the following. To this end, the well is reduced to its center-line  $\Lambda$ . The rock matrix domain is denoted by  $\Omega$ . The rock matrix domain is discretized by the mesh  $\Omega_b$  with hexahedral cells  $K_\Omega \in \Omega_b$ . The well index provides a relation between the discrete pressure values, given at the degrees of freedom where the well intersects the computational grid, and the actual well pressure. As an example, the degrees of freedom for a 5-point finite difference stencil are shown in Fig. 5.2. With the symbols introduced in Fig. 5.2, the well index is defined as (Aavatsmark and Klausen, 2003)

$$\text{WI}_{K_\Omega} = \frac{\mu Q_{K_\Omega}}{\rho(p_\omega - p_0)}, \quad (5.10)$$

where  $Q_{K_\Omega} = \hat{q}L_{K_\Omega}$  is the mass flow rate in  $\text{kg s}^{-1}$  into the discrete matrix domain cell  $K_\Omega$ , which is often called well block, and  $L_{K_\Omega}$  the length of the well segment contained in  $K_\Omega$ . The first well-index-based model for isotropic permeabilities and structured rectangular grids in two dimensions is derived by Peaceman (1978). Peaceman (1983) derives a more accurate well model for anisotropic diagonal permeability tensors and two-dimensional non-cubic but structured rectangular grids, for the 5-point finite difference stencil (shown in Fig. 5.2), yielding the following well index

$$\text{WI}_{K_\Omega} = 2\pi L_{K_\Omega} \frac{\sqrt{k_{11}k_{22}}}{\ln\left(\frac{r_0}{r_\omega}\right)}, \quad (5.11)$$

$$r_0 = \frac{e^{-\gamma} \left[ \left(\frac{k_{22}}{k_{11}}\right)^{\frac{1}{2}} \Delta x_1^2 + \left(\frac{k_{11}}{k_{22}}\right)^{\frac{1}{2}} \Delta x_2^2 \right]^{\frac{1}{2}}}{2 \left[ \left(\frac{k_{11}}{k_{22}}\right)^{\frac{1}{4}} + \left(\frac{k_{22}}{k_{11}}\right)^{\frac{1}{4}} \right]}, \quad (5.12)$$

where  $\Delta x_1$  and  $\Delta x_2$  are the horizontal dimensions of the cell containing the well,  $\gamma$  the Euler–Mascheroni constant, and  $k_{11}$  and  $k_{22}$  are the diagonal entries of the permeability tensor  $\mathbf{K}$ . Well indices for various other discretization schemes have since been developed. An overview is given by Chen and Zhang (2009).

The Peaceman model has several known limitations. Its derivation only applies to K-orthogonal structured grids, where the well is oriented along one of the grid axes, and perfectly horizontally centered within a vertical column of computational cells  $K_\Omega$ . Further-

more, the derivation is specific to cell-centered finite difference schemes with 5-point stencil. Moreover, computational cells may have to be significantly larger than the well radius (depending on the degree of anisotropy) for optimal accuracy. However, if all assumptions are satisfied, the Peaceman model yields a very accurate approximation of the source term. The Peaceman model has been generalized for slanted wells with arbitrary orientation in  $\mathbb{R}^3$ , for example in (Alvestad et al., 1994). Such extensions usually constitute a reasonable directional weighting of the original Peaceman model but are not directly derived from the mathematical analysis of the underlying problem (Aavatsmark and Klausen, 2003). For a given well direction  $\psi = [\psi_1, \psi_2, \psi_3]^T$  and a discretization cell  $K_\Omega$  with dimensions  $\Delta x_1, \Delta x_2, \Delta x_3$ , to obtain the generalized well model due to Alvestad et al. (1994), reformulated for cell-centered finite volume schemes in (Aavatsmark and Klausen, 2003), replace  $k = \sqrt{k_{11}k_{22}}$  in Eq. (5.11) by

$$k = (\psi_1^2 k_{22} k_{33} + \psi_2^2 k_{11} k_{33} + \psi_3^2 k_{11} k_{22})^{\frac{1}{2}} \quad (5.13)$$

and the expression for  $r_0$  by

$$r_0 = \frac{e^{-\gamma} (\Delta L_1^2 + \Delta L_2^2)^{\frac{1}{2}}}{2 (\sqrt{A_1} + \sqrt{A_2})}, \quad \text{with} \quad (5.14)$$

$$\Delta L_1^2 = \left(\frac{k_{22}}{k_{33}}\right)^{\frac{1}{2}} \Delta x_3^2 \psi_1^2 + \left(\frac{k_{33}}{k_{11}}\right)^{\frac{1}{2}} \Delta x_1^2 \psi_2^2 + \left(\frac{k_{11}}{k_{22}}\right)^{\frac{1}{2}} \Delta x_2^2 \psi_3^2,$$

$$\Delta L_2^2 = \left(\frac{k_{33}}{k_{22}}\right)^{\frac{1}{2}} \Delta x_2^2 \psi_1^2 + \left(\frac{k_{11}}{k_{33}}\right)^{\frac{1}{2}} \Delta x_3^2 \psi_2^2 + \left(\frac{k_{22}}{k_{11}}\right)^{\frac{1}{2}} \Delta x_1^2 \psi_3^2,$$

$$A_1 = \left(\frac{k_{22}}{k_{33}}\right)^{\frac{1}{2}} \psi_1^2 + \left(\frac{k_{33}}{k_{11}}\right)^{\frac{1}{2}} \psi_2^2 + \left(\frac{k_{11}}{k_{22}}\right)^{\frac{1}{2}} \psi_3^2,$$

$$A_2 = \left(\frac{k_{33}}{k_{22}}\right)^{\frac{1}{2}} \psi_1^2 + \left(\frac{k_{11}}{k_{33}}\right)^{\frac{1}{2}} \psi_2^2 + \left(\frac{k_{22}}{k_{11}}\right)^{\frac{1}{2}} \psi_3^2.$$

Alvestad's formula reduces to Eq. (5.11), if  $\psi$  is aligned with a coordinate axis.

## 6 Mixed-dimension embedded methods and applications\*

The following chapter introduces the main modeling concept used and analyzed throughout this work, alongside with the considered applications and their particularities. Formally, we analyze porous structures, containing one or more embedded transport networks which supply substances to, or extract substances from the embedding structure, using fluid-mechanical or thermodynamic transport mechanisms. The transport networks commonly consist of tubular segments with bifurcations, joints, and possibly loops. As the common defining feature, the radial dimension of these segments is small in comparison with the relevant domain size.

We attempt to introduce a consistent framework and terminology for the description of a class of similar numerical methods. Embedded in a porous domain  $\Omega$ , is a network of tubular segments (connected at joints / bifurcations) described by the network of center-lines  $\Lambda$  and a radius field  $r_v$  defined on  $\Lambda$ , where the center-line is parameterized by  $s$ . Furthermore, we introduce a segment-local cylindrical coordinate system with axial, angular and radial coordinates  $z, \theta, r$ . A small example of such a network is shown in Fig. 6.1. With these definitions, a simple mixed-dimension flow problem in terms of the fluid pressure  $p$  is given by

$$-\pi r_v^2 \frac{k_v}{\mu_c} \frac{\partial^2 p_v}{\partial s^2} = -\hat{q} \quad \text{in } \Lambda, \quad (6.1a)$$

$$-\frac{k_m}{\mu_c} \nabla \cdot \nabla p_m = \hat{q} \delta_\Lambda \quad \text{in } \Omega, \quad (6.1b)$$

and suitable boundary conditions on  $\partial\Omega$  and  $\partial\Lambda$ , where  $k_v, k_m$ , are the characteristic intrinsic permeabilities of the tube and the porous medium, respectively,  $\mu_c$  is a characteristic viscosity, and  $\hat{q}$  ( $\text{m}^3 \text{s}^{-1} \text{m}^{-1}$ ) is a source function modeling fluid exchange. To distinguish the pressure in the different compartments, we use different subscripts, although it is physically the same quantity. The line source function  $\hat{q}(s)$  couples Eqs. (6.1a) and (6.1b). Equation

---

\*The introductory section is based on Koch, Schneider, Helmig, and Jenny (2020d), © 2020 Elsevier Inc.

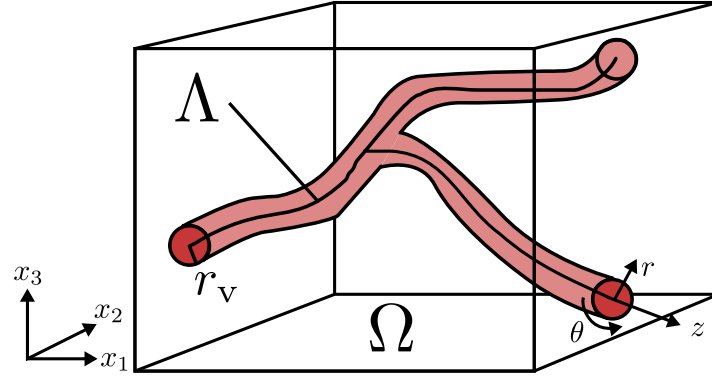


**Figure 6.1 – Bifurcating tubular network—schematic representation.** The network with center-line  $\Lambda$  is embedded in the porous domain  $\Omega$ . A segment-local cylindrical coordinate system is shown with the coordinates  $z, \theta, r$ , as well as a Cartesian coordinate system for  $\mathbb{R}^3$  with the coordinates  $x_1, x_2, x_3$ . The tube radius at any segment cross-section is denoted by  $r_v$ . Reprinted with permission from Koch et al. (2020d), © 2020 Elsevier Inc.

systems similar to Eq. (6.1) can be used to describe the transport of molecules or energy in similar systems. We call the PDEs mixed-dimensional (in space) because Eq. (6.1a) is a one-dimensional equation, parameterized in space by the scalar  $s$ , whereas Eq. (6.1b) is a three-dimensional equation with spatial dependence on a position  $x \in \Omega \subset \mathbb{R}^3$ . We call PDE systems like Eq. (6.1), mixed-dimension embedded systems, since the network domain is geometrically embedded into the porous medium. Although the two PDEs can be mathematically separated in an abstract sense, and are commonly discretized in space using two independent non-conforming computational grids, this geometrical embedding is important when seeking a mathematically and physically consistent description of the coupling term  $\hat{q}$ .

The right-hand-side of Eq. (6.1b) contains the Dirac delta distribution which restricts the source term  $\hat{q}$  to the tube center-line for the three-dimensional flow problem (cf. Cattaneo and Zunino, 2014; D’Angelo, 2007), and has the properties

$$\int_0^\infty \int_0^{2\pi} \delta_\Lambda r d\theta dr = 1 \quad \text{and} \quad \int_\Omega f \delta_\Lambda dx = \int_\Lambda f ds, \quad (6.2)$$

for some function  $f$ . The source term  $\hat{q}$  usually depends both on the pressure in the tube and the pressure in the porous medium. In order for Eq. (6.1) to be mathematically sound, the function  $\hat{q}$  has to be defined on the tube center-line. However, in the physical space, the tubes of the embedded network have a finite volume. This apparent inconsistency led to



the development of several methods of describing fluid exchange between the tubes and the porous compartment. A possible formulation for  $\hat{q}$  is given by

$$\hat{q} = \frac{k_\omega}{\mu_c d_\omega} 2\pi r_v (p_v - \bar{p}_m), \quad \text{with} \quad \bar{p}_m = \frac{1}{2\pi} \int_0^{2\pi} p_m \Big|_{r_v} d\theta, \quad (6.3)$$

where  $\bar{p}_m$  is the average fluid pressure in the porous domain on the perimeter of a given tube cross-section with radius  $r_v$ ,  $k_\omega$  is the characteristic intrinsic permeability of a membrane separating network and porous compartment, and  $d_\omega$  the membrane thickness.

The line source formulation, that is Eq. (6.1) and Eq. (6.3), has been derived and discussed by D'Angelo (2007). The derivation is based on scaling the tube radius to the zero limit under the constraint of flux equality. Unfortunately, solutions to Eq. (6.1) exhibit a singularity of  $p_m$  at  $r = 0$  (tube center-line), which is both nonphysical and challenging for numerical methods. D'Angelo (2012) proves convergence of standard finite element methods in weighted norms for the line source problem. Köppl et al. (2016) show optimal convergence rates up to a log-factor in classical but local norms excluding a small neighborhood around the singularity. It is argued that the solution is only physically meaningful for  $r > r_v$ . However, numerical experiments with standard finite element methods show that optimal convergence rates can only be achieved, if the cell size  $h_\Omega$  of the grid discretizing  $\Omega$ , is in the order of magnitude of the tube radius  $r_v$  and smaller.

Secomb et al. (2004) use Green's functions to solve a system of equations similar to Eq. (6.1) semi-analytically. The authors exploit the superposition property of the Laplace operator. The tube network is represented by a collection of point sources along the tube center-lines. The solution in  $\Omega$  is constructed by adding up the contributions of all point sources and a harmonic correction function to satisfy the boundary conditions. However, due to global interaction of those contributions, the numerical solution of the point source strengths results in dense system matrices. Note that in this method the three-dimensional equations are only solved by analytical solutions which makes the method less flexible with respect to arbitrary boundary conditions and domain shapes, and unsuitable for transient problems, nonlinear problems, or problems with heterogeneous material parameters. Gjerde et al. (2019) narrow the support of the line source contributions by a smooth cut-off function and the correction function is numerically approximated. This yields sparse system matrices. The method is also known as subtraction method from the field of electroencephalography (EEG) source reconstruction (Engwer et al., 2017). A local version of such methods has been

well-studied in petroleum engineering and is known as the Peaceman well model (Peaceman, 1983; Chen and Zhang, 2009) in its simplest form. However, local approximations are difficult to construct for arbitrarily oriented wells (Wolfsteiner et al., 2003; Aavatsmark and Klausen, 2003). Moreover, these well models can only be derived in a discrete setting, see Chapter 5. Similar approaches have been used, for example, to reconstruct the pressure profiles around roots (Schröder et al., 2009a; Beudez et al., 2013; Mai et al., 2019). For these methods it is generally not possible to show grid convergence for arbitrary grids, boundary conditions, or orientations of the network segments.

A different approach is taken by Köppl et al. (2018). Instead of using line sources, the exchange term between network and embedding medium is distributed on the actual surface of the cylindrical tubes, thus increasing the dimension of the source term by one. As a consequence, the singularity is replaced by a smoother continuation of the pressure function for  $r < r_v$ , leading to better numerical properties. However, good approximations of the exchange flux  $\hat{q}$  still requires very fine grid resolutions.

In this work, we generalize Eq. (6.1), such that several methods can be described in the same mathematical framework. To this end, we consider the generalized problem

$$-\pi r_v^2 \frac{k_v}{\mu_c} \frac{\partial^2 p}{\partial s^2} = -\hat{q} \quad \text{in } \Lambda, \quad (6.4a)$$

$$-\nabla \cdot \left( \frac{k_m}{\mu_c} \nabla p \right) = \hat{q} \Phi_\Lambda \quad \text{in } \Omega, \quad (6.4b)$$

$$\hat{q} = \frac{k_\omega}{\mu_c r_\omega} 2\pi r_v (p_v - p_{m,0}) \Xi, \quad (6.4c)$$

where  $\Phi_\Lambda$  is defined in terms of non-negative local kernel functions  $\Phi_{\Lambda,i}(s)$  that distribute  $\hat{q}(s)$  over a small radially-symmetric tubular support region,  $\mathcal{S}(\Phi_{\Lambda,i})$ , with radius  $\varrho(s)$ , around a tube segment  $i$ , such that  $\Phi_{\Lambda,i} = 0$  outside the support region (compact support). The flux  $\hat{q}$  in Eq. (6.3) is now formulated in terms of the extra-vascular pressure  $p_{m,0}$ , evaluated at the tube center-line. The function  $\Xi = \Xi(\varrho(s), \Phi(s), \dots)$  is a flux scaling factor depending on the support radius, and the chosen kernel function. We choose kernel functions  $\Phi_{\Lambda,i}(s)$  in the plane perpendicular to segment  $i$  in the form

$$\Phi_{\Lambda,i}(s, \varrho) = \varrho^{-2} \varphi(r \varrho^{-1}) \quad \text{with} \quad \int_0^{2\pi} \int_0^{\varrho(s)} \Phi_{\Lambda,i} r \, dr \, d\theta = 1 \quad \forall s, \quad (6.5)$$

where the function  $\varphi$  is a positive symmetric mollifier (Friedrichs, 1944, 1953) defined on a disc perpendicular to the tube segment.

It can be shown that for  $\varrho \rightarrow 0$ , such  $\Phi_{\Lambda,i}$  converge to the Dirac delta distribution for every position  $s$ , in the sense of distributions (Dang and Ehrhardt, 2012). Therefore, if the flux scaling factor is chosen as

$$\Xi = \frac{(p_v - \bar{p}_m)}{(p_v - p_{m,0})}, \quad (6.6)$$

and the kernel is chosen as  $\Phi_\Lambda = \delta_\Lambda$ , Eq. (6.4) is equal to Eq. (6.1) and Eq. (6.3). Moreover, with the kernel function properties introduced above, in the limit of  $\varrho \rightarrow 0$ , Eq. (6.4) is equal to Eq. (6.1) and Eq. (6.3) as well. The formulation of Köppl et al. (2018) is obtained by choosing kernel functions that are  $P_v^{-1} = (2\pi r_v)^{-1}$  on the tube cross-section perimeter, and zero elsewhere. Hence, the mixed-dimension embedded formulations presented by D'Angelo (2007); Köppl et al. (2018) are special cases of this generalized formulation. A similar formulation to Eq. (6.4) is introduced by Karvounis and Jenny (2016) for an embedded discrete fracture model (2D-3D), but the properties of the given kernel functions are not further analyzed or numerically exploited.

Beyond the existing methods by D'Angelo (2007) and Köppl et al. (2018), the generalized formulation gives rise to a new mixed-dimension embedded method with distributed sources if the kernel function is chosen such that the fluid exchanged with the network domain is distributed over a small three-dimensional volume in the vicinity of the tubes. This method is introduced and analyzed in Chapter 7 and the different mixed-dimension embedded methods are compared in several numerical experiments.

**Summary** The different methods for describing and solving mixed-dimension problems with embedded tubular network can be categorized by two criteria:

- the type of distribution of the exchange source term ( $\hat{q}$ ) in the porous domain (line, surface, volume),
- the type of evaluation and/or reconstruction of variables of the porous domain problem needed to evaluate the source term.

Figure 6.2 is an attempt to visualize different mixed-dimension methods in a schematic representation. Method (a) represents a rather naive approach. The source term is distributed

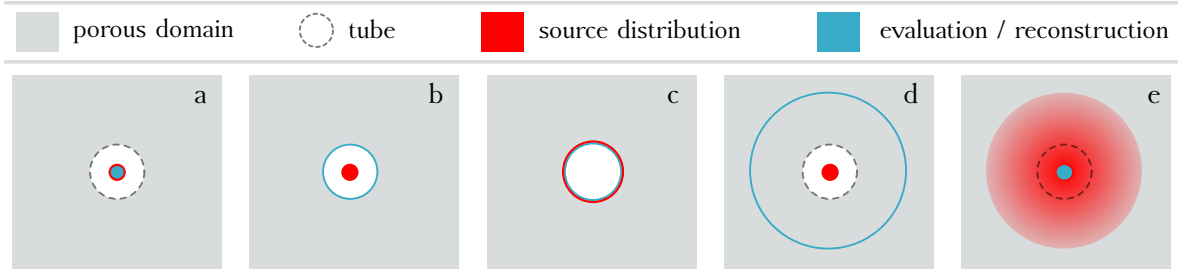


**Figure 6.2 – Mixed-dimension coupling methods.** Schematic representation of different numerical coupling methods for modeling porous domains with embedded tubular networks. The methods are distinguished by the type of source distribution in the 3D domain, and the type of 3D variable evaluation for the source term computation. (a) line source, reconstruction based on center-line quantity; (b) line source, reconstruction based on average operator; (c) area/surface source, reconstruction based on average operator; (d) line source, reconstruction based on a local model in the neighborhood of the tube; (e) volume source, reconstruction based on center-line quantity.

on a line (line source) and the variables are evaluated on the tube center-line. This method does not lead to mathematically sound equations for systems like Eq. (6.1), as the solutions of the three-dimensional problem exhibit a singularity on the center-line (due to the line source). Hence, the primary variable cannot be evaluated on the center-line. However, in a discrete setting and when the three-dimensional discretization length is much larger than the tube radius, this method is equal to the other methods. Method (b) represents the method of D’Angelo (2007), where the source term is distributed as a line source while its variables are evaluated as the average on the tube surface, leading to well-posed problems for systems like Eq. (6.1). For method (c), the source term is distributed on the tube surface (surface source) while the variables are evaluated as for (b), cf. Köppl et al. (2018). In a variation of method (c), the one-dimensional solution is projected onto the tube surface and the source term can be evaluated by integration over the tube surface. By effectively increasing the dimension of the source term by one, the solution is regularized and does not exhibit singularities. However, the solution may still exhibit kinks on the tube interface, see e.g. Section 7.3.3. Method (d) represents a class of approaches which evaluate the variables of the three-dimensional problem in some distance to the tubes, and reconstruct the variables on the tube surface by means of analytical or numerical approximations of the equations in the near-surface region. The Peaceman well model also falls in this category, where the numerical well-block pressure is measured and related with a local analytical solution to the well-bore pressure. Mai et al. (2019) solve local one-dimensional radially-symmetric problems numerically to obtain the source term. For method (e), the source term is distributed over a volume (volume source). Consequently, the local solution inside

this volume is regularized. The variables for computing the source term can be evaluated, for example, on the tube center-line. In order to recover the exact value of the variable on the tube surface, a reconstruction step is necessary. Methods of type (e) are developed in Chapters 7 and 8.

Finally, we note that to the best of our knowledge, all existing methods are derived for tube segments without bifurcations. How to rigorously analyze and how to formulate mixed-dimension models for coupling processes at the interface of the tubes at bifurcations (under consideration of the bifurcation geometry) is an open research question. Unfortunately, solving this problem is beyond the scope of this work. Nevertheless, all mentioned methods have also been applied to networks with bifurcations. As no analytical solutions exist for such problems, the error which different schemes introduce at bifurcations is currently unknown. Yet, we know that a difference at bifurcations between the different methods exists, as observed in Section 7.3.4 and Section 7.3.5 in this work.

## 6.1 Generalized mixed-dimension embedded problem

Independent of the application, we can formulate a generalized conservation problem for the type of mixed-dimension embedded systems considered in this work. The coupled mixed-dimensional PDEs are of the general form

$$\frac{\partial \hat{c}(\mathbf{u})}{\partial t} + \frac{\partial f(\mathbf{u})}{\partial s} = \hat{q}_E(\mathbf{u}) - \hat{q}(\mathbf{u}, \boldsymbol{\omega}) \quad \text{in } \Lambda, \quad (6.7a)$$

$$\frac{\partial c(\boldsymbol{\omega})}{\partial t} + \nabla \cdot \mathbf{F}(\boldsymbol{\omega}) = q_E(\boldsymbol{\omega}) + \hat{q}(\mathbf{u}, \boldsymbol{\omega}) \Phi_\Lambda \quad \text{in } \Omega, \quad (6.7b)$$

where  $\hat{c}(\mathbf{u})$  and  $c(\boldsymbol{\omega})$  are the respective conserved quantities,  $f(\mathbf{u})$  and  $\mathbf{F}(\boldsymbol{\omega})$  are flux functions, and  $\hat{q}_E(\mathbf{u})$  and  $q_E(\boldsymbol{\omega})$  are external sources, given in terms of the primary variables  $\mathbf{u} = \mathbf{u}(s, t)$  and  $\boldsymbol{\omega} = \boldsymbol{\omega}(x, t)$ . Equations (6.7a) and (6.7b) are coupled via the source terms  $\hat{q}(\mathbf{u}, \boldsymbol{\omega})$ . All mixed-dimension PDE systems introduced in the previous chapters, namely Eqs. (3.22) and (3.23) for the tissue perfusion problem, Eq. (4.8) for the root water uptake problem, and Eqs. (2.5), (5.3) and (5.9) for well modeling, fit into this generalized form. Table 6.1 exemplarily shows the generalized coupled mixed-dimension form for the tissue perfusion problem presented in Chapter 3. In the general case, the flux function  $\mathbf{F}$  is a second-order tensor field and all other quantities defined in Eq. (6.7) are first-order tensor

**Table 6.1 – Tissue perfusion problem in generalized form.** Representation of Eqs. (3.22) and (3.23) in the generalized coupled mixed-dimension form  $\rightarrow$  Eq. (6.7). Some quantities are written as matrix-vector products to avoid duplication. The external sources  $\hat{q}_E$  and  $q_E$  are zero.

$$\begin{array}{l}
 \mathbf{u} = \begin{bmatrix} p_v \\ c_v^\kappa \end{bmatrix} \quad \hat{\mathbf{c}} = \begin{bmatrix} 0 \\ 0 \end{bmatrix} \quad \mathbf{f} = \begin{bmatrix} \rho_B & 0 \\ c_v^\kappa & 1 \end{bmatrix} \begin{bmatrix} A_v v \\ -A_v D_B \partial_s c_v^\kappa \end{bmatrix} \\
 \mathbf{w} = \begin{bmatrix} p_t \\ c_t^\kappa \end{bmatrix} \quad \mathbf{c} = \begin{bmatrix} 0 \\ 0 \end{bmatrix} \quad \mathbf{F} = \begin{bmatrix} \rho_I & 0 \\ c_t^\kappa & 1 \end{bmatrix} \begin{bmatrix} v \\ -D_{l,e}^\kappa \nabla c_t^\kappa \end{bmatrix} \quad \hat{\mathbf{q}} = \begin{bmatrix} \rho_I & 0 \\ (1-\sigma_c)c_{up}^\kappa & 1 \end{bmatrix} \begin{bmatrix} L_p P_v (p_v - \bar{p}_t) \\ D_\omega P_v (c_v^\kappa - \bar{c}_t^\kappa) \end{bmatrix}
 \end{array}$$

fields. In the case of one primary variable, for example, for the single-phase well model of Chapter 5, the balance equations, Eq. (6.7), reduce to scalar conservation equations.

In the following chapters, in particular in Chapters 7 and 8 which focus on method development, some terms in Eq. (6.7) are not considered. We want to contribute a discussion of several fundamental aspects of mixed-dimension methods for embedded tubular network systems, however, not all aspects can be discussed or analyzed in the scope of this work. For example, the analysis of transient, non-linear problems in the mixed-dimensional context is yet to be better understood. This has to be taken in account, in particular, for the interpretation of results for the root water uptake model. Nevertheless, the analysis of simplified problem can help to better understand more complex problems.

## 6.2 Dimensional analysis

In Chapters 3 to 5, we derived models for three different applications. The same numerical methods can be used to perform numerical simulations with these models. While the model equations are mathematically similar, the model parameters describe different materials and processes. To get a better idea of how the flow processes in both subdomains interact and how this interaction differs for the different applications, we perform a dimensional analysis for simplified problems. To this end, we choose a pressure scale  $P$  such that  $p^* = pP^{-1}$  is dimensionless. We introduce two characteristic length scales: the characteristic axial length scale of the tubes,  $l_v$ , and the characteristic length scale of the porous domain,  $l_m$ . Furthermore, we introduce the dimensionless gradients  $\nabla^* = l_m^{-1} \nabla$  and  $\partial / \partial s^* = l_v^{-1} \partial / \partial s$ , and the dimensionless kernel function  $\Phi_\Lambda^* = \pi^{-1} l_r^{-2} \Phi_\Lambda$ .

### 6.2.1 Tissue perfusion

The dimensional analysis is performed on the stationary mixed-dimensional one-phase flow problem given by Eq. (6.4). A dimensionless form of Eq. (6.4) is given by

$$-\Theta_v \frac{\partial^2 p^*}{\partial s^{*2}} = -\hat{q}^* \quad \text{in } \Lambda, \quad (6.8a)$$

$$-\nabla^* \cdot (\Theta_m \nabla^* p^*) = \hat{q}^* \Phi_\Lambda^* \quad \text{in } \Omega, \quad (6.8b)$$

$$\hat{q}^* = \Theta_\omega \Delta p^*, \quad (6.8c)$$

with the dimensionless pressure jump across the membrane  $\Delta p^* = (p_v^* - p_{m,0}^*)\Xi$  and the dimensionless groups

$$\Theta_v = \frac{k_v}{l_v^2}, \quad \Theta_m = \frac{k_m}{l_m^2}, \quad \Theta_\omega = 2 \frac{k_\omega}{r_v d_\omega}. \quad (6.9)$$

In the following, we estimate values for these dimensionless groups. Generally, a ratio of two of these dimensionless numbers close to 1 means that the processes described by them are similarly important. For example, a ratio  $\Theta_v/\Theta_\omega \gg 1$  indicates that the transmural exchange has little influence on the flow field in the tubes. On the other hand, a ratio  $\Theta_v/\Theta_\omega \ll 1$  would mean that the flow field in the tube is dominated by the transmural exchange.

We choose the porous length scale as the mean distance between capillaries estimated as  $l_m \approx 50 \mu\text{m}$  (rodent cerebral cortex, from Lückner (2017)), and the axial length scale as a mean capillary length,  $l_v \approx 300 \mu\text{m}$  (rodent cerebral cortex, from Sakadzic et al. (2014)). We estimate the mean capillary radius as  $r_v \approx 3 \mu\text{m}$ , which gives  $k_v = r_v^2/8 = 1.125 \cdot 10^{-12} \text{m}^2$ . The tissue permeability is estimated as  $k_m \approx 8 \cdot 10^{-18} \text{m}^2$  (Baxter and Jain, 1989). The membrane thickness is given by the thickness of the endothelium,  $d_\omega \approx 0.6 \mu\text{m}$  (Bertossi et al., 1997). Finally,  $k_\omega$  is given by  $k_\omega = L_p \mu_c d_\omega$ , where we choose  $\mu_c \approx 2 \cdot 10^{-3} \text{Pa s}$ , and the filtration coefficient ranges from  $1 \cdot 10^{-12} \text{m Pa}^{-1} \text{s}^{-1}$  (continuous capillaries) to  $1 \cdot 10^{-9} \text{m Pa}^{-1} \text{s}^{-1}$  (fenestrated capillaries) (Baber, 2014). Baxter and Jain (1989) suggest  $L_p = 2.7 \cdot 10^{-12} \text{m Pa}^{-1} \text{s}$  for normal subcutaneous and  $L_p = 2.1 \cdot 10^{-11} \text{m Pa}^{-1} \text{s}$  for tumor tissue. Therefore, we obtain  $\Theta_v \approx 1.25 \cdot 10^{-5}$ ,  $\Theta_\omega \approx 7 \cdot 10^{-10}$  to  $7 \cdot 10^{-7}$ , and  $\Theta_m \approx 3 \cdot 10^{-9}$ . Consequently, the system is dominated by the flow in the vascular compartment (cf. Cattaneo and Zunino, 2014). Furthermore, the transmural exchange has only little influence on the vascular flow field

( $\Theta_v/\Theta_\omega \gg 1$ ). Considerable influence is only expected for fenestrated capillaries, or if the endothelium is degenerated or diseased (high  $L_p$ ). On the other hand, the flow field in the extra-vascular space is largely affected or dominated by the transmural exchange. These results coincide with the common understanding that the microvasculature is the driving factor for fluid movement in most tissues. By analyzing a simplified problem with a single capillary embedded in a tissue cylinder, see Appendix A.1, we estimate that the pressure drop across the vascular wall is of similar order of magnitude than the radial pressure drop in the tissue cylinder. Only for very permeable vascular walls (high  $L_p$ ), the extra-vascular compartment becomes limiting for transmural fluid transport. Furthermore, we can estimate that due to the logarithmic nature of the pressure profile around the capillaries, flow velocities in the interstitial space are almost 20 times larger at the vessel surface than in a distance of  $l_m = 50 \mu\text{m}$  to the vessel center-line.

### 6.2.2 Root water uptake

For the analysis of the root-soil system, we consider the dimensionless Richards equation in the soil domain. To this end, we choose a time scale  $T$  such that  $t^* = tT^{-1}$  is dimensionless. Assuming that the change of water saturation in the domain is dominated by the root water uptake (neglecting gravity, no irrigation, closed planting container), we choose  $T$  proportional to the root water uptake rate,  $T = \mu_c P^{-1} \Theta_\omega^{-1}$ , where the dimensionless group  $\Theta_\omega$  is defined as in Eq. (6.9). Then, a dimensionless form of Eq. (4.8) is given by

$$-\Theta_v \frac{\partial^2 p^*}{\partial s^{*2}} = -\hat{q}^* \quad \text{in } \Lambda, \quad (6.10a)$$

$$\Theta_\omega \phi \frac{\partial S_1}{\partial t^*} - \nabla^* \cdot (k_{r1}(S_1) \Theta_m \nabla^* p^*) = \hat{q}^* \Phi_\Lambda \quad \text{in } \Omega, \quad (6.10b)$$

$$\hat{q}^* = \Theta_\omega \Delta p^*, \quad (6.10c)$$

where water saturation,  $S_1$ , soil porosity,  $\phi$ , and relative permeability,  $k_{r1}$ , are dimensionless by definition, and all other quantities are defined analogously to Eq. (6.4).

The analysis for root systems depends on the root system age, the analyzed species, and the soil water distribution. In the following, we consider a young lupin root system, as used in the simulations in Chapter 10. We estimate the mean root length of the tap root by the rooting depth, so that  $l_v \approx 10 \text{ cm}$ . For lateral roots, we choose  $l_v \approx 5 \text{ cm}$ . Assuming a single plant



growing in a lab-scale cylindrical rizotron, we choose its radius as the relevant porous scale,  $l_m \approx 5$  cm. For the 8-day-old lupin root system shown in Fig. 6.3, the root-length-weighted mean radius is  $r_v = 0.68$  mm for the entire root system,  $r_v = 0.95$  mm for the tap root and  $r_v = 0.58$  mm for laterals. With the characteristic viscosity  $\mu_c = 1 \cdot 10^{-3}$  Pa s (water at 20 °C), the characteristic permeabilities are given by  $k_v = k_{ax} \mu_c \pi^{-1} r_v^{-2}$ ,  $k_m = k$ ,  $k_\omega = k_{rad} \mu_c d_\omega$ . The root hydraulic conductivities  $k_{ax}$  and  $k_{rad}$  depend on root age (Steudle and Peterson, 1998), root radius (Vercambre et al., 2002), and environmental conditions (Lovisolo and Schubert, 1998). For this analysis, we choose the age-dependent root hydraulic conductivities given in Fig. 6.3. The relative and intrinsic permeabilities largely vary with soil type and water saturation, see Fig. 6.4. To estimate the characteristic permeability  $k_v$ , we choose an

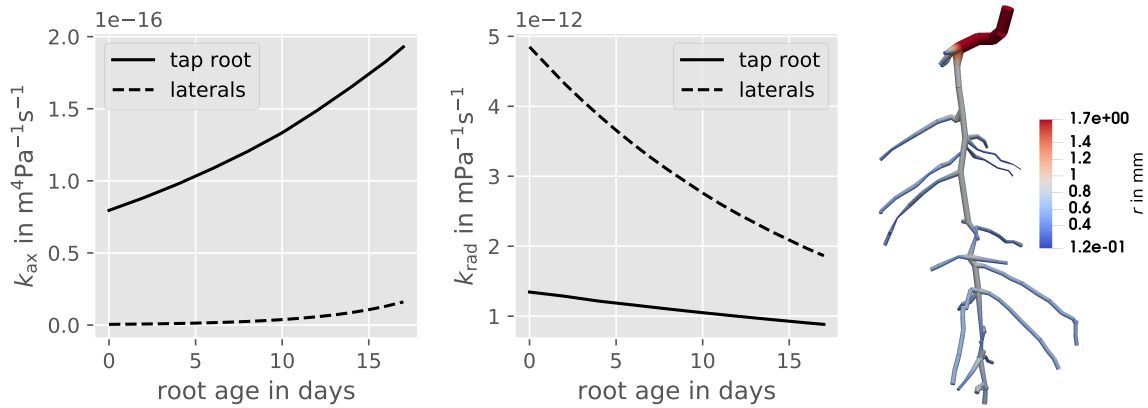


**Figure 6.3 – Root conductivities for a lupin root system.** Left and middle, age-dependent hydraulic root conductivities from Schnepf et al. (2020). Right, 8-day-old lupin root system reconstructed from MRI data (courtesy of M. Landl, FZ Jülich). The root segment radius is visualized to scale. The rooting depth is about 10 cm.

average age of 4 d to determine  $k_{ax}$  and  $k_{rad}$ . Then for the tap root, we obtain  $\Theta_v \approx 3.5 \cdot 10^{-12}$  and  $\Theta_\omega = 2.5 \cdot 10^{-12}$ , and for lateral roots, we compute  $\Theta_v \approx 3.8 \cdot 10^{-13}$  and  $\Theta_\omega = 1.3 \cdot 10^{-11}$ . Therefore, the estimated relevant time scale for flow processes in the soil is in the order of hours.

For  $\Theta_m$ , we obtain  $\Theta_m \approx 5.0 \cdot 10^{-9}$  for *Sand1*,  $\Theta_m \approx 2.5 \cdot 10^{-10}$  for *Loam*, and  $\Theta_m \approx 5.0 \cdot 10^{-11}$  for *Clay*, using the soil types shown in Fig. 6.4. The values of  $\Theta_m$  are rather high in comparison with the other dimensionless groups. However, they still need to be multiplied with the relative permeability, cf. Eq. (6.10b), which strongly and nonlinearly scales with the soil water saturation. The usual water flow path in the context of root water uptake starts in the soil, goes over the root cortex into the xylem, and then upwards in the hierarchical root

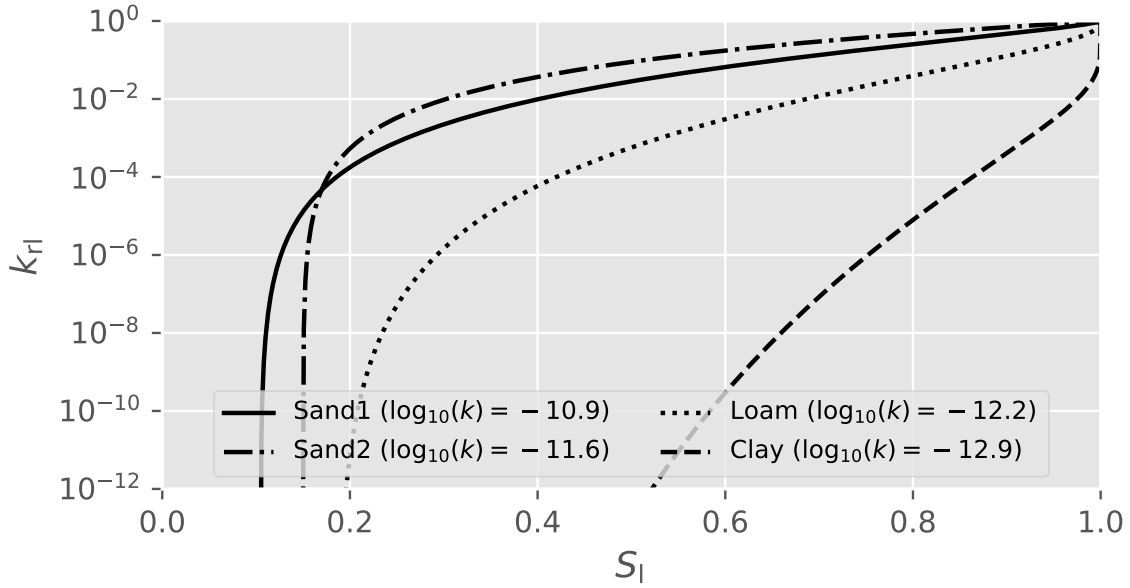


**Figure 6.4 – Relative permeabilities for different soil types.** Van Genuchten-Mualem model with parameters for *Sand1*, *Loam*, *Clay* from Vanderborght et al. (2005), *Sand2* from Koch et al. (2018b).

tree. Hence, for a small value of  $k_{r1}\Theta_m$  (in comparison with  $\Theta_\omega$  and  $\Theta_v$ ), we would expect the soil resistance to be limiting for root water uptake, while for a high value, we would expect either the root cortex or the root xylem to be limiting. Given the relative permeability curves in Fig. 6.4, it is evident that even for moderately low soil water saturation, values for  $k_{r1}$  are  $1 \cdot 10^{-2}$  and lower. Comparing this with the values estimated for the dimensionless groups given above, we conclude that the soil permeability is limiting root water uptake for dry soils. For very wet soils ( $S_1 > 0.9$ ), either the resistance of the root cortex or the root xylem (especially for young lateral roots) seems to limit water uptake. We note at this point that it has been suggested that in the presence of mucilage (a gel-like substance exerted by some roots) soil water saturation values close to roots may be significantly altered towards higher values (Carminati et al., 2010). Herein, mucilage is not considered. However, there is also experimental evidence of high local water saturation gradients close to the root for dry soils (Garrigues et al., 2006). There is a range of system states (mid-range water saturation) for which it is still unclear which compartment limits root water uptake (Beudez et al., 2013).

The pressure drop along the root in comparison with the pressure drop across the root cortex is analyzed in Appendix A.2. We can show that the ratio of these pressure drops can

be estimated by the ratio  $0.5\Theta_\omega\Theta_v^{-1}$ . Using the values estimated above,  $0.5\Theta_\omega\Theta_v^{-1} \approx 0.7$  for the tap root, and  $0.5\Theta_\omega\Theta_v^{-1} \approx 0.01$  for lateral roots. Thus, the expected pressure differences along the root are expected to be similar to the cortex pressure drop for the tap root, while the longitudinal root resistance dominates the pressure drop for lateral roots.

### 6.2.3 Well modeling

Instead of discussing well segments with permeable wall, we neglect any well casing, assuming that its permeability is much higher than that of the rock matrix. We assume that the well bore surface is impermeable everywhere, except for some segment located at the end of the well bore hole, where the fluid transfer into the matrix happens. We analyze the same dimensionless groups  $\Theta_v = k_v l_v^{-2}$  (for well bore) and  $\Theta_m = k_m l_m^{-2}$  (for rock matrix), as defined above for the other applications. The well permeability is typically in the order of  $k_v = r_\omega^2/8 \approx 1 \cdot 10^{-3} \text{ m}^2$  (assuming a well bore radius of 10 cm), while the order of the matrix permeability ranges from  $k_m \approx 1 \cdot 10^{-12}$  to  $1 \cdot 10^{-15} \text{ m}^2$  for sandstone (Doyen, 1988) down to a range of  $k_m \approx 1 \cdot 10^{-17}$  to  $1 \cdot 10^{-23} \text{ m}^2$  in clay and shale formations (Neuzil, 1994). We estimate that typical lateral length scales of the rock formations or aquifers are in the order of  $l_m \approx 100$  to  $1000 \text{ m}$ , while the permeable section of the well is in the order of  $l_v \approx 10$  to  $100 \text{ m}$ , and the total well length can be up to  $5000 \text{ m}$  for some geological formations. Therefore, we obtain  $\Theta_v \approx 1 \cdot 10^{-9}$  to  $1 \cdot 10^{-5}$ ,  $\Theta_m \approx 1 \cdot 10^{-29}$  to  $1 \cdot 10^{-16}$ . Hence, injection and extraction are limited by low rock matrix permeabilities. Furthermore, we conclude that a good assumption is that of a spatially constant well pressure in the permeable segment. We note that in this work we restrict ourselves to the analysis of rather simple models of the fluid flow around wells. We only consider single fluid phase systems, while in many applications, for example in petroleum engineering, two-phase flow occurs. The fluid is considered incompressible, so that we cannot describe the injection of gases, such as for example for energy storage systems or  $\text{CO}_2$  sequestration scenarios. Only isothermal systems are modeled, and the rock matrix does not change properties (e.g. fracking). Consequently, the analysis of well modeling in Chapter 8 is focused on the numerical aspect of the mixed-dimensional coupling. Again, we believe that the analysis of simpler systems may also lead to a better understanding of more complex models.

### 6.2.4 Conclusion

After introducing the particularities of the different applications, we conclude with a comparison of different characteristic features of the described systems.

**Network structure** An important difference between the three applications is the structure of the (hierarchical) network. While the network is a closed circuit for the cardiovascular system which contains diverging and converging bifurcations as well as loops, the network for the roots resemble a tree structure where the smallest roots end in the form of root tips and root sprout from a single stem at the root collar. Likewise, wells consist of either single bore holes or tree-like branching structures with a main duct that may branch out into several channels inside the subsurface which end in the target rock formation. Hence, for roots and wells, a fluid particle has a flow path with a clear direction through all compartments, from the porous medium, across a membrane, through the network structure (or in opposite direction for injection wells). Therefore, the flow resistance is expected to be dominated by the compartment with the highest resistance. For the cardiovascular system, particles may stay within the vascular network, and only some particles cross the capillary wall in a selected organ. These differences may be explained with different functional purposes. The well system is designed to inject or extract fluid with minimal additional friction from or into a formation, while minimizing drilling costs. This explains relatively few network segments with high permeability. The root system is designed to transport water upwards withstanding large pressure gradients. The cardiovascular system is designed to supply a large volume of tissue with fluid and nutrients as evenly as possible.

**Driving force** While the well and the cardiovascular system are driven by an active pumping unit, root water uptake is assumed to be passive. The evaporation of water in the leaf stomata is the main driving force for the fluid transport in the system. This could explain why roots are significantly less permeable than blood vessels or wells. Thin structures are required to make use of capillary, cohesive and adhesive forces for the upward transport of water against gravity (cohesion-tension theory, see Tyree (1997)). Despite these differences, the driving force in all systems is firstly exerted on the system through the network structure, while the embedding porous medium takes a passive role.

---

**Porous medium** All described systems have in common that the embedded networks enable fast transport, and act as channels for fluid flow through porous media with otherwise low permeability. This means that the network structure and its interaction with the embedding porous medium is essential for the modeling of flow problems in these systems.

**Localized flow patterns** Because the network structures are thin and the porous media have low permeability, flow patterns in the porous structure will exhibit strong nonlinear local features in the vicinity of the network tubes. Near-field pressures follow a logarithmic profile with increasing gradients towards the tubes. Likewise, flow velocities increase towards the tubes. We also note (without proving it here) that the locality of this effect is much stronger than for the case of embedded planar networks such as fracture networks in rocks. This is because the embedded tube structures are thin with respect to two dimensions, while fractures or other planar interfaces are thin with respect to only one dimension.

Localized flow patterns turn out to be the most challenging aspect for the design of numerical methods approximating flow and transport processes in such systems. Therefore, the subsequent chapters of this work focus not only on using mixed-dimension methods for the described applications, but also on the development of suitable numerical methods.



# 7 A new method for the simulation of tissue perfusion\*

In this chapter, a new numerical method for mixed-dimension embedded problems with tubular network inclusions is introduced, analyzed and tested with several numerical examples. The method is derived in Section 7.1. The discrete equations are discussed in Section 7.2. Finally, the method is numerically analyzed in Section 7.3, and compared with existing methods for increasingly complex scenarios.

## 7.1 Mixed-dimension problem with distributed sources

Flow in a given brain tissue sample can be described by the coupled system of partial differential equations presented in Eq. (3.22), (cf. Cattaneo and Zunino, 2014; D'Angelo, 2007). In this chapter, we consider the set of equations

$$-\frac{\partial}{\partial s} \left( \rho_B \frac{A_v r_v^2}{8\mu_B} \frac{\partial p_v}{\partial s} \right) = -\hat{q}_m \quad \text{in } \Lambda, \quad (7.1a)$$

$$-\nabla \cdot \left( \frac{\rho_I}{\mu_I} k \nabla p_t \right) = \hat{q}_m \Phi_\Lambda \quad \text{in } \Omega, \quad (7.1b)$$

$$\hat{q}_m = \rho_I L_p P_v (p_v - p_{t,0}) \Xi, \quad (7.1c)$$

formulated in terms of effective pressures,  $p_\alpha = \tilde{p}_\alpha - \pi_\alpha$ ,  $\alpha \in \{v, t\}$ , where  $\tilde{p}_\alpha$  denotes the hydraulic pressure and  $\pi_\alpha$  the colloid osmotic pressure introduced in Section 3.2. Equation (7.1) differs from Eq. (3.22) only in the source term, which is now formulated in terms of  $p_{t,0}$ , the extra-vascular pressure evaluated on the vessel center-line. The flux scaling factor  $\Xi$  is given by Eq. (6.6).

We introduce the method of distributed sources by choosing cylindrical, radially-symmetric kernel functions,  $\Phi_{\Lambda,i}(\varrho)$ , with finite support radius  $\varrho$ , for each straight vessel segment  $i$  in a network of vessels. We recall that this is in contrast to the method introduced by D'Angelo

---

\*This chapter is based on Koch, Schneider, Helmig, and Jenny (2020d), © 2020 Elsevier Inc.

(2007), where the kernel functions are chosen as the Dirac delta distribution (line source), or the method introduced by Köppl et al. (2018) (surface source), where the kernel function is chosen as a constant on the surface of the vessel ( $r = r_v$ ) and zero everywhere else. Moreover, these methods require computing  $p_{t,\mathbb{W}}$ , the mean pressure on a given vessel cross-section perimeter, see Eq. (6.3), numerically. For non-zero support,  $\varrho > 0$ , smooth kernel functions regularize the pressure solution in the kernel support region. Hence, solutions to Eq. (7.1), unlike solutions to Eq. (6.1), have no singularities at the vessel center-line. To evaluate the function  $\hat{q}_m$ , the pressure  $p_t$  can thus be evaluated on the vessel center-line. The pressure at the location of the vessel center-line is denoted by  $p_{t,0}$ . In the following section, we show that for a single straight vessel, we can replace the definition for  $\Xi$ , Eq. (6.6), by an equivalent formula, independent of the pressure. This allows us to compute the same  $\hat{q}_m$  as for the line source method or the surface source method as a function of  $p_{t,0}$  instead of  $p_{t,\mathbb{W}}$ . Section 7.1.2 discusses the choice of the kernel support region radius,  $\varrho$ , and Section 7.1.3 the case of multiple vessels.

### 7.1.1 Flux scaling factor $\Xi$ (single straight vessel)

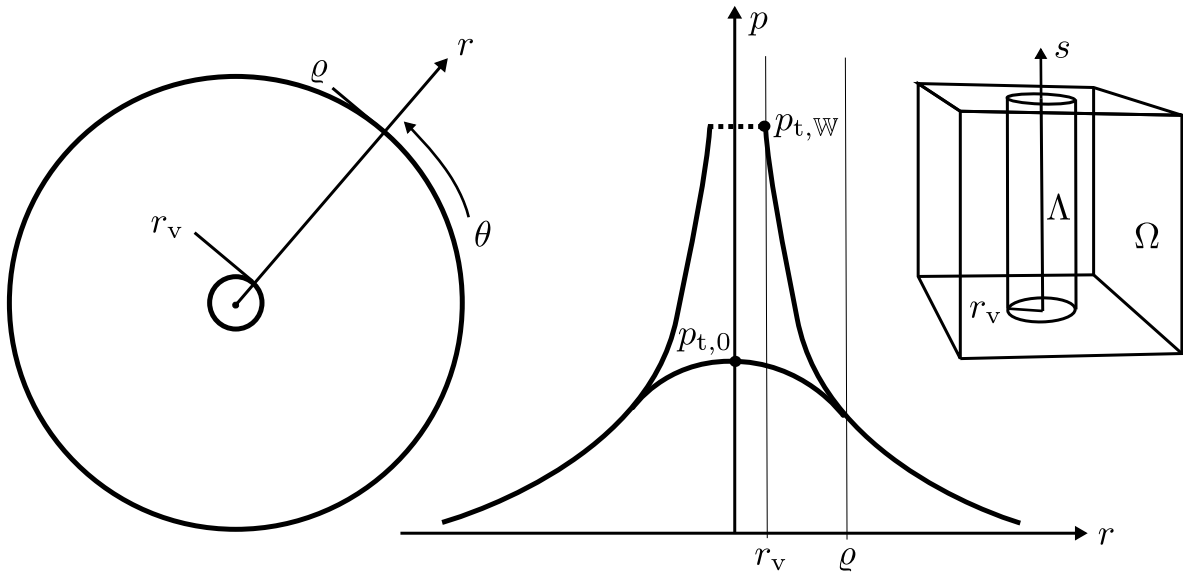


**Figure 7.1 – Pressure solution near vessel.** Location of different pressures in radial distance to the vessel center-line for the case of extravasation. The solution to the line source problem approaches  $\infty$  for  $r \rightarrow 0$ , while the regularized solution has the finite value  $p_{t,0}$  at  $r = 0$ . Reprinted with permission from Koch et al. (2020d), © 2020 Elsevier Inc.



The scaling factor  $\Xi$  can be analytically derived in terms of the kernel support radius  $\varrho$  and the constraint Eq. (6.6) under some assumptions. First, let us consider a single straight and long vessel. Looking at a cross-sectional plane cutting through this vessel (see Fig. 7.1), we assume that the flow field in a small neighborhood around the vessel is strictly radial. Now, let us exemplarily consider the following radial kernel function

$$\Phi^{\text{const}}(r) = \begin{cases} \frac{1}{\pi\varrho^2} & r \leq \varrho, \\ 0 & r > \varrho. \end{cases} \quad (7.2)$$

The flux outside the kernel support region,  $r > \varrho$ , is identical to the flux of the formulation with line sources, as the same total mass is injected in both formulations, if the flux scaling factor  $\Xi$  is chosen as in Eq. (6.6). Under the given assumption, and using a coordinate transformation to local cylindrical coordinates, Eq. (7.1b) is transformed to

$$-\frac{1}{r} \frac{\partial}{\partial r} \left( r \frac{\partial p_t}{\partial r} \right) = \frac{\mu_I}{\rho_I k} \hat{q}_m \Phi^{\text{const}}(r). \quad (7.3)$$

The pressure outside the kernel support region admits the following solution

$$p_t(r) = p_{t,\mathbb{W}} - \frac{\hat{q}_m \mu_I}{2\pi \rho_I k} \ln\left(\frac{r}{r_v}\right), \quad r > \varrho, \quad (7.4)$$

derived from the fundamental solution of the Laplace equation (Evans, 2010). We note that the mean pressure on the vessel surface,  $p_{t,\mathbb{W}}$ , is equal to the pressure evaluated at  $r = r_v$ , if  $\varrho \leq r_v$ . To derive the pressure solution inside the kernel support, we apply Leibniz's rule to Eq. (7.3)

$$\frac{\partial p_t}{\partial r} = -\frac{1}{r} \int_0^r \frac{\mu_I}{\rho_I k} \hat{q}_m \Phi^{\text{const}}(r') r' dr', \quad (7.5)$$

and integrating once more yields

$$p_t(r) = -\frac{\hat{q}_m \mu_I}{2\pi \rho_I k} \frac{r^2}{2\varrho^2} + C_0, \quad r \leq \varrho. \quad (7.6)$$

It is easy to verify that for  $r = \varrho$ , Eqs. (7.4) and (7.6) have equal derivatives which ensures flux continuity. The integration constant  $C_0$  is determined such that the pressure is continuous

at  $r = \varrho$ , yielding

$$p_t(r) = \begin{cases} p_{t,\mathbb{W}} - \frac{\hat{q}_m \mu_I}{2\pi \rho_1 k} \left[ \frac{r^2}{2\varrho^2} + \ln\left(\frac{\varrho}{r_v}\right) - \frac{1}{2} \right] & r \leq \varrho, \\ p_{t,\mathbb{W}} - \frac{\hat{q}_m \mu_I}{2\pi \rho_1 k} \ln\left(\frac{r}{r_v}\right) & r > \varrho. \end{cases} \quad (7.7)$$

This function is shown qualitatively in Fig. 7.1. To derive a suitable  $\Xi$ , let us first evaluate Eq. (7.7) at  $r = 0$ , so that  $p_{t,\mathbb{W}}$  is expressed in terms of  $p_{t,0}$ ,

$$p_{t,0} = p_{t,\mathbb{W}} - \frac{L_p r_v \mu_I}{k} (p_v - p_{t,0}) \Xi \left[ \ln\left(\frac{\varrho}{r_v}\right) - \frac{1}{2} \right], \quad (7.8)$$

where  $\hat{q}_m$  was replaced by inserting Eq. (7.1c). It directly follows from Eqs. (6.6) and (7.8) that the flux scaling factor can be expressed independently of the pressure,

$$\Xi = \frac{(p_v - p_{t,\mathbb{W}})}{(p_v - p_{t,0})} = \frac{(p_v - p_{t,0}) - \frac{L_p r_v \mu_I}{k} (p_v - p_{t,0}) \Xi \left[ \ln\left(\frac{\varrho}{r_v}\right) - \frac{1}{2} \right]}{(p_v - p_{t,0})} \quad (7.9)$$

$$\Rightarrow \Xi = \left\{ 1 + \frac{r_v L_p \mu_I}{k} \left[ \ln\left(\frac{\varrho}{r_v}\right) - \frac{1}{2} \right] \right\}^{-1} \quad (\text{for } \Phi^{\text{const}}). \quad (7.10)$$

The flux factor has a very similar structure, when derived for other kernel functions. For instance, for the cubic kernel function

$$\Phi^{\text{cubic}}(r) = \begin{cases} \frac{10}{3\pi \varrho^2} \left[ \frac{2r^3}{\varrho^3} - \frac{3r^2}{\varrho^2} + 1 \right] & r \leq \varrho, \\ 0 & r > \varrho, \end{cases} \quad (7.11)$$

we obtain

$$p_t(r) = \begin{cases} p_{t,\mathbb{W}} - \frac{\hat{q}_m \mu_I}{2\pi \rho_1 k} \left[ \frac{r^2}{\varrho^2} \left( \frac{8r^3}{15\varrho^3} - \frac{5r^2}{4\varrho^2} + \frac{5}{3} \right) + \ln\left(\frac{\varrho}{r_v}\right) - \frac{19}{20} \right] & r \leq \varrho, \\ p_{t,\mathbb{W}} - \frac{\hat{q}_m \mu_I}{2\pi \rho_1 k} \ln\left(\frac{r}{r_v}\right) & r > \varrho, \end{cases} \quad (7.12)$$

and

$$\Xi(\Phi^{\text{cubic}}) = \left\{ 1 + \frac{r_v L_p \mu_I}{k} \left[ \ln\left(\frac{\varrho}{r_v}\right) - \frac{19}{20} \right] \right\}^{-1}. \quad (7.13)$$

The kernel function in Eq. (7.11) distributes mass with spatially varying weights. The corresponding local pressure solution will be closer to the line source solution than the solution with the constant kernel function, Eq. (7.2). In the following, we choose Eq. (7.2)

since it simplifies numerical integration of the kernel functions over discrete grid cells, see Section 7.2.4.

The dimensionless group  $\Theta = r_v L_p \mu_I k^{-1}$  is the ratio of the hydraulic conductivity of the vessel wall to the hydraulic conductivity of the extra-vascular space. If the filtration coefficient  $L_p$  is low relative to  $k$ , the regularized pressure profile is rather flat, so that the difference between  $p_{t,r_v}$  and  $p_{t,0}$  is low. This is reflected in a flux scaling factor close to 1. If the filtration coefficient is elevated, for example, when the blood-brain barrier is impaired in a tumor,  $\Theta$  can be larger than 1, hence  $\Xi$  may significantly defer from 1. Comparing Eqs. (7.10) and (7.13), we observe that a kernel function with higher weights towards the vessel center-line tends to result in a  $\Xi$  further away from 1.

### 7.1.2 Kernel support radius $\varrho$

Considering that the physically meaningful part of the pressure solution is actually given for  $r \geq r_v$ , if  $\varrho < r_v$ , our formulation gives identical solutions (for  $r \geq r_v$ ) to the methods by D'Angelo (2007) and Köppl et al. (2018). However, the smoothness of the solution for  $r < r_v$  can be controlled by the choice of kernel functions. For  $\varrho > r_v$ , the physical pressure solution  $p_t$  is altered. The source term, as well as  $p_v$ , remain the same for the derived  $\Xi$ . For  $\varrho > r_v$ , the action of the coupling term on  $p_t$  is effectively distributed over an artificially enlarged vessel volume.

### 7.1.3 Multiple vessels

In the capillary bed, vessels form a dense network. The vessel diameters are small, such that average distances between vessels are about one order of magnitude larger than the radii, and the vessel volume fraction is in the range of 2 to 5 %. In the following, we present our considerations for choosing  $\Xi$  in such a network.

To this end, let us consider a setup of  $N$  parallel long vessels with given boundary conditions, such that the resulting pressure solution in each plane,  $\mathbb{P} \subset \mathbb{R}^3$ , perpendicular to the vessel, is equal to the two-dimensional problem on that plane (the in-plane solutions are independent

of the solution in any parallel plane). Due to the linearity of the Laplace operator the solution can be split into contributions by the individual vessels (superposition principle),

$$p_t(\mathbf{x}) = \sum_{i=1}^N p_{t,i}(\mathbf{x}), \quad (7.14)$$

where  $r_i := \|\mathbf{x}_i - \mathbf{x}\|_2$  is defined as the distance between a point  $\mathbf{x} \in \mathbb{P}$  and the center  $\mathbf{x}_i$  of the vessel  $i$ . The source term contributions of the individual vessels are denoted by  $\hat{q}_{m,i}$ . It is important to note that  $\hat{q}_{m,i}$  is a function of  $p_t$  rather than  $p_{t,i}$ ,

$$\hat{q}_{m,i} = 2\pi r_{v,i} \rho_1 L_p (p_v - p_t(\mathbf{x}_i)) \Xi_i, \quad (7.15)$$

so that the partial solutions  $p_{t,i}$  are not independent of each other. Each partial solution,  $p_{t,i}$ , assumes the same form as Eq. (7.7). Furthermore,  $p_{t,i}$  is a harmonic function, satisfying the Laplace equation  $\nabla \cdot \nabla p_{t,i} = 0$ , for  $r_i > \varrho_i$ . Assuming that the kernel support regions of two neighboring vessels do not overlap, we observe that

$$p_{t,j}(\mathbf{x}_i) = \frac{1}{2\pi} \int_0^{2\pi} p_{t,j} \Big|_{r_{v,i}} d\theta =: p_{t,j,\mathbb{W}_i} =: C_{j,i} \quad (7.16)$$

using the mean value property of harmonic functions (Axler et al., 1992, p.4f), where  $p_{t,j,\mathbb{W}_i}$  is defined as the mean of  $p_{t,j}$  over the cross-sectional vessel surface of vessel  $i$ . From Eqs. (7.14) and (7.16) follows that

$$p_{t,i}(\mathbf{x}_i) - p_{t,i,\mathbb{W}_i} = p_{t,i}(\mathbf{x}_i) + \sum_{\substack{j=1 \\ j \neq i}}^N C_{j,i} - (p_{t,i,\mathbb{W}_i} + \sum_{\substack{j=1 \\ j \neq i}}^N C_{j,i}) = p_t(\mathbf{x}_i) - p_{t,\mathbb{W}_i}, \quad (7.17)$$

where

$$p_{t,\mathbb{W}_i} := \frac{1}{2\pi} \int_0^{2\pi} p_t \Big|_{r_{v,i}} d\theta. \quad (7.18)$$

This allows us to derive the flux scaling factors  $\Xi_i$  analogously to the single vessel case (cf. Eqs. (7.8) and (7.10)),

$$\Xi_i(\Phi^{\text{const}}) = \frac{p_{v,i} - p_{t,\mathbb{W}_i}}{p_{v,i} - p_t(\mathbf{x}_i)} = \left\{ 1 + \frac{r_{v,i} L_p \mu_1}{k} \left[ \ln \left( \frac{\varrho_i}{r_{v,i}} \right) - \frac{1}{2} \right] \right\}^{-1}. \quad (7.19)$$

In Section 7.3.3, we construct an analytical solution with multiple parallel vessels using these observations. The same observations hold for non-uniform boundary conditions, for which the solution can be decomposed into contributions by the vessels and a harmonic correction function which is chosen such that the boundary conditions are satisfied.

Unfortunately, the derivation using the mean value property of harmonic functions is no longer valid for arbitrarily-oriented vessels. In a fully three-dimensional setup, the mean value property concerns the integral over a sphere, while in our model we are integrating over the boundary of a circular cross-section. However, numerical experiments have shown that using an unmodified flux scaling factor does not introduce a significant modeling error. A possible explanation is that at a large enough distance to the neighboring vessels, the integral over the circular cross-section is expected to be very close to the integral over a sphere with the same radius and center point, given that the pressure gradient decays with  $r_i^{-1}$ . Moreover, realistic segmented vessel networks contain vessel bifurcations and may contain bends with sharp angles. In the vicinity of such features, the kernel support regions of two connected vessels may overlap. In such a case the correct flux scaling factor is not easily determined. However, we herein still employ the flux scaling factor shown in Eq. (7.10), assuming that possible errors are small, only occur in the close vicinity of such features and that the influence on the global solution is negligible in realistic applications. These assumptions and the corresponding modeling errors are investigated in a numerical experiment in Section 7.3.5.

## 7.2 Discretization

We discretize Eq. (7.1) using a cell-centered finite volume method with two-point flux approximation. To this end,  $\Omega$  and  $\Lambda$  are decomposed into two independent meshes  $\Omega_b$  and  $\Lambda_b$  consisting of control volumes  $K_\Omega \in \Omega_b$  and  $K_\Lambda \in \Lambda_b$ . Herein,  $K_\Omega$  are chosen to be hexahedra and  $K_\Lambda$  are line segments. Furthermore, the control volume boundary,  $\partial K$ , can be split into a finite number of faces  $\sigma \subset \partial K$ , such that each  $\sigma = K \cap L$ , for a neighboring control volume  $L$ . Integrating Eq. (7.1b) over a control volume  $K_\Omega$  and applying the Gauss divergence theorem to the left-hand side yields

$$-\int_{\partial K_\Omega} \left[ \frac{\rho_l}{\mu_l} k \nabla p_t \right] \cdot \mathbf{n}_{K_\Omega, \sigma} dA = \int_{K_\Omega} \hat{q}_m \Phi_\Lambda dx, \quad (7.20)$$

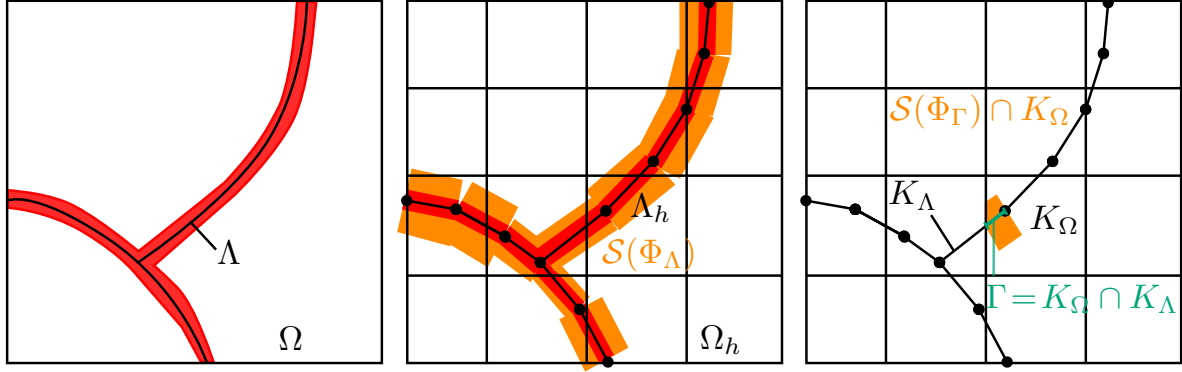


**Figure 7.2 – Visualization of the discretization.** The domains  $\Omega$  and  $\Lambda$  (left) are represented by a set of control volumes  $K_\Omega \in \Omega_h$  and  $K_\Lambda \in \Lambda_h$  (middle). The red area shows a tube with a radius  $r_v$  around the vessel center-line. The orange area visualizes the kernel support  $\mathcal{S}(\Phi_{\Lambda_h})$  of the kernel functions  $\Phi_{\Lambda_h}$  in the middle, and on the right, the kernel support associated with the intersection  $\Gamma$  intersected with a control volume  $K_\Omega$ . In this example, the kernel functions with cylindrical support, are chosen to have radii  $\varrho > r_v$ . Reprinted with permission from Koch et al. (2020d), © 2020 Elsevier Inc.

where  $\mathbf{n}_{K_\Omega, \sigma}$  is the unit outward-pointing normal on face  $\sigma \subset \partial K_\Omega$ . The exact fluxes are approximated by numerical fluxes

$$F_{K_\Omega, \sigma} \approx - \int_\sigma \left[ \frac{\rho_l}{\mu_l} k \nabla p_t \right] \cdot \mathbf{n}_{K_\Omega, \sigma} dA. \quad (7.21)$$

Let  $\mathcal{I}$  be the set of intersections  $\Gamma = K_\Omega \cap K_\Lambda$ . Furthermore, let  $\Phi_\Gamma \in \Phi_\Lambda$  denote a kernel function with the support  $\mathcal{S}(\Phi_\Gamma)$  associated with  $\Gamma$ . The discrete source term is computed as

$$\int_{K_\Omega} \hat{q}_m \Phi_\Lambda dx \approx Q_{K_\Omega} := \sum_{\Gamma \in \mathcal{I}} Q_\Gamma \frac{1}{|\Gamma|} \int_{K_\Omega \cap \mathcal{S}(\Phi_\Gamma)} \Phi_\Gamma dx, \quad (7.22)$$

where  $Q_\Gamma$  is the numerical approximation of the source term integrated over the intersection  $\Gamma$ ,

$$Q_\Gamma \approx \int_\Gamma \rho_l L_p P_v (p_v - p_{t,0}) \Xi ds. \quad (7.23)$$

Hence, Eq. (7.20) can be reformulated as

$$\sum_{\sigma \subset \partial K_\Omega} F_{K_\Omega, \sigma} = Q_{K_\Omega}, \quad \forall K_\Omega \in \Omega_h. \quad (7.24)$$

The discretization of the domains  $\Omega$  and  $\Lambda$  are visualized in Fig. 7.2, including an illustration of the kernel support region.

We mention that due to the approximation of the vessel segments as cylindrical tubes around the center-line, segments may overlap, in particular, at bifurcations and bends with sharp angles. To the knowledge of the authors, the resulting discretization errors are neglected throughout the present literature. This is a fair assumption, given that these overlaps are small and the corresponding discretization error is expected to be small in comparison with errors resulting from the vessel network segmentation.

### 7.2.1 Numerical fluxes $F_{K_\Omega, \sigma}$

We compute the numerical fluxes using a two-point flux approximation,

$$F_{K_\Omega, \sigma} = \frac{t_{K_\Omega, \sigma} t_{L_\Omega, \sigma}}{t_{K_\Omega, \sigma} + t_{L_\Omega, \sigma}} (p_{K_\Omega} - p_{L_\Omega}) \quad (7.25)$$

for two neighboring control volumes  $K$  and  $L$ , with the pressure degrees of freedom  $p_{K_\Omega}$  and  $p_{L_\Omega}$  associated with these control volumes, and with the transmissibilities

$$t_{K_\Omega, \sigma} = |\sigma| \frac{\rho_1 k \mathbf{d}_{K_\Omega, \sigma} \cdot \mathbf{n}_{K_\Omega, \sigma}}{\mu_1 \|\mathbf{d}_{K_\Omega, \sigma}\|^2}, \quad (7.26)$$

where  $\mathbf{d}_{K_\Omega, \sigma} = \mathbf{x}_\sigma - \mathbf{x}_{K_\Omega}$  is a vector from the center of the control volume  $K_\Omega$  to the center of the face  $\sigma$ , and  $|\sigma|$  denotes the area of face  $\sigma$ .

### 7.2.2 Numerical fluxes $F_{K_\Lambda, \sigma}$

Analogously to the derivation above, a discrete representation of Eq. (7.1a) is given by

$$\sum_{\sigma \subset \partial K_\Lambda} F_{K_\Lambda, \sigma} = Q_{K_\Lambda}, \quad \forall K_\Lambda \in \Lambda_b, \quad (7.27)$$

with

$$F_{K_\Lambda, \sigma} = t_{K_\Lambda, \sigma} (p_{K_\Lambda} - p_\sigma), \quad Q_{K_\Lambda} = \sum_{\Gamma \in K_\Lambda \cap \Omega_b} Q_\Gamma, \quad (7.28)$$

where  $p_\sigma$  denotes the pressure at  $x_\sigma$ , and the transmissibilities are defined analogously to Eq. (7.26),

$$t_{K_\Lambda, \sigma} = |\sigma| \frac{\pi r_{v,K}^4 \rho_B}{8\mu_B} \frac{\mathbf{d}_{K_\Lambda, \sigma} \cdot \mathbf{n}_{K_\Lambda, \sigma}}{\|\mathbf{d}_{K_\Lambda, \sigma}\|^2}, \quad (7.29)$$

with  $r_{v,K}$  denoting the vessel radius of control volume  $K$ . Since  $\Lambda_b$  consists of a network of segments  $K_\Lambda$ , it occurs that a face  $\sigma$  has more than two neighboring cells, i.e. a set of neighboring cells  $\mathcal{K}_\sigma \subset \Lambda_b$ . At such bifurcation faces, we enforce flux conservation, just like for faces with exactly two neighbors,

$$\sum_{K_\Lambda \in \mathcal{K}_\sigma} F_{K_\Lambda, \sigma} = 0. \quad (7.30)$$

Inserting Eq. (7.28) into Eq. (7.30) yields

$$p_\sigma = \frac{\sum_{K_\Lambda \in \mathcal{K}_\sigma} t_{K_\Lambda, \sigma} p_{K_\Lambda}}{\sum_{K_\Lambda \in \mathcal{K}_\sigma} t_{K_\Lambda, \sigma}}, \quad (7.31)$$

so that the face unknown in Eq. (7.28) can be replaced by an expression in terms of control volume unknowns  $p_{K_\Lambda}$ .

### 7.2.3 Numerical source term $Q_\Gamma$

In the following, we consider three different methods: the method proposed by D'Angelo (2007) using line sources (LS), the method suggested by Köppl et al. (2018) using cylinder surface sources (CSS), and the above introduced method with distributed volume sources (DS). The methods can be distinguished by the choice of kernel functions, and the approximation of  $Q_\Gamma$ . For the LS and CSS method, we are looking for the discrete approximation

$$Q_\Gamma^{\text{LS, CSS}} \approx \int_\Gamma \rho_\Gamma L_p P_v \left[ p_v - \frac{1}{2\pi r_v} \int_{\partial \mathcal{D}_{r_v}(s)} p_t d\theta \right] ds, \quad (7.32)$$



where  $\partial \mathcal{D}_{r_v}(s)$  is the boundary of a disc at position  $s$ , perpendicular to the intersection segment  $\Gamma$  with radius  $r_v$ . We compute

$$Q_{\Gamma}^{\text{LS,CSS}} \approx \int_{\Gamma} \rho_1 L_p P_v \left[ p_v - \frac{1}{2\pi r_v} \sum_{I_K \in \mathcal{I}_{\partial \mathcal{D}_{r_v}}} |I_K| p_{K_{\Omega}} \right] ds, \quad (7.33)$$

where  $\mathcal{I}_{\partial \mathcal{D}_{r_v}}$  is the set of intersections  $I_K = \partial \mathcal{D}_{r_v}(s) \cap K_{\Omega}$ ,  $K_{\Omega} \in \Omega_b$ , and the integral is approximated by a Gaussian quadrature rule. For the method DS, we seek

$$Q_{\Gamma}^{\text{DS}} \approx \int_{\Gamma} \rho_1 L_p P_v [p_v - p_{t,0}(s)] \Xi ds. \quad (7.34)$$

The center-line pressure  $p_{t,0}(s)$  could be approximated by the pressure  $p_{K_{\Omega}}$  in the control volume  $K_{\Omega}$  containing  $\Gamma$ . However, this approximation is poor, if  $K_{\Omega}$  is not significantly smaller than the vessel radius  $r_v$ . Assuming radial flux in a small neighborhood of  $\Gamma$ , we can reformulate Eq. (7.34) as

$$Q_{\Gamma}^{\text{DS}} \approx \int_{\Gamma} \rho_1 L_p P_v [p_v - p_{t,0}(s)] \Xi ds = \int_{\Gamma} \rho_1 L_p P_v [p_v - p_{t,\delta}(s)] \Xi_{\delta} ds, \quad (7.35)$$

where  $p_{t,\delta}$  is evaluated at some distance  $\delta \geq 0$  to the vessel center-line, and  $\Xi_{\delta}$  is a modified flux scaling factor, ensuring equality. Now,  $p_{K_{\Omega}}$  may better approximate  $p_{t,\delta}$  than  $p_{t,0}$ , for a certain  $\delta$ . As  $p_{K_{\Omega}}$  is commonly defined as the mean pressure in the control volume  $K_{\Omega}$ , we choose  $\delta$  as the mean distance of  $\Gamma$  to the control volume  $K_{\Omega}$ ,

$$\delta = \frac{1}{|K_{\Omega}|} \int_{K_{\Omega}} \min_{x' \in \Gamma} \|x - x'\|_2 dx. \quad (7.36)$$

The corresponding  $\Xi_{\delta}$  is computed using the analytical derivations in Section 7.1.1, and is dependent on the kernel functions. Choosing  $\Phi^{\text{const}}$  yields

$$\Xi_{\delta}(\Phi^{\text{const}}) = \left\{ 1 + \frac{r_v L_p \mu_1}{k} \left[ \frac{\delta^2}{2\varrho^2} + \ln\left(\frac{\varrho}{r_v}\right) - \frac{1}{2} \right] \right\}^{-1} \quad \text{for } \delta \leq \varrho, \quad (7.37)$$

so that

$$Q_{\Gamma}^{\text{DS}} = \rho_1 L_p P_v [p_{K_{\Omega}} - p_{K_{\Omega}}] \Xi_{\delta}. \quad (7.38)$$

Denoting the maximum size of all control volumes  $K_\Omega$  by  $h_\Omega$ , note that for  $h_\Omega \rightarrow 0 \implies \delta \rightarrow 0$ , and  $p_{t,\delta} \rightarrow p_{t,0}$ , so that Eq. (7.34) is recovered. For  $\delta > \varrho$ , a better approximation, independent of the chosen kernel function, can be derived from the analytical solution for  $r > \varrho$ , Eq. (7.7), yielding

$$\Xi_\delta = \left\{ 1 + \frac{r_v L_p \mu_I}{k} \ln \left( \frac{\delta}{r_v} \right) \right\}^{-1} \quad \text{for } \delta > \varrho. \quad (7.39)$$

We note that replacing  $\Xi$  by  $\Xi_\delta$  is a sensible flux correction for the methods LS and CSS, too. However, herein, we do not modify  $\hat{q}_m$  for these methods and implement them as described by D'Angelo (2007) and Köppl et al. (2018), respectively.

#### 7.2.4 Kernel integration

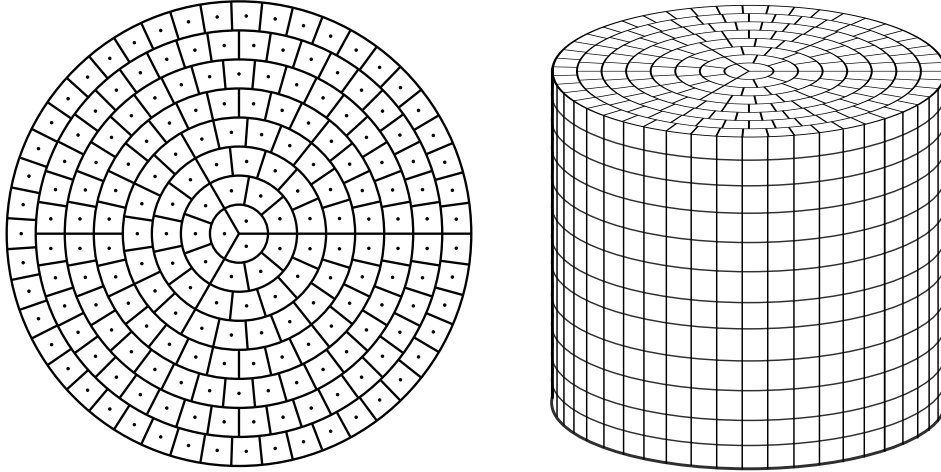


**Figure 7.3 – Kernel integration.** Left, integration points and volume elements in top view. Almost equally-sized integration volumes after the idea presented in Beckers and Beckers (2012). Right, the cylindrical integration domain, i.e. the kernel support  $\mathcal{S}(\Phi_\Gamma)$ , partitioned into volume elements.

The kernel integral in Eq. (7.22)

$$\mathbb{I}_{\Phi, K_\Omega} := \int_{K_\Omega \cap \mathcal{S}(\Phi_\Gamma)} \Phi_\Gamma \, dx, \quad (7.40)$$

is hard to approximate with standard quadrature rules, since  $K_\Omega \cap \mathcal{S}(\Phi_\Gamma)$  is difficult to compute. However, the integral over the entire support  $\mathcal{S}(\Phi_\Gamma)$  is known exactly. Hence, the problem can be reformulated as distributing the whole integral over the control volumes

$K_\Omega$  weighted with the respective support volume fractions. To this end, we create  $n_\Gamma$  points  $\mathbf{x}_i \in \mathcal{S}(\Phi_\Gamma)$  with associated volume elements  $V_i$  of similar size and shape, so that

$$\mathbb{I}_{\Phi, K_\Omega} \approx \sum_{i=1, \mathbf{x}_i \in K_\Omega}^{n_\Gamma} V_i \Phi_\Gamma(\mathbf{x}_i), \quad \sum_{i=1}^{n_\Gamma} V_i = |\mathcal{S}(\Phi_\Gamma)|. \quad (7.41)$$

An example for such integration points and associated volume elements is shown in Fig. 7.3.

## 7.3 Numerical experiments

All three introduced numerical methods (denoted by the superscripts LS, CSS, and DS) are considered for solving Eq. (7.1). The methods yield different solutions for  $p_t$  and  $r < r_v$  (LS, CSS), or  $r < \varrho$  (DS), due to the difference in the kernel function and the numerical approximation of  $\Xi$ . However, the solutions for  $p_v$  and  $\hat{q}_m$  are directly comparable. We denote the different pressure solutions in  $\Omega$  by  $p_t^{\mathbb{M}}$ ,  $\mathbb{M} \in \{\text{LS}, \text{CSS}, \text{DS}\}$ . We analyze these methods with different vessel configurations in a series of numerical experiments. In Section 7.3.2, we consider a single straight vessel. The numerical methods are investigated in terms of the ratio of grid resolution to vessel radius, comparing with analytical solutions. In Section 7.3.3, we construct an analytical solution for three parallel vessels, and show that the optimal flux scaling factor  $\Xi$  is independent of perturbations caused by neighboring vessels. For each numerical experiment, the setup is described and the results are presented and discussed.

### 7.3.1 Implementation and linear solver

The linear equation system resulting from the discretization of Eq. (7.1) is solved using a left-preconditioned stabilized bi-conjugate gradient method with block-diagonal preconditioner based on an incomplete LU-factorization, see Section 11.4. All methods use the same solver. We did not observe significant differences in the solver performance with respect to the employed methods. This suggests that the number of grid cells is a suitable indicator to compare the computational efficiency of the methods. However, a rigorous analysis of the solver performance is beyond the scope of this work.

### 7.3.2 Single vessel

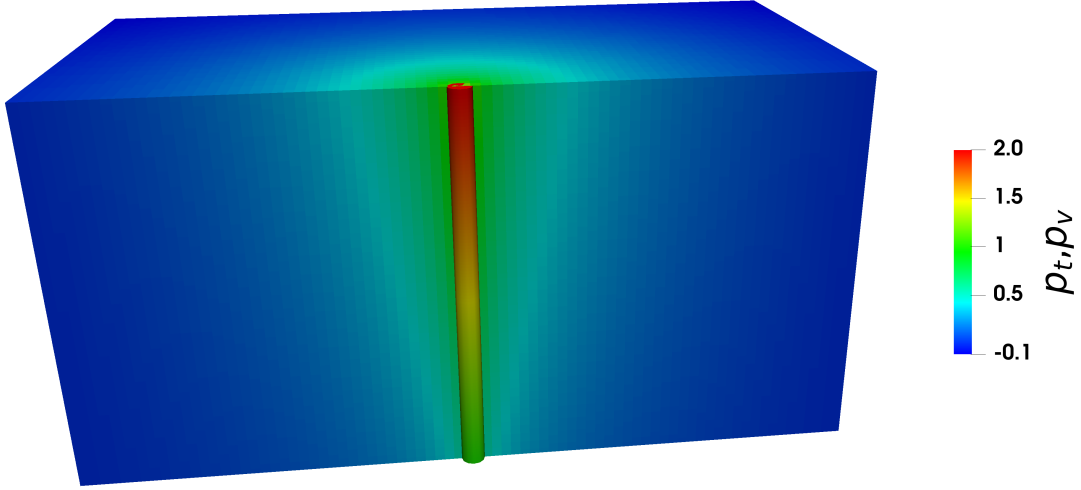


**Figure 7.4** – Numerical solution  $p_t^{\text{DS}}$  for  $r_v = 0.03$  and  $\varrho = r_v$ . The grid resolution in the extra-vascular domain is  $80 \times 80 \times 80$ , so that  $h = 0.025$ . The vascular pressure solution  $p_v$  is projected on a tube with radius  $r_v$ . Reprinted with permission from Koch et al. (2020d), © 2020 Elsevier Inc.

Let us consider a slightly simplified problem, adapted from D’Angelo (2007),

$$-\frac{\partial}{\partial s} \left( k_v \frac{\partial p_v}{\partial s} \right) = -\hat{q}_m \quad \text{in } \Lambda, \quad (7.42a)$$

$$-\nabla^2 p_t = \hat{q}_m \Phi_\Lambda \quad \text{in } \Omega, \quad (7.42b)$$

$$\hat{q}_m = \beta (p_v - p_{t,0}) \Xi, \quad (7.42c)$$

with the domains  $\Omega = [-1, 1] \times [-1, 1] \times [-1, 1]$  and  $\Lambda = \{0\} \times \{0\} \times [0, 1]$ , i.e the vessel center-line coincides with the  $x_3$ -axis. By choosing the parameters as

$$k_v = 1 + x_3 + \frac{1}{2} x_3^2, \quad \beta = \frac{2\pi}{2\pi + \ln r_v},$$

the pressure solutions,

$$p_{v,e} = 1 + x_3, \quad (7.43a)$$

$$p_{t,e}^{LS} = -\frac{1+x_3}{2\pi} \ln r, \quad (7.43b)$$

$$p_{t,e}^{CSS} = \begin{cases} -\frac{1+x_3}{2\pi} \ln r_v & r \leq r_v, \\ -\frac{1+x_3}{2\pi} \ln r & r > r_v, \end{cases} \quad (7.43c)$$

$$p_{t,e}^{DS} = \begin{cases} -\frac{1+x_3}{2\pi} \left[ \frac{r^2}{2\varrho^2} + \ln\left(\frac{\varrho}{r_v}\right) - \frac{1}{2} \right] & r \leq \varrho, \\ -\frac{1+x_3}{2\pi} \ln r & r > \varrho, \end{cases} \quad (7.43d)$$

with  $r = \sqrt{x_1^2 + x_2^2}$ , solve Eq. (7.42) given the boundary conditions

$$\begin{aligned} p_v &= 1 && \text{on } \partial\Lambda \cap \{x_3 = 0\}, \\ p_v &= 2 && \text{on } \partial\Lambda \cap \{x_3 = 1\}, \\ \nabla p_t \cdot \mathbf{n} &= -\frac{1}{2\pi} \ln r && \text{on } \partial\Omega \cap \{x_3 = 1\}, \\ \nabla p_t \cdot \mathbf{n} &= \frac{1}{2\pi} \ln r && \text{on } \partial\Omega \cap \{x_3 = 0\}, \\ p_t &= -\frac{1+x_3}{2\pi} \ln r && \text{on } \partial\Omega \setminus \{x_3 = 0, x_3 = 1\}, \end{aligned} \quad (7.44)$$

where  $\mathbf{n}$  is the outward-pointing unit normal vector on the boundary  $\partial\Omega$  of the domain  $\Omega$ . From the analytical pressure solutions follows that  $\hat{q}_{m,e} = 1 + x_3$  is the analytical source term.

The pressure discretization errors are computed in the normalized discrete norm

$$\|p_t - p_{t,e}\|_2 := \frac{\left[ \sum_{\Omega_b} |K_{\Omega}| (p_{K_{\Omega},e} - p_{K_{\Omega}})^2 \right]^{1/2}}{\sum_{\Omega_b} |K_{\Omega}|}, \quad (7.45)$$

where  $p_{K_{\Omega}}$ ,  $p_{K_{\Omega},e}$  denote numerical and exact pressure evaluated at the center of a control volume  $K_{\Omega}$  and  $|K_{\Omega}|$  its volume. The error for  $p_v$  in  $\Lambda_b$  is computed analogously. The error in the source term  $\hat{q}_m$  is computed as

$$\|q - q_e\|_2 = \frac{\left[ \sum_{\Lambda_b} |K_{\Lambda}| (q_{K_{\Lambda},e} - q_{K_{\Lambda}})^2 \right]^{1/2}}{\sum_{\Lambda_b} |K_{\Lambda}|}, \quad (7.46)$$

where

$$q_{K_{\Lambda},e} = \int_{K_{\Lambda}} \hat{q}_{m,e} ds \quad \text{and} \quad q_{K_{\Lambda}} = \int_{K_{\Lambda}} \hat{q}_m ds. \quad (7.47)$$

The maximum control volume size,  $h$ , is given by the maximum edge length in both domains. We choose the edge length so that  $h = h_{\Omega} = h_{\Lambda}$ .

The numerical solutions  $p_t^{\text{DS}}$ ,  $p_v$ , for  $r_v = 0.03$  and  $\varrho = r_v$ , are exemplarily shown in Fig. 7.4. The discretization error and the convergence rates are computed for  $p_t$ ,  $p_v$ , and  $q$ . Fig. 7.5 shows the discretization errors for  $r_v = 0.1$ ,  $\varrho = r_v$  and  $\Phi^{\text{const}}$ . It can be seen that DS is the only method with second-order convergence for  $p_t$  in the given norm. The error in  $p_t$  cannot directly be compared, since it is computed with respect to the respective analytical solution corresponding to the chosen method, which differ for  $r < \varrho$ . However, all methods are expected to converge to the same analytical solution for  $p_v$  and  $q$ . It is evident from the error plots of  $p_v$  and  $q$  that DS shows the lowest discretization error of all three methods. Furthermore, for the presented numerical experiment DS achieves convergence rates in  $q$  of approx. 2.5, while LS, CSS show convergence rates of approx. 2. We conclude that the increased discretization error for LS and CSS in  $p_t$ , influences the approximation of  $p_v$ ,  $q$ , and is likely due to the insufficient approximation of  $p_{t,\text{WW}}$ . Fig. 7.6 shows the discretization errors for  $r_v = 0.05$ ,  $\varrho = r_v$  and  $\Phi^{\text{const}}$ . The first two error measurements show the situation  $h > \varrho$ . If the discretization length  $h$  is larger than the kernel radius  $\varrho$ , the three methods do not differ in the representation of the source term. However, for the DS method, we introduced a source term correction by an adjusted flux scaling factor dependent on the discrete distance  $\delta$ , see Eq. (7.37), which is proportional to  $h$ . This adjustment significantly reduces the error for all quantities for  $r > r_v$ . Note that the results for the DS method without source term correction have been omitted in Fig. 7.6 for clarity. The source term correction factor for  $r > r_v$ , can also be applied for the other methods (LS and CSS), although its motivated by the new formulation of the perfusion problem in Eq. (7.1).

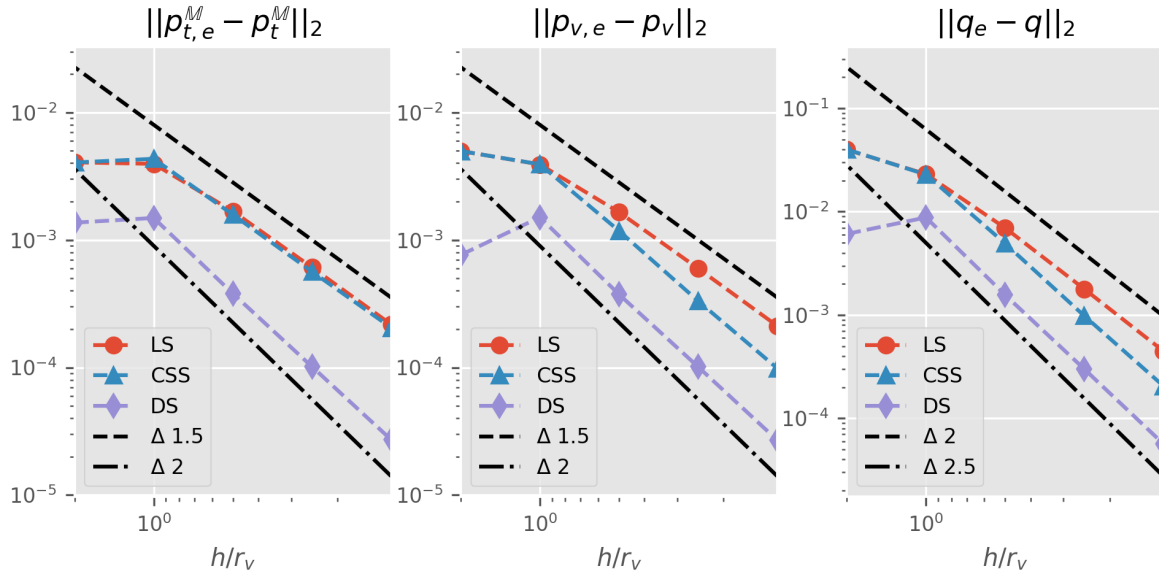


**Figure 7.5 – Discretization errors in  $p_t$ ,  $p_v$ , and  $\hat{q}_m$  ( $r_v = 0.1$ ).** Shown are different methods LS, CSS, for DS, with vessel radius  $r_v = 0.1$ , and kernel support radius  $\varrho = r_v$  (only DS). The exact solution  $p_{t,e}$  is the analytical solution  $p_t^{\text{LS}}(x)$ ,  $p_t^{\text{CSS}}(x)$ , or  $p_t^{\text{DS}}(x)$ , corresponding to the respective method. The black lines are curves with slopes of 1.5, 2, and 2.5 for comparison. Reprinted with permission from Koch et al. (2020d), © 2020 Elsevier Inc.

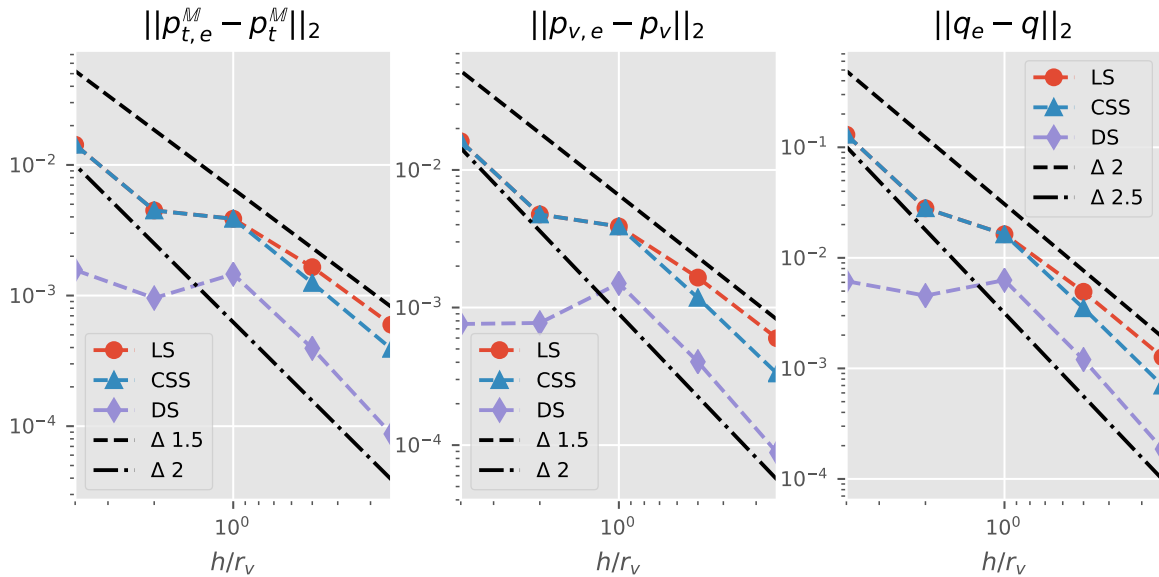


**Figure 7.6 – Discretization errors in  $p_t$ ,  $p_v$ , and  $\hat{q}_m$  ( $r_v = 0.05$ ).** Shown are different methods LS, CSS, and DS, for vessel radius  $r_v = 0.05$ , and kernel support radius  $\varrho = r_v$  (only DS). The exact solution  $p_{t,e}$  is the analytical solution  $p_t^{\text{LS}}(x)$ ,  $p_t^{\text{CSS}}(x)$ , or  $p_t^{\text{DS}}(x)$ , corresponding to the respective method. Reprinted with permission from Koch et al. (2020d), © 2020 Elsevier Inc.

### 7.3.3 Multiple parallel vessels

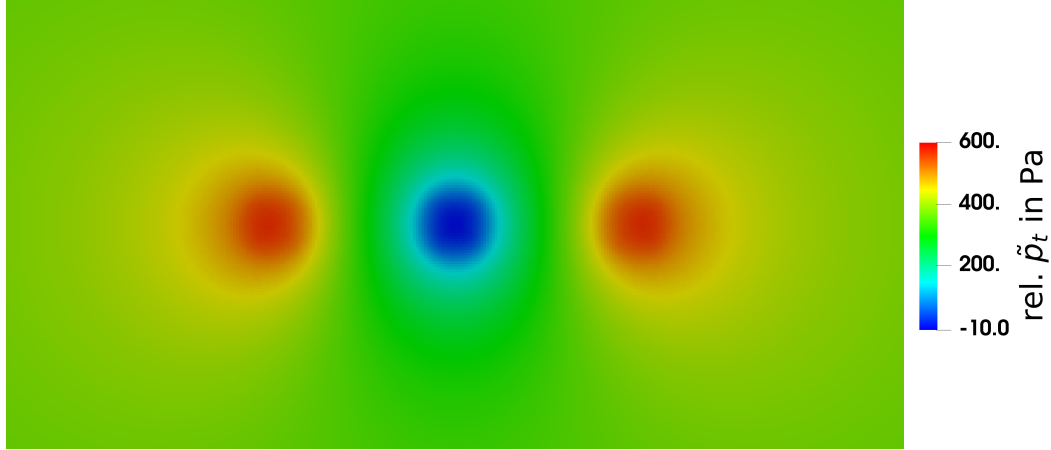


**Figure 7.7** – Numerical solution of hydraulic pressure  $\tilde{p}_t^{\text{DS}}$ . Pressure is relative to  $\tilde{p}_{\text{atm}} = 1 \cdot 10^5$  Pa. The kernel support radius is  $\varrho = 2r_v$ , and  $r_v = r_{v,1} = r_{v,2} = r_{v,3} = 4 \mu\text{m}$ . The grid resolution in the extra-vascular domain is  $320 \times 160$ , so that  $h = 0.625 \cdot 10^{-6} \mu\text{m}$ . Reprinted with permission from Koch et al. (2020d), © 2020 Elsevier Inc.

In the next experiment, we consider three parallel vessels, from which two are emitting fluid (arterial side), and one vessel is absorbing fluid (venous side). We assume constant pressures in the vessels,  $\tilde{p}_{v,1} = \tilde{p}_{v,3} = 3400$  Pa,  $\tilde{p}_{v,2} = 2300$  Pa, which renders the problem effectively two-dimensional. Then, exploiting the linearity of the Laplace operator, we can construct a solution of Eq. (7.1b) with line sources using the superposition principle, i.e.,

$$p_t^{\text{LS}}(\mathbf{x}) = \sum_{i=1}^3 p_{t,i} = \sum_{i=1}^3 -\frac{\mu_1 \hat{q}_{m,i}}{2\pi k \rho_1} \ln r_i, \quad r_i = \|\mathbf{x}_i - \mathbf{x}\|_2, \quad (7.48)$$

where  $\mathbf{x}_i$  is the position of the center-line of vessel  $i$ , and  $\mathbf{x} = [x_1, x_2, x_3]^T$  a point in  $\Omega$ . Recall that  $\hat{q}_{m,i} = \rho_1 L_p 2\pi r_{v,i} (p_{v,i} - p_{t,\mathbb{W}_i})$  is a linear function in the arguments  $p_{v,i}$  and  $p_{t,\mathbb{W}_i}$ , and

$$p_{t,\mathbb{W}_i} = \frac{1}{2\pi} \int_0^{2\pi} p_t^{\text{LS}} \Big|_{r_{v,i}} d\theta, \quad (7.49)$$



is the mean pressure on the surface of vessel  $i$ . Thus, using the mean value property of harmonic functions yields

$$p_{t, \mathbb{W}_i} = \sum_{\substack{j=1 \\ j \neq i}}^3 \left( -\frac{\mu_1 \hat{q}_{m,j}}{2\pi k \rho_1} \ln r_{ij} \right) - \frac{\mu_1 \hat{q}_{m,i}}{2\pi k \rho_1} \ln r_{v,i}, \quad (7.50)$$

where  $r_{ij}$  denotes the Euclidean distance of the center-lines of vessels  $i$  and  $j$  and  $r_{v,i}$  the radius of vessel  $i$ . Eq. (7.50) constitutes a system of three linear equations with the unknowns  $p_{t, \mathbb{W}_1}$ ,  $p_{t, \mathbb{W}_2}$ ,  $p_{t, \mathbb{W}_3}$ . As the analytical solution of Eq. (7.50) results in a rather lengthy expression, we compute  $p_{t, \mathbb{W}_i}$  numerically. Using the parameter values,  $r_{12} = r_{23} = 40 \mu\text{m}$ ,  $r_{13} = 80 \mu\text{m}$ ,  $r_{v,1} = r_{v,2} = r_{v,3} = 4 \mu\text{m}$ ,  $L_p = 1 \cdot 10^{-9} \text{mPa}^{-1} \text{s}$ ,  $k = 8.3 \cdot 10^{-18} \text{m}^2$ ,  $\mu_1 = 1.339 \cdot 10^{-3} \text{Pa s}$ ,  $\rho_1 = 1030 \text{kg m}^{-3}$ ,  $\pi_t = 666 \text{Pa}$ ,  $\pi_v = 3300 \text{Pa}$ ,  $\sigma = 1.0$ , cf. Koch et al. (2020a), we obtain  $\tilde{p}_{t, \mathbb{W}_1} = \tilde{p}_{t, \mathbb{W}_3} \approx 587.29 \text{Pa}$ , and  $\tilde{p}_{t, \mathbb{W}_2} \approx -89.350 \text{Pa}$ . Recall that  $p_{t/v} = \tilde{p}_{t/v} - \pi_{t/v}$ . We compute the analytical solution for a domain  $\Omega = [-100, 100] \times [-50, 50] \mu\text{m}$  with  $\mathbf{x}_1 = [-40, 0]^T \mu\text{m}$ ,  $\mathbf{x}_2 = [0, 0]^T \mu\text{m}$ ,  $\mathbf{x}_3 = [40, 0]^T \mu\text{m}$ .

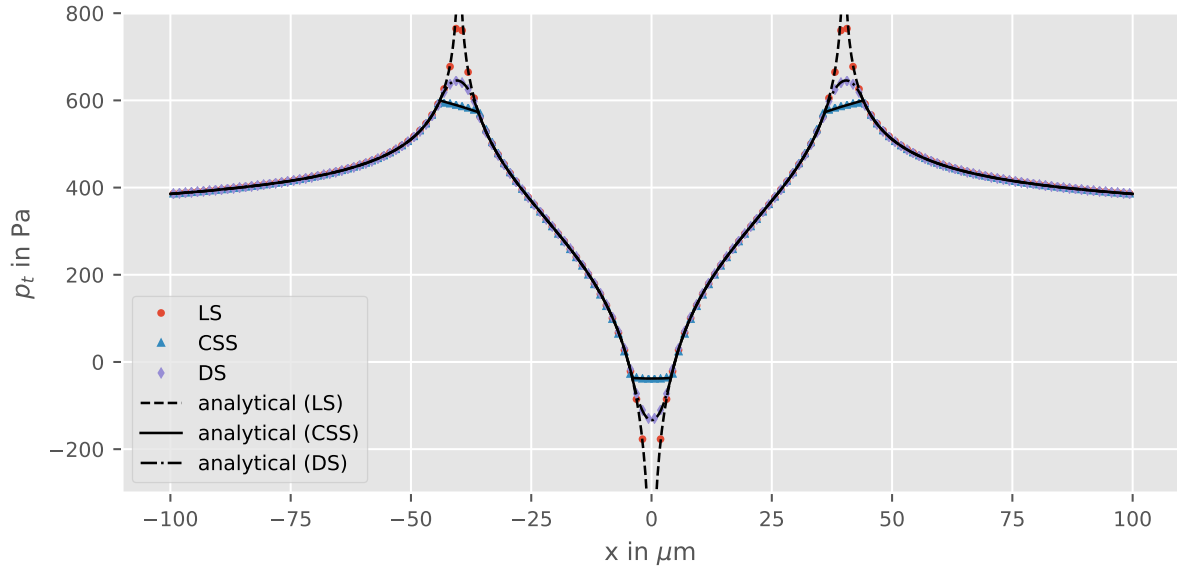
We recall that the solution with line sources is equal to the solution with distributed sources outside the kernel support radius. Furthermore, the superposition principle equally applies for the distributed source model so that, for instance, for the kernel function  $\Phi^{\text{const}}$ ,

$$p_t^{\text{DS}}(\mathbf{x}) = \begin{cases} \sum_{i=1}^3 -\frac{\mu_1 \hat{q}_{m,i}}{2\pi k \rho_1} \ln r_i & r_i > \varrho_i, \\ \sum_{\substack{j=1 \\ j \neq i}}^3 -\frac{\mu_1 \hat{q}_{m,j}}{2\pi k \rho_1} \ln r_j - \frac{\mu_1 \hat{q}_{m,i}}{2\pi k \rho_1} \left[ \frac{r_i^2}{2\varrho_i^2} + \ln \varrho_i - \frac{1}{2} \right] & r_i \leq \varrho_i, \end{cases} \quad (7.51)$$

is a solution to Eq. (7.1), given that the kernel support regions of the vessels do not overlap. For the css method the solution is given by a linear continuation of the pressure for  $r_i \leq r_{v,i}$ , cf. Köppl et al. (2018),

$$p_t^{\text{CSS}}(\mathbf{x}) = \begin{cases} \sum_{i=1}^3 -\frac{\mu_1 \hat{q}_{m,i}}{2\pi k \rho_1} \ln r_i & r_i > r_{v,i}, \\ \sum_{\substack{j=1 \\ j \neq i}}^3 -\frac{\mu_1 \hat{q}_{m,j}}{2\pi k \rho_1} \ln r_j - \frac{\mu_1 \hat{q}_{m,i}}{2\pi k \rho_1} \ln r_{v,i} & r_i \leq r_{v,i}. \end{cases} \quad (7.52)$$

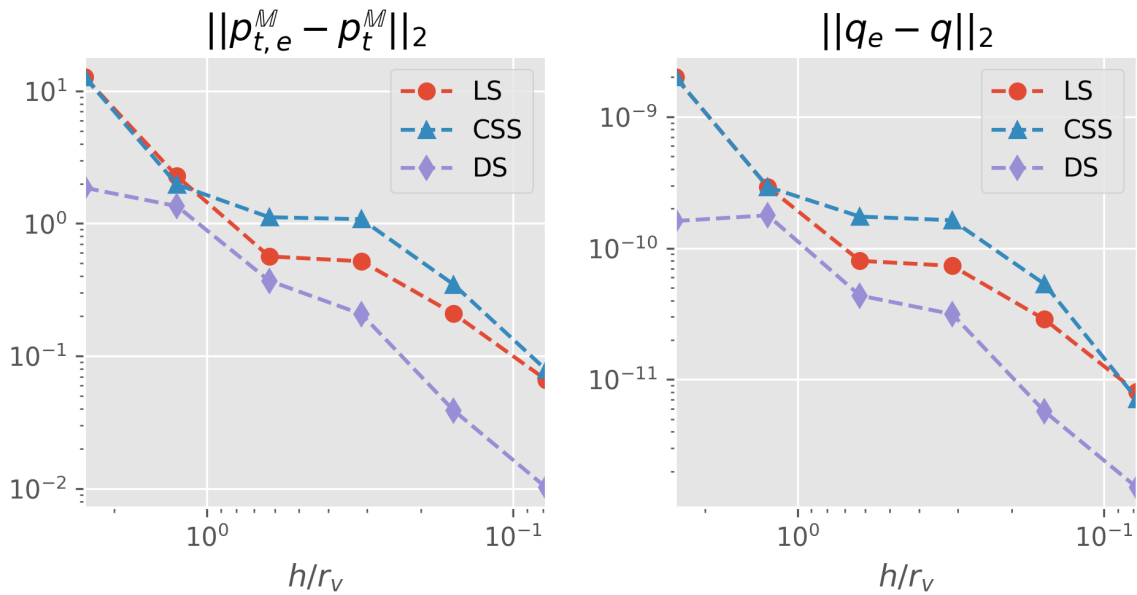
The analytical solutions  $p_t^{\text{LS}}(\mathbf{x})$ ,  $p_t^{\text{CSS}}(\mathbf{x})$ ,  $p_t^{\text{DS}}(\mathbf{x})$  along the  $x_1$ -axis are shown in Fig. 7.8. The numerical solution  $\tilde{p}_t^{\text{DS}} = p_t^{\text{DS}} - \pi_t$ , for  $\varrho = 2r_v$ , is exemplarily shown in Fig. 7.7. The discretization errors with respect to the analytical solutions for  $p_t^{\text{M}}$  and  $q$  are shown in



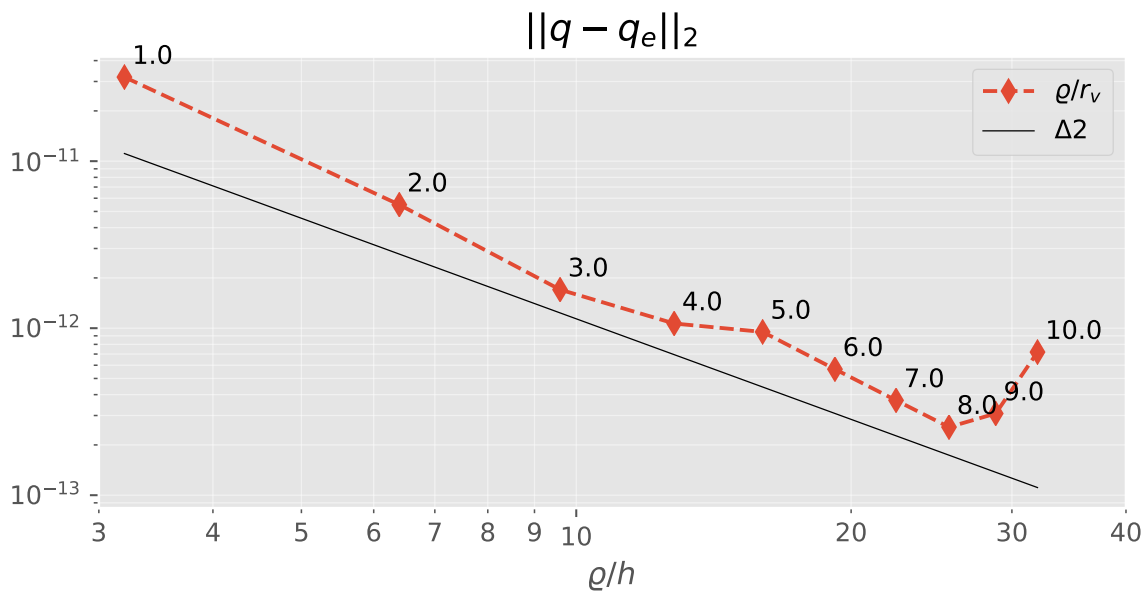
**Figure 7.8 – Analytical and numerical solutions for three methods.** Analytical solutions (black lines)  $p_t^{\text{LS}}(\mathbf{x})$ ,  $p_t^{\text{CSS}}(\mathbf{x})$ , and  $p_t^{\text{DS}}(\mathbf{x})$ , and the corresponding numerical solutions (colored markers) obtained with a grid resolution of  $160 \times 80$ . The solution for DS uses a kernel support radius of  $\varrho = r_v$ . The middle peak corresponds to the fluid-absorbing vessel, whereas the left and the right peak correspond to the fluid-emitting vessels. Reprinted with permission from Koch et al. (2020d), © 2020 Elsevier Inc.

Fig. 7.9. As for the numerical experiment with a single vessel, method DS shows the lowest error for the multi-vessel experiment. Additionally, it can be seen that the flux-scaling for  $r > \varrho$  significantly improves the approximation of  $q$ , although the analytical solution is no longer strictly radial around the individual vessels.

In a second experiment, the grid resolution is fixed to  $h = 1.25 \mu\text{m}$ . Then, the kernel support radius is step-wise increased starting from  $\varrho = r_v$ , for all vessels. The discretization errors for  $q$  are shown in Fig. 7.10. Recall that the distances  $r_{12} = r_{23} = 40 \mu\text{m}$ , such that the kernel support region for two neighboring vessels start intersecting for  $\varrho > 5r_v$ , and the kernel support region includes the location of the center-line of the neighboring vessel for  $\varrho > 10r_v$ . It can be seen that with increasing kernel radius the approximation of the source term improves significantly. Comparing Fig. 7.10 and Fig. 7.9 it seems that an increase of the kernel support radius has the same effect as increasing the grid resolution. An increase of the kernel support area by a factor of 2 reduces the discretization error by a factor of 2. However, note that the pressure solution is increasingly regularized and thus deviates from the physically sensible solution. If the kernel support radius is chosen too large, the



**Figure 7.9 – Discretization errors in  $p_t$  and  $\hat{q}_m$ .** Shown for the different methods LS, CSS, and DS with kernel support radius  $\varrho = r_v$  (only DS). Reprinted with permission from Koch et al. (2020d), © 2020 Elsevier Inc.



**Figure 7.10 – Discretization errors for different kernel support radii.** The annotated values show the ratio of the kernel support radii to the vessel radii  $\varrho/r_v$ . The black line has a slope of 2 and is shown for reference. Reprinted with permission from Koch et al. (2020d), © 2020 Elsevier Inc.

regularization affects neighboring vessels, such that the error in the source term increases

again. The results suggest that the variable kernel support region, to some extent, decouples the source term approximation error from the 3D grid resolution.

### 7.3.4 Multiple arbitrarily-oriented vessel

In this experiment, we consider multiple arbitrarily-oriented vessels embedded in a cubic extra-vascular domain, for which no analytical solution is given. Recall that for such a system, the methods LS, CSS and DS do not generally give the same solutions, but the differences are expected to be small. In order to isolate differences stemming from the different source models from other sources of error, the vessels do not bifurcate and are constructed in a way that they intersect the 3D domain boundary perpendicularly. The computational domain is shown in Fig. 7.11. Two arterial (fluid-emitting) and two venous (fluid absorbing) capillaries are embedded in a cubic extra-vascular domain with dimensions  $100\ \mu\text{m} \times 100\ \mu\text{m} \times 100\ \mu\text{m}$ . For each vessel, one end is chosen as inflow and the other as outflow boundaries. On the

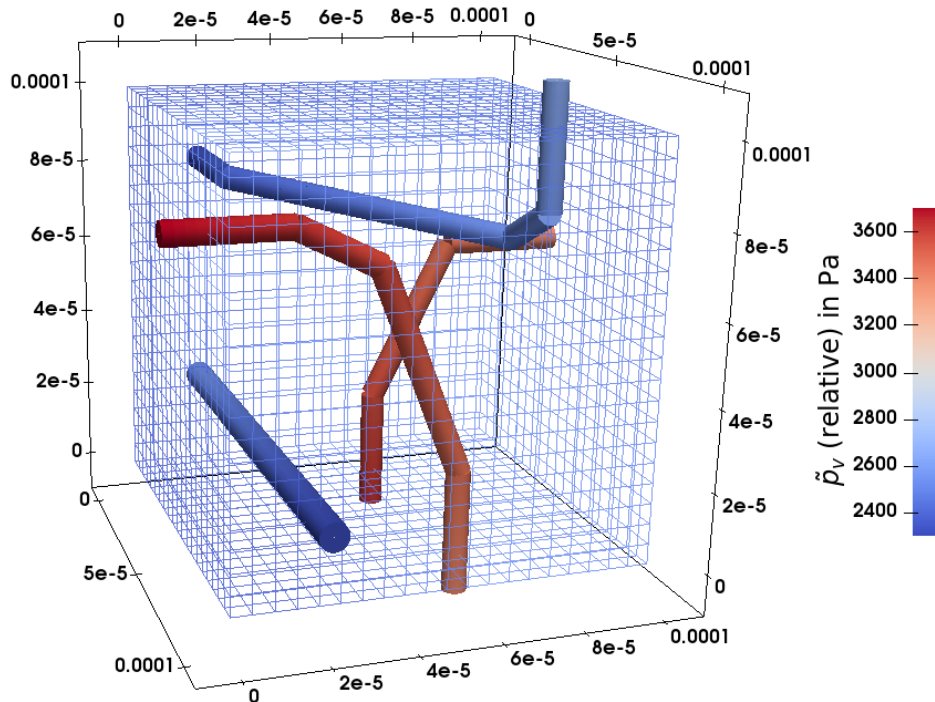


**Figure 7.11 – Computational domain—multiple arbitrarily-oriented vessels.** The vessel segments are shown as cylinders scaled with the respective vessel radius. The vessel segment color corresponds to the relative hydraulic vessel pressure  $\tilde{p}_v$ . The cubic extra-vascular domain has the dimensions  $100\ \mu\text{m} \times 100\ \mu\text{m} \times 100\ \mu\text{m}$ . Reprinted with permission from Koch et al. (2020d), © 2020 Elsevier Inc.

inflow boundary of vessel  $i$ , a constant inflow rate,  $q_{v,i,\text{in}} = \rho_B \pi r_{v,i}^2 v_i$  is enforced, where  $r_{v,i}$  is the inflow segment radius and  $v_i$  the inflow velocity. On outflow boundaries, we fix the pressure,  $\tilde{p}_{v,i,\text{out}}$ . The data for the geometry of the vessel and boundary conditions is given in Table A.1 in Appendix A.3. The remaining model parameters are chosen as in the previous multiple vessel experiment. The boundaries of the extra-vascular domain are considered symmetry boundaries, hence  $\frac{\partial p_i}{\partial n} = 0$  on  $\partial\Omega$ .

We produce a reference solution using the CSS method, with  $h_\Omega = 0.625 \mu\text{m}$ ,  $h_\Lambda = 0.5 \mu\text{m}$ . The source term  $\hat{q}_m$  is computed for every cell  $K \in \Lambda_h$ , resulting in a source vector  $q_{\text{ref}}$ . Then, the corresponding source term,  $q$ , for  $h_\Lambda = 0.5 \mu\text{m}$ , is computed for different  $h_\Omega$  using the methods CSS, LS, and DS with different kernel radii  $\varrho/r_{v,i} = 1, 3$ , and  $5$ . Furthermore, we compute the total mass flux,  $q_{\text{out}}$ , emitted by the arterial vessels, as the sum of all fluxes leaving the vessel domain into the extra-vascular domain. The results are shown in Fig. 7.12. First, it can be seen that with a coarse grid, the difference in the source term computed

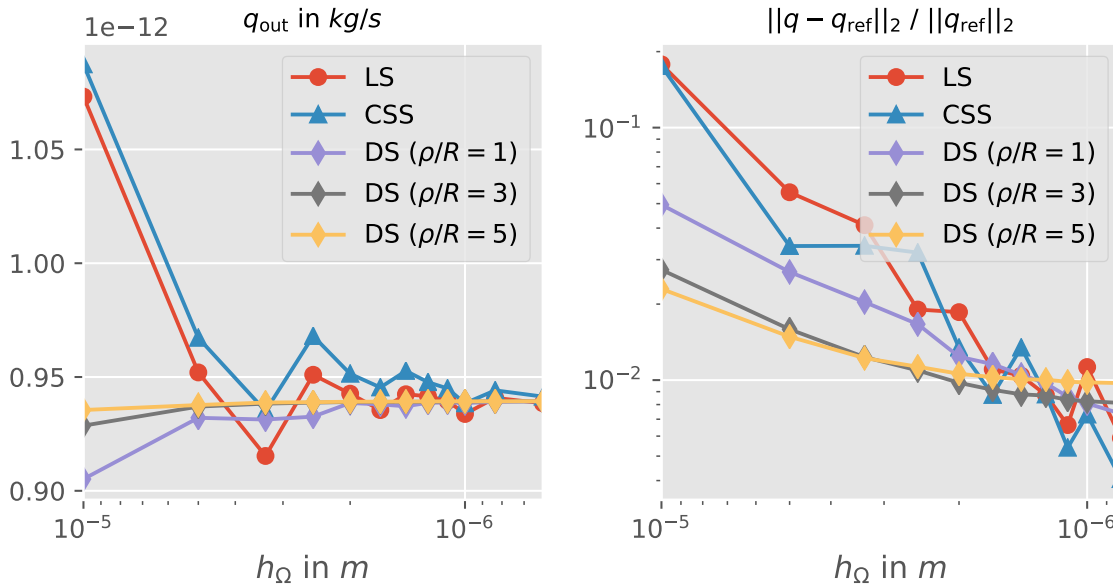


**Figure 7.12 – Differences in source term with respect to the reference solution.** Left, the total mass flux emitted by the arterial vessel  $q_{\text{out}}$  for the different methods (CSS, LS, and DS) with grid refinement. Right, the difference in the source term between the different methods with grid refinement with respect to the reference solution (CSS). Reprinted with permission from Koch et al. (2020d), © 2020 Elsevier Inc.

by the different schemes is quite large ( $\approx 10\%$  relative to the reference solution). Notably, the lowest difference with respect to the reference solution at coarse resolutions is achieved by the DS with the largest kernel support region. With grid refinement these differences

decrease to less than 1 %. However, it can be seen that the curve flattens for the DS methods with larger kernel for fine grid resolutions. The results suggest that the difference cannot be reduced to much less than 1 %. At the given grid resolutions, such a behavior is not observed yet for the DS with the smallest kernel support.

We conclude that the flattening of the error curve for the DS methods with larger kernel is rather caused by overlapping kernels of neighboring vessels as well as at bends. This effect, which is further investigated in the next numerical example, is minimized for the smallest kernel support. From the fact, that the kernel curve still suggests convergence until a very fine grid resolution leads us to the conclusion that the error caused by the approximation of the flux scaling factor  $\Xi$  (as discussed in Section 7.1.3) is much smaller. In perspective of the rather big uncertainties stemming from vessel segmentation and modeling error, the difference of 1 % between the different methods present in Fig. 7.12 will most certainly be acceptable in practical simulations. Furthermore, the observations in this experiment support our results from the previous experiment that for coarser mesh resolutions it is better to choose a larger kernel support, if a good approximation of the source term  $\hat{q}_m$  is important.

### 7.3.5 Vessel network

In the last numerical experiment, we consider a network of capillaries extracted from the superficial cortex of a rat brain (Motti et al., 1986; Secomb et al., 2000). Inlets and outlets are annotated in the data set. For the inlets, velocity estimates based on the vessel radius are given by Secomb et al. (2000), and herein enforced as Neumann boundary conditions. The vessel radii are in the range of 2 to 4.5  $\mu\text{m}$ . Dirichlet boundary conditions enforce  $p_{v,\text{out}} = 1.025 \cdot 10^5 \text{ Pa}$  at the outlets. The extra-vascular domain  $\Omega$  is given by a rectangular box,  $200 \mu\text{m} \times 210 \mu\text{m} \times 190 \mu\text{m}$ . All boundaries  $\partial\Omega$  are considered symmetry boundaries,  $\frac{\partial p_t}{\partial n} = 0$  on  $\partial\Omega$ . The network boundaries are extended by 30  $\mu\text{m}$  segments with perpendicular intersections on  $\partial\Omega$ . This adjustment to the network structure is chosen to better match the assumption of symmetry boundaries in the extra-vascular domain. Vessels intersecting the boundary at acute angles lead to non-physical, non-radial flows around the vessel end at symmetry boundaries on  $\partial\Omega$ .

A reference solution is computed using the CSS method with  $h_\Omega = 1.3125 \mu\text{m}$  and  $h_\Lambda = 0.5 \mu\text{m}$ . The network geometry and the  $p_v$  reference solution are shown in Fig. 7.13. The source

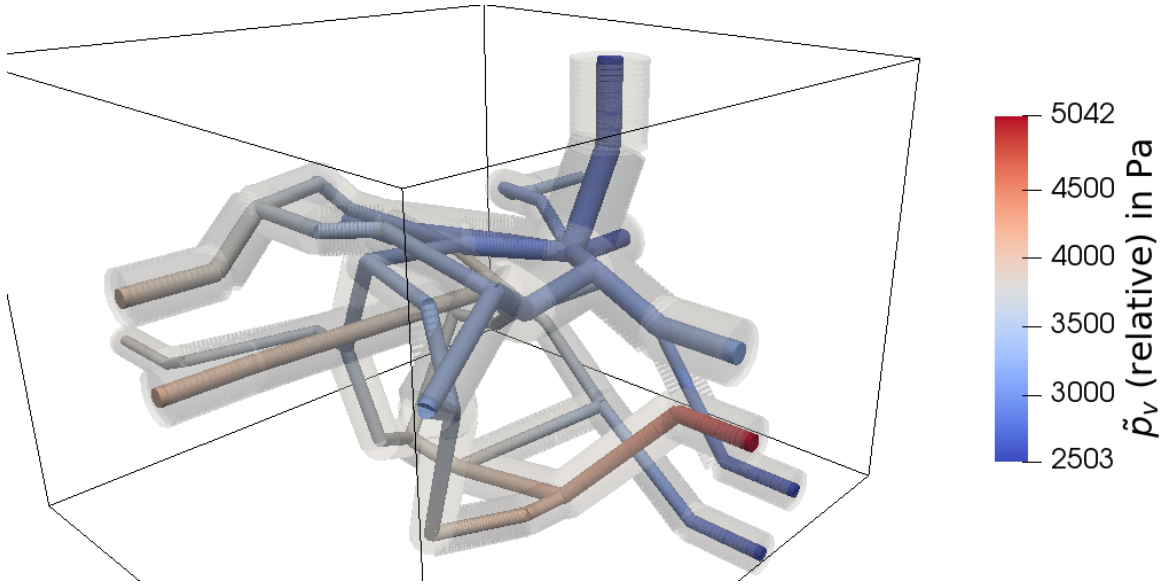


**Figure 7.13 – Vessel network from the superficial cortex of a rat brain.** Data from Motti et al. (1986); Secomb et al. (2000). The vessel segments are shown as cylinders scaled with the respective vessel radius. The vessel segment color corresponds to the relative hydraulic vessel pressure  $\tilde{p}_v$ . The cubic extra-vascular domain has the dimensions  $200\mu\text{m} \times 210\mu\text{m} \times 190\mu\text{m}$ . The kernel support volume for  $\varrho_i = 3r_{v,i}$  is visualized in opaque gray. Reprinted with permission from Koch et al. (2020d), © 2020 Elsevier Inc.

term,  $q$ , for  $h_\Lambda = 0.5\mu\text{m}$ , is computed for different  $h_\Omega$  using the methods CSS, LS, and DS with different kernel radii  $\varrho/r_{v,i} = 1, 3$ , and  $5$ . As in the previous example, we compute the total mass flux,  $q_{\text{out}}$ . The results are shown in Fig. 7.14. Firstly, it can be seen that all methods agree well for the total mass flux on the finest grid with maximum differences of about 2%. Secondly, it is evident that the DS approximates  $q_{\text{out}}$  much better for coarser grids, and the approximation gets better with larger kernel support. The DS method with a kernel support radius  $\varrho_i = 5r_{v,i}$  very closely approximates  $q_{\text{out}}$  for the coarsest grid, where  $h_\Omega$  is about five times the radius of the largest vessel. If the difference is measured in the relative 2-norm,  $\Delta q = \|q - q_{\text{ref}}\|_2 / \|q_{\text{ref}}\|_2$ , we observe slightly larger differences. On the one hand, this is due to differences along vessels oscillating around zero, i.e., due to terms that cancel when computing  $q_{\text{out}}$ , but not for  $\Delta q$ . On the other hand,  $\Delta q$  emphasizes larger differences stronger.

The locality of the difference is visualized in Fig. 7.15, where we computed the absolute local differences of source terms  $\hat{q}_{m,i}$  between the LS and DS methods ( $\varrho/r_{v,i} = 1$ ) and the reference solution (with CSS) for every vessel cell  $K_\Lambda$ . The largest differences can be observed in the neighborhood of bifurcations and sharp bends. This difference can be explained

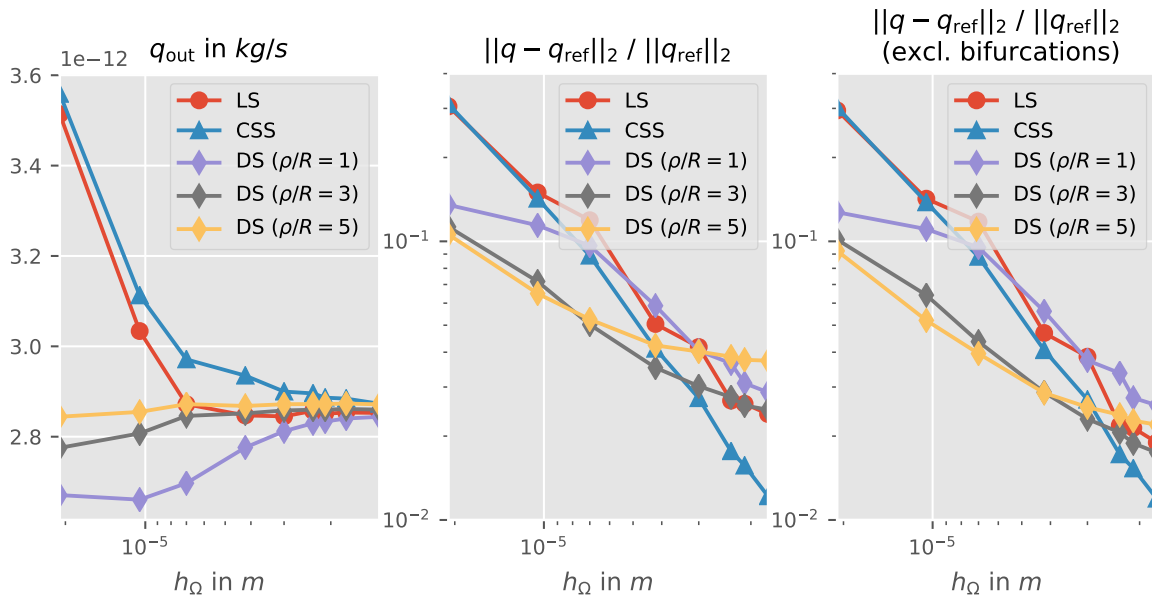


**Figure 7.14 – Differences to reference solution—network with bifurcations.** Left, the total mass flux emitted by the arterial vessel  $q_{\text{out}}$  for the different methods (css, ls, and ds) with grid refinement. Center, the relative difference in the 2-norm of the source term for the different methods and grid refinement, with respect to the reference solution (css). Right, the relative difference in the 2-norm of the source term, excluding all cells  $K_{\Lambda}$  that are closer than  $10\ \mu\text{m}$  to a vessel bifurcation. Reprinted with permission from Koch et al. (2020d), © 2020 Elsevier Inc.

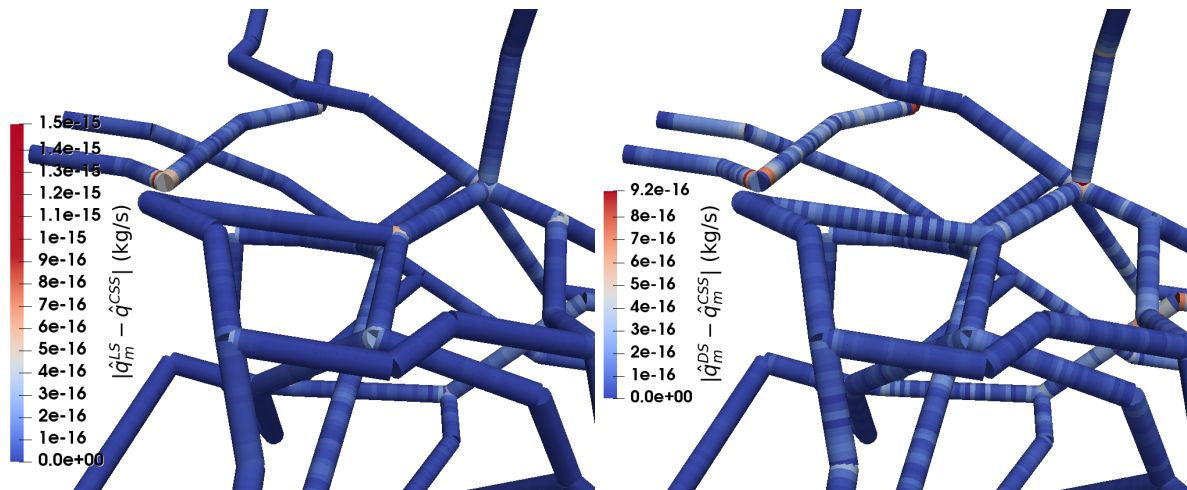


**Figure 7.15 – Local distribution of differences in the source term.** Shown for the ls and ds methods in comparison with the css method. Vessel segments visualized as tubes with a constant radius. The largest differences between the methods can be seen in the neighborhood of bifurcations and sharp bends. Reprinted with permission from Koch et al. (2020d), © 2020 Elsevier Inc.



by the fact that the vessels are discretely represented as cylindrical tubes and no explicit intersection geometry is assumed for such features. To the best of our knowledge, there is currently no mixed-dimension embedded method available that considers particular bifurcation geometries. For the LS method this means that at such features the mean surface pressure  $p_{t,\mathbb{W}}$  contains contributions from the non-physical part of the pressure solution ( $r < r_v$ ) of the neighboring vessels, leading to an overestimation of  $p_{t,\mathbb{W}}$ . This defect is improved in the CSS method, where, due to the linear continuation of the solution for  $r < r_v$ , the value of  $p_{t,\mathbb{W}}$  is closer to the actual pressure on the vessel wall surface. For the DS method, the approximation of  $p_{t,\mathbb{W}}$  is based on an analytical reconstruction from the center-line pressure  $p_{t,0}$ . However, at bifurcations the kernel support of the neighboring vessels overlap, which leads to imprecision in the approximation of  $\Xi$ . Fig. 7.14 shows that these effects lead to differences of 3 to 4 % in  $\Delta q$  between the methods. Furthermore, it is shown that if the source contributions in the vicinity of bifurcations ( $K_\Lambda$  closer than 10  $\mu\text{m}$ ) are excluded from the norm, the differences decrease to 2 to 3 %. This shows that the differences are rather local to the bifurcation neighborhood. Finally, while it cannot be concluded which method is best for the fine grid solutions, we again observe that the DS method, especially the variants with larger kernel support, better approximate the fine scale solution for large  $h_\Omega$  (coarse grid). In fact, the difference to the fine scale solution (obtained with the CSS method) for the coarsest grid ( $h_\Omega = 21 \mu\text{m}$ ) is 10 % for the DS method with  $\varrho_i = 5r_{v,i}$ , while it is 30 % for the LS and CSS methods.

## 7.4 Summary and conclusion

We presented a new method for modeling tissue perfusion using a mixed-dimension embedded method with distributed sources. The most prominent difference to existing schemes is that the source term, coupling the vascular and the extra-vascular domains, is spatially distributed using kernel functions. The mean pressure on the vessel surface is not explicitly computed but locally reconstructed from the pressure at the vessel center-line using an analytically derived scaling factor. We showed in four numerical experiments that the result obtained with the new method match well with the results obtained with existing methods. It was consistently shown in the experiments that the new method converges with a higher rate for the source term  $\hat{q}_m$  and the vessel pressure  $p_v$  due to an increased regularity in the extra-vascular pressure  $p_t$ . Furthermore, in all experiments the new method provided better

approximations of the source term  $\hat{q}_m$  for coarse extra-vascular grids. In a test with a realistic vessel network from the rat cortex, using the new method resulted in a three-fold reduction of the error in the source term for coarse grids in comparison to state-of-the-art methods with respect to a reference solution computed on a fine grid.

In four numerical experiments the new method was compared to existing methods. To this end, all methods have been implemented in the open source software framework DuMu<sup>x</sup>. The implementation effort and computational costs (at the same grid resolution) of the new method are comparable with existing methods. However, our results suggest that the new methods can be considered computationally more efficient, since a good approximation of the source term is already achieved at lower grid resolutions.

The results in this paper suggest that the new method provides the best source term approximations, if the source is distributed over a volume larger than the vessel itself. In such a case the pressure solution in the extra-vascular space is regularized and thus may deviate from the physical solution. In turn, the regularized extra-vascular pressure results in better approximations of source term and vessel pressure. A good approximation of the fluid exchange between vascular and extra-vascular compartments is crucial in many applications involving transmural transport processes such as the estimation of contrast agent leakage from the brain microvasculature in multiple sclerosis. A regularized extra-vascular pressure may be acceptable in cases where it is more interesting how much of a substance leaves the vascular system rather than its accurate distribution in the extra-vascular space. Furthermore, it is always acceptable to choose the distribution volume similar to the size of the coarsest neighboring extra-vascular discretization cell. In such a case, a possible error in the extra-vascular pressure is masked by other discretization errors. Nevertheless, the description of the source term and thus the vessel pressure may still be improved significantly by a better reconstruction of the mean vessel surface pressure.

The last numerical experiment revealed that the largest differences between the different mixed-dimension embedded methods occur in the vicinity of bifurcations. This is due to an imprecise description of bifurcation geometries in the discrete setting. In order to evaluate methods with respect to the error at bifurcations, and to develop improved descriptions of the flow around bifurcations, a comparison with methods with spatially resolved interfaces is necessary. However, our results suggest that discretization errors around bifurcations only affect small parts of the entire system, such that the current models might be sufficient approximations for most applications.

Finally, due to the improved accuracy at coarse grid resolutions, we consider the new method an important step towards simulations of larger vessel networks, where fine grid resolutions in the extra-vascular space may get computationally prohibitively expensive.

The code to reproduce the simulations in this chapter can be found at <https://git.iws.uni-stuttgart.de/dumux-pub/Koch2019b>.



# 8 A new well model using distributed sources\*

In this chapter, a new approach for obtaining a more accurate source term for a given well bottom hole pressure is presented. The new model is, in contrast to most of the existing methods, independent of the discretization scheme and can be used for general unstructured grids. Additionally, the presented method is not restricted to diagonal tensors and thus works for general anisotropic permeabilities. In Section 8.1, we derive a well model, initially for isotropic porous media, for which the fluid mass injected by a well is distributed over a small neighborhood around the well, using kernel functions. The derivation follows the idea presented in Chapter 7. However we herein discuss the case without membrane or casing. The model yields a pressure solution without singularity, from which the source term can be reconstructed using a relation found with the analytical solution for the case of an infinite well in an infinite medium. The model generalizes to more complex problems due to the superposition principle valid for the Laplace operator. In Section 8.2, the model is generalized to porous media with general anisotropic permeabilities, based on an analytical solution constructed in Section 8.2.1 using a series of coordinate transformations. We show that the general model reduces to the model derived in Section 8.1 for isotropic permeabilities. After describing the spatial discretization in Section 8.3, the new well model is analyzed with several numerical experiments in Section 8.4. The results indicate that the model is consistent for different anisotropy ratios, robust with respect to rotations of the well relative to the computational grid, and to rotations of an anisotropic permeability tensor. A comparison with a Peaceman-type well model in a setup with a K-orthogonal grid and an embedded slanted well suggests that the new model more accurately approximates the fluid exchange between well and rock matrix.

---

\*This chapter is based on Koch, Helmig, and Schneider (2020c), © 2020 Elsevier Inc.

## 8.1 The distributed source method for isotropic media

First, we derive a well model with distributed source for porous media with isotropic permeability tensor, without well casing. Stationary single-phase flow around a well with radius  $r_\omega$ , in an isotropic porous medium with permeability  $k$ , can be described by Eq. (5.1). For a given well pressure  $p_\omega$ , the source term describing the mass exchange between well and embedding porous rock matrix is given by Eq. (5.9). We choose the compact radially symmetric kernel function given in Eq. (7.2), which has a finite support radius  $\varrho$  and regularizes the pressure solution for  $r \leq \varrho$ . Furthermore,  $\varrho \leq \delta$ , where  $\delta > r_\omega$  is the radius of the well-neighborhood region as introduced in Section 5.3 and shown in Fig. 8.1. The matrix fluid pressure,  $p$ , for  $r < \rho$  can be obtained by integration of Eq. (5.1). We obtain

$$p(r) = \begin{cases} p_\omega - \frac{\mu}{k\rho} \frac{q}{2\pi} \left[ \frac{r^2}{2\varrho^2} + \ln\left(\frac{\varrho}{r_\omega}\right) - \frac{1}{2} \right] & r \leq \varrho, \\ p_\omega - \frac{\mu}{k\rho} \frac{q}{2\pi} \ln\left(\frac{r}{r_\omega}\right) & r > \varrho, \end{cases} \quad (8.1)$$

cf. Eq. (7.7), where  $p_\omega$  is the average pressure on the well-matrix interface for a given well cross-section, defined analogously to  $p_{m,\mathbb{W}}$  in Eq. (6.3). Figure 8.1 graphically explains the

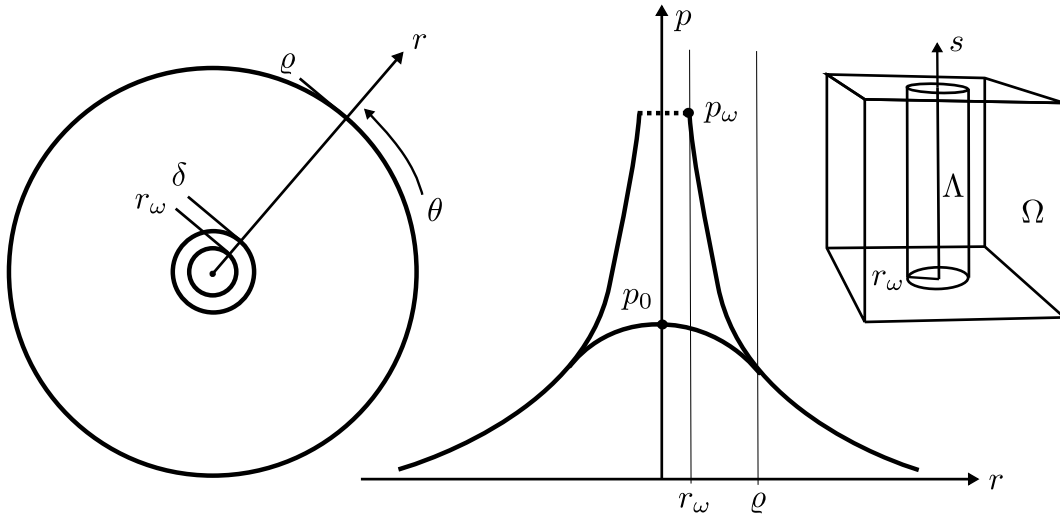


**Figure 8.1 – Near-well pressure solution.** Schematic representation of the introduced symbols for an infiltration scenario in an isotropic porous medium. An infinite well with radius  $r_\omega$ , center-line  $\Lambda$  with local cylindrical coordinate system  $(r, \theta, s)$  is embedded in the porous domain  $\Omega$ . The kernel function with radius  $\varrho$  regularizes the pressure solution which can then be evaluated at  $r = 0$ :  $p(r = 0) = p_0$ . Reprinted with permission from Koch et al. (2020c), © 2020 Elsevier Inc.

most important symbols used in this section. As the regularized pressure can be evaluated

at the well center-line we can reformulate Eq. (5.9) as

$$q = 2\pi \frac{\rho k}{\mu} (p_\omega - p_0) \Xi, \quad \text{with } \Xi = \frac{(p_\omega - p_\delta)}{(p_\omega - p_0)} \frac{1}{\ln\left(\frac{\delta}{r_\omega}\right)} \quad (8.2)$$

where  $\Xi$  is the flux scaling factor introduced in Chapter 7. The flux scaling factor can be expressed independent of the pressure. To this end, Eq. (8.1) is evaluated at  $r = 0$ , so that  $p_\omega$  is expressed in terms of  $p_0$ ,

$$p_0 = -(p_\omega - p_0) \Xi \left[ \ln\left(\frac{\rho}{r_\omega}\right) - \frac{1}{2} \right] + p_\omega, \quad (8.3)$$

where  $q$  was replaced by inserting Eq. (8.2). It directly follows from Eq. (8.3) that

$$\Xi = \left[ \ln\left(\frac{\rho}{r_\omega}\right) - \frac{1}{2} \right]^{-1}. \quad (8.4)$$

Comparing Eq. (8.4) with Eq. (7.10), we note that in the absence of a casing, the flux scaling parameter is purely geometric and does not contain additional model parameters such as wall permeability or fluid viscosity.

## 8.2 Extension to anisotropic media

In the following section, the developed well model is extended to porous media with anisotropic permeability. In Section 8.2.1, we derive an analytical solution for one-phase flow around an infinitely long cylindrical well embedded in an infinite porous domain in  $\mathbb{R}^3$ . This derivation motivates the choice of a suitable kernel function for anisotropic problems, presented in Section 8.2.2.

### 8.2.1 Analytical solution

In the following section, we derive an analytical solution for one-phase flow around an infinite cylindrical (possibly slanted) well  $\Gamma$  with radius  $r_\omega$  in an infinite porous domain  $\hat{\Omega} = \mathbb{R}^3 \setminus \Gamma$  with anisotropic, homogeneous permeability. We assume, without loss of generality, that the well axis passes through the origin of the Cartesian coordinate system,

and denote by  $\psi$  a unit vector parallel to the well signifying the well orientation. We seek an analytical expression for the hydraulic pressure  $p$  such that

$$-\nabla \cdot \left( \frac{\rho}{\mu} K \nabla p \right) = 0 \quad \text{in } \hat{\Omega}, \quad (8.5)$$

for a constant well pressure  $p_\omega$  in Pa and some specific pumping rate  $q$  in  $\text{kg s}^{-1} \text{m}^{-1}$  given on  $\partial\Gamma$ . The total mass flow over the boundary of a well segment of length  $L$  is thus given by  $Q = qL$ .  $K$  is a positive definite and symmetric, second-order tensor field. Hence,  $K$  can be decomposed such that  $K = QDQ^T$ , where  $D = \text{diag}(\lambda_1, \lambda_2, \lambda_3)$  is a diagonal matrix composed of the eigenvalues  $\lambda_i$  of  $K$ ,  $Q = [\mathbf{v}_{K,1} | \mathbf{v}_{K,2} | \mathbf{v}_{K,3}]$  is a rotation matrix with the corresponding eigenvectors as columns, and  $A^T$  denotes the transposed of a matrix  $A$ . Further useful properties derived from the decomposition are  $\det(K) = \lambda_1 \lambda_2 \lambda_3$ , where  $\det(A)$  denotes the determinant of  $A$ , and  $K^n = Q \Lambda^n Q^T$ , where  $D^r = \text{diag}(\lambda_1^r, \lambda_2^r, \lambda_3^r)$ ,  $r \in \mathbb{R}$ .

It is well known that the anisotropic one-phase flow problem can be transformed to an isotropic problem using a coordinate transformation (Aavatsmark and Klausen, 2003; Fitts, 2006; Aavatsmark, 2016; Peaceman, 1983; Bear and Dagan, 1965)

$$U : \mathbb{R}^3 \rightarrow \mathbb{R}^3, \mathbf{x} \mapsto \mathbf{u} = \tilde{S}\mathbf{x}, \quad (8.6)$$

with the stretching matrix  $\tilde{S} = k_{\text{iso}}^{1/2} K^{-1/2}$ , where  $k_{\text{iso}}$  is an arbitrary scalar constant, that we choose as  $k_{\text{iso}} = \det(K)^{-1/3}$  (cf. Aavatsmark and Klausen, 2003), rendering the transformation isochoric. The transformation  $\mathbf{u} = \tilde{S}\mathbf{x}$  deforms the well cylinder such that a cross-section orthogonal to the transformed well direction is elliptical. The solution to the isotropic problem in the transformed coordinates  $\mathbf{u}$  is identical on two parallel planes perpendicular to the transformed (normalized) well direction,  $\psi' = \tilde{S}\psi / \|\tilde{S}\psi\|^{-1}$ . This motivates the rotation of the coordinate system such that the first and second axis are aligned with the major and minor axis of the well-bore ellipse and third axis is aligned with  $\psi'$ . The desired rotation is given by

$$V : \mathbb{R}^3 \rightarrow \mathbb{R}^3, \mathbf{u} \mapsto \mathbf{v} = \tilde{R}\mathbf{u}, \quad (8.7)$$

where  $\tilde{R}$  is the corresponding rotation matrix. The derivation of  $V$  is conducted in detail in Appendix A.4.

We now have to solve a two-dimensional isotropic Laplace problem with boundary conditions prescribed on an ellipse. To this end, we note that the transformation of a harmonic



function  $f$  (a function satisfying Laplace's equation  $\nabla \cdot \nabla f = 0$ ) with a conformal (angle-preserving) mapping yields another harmonic function (Nehari, 1975), see Appendix A.7. Using a Joukowski transformation, a conformal mapping well-known from aerodynamics (Joukowski, 1910), the isotropic problem with a well with elliptic cross-sections, can be transformed to an isotropic problem with circular cross-sections (Fitts, 2006). Transforming into the complex plane (parameterizing the well-bore ellipse plane)

$$Z : \mathbb{R}^3 \rightarrow \mathbb{C}, \mathbf{v} \mapsto z = \tilde{Z}\mathbf{v} = [1, i, 0]\mathbf{v} = v_1 + i v_2, \quad (8.8)$$

the (inverse) Joukowski transformation

$$T : \mathbb{C} \rightarrow \mathbb{C}, z \mapsto w = z + \sqrt{z-f}\sqrt{z+f}, \quad f = \sqrt{a^2 - b^2} \quad (8.9)$$

transforms elliptic isobars into circular isobars, where  $a$  and  $b$ ,  $a \geq b$ , are the major and minor axis of the well-bore ellipse, as derived in Appendix A.4. In particular, the well-bore ellipse (where  $p = p_\omega$ ) is mapped onto a circle with radius  $r_o = a + b$ . Finally, in the new coordinate system, we find the (now) radially symmetric analytical solution to problem Eq. (8.5)

$$p(w) = p_\omega - \frac{\mu}{\rho k_{\text{iso}}} \frac{\hat{q}}{2\pi} \ln\left(\frac{|w|}{r_o}\right) \zeta, \quad \hat{q} = q\zeta = q \frac{ab}{r_\omega^2}, \quad (8.10)$$

where the source scaling factor  $\zeta$  is necessary to recover the original source  $q$  on  $\partial\Gamma$ . This can be derived from simple geometric considerations as shown in Appendix A.8. Every  $w$  corresponding to some  $x \in \hat{\Omega}$  in original coordinates is obtained by using all above-mentioned transformations after each other as follows

$$w = T(Z(V(U(\mathbf{x})))) = T(\tilde{Z}\tilde{R}\tilde{S}\mathbf{x}). \quad (8.11)$$

In summary, we can find a closed-form analytical solution in a transformed coordinate system. The transformation is composed of four steps. First,  $U$  stretches the domain rendering the problem isotropic and a circular well-bore cross-section turns into an ellipse. Second,  $V$  rotates into the principal axes of the well-bore ellipse. Third,  $Z$  projects onto the complex plane. And finally,  $T$  is a conformal mapping transforming the well-bore ellipse into a circular cross-section while preserving divergence-free velocity fields.

A solution for a slanted well ( $30^\circ$  with respect to vertical axis) and anisotropic permeability tensor

$$K_A = \begin{bmatrix} 1 & 0 & 0 \\ 0 & 5 & 4 \\ 0 & 4 & 5 \end{bmatrix} 1 \cdot 10^{-10} \text{ m}^2 \quad (8.12)$$

is exemplarily visualized in Fig. 8.2.

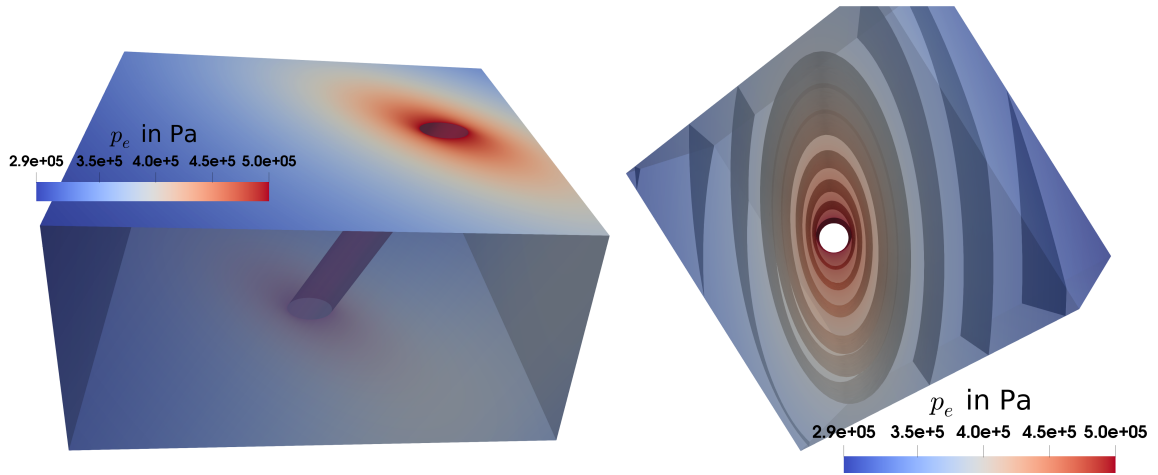


**Figure 8.2 – Analytic pressure solution for a slanted well.** Well radius is  $r_\omega = 0.1$  m, well pressure  $p_\omega = 5.0 \cdot 10^5$  Pa, total mass injection rate  $Q_\omega = 115.47 \text{ kg s}^{-1}$ , and permeability is anisotropic ( $K_A$ ). The top view is oriented in well direction and shows pressure contour surfaces highlighting their elliptical shape. Reprinted with permission from Koch et al. (2020c), © 2020 Elsevier Inc.

### 8.2.2 A kernel function for anisotropic media

Instead of excluding the well domain  $\Gamma$  from  $\Omega = \mathbb{R}^3$  and modeling infiltration or extraction by a flux boundary condition, we will now model the action of the well on the flow field by a spatially distributed source term, as presented for the isotropic problem,

$$-\nabla \cdot \left( \frac{\rho}{\mu} K \nabla p \right) = q \zeta \Phi_A \quad \text{in } \Omega. \quad (8.13)$$

From the above derivations, we know that solving Eq. (8.13) in  $w$ -coordinates is straightforward. Hence, we choose kernel functions in  $w$ -coordinates and then transform to  $x$ -coordinates so that the pressure solution satisfies Eq. (8.13). Motivated by the properties of the Joukowski transform, as analyzed in more detail in Appendix A.6, we choose a

local kernel that is constant on the annulus with inner radius  $f < \varrho_i \leq r_o$  and outer radius  $\varrho_o > r_o$ ,

$$\Phi_A(\mathcal{w}) = \begin{cases} \frac{1}{\pi(\varrho_o^2 - \varrho_i^2)} & \varrho_i \leq |\mathcal{w}| \leq \varrho_o, \\ 0 & \text{elsewhere.} \end{cases} \quad (8.14)$$

In  $w$ -coordinates, we can find a solution to the problem

$$-\nabla_w \cdot \nabla_w p = \hat{q} \frac{\mu}{\rho k_{\text{iso}}} \Phi_A \quad \text{in } \Omega_w = T(Z(V(U(\Omega)))), \quad (8.15)$$

for a given constant well pressure  $p_\omega$ ,  $\hat{q} = q\zeta$  and constant density and viscosity. By means of integration (cf. Chapter 7), we get

$$p(w) = \begin{cases} p_\omega - \frac{\mu}{K\rho} \frac{\hat{q}}{2\pi} \left[ \frac{(|w|^2 - \varrho_o^2)}{2\xi^2} - \frac{\varrho_i^2}{\xi^2} \ln\left(\frac{|w|}{\varrho_o}\right) + \ln\left(\frac{\varrho_o}{r_\omega}\right) \right] & \varrho_i \leq |w| \leq \varrho_o, \\ p_\omega - \frac{\mu}{K\rho} \frac{\hat{q}}{2\pi} \left[ -\frac{1}{2} - \frac{\varrho_i^2}{\xi^2} \ln\left(\frac{\varrho_i}{\varrho_o}\right) + \ln\left(\frac{\varrho_o}{r_\omega}\right) \right] & |w| < \varrho_i, \\ p_\omega - \frac{\mu}{K\rho} \frac{\hat{q}}{2\pi} \ln\left(\frac{|w|}{r_\omega}\right) & |w| > \varrho_o, \end{cases} \quad (8.16)$$

where  $\xi^2 = \varrho_o^2 - \varrho_i^2$ . This shows that outside the kernel support region ( $|w| > \varrho_o$ ), we obtain the exact analytical solution derived in Section 8.2.1. Moreover, the source term can be reformulated,

$$\hat{q} = 2\pi \frac{\rho k_{\text{iso}}}{\mu} (p_\omega - p_0) \Xi, \quad \Xi = \left[ \ln\left(\frac{\varrho_o}{r_\omega}\right) - \frac{1}{2} - \frac{\varrho_i^2}{\xi^2} \ln\left(\frac{\varrho_i}{\varrho_o}\right) \right]^{-1}, \quad (8.17)$$

where  $p_0 := p(|w| = 0) = p(|w| = \varrho_i)$  is the fluid pressure evaluated on the well center-line. Note that for  $f = 0$  and  $\varrho_i = f = 0$ , the isotropic solution with for a circular constant kernel (Eqs. (8.1) and (8.4)) is obtained. From the transformation of the Laplace operator, Eq. (A.22), we see that the problem

$$-\nabla_z \cdot \nabla_z p = \hat{q} \frac{\mu}{\rho k_{\text{iso}}} \Phi_A \Phi_J \quad \text{in } \Omega_z = Z(V(U(\Omega))), \quad (8.18)$$

with altered kernel function  $\Phi_\Lambda = \Phi_A \Phi_J$  is equivalent to Eq. (8.15).

The transformation  $T^{-1}$  changes the shape of the kernel support  $\mathcal{S}(\Phi_\Lambda)$  from an annulus to an ellipse  $E_{\Phi,v}$ . Inverting  $Z$  extrudes the solution along the well center-line, and inverting the rotation and stretch described by  $V$  and  $U$  results in a kernel support region in the shape of an elliptic cylinder. Moreover, each ellipse  $E_{\Phi,v}$  with normal vector  $e_3$  is transformed

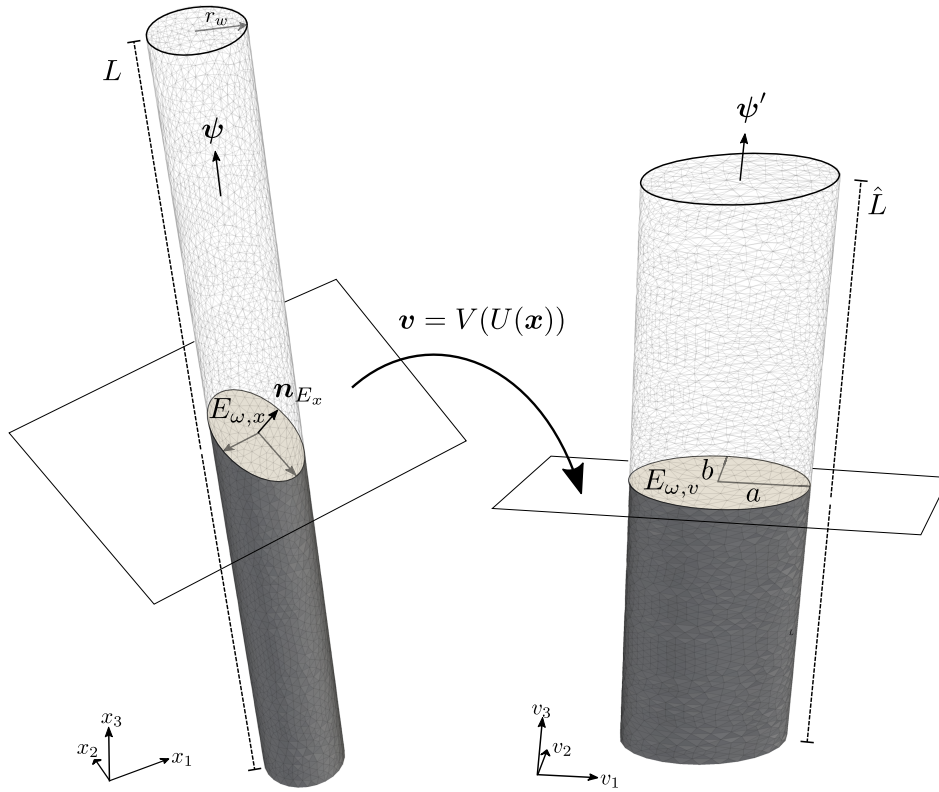


**Figure 8.3 – Visualization of the coordinate transformation  $\mathbf{v} = V(U(\mathbf{x})) = \tilde{\mathbf{R}}\tilde{\mathbf{S}}\mathbf{x}$ .** The ellipse  $E_v$  is orthogonal to the well direction  $\psi'$  which is equal to  $\mathbf{e}_3 = [0, 0, 1]^T$  in  $\mathbf{v}$ -coordinates. Reprinted with permission from Koch et al. (2020c), © 2020 Elsevier Inc.

to an ellipse  $E_{\Phi,x}(s)$ , that is the intersection of the elliptic cylinder with a plane with the normal vector  $\mathbf{n}_{E_x} = \tilde{\mathbf{S}}\tilde{\mathbf{R}}^T \mathbf{e}_3$ , centered at  $s$  on the well center-line. The transformation and the normal vector  $\mathbf{n}_{E_x}$  are visualized in Fig. 8.3. We note that if none of the principal axes of the permeability tensor are aligned with the well direction,  $\mathbf{n}_{E_x}$  is not parallel to the well direction  $\psi$  in  $x$ -coordinates. The integral of the right-hand side of Eq. (8.13) for a well segment  $\Lambda_i$  with length  $L_i$  is equal to the integral over the kernel support  $\mathcal{S}(\Phi_{\Lambda_i})$  which has the shape of the elliptic cylinder given by

$$\mathbb{E} := \bigcup_{0 \leq s \leq L_i} E_{\Phi,x}(s). \quad (8.19)$$

Using  $\hat{q} = q\zeta$ , and exploiting that  $k_{\text{iso}}$  was chosen such that  $\det(\tilde{R}\tilde{S}) = 1$ , it can be shown that

$$\int_{\mathbb{E}} \hat{q}\Phi_{\Lambda,i} dx = \int_{V(U(\mathbb{E}))} \hat{q}\Phi_{\Lambda,i} dv = \int_0^{\hat{L}_i} \int_{E_{\Phi,v}(\hat{s})} \hat{q}\Phi_{\Lambda} d\hat{A}d\hat{s} = \hat{q}\hat{L}_i = qL_i, \quad (8.20)$$

where  $\hat{s} \in [0, \hat{L}_i]$  is a local coordinate along the transformed well direction, and the last equality is proven in Appendix A.9. This is the desired property of the kernel function for the anisotropic case corresponding to Eq. (6.5).

### 8.3 Numerical method

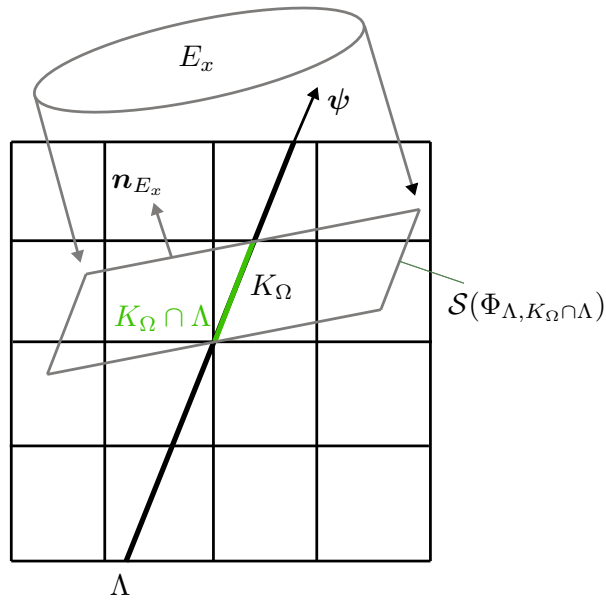


**Figure 8.4 – Visualization of the discretization process.** The domain  $\Omega$  is represented by a set of control volumes  $K_\Omega \in \Omega_b$ . The well center-line  $\Lambda$  with direction  $\psi$  intersects with a  $K_\Omega$  shown in green. The gray parallelogram is a 2D-projection of the elliptic cylinder that is the part of the kernel support  $\mathcal{S}(\Phi_\Lambda)$  associated with  $K_\Omega \cap \Lambda$ . Reprinted with permission from Koch et al. (2020c), © 2020 Elsevier Inc.

We discretize Eq. (8.13) using a cell-centered finite volume method with multi-point flux approximation (MPFA) (Aavatsmark, 2002). In contrast to the two-point flux approximation (TPFA) used in Chapter 7, MPFA is designed to be consistent for computational grids which are not aligned with the principle directions of the permeability tensor (Schneider, 2018).

The domain  $\Omega$  is decomposed into control volumes  $K_\Omega \in \Omega_b$  such that the computational mesh  $\Omega_b$  is a discrete representation of  $\Omega$ . Furthermore, each control volume boundary,  $\partial K_\Omega$ , can be split into a finite number of faces  $\sigma \subset \partial K_\Omega$ , such that  $\sigma = K_\Omega \cap L_\Omega$ , with  $L_\Omega$  denoting a neighboring control volume. Integrating Eq. (8.13) over a control volume  $K_\Omega$  and applying the Gauss divergence theorem on the left-hand side yields

$$-\int_{\partial K_\Omega} \left[ \frac{\rho}{\mu} K \nabla p \right] \cdot \mathbf{n}_{K_\Omega, \sigma} dA = \int_{K_\Omega} \hat{q} \Phi_\Lambda dx, \quad (8.21)$$

where  $\mathbf{n}_{K_\Omega, \sigma}$  is the unit outward-pointing normal on face  $\sigma \subset \partial K_\Omega$ . The exact fluxes are approximated by numerical fluxes

$$F_{K_\Omega, \sigma} \approx -\int_{\sigma} \left[ \frac{\rho}{\mu} K \nabla p \right] \cdot \mathbf{n}_{K_\Omega, \sigma}, \quad (8.22)$$

which are computed using the MPFA-O method described in (Aavatsmark, 2002). The discrete source term is computed as

$$Q_{K_\Omega} \approx \int_{K_\Omega} \hat{q} \Phi_\Lambda dx, \quad Q_{K_\Omega} = \frac{Q_\mathcal{S}}{|\mathcal{S}|} \int_{K_\Omega \cap \mathcal{S}(\Phi_\Lambda, \mathcal{S})} \Phi_\Lambda dx, \quad (8.23)$$

where  $Q_\mathcal{S}$  is a numerical approximation of the source term integral over the intersection  $\mathcal{S} = K_\Omega \cap \Lambda$ ,

$$Q_\mathcal{S} = |\mathcal{S}| 2\pi \frac{\rho k_{\text{iso}}}{\mu} (p_\omega - p_0) \Xi, \quad (8.24)$$

and  $\mathcal{S}(\Phi_\Lambda, \mathcal{S})$  is the kernel support associated with  $\mathcal{S}$  as depicted in Fig. 8.4. In summary, the discrete form of Eq. (8.21) is

$$\sum_{\sigma \subset \partial K_\Omega} F_{K_\Omega, \sigma} = Q_{K_\Omega}, \quad K_\Omega \in \Omega_b. \quad (8.25)$$

We note that due to the dependency of  $Q_\mathcal{S}$  on  $p_0$ , the proposed method is non-local in the sense that non-neighbor cells  $M_\Omega \in \Omega_b$  (where  $M_\Omega \cap K_\Omega$  is the empty set or a single point) may have an associated degree of freedom that depends on the degree of freedom of  $K_\Omega$ .

### 8.3.1 Kernel integration

The kernel integral in Eq. (8.23)

$$\mathbb{I}_{\Phi, K_\Omega} := \int_{K_\Omega \cap \mathcal{S}(\Phi_{\Lambda, \mathcal{S}})} \Phi_\Lambda \, dx, \quad (8.26)$$

is not easily approximated with a quadrature rule, since the intersection  $K_\Omega \cap \mathcal{S}(\Phi_{\Lambda, \mathcal{S}})$ , that is the intersection of an elliptic cylinder with, for example, a hexahedron is difficult to compute. However, we use the same idea as in Chapter 7, and remark that the integral over the entire support  $\mathcal{S}(\Phi_{\Lambda, \mathcal{S}})$  is known exactly; see Eq. (8.20). Hence, the integration problem can be reformulated as the distribution of the known integral over all intersected control volumes  $K_\Omega$  weighted with the respective support volume fractions.

## 8.4 Numerical experiments and discussion

We present numerical experiments using the presented method in different setups. All experiments are conducted with constant fluid density  $\rho = 1000 \text{ kg m}^{-3}$  and viscosity  $\mu = 1 \cdot 10^{-3} \text{ Pas}$ . The well pressure is constant,  $p_\omega = 1 \cdot 10^6 \text{ Pa}$ , and the well radius is  $r_\omega = 0.1 \text{ m}$  if not specified otherwise. The permeability tensor is given as

$$K(\gamma_1, \gamma_2) = R_1(\gamma_1)R_2(\gamma_2)K_\alpha R_2^T(\gamma_2)R_1^T(\gamma_1), \quad K_\alpha = \begin{bmatrix} 1 & 0 & 0 \\ 0 & 1 & 0 \\ 0 & 0 & \alpha \end{bmatrix} 1 \cdot 10^{-12} \text{ m}^2, \quad (8.27)$$

where

$$R_1(\gamma_1) = \begin{bmatrix} 1 & 0 & 0 \\ 0 & \cos \gamma_1 & -\sin \gamma_1 \\ 0 & \sin \gamma_1 & \cos \gamma_1 \end{bmatrix}, \quad R_2(\gamma_2) = \begin{bmatrix} \cos \gamma_2 & 0 & \sin \gamma_2 \\ 0 & 1 & 0 \\ -\sin \gamma_2 & 0 & \cos \gamma_2 \end{bmatrix} \quad (8.28)$$

are rotation matrices rotating vectors about  $e_1, e_2$  by the rotation angle  $\gamma_1, \gamma_2$ , respectively, and  $\alpha$  is a given dimensionless  $k$ -anisotropy ratio  $\alpha = k_{33}k_{11}^{-1} = k_{33}k_{22}^{-1}$ . The domain  $\Omega_0 = [-100, 100] \times [-100, 100] \times [-50, 150] \text{ m}^3$  is split in two regions,  $\Omega = [-100, 100] \times [-100, 100] \times [0, 100] \text{ m}^3$  and  $\Omega_D = \Omega_0 \setminus \Omega$ . The well center-line  $\Lambda$  is given by the line

through the origin and  $\psi = R_1(\beta_1)R_2(\beta_2)e_3$ , where  $R_1, R_2$  are given in Eq. (8.28) and  $\beta_1, \beta_2$ , are rotation angles. The analytical solution for all cases is given in Eq. (8.16),  $q = 1 \text{ kg s}^{-1} \text{ m}^{-1}$ , and  $L = |\Lambda \cap \Omega|$  (in m). For all setups the inner kernel radius is chosen as  $\varrho_i = f$ , as defined in Eq. (8.9). In all of  $\Omega_D$  and on the boundary  $\partial\Omega$  the analytical solution is enforced by Dirichlet constraints, modeling the infinite well. The computational mesh  $\Omega_b$  is a structured grid composed of regular hexahedra  $K_\Omega$ . Furthermore, we define two error measures.

$$E_p = \frac{1}{p_\omega} \left[ \frac{1}{|\Omega_b|} \sum_{K_\Omega \in \Omega_b} |K_\Omega| \left( p_{e, x_{K_\Omega}} - p_{K_\Omega} \right)^2 \right]^{\frac{1}{2}} \quad (8.29)$$

is the relative discrete  $L^2$ -norm of the pressure, where  $p_{e, x_{K_\Omega}}$  is the exact pressure evaluated at the cell centroid  $x_{K_\Omega}$  and  $p_{K_\Omega}$  the discrete numerical cell pressure, and

$$E_q = \frac{1}{q} \left[ \frac{1}{|\Lambda \cap \Omega_b|} \sum_{\substack{K_\Omega \in \Omega_b \\ K_\Omega \cap \Lambda \neq \emptyset}} |\mathcal{I}| \left( q - \frac{Q_{\mathcal{I}}}{|\mathcal{I}| \zeta} \right)^2 \right]^{\frac{1}{2}} \quad (8.30)$$

is the relative discrete  $L^2$ -norm of the source term, where  $|\mathcal{I}| = |K_\Omega \cap \Lambda|$  is the length of the intersection of cell  $K_\Omega$  and the well center-line  $\Lambda$ ,  $Q_{\mathcal{I}}$  is the discrete source term given in Eq. (8.24). All setups are implemented in DuMu<sup>x</sup> (Flemisch et al., 2011; Koch et al., 2020b), an open-source porous media simulator based on DUNE (Bastian et al., 2008b,a).

#### 8.4.1 Grid convergence for different anisotropy ratios

In the first numerical experiment grid convergence is investigated for different anisotropy ratios  $\alpha$ . To this end,  $h_{\max} := \max_{K_\Omega \in \Omega_b} h_{K_\Omega}$ , where  $h_{K_\Omega}$  is defined as the maximum distance between two vertices of the cell  $K_\Omega$ . Starting at a grid resolution for  $\Omega_b$  of  $20 \times 20 \times 10$  cells ( $h_{\max} = 10\sqrt{3}$  m), the grid is refined uniformly. Figure 8.5 shows the errors  $E_p$  and  $E_q$  for different grid resolutions and values of  $\alpha$ , for  $\beta_1 = \beta_2 = 20^\circ$  and  $\gamma_1 = \gamma_2 = -20^\circ$ , so that  $K$  is a full tensor and none of the principal axis of  $K$  is aligned with the well direction. For all  $\alpha$ , the method shows second order convergence for the pressure in the given norm, as expected for the MPFA-O method (Schneider et al., 2018) (super convergence at cell centers). The source term  $q$  is a linear function of the pressure  $p$  and also exhibits second order convergence. We note that the errors for different  $\alpha$  are not directly comparable since the



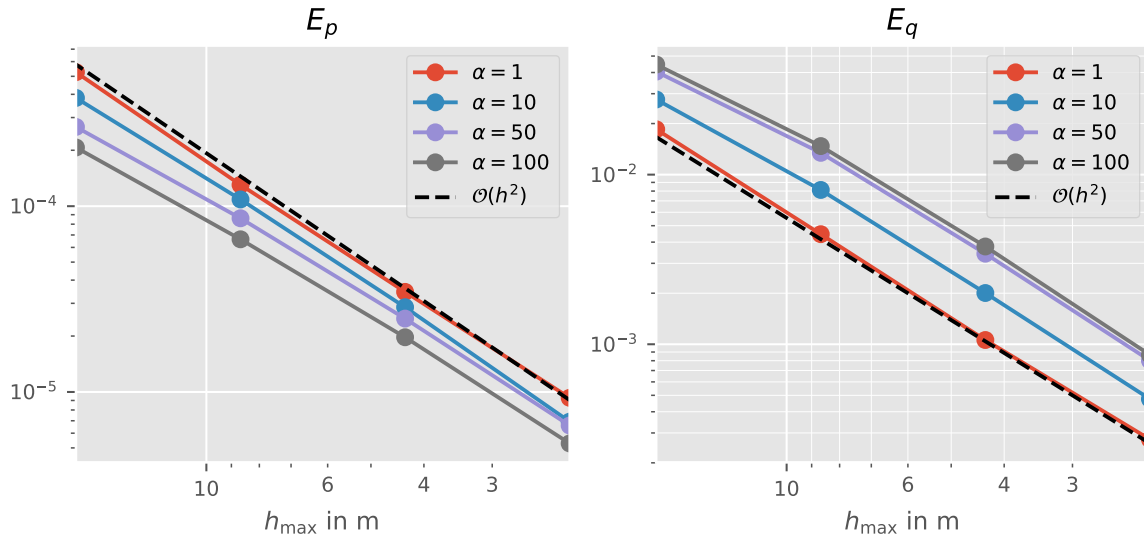


**Figure 8.5 – Grid convergence for different anisotropy ratios.** The relative discrete  $L^2$ -norm of pressure  $E_p$  and source  $E_q$  for different anisotropy ratios  $\alpha$ . None of the principal axis of the permeability tensor is aligned with the slanted well axis  $\psi$  or any of the grid axes. Reprinted with permission from Koch et al. (2020c), © 2020 Elsevier Inc.

analytical solution for  $p$  changes with  $\alpha$ , although  $q$  is constant. However, the convergence rates are shown to be independent of  $\alpha$  with increasing grid resolution. The convergence rates for  $E_q$  (slope of the lines in Fig. 8.5) are presented in Table A.2 in Appendix A.10. It can be seen that rates for large grid cells and large  $\alpha$  are slightly smaller. This is because the kernel support is still under-resolved by the computational grid. For example, for  $\alpha = 100$ , the kernel ellipse in  $x$ -coordinates has major and minor axis of  $a_x \approx 55.9$  m,  $b_x \approx 5.6$  m, respectively, while  $h_{\max} \approx 17.32$  m for the lowest grid resolution.

#### 8.4.2 Influence of the outer kernel radius $\varrho_o$

In Chapter 7, it is suggested that increasing the kernel support region (increasing  $\varrho_o$ ), has a similar effect on  $E_q$  as refining the grid. However, the pressure solution is then regularized in a larger region, so that there is a trade-off between the accuracy of the source term and the accuracy of the pressure field with respect to the unmodified problem ( $\varrho_o \rightarrow \varrho_i, \Phi_\Lambda \rightarrow \delta_\Lambda$ ). However, every discrete cell  $K_\Omega$  can be also interpreted as a kernel support region, such that

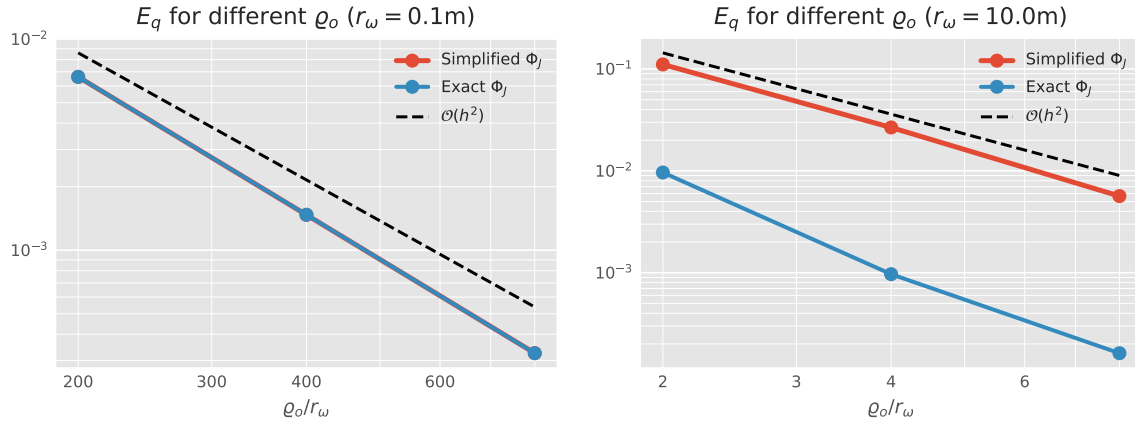


**Figure 8.6 – Grid convergence for different kernel support radii.** The source error  $E_q$  for different kernel supports and the same  $20 \times 20 \times 10$  computational grid ( $h_{\max} \approx 17.32\text{m}$ ). On the left, the case where  $\varrho_o$  is only slightly larger than  $r_\omega$ . On the right, the case  $\varrho_o \gg r_\omega$ . Reprinted with permission from Koch et al. (2020c), © 2020 Elsevier Inc.

the choice of  $\Phi_\Lambda$  enables us to better control the discretization error as soon as  $\mathcal{S}(\Phi_\Lambda, \mathcal{I})$  becomes larger than  $K_\Omega$ .

As shown in (Peaceman, 1983) and Fig. A.2, isobars become circular, in the transformed domain  $U(\Omega)$ , with increasing distance to the well. Therefore, a reasonable simplification is  $\Phi_j \approx 4$  if  $\varrho_o \gg r_\omega$ . This is completely analogous to the assumption of circular isobars in (Peaceman, 1983), where an estimate of the error introduced by the assumptions is given for the two-dimensional case.

In the following numerical experiment, we step-wise increase the kernel radius  $\varrho_o$ , for the same  $20 \times 20 \times 10$  grid. This is done once for the case where  $\varrho_o \gg r_\omega$ , and for the case for which  $\varrho_o$  is only slightly larger than  $r_\omega$ . Furthermore,  $\beta_1 = \beta_2 = 20^\circ$  and  $\gamma_1 = \gamma_2 = -20^\circ$ . The results are shown in Fig. 8.6. First, it can be seen that doubling  $\varrho_o$  leads to a 4-times smaller error  $E_q$ . This can be explained by the fact that the larger the kernel, the more grid cells resolve the kernel support, and the better is the approximation of  $p_0$ . Moreover, Fig. 8.6 suggests that for  $\varrho_o \gg r_\omega$  the simplification of the kernel function ( $\Phi_j \approx 4$ ) is not visible in  $E_q$ , while for kernel radii slightly smaller than the well radius, the simplification increases  $E_q$  by an order of magnitude in comparison to the case using the exact kernel function as derived in Section 8.2.2. The results show that the presented method is also applicable in cases where the grid resolution is very close to the well radius. An adaption of

the presented method for other applications, such as the simulation of flow in vascularized tissue, where such ratios of vessel radius to cell size are typical, is therefore well-conceivable.

### 8.4.3 Robustness with respect to rotation

In the following numerical experiment, we use a single computational mesh with a given resolution for  $\Omega_h$ :  $20 \times 20 \times 10$ . First, the well direction is fixed, and the permeability tensor is rotated by varying  $\gamma_1$  and  $\gamma_2$ . Then the permeability tensor is fixed and the well is rotated by varying  $\beta_1$  and  $\beta_2$ . The results are shown in Fig. 8.7. It can be seen that the

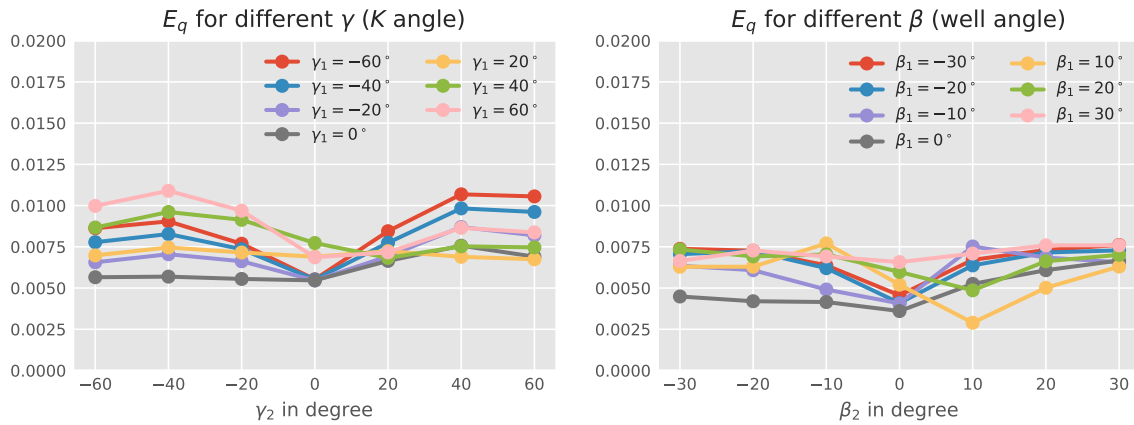


**Figure 8.7 – Source error for different  $K$  and well orientations.** Left – Source error  $E_q$  for rotations of the permeability tensor. Right –  $E_q$  for different well orientations. Reprinted with permission from Koch et al. (2020c), © 2020 Elsevier Inc.

presented well model is rather robust with respect to rotations. Possible effects influencing the approximation error  $E_q$ , include the different quality of the kernel integral for different angles with respect to the grid axes, and differences in the flux approximation quality of the MPFA-O method depending on the face co-normal  $\mathbf{d}_{K_\Omega, \sigma} = K \mathbf{n}_{K_\Omega, \sigma}$ . Additionally, for different well angles the number and size of intersections  $K_\Omega \cap \Lambda$  can have an influence on the discrete error.

#### 8.4.4 Comparison with a Peaceman-type well model

The Peaceman model has been introduced in Chapter 5, as well as its generalization to slanted wells with arbitrary orientation due to Alvestad et al. (1994) (subsequently referred to as  $\text{PM}$  well model). In Section 5.4, we describe the limitations of the  $\text{PM}$  well model. The herein presented model has none of the mentioned limitations. In particular, the presented model is valid for arbitrary positive definite and symmetric permeability tensors, unstructured grids, and is independent of the discretization scheme. Moreover, the presented model is consistent with grid refinement, and we show grid convergence in the numerical experiments in Section 8.4.1. However, the Peaceman-type models are cell-local, thus computationally cheaper and easier to implement.

The limitations of the Peaceman well models make it difficult to fairly compare it with our new model. For cases for which all assumptions of Peaceman are valid, our numerical studies (not shown here) suggest that the Peaceman well model is generally superior to the presented model with distributed sources. This is because it takes the analytical solution as well as the spatial discretization method into account. For cases where some assumptions are violated, for example off-center wells or slanted wells, it is difficult to construct cases where the analytical solution is readily constructed but does not feature a singularity on the boundary. Our preliminary numerical studies for such cases (for example the slanted well case in Section 8.4.1 without rotation of the permeability tensor) show large deviations ( $> 10\%$  error in total source term) from the analytical solution for the  $\text{PM}$  well model. However, these errors may be distorted by errors made in the discrete approximation of the singular boundary condition, where the well intersects the boundary. Finally, for the general case of unstructured grids, simplex grids, and full permeability tensors it is unclear how to apply the original Peaceman model. However, we know that the presented method is consistent (at least for a single straight well), and thus, the numerical solution converges to the exact solution with grid refinement. Therefore, we expect that the numerical solution on a very fine grid using the distributed source model is a reasonable reference solution.

We compare our model to the  $\text{PM}$  well model in a numerical experiment. The computational domain  $\Omega = [-50, 50] \times [-100, 100] \times [0, 100]$  m<sup>3</sup> contains a slanted straight well  $\Lambda$  with end points at  $\mathbf{x}_{\Lambda,1} = [-20, -50, 25]^T$  m,  $\mathbf{x}_{\Lambda,2} = [20, 50, 75]^T$  m. The permeability tensor is a diagonal tensor  $K(\gamma_1, \gamma_2)$ , with  $\gamma_1 = 0^\circ, \gamma_2 = 90^\circ, \alpha = 0.1$ . The structured cube grid  $\Omega_b$  is successively, uniformly refined starting with  $10 \times 20 \times 10$  cells ( $h_{\max} \approx 17.32$  m). The well radius is  $r_\omega = 0.1$  m ( $\Delta x/r_\omega = 200$  for the coarsest grid). The kernel support

region (chosen as  $\varrho_o/r_\omega = 100$ ) only extends over few cells in the coarsest grid, so that the regularization effect is minimized. On the boundary  $\partial\Omega$ , we specify Neumann no-flow boundary conditions, that is  $(K\nabla p) \cdot \mathbf{n} = 0$ , except for the planes perpendicular to the  $x_1$ -axis, where the Dirichlet boundary condition  $p_D(x_2 = -100) = 1 \cdot 10^5$  Pa,  $p_D(x_2 = 100) = 3 \cdot 10^5$  Pa are enforced. The reference solution is computed with  $160 \times 320 \times 160$  cells ( $h_{\max} \approx 1.08$  m). The computational domain with pressure iso-surfaces of the reference solution are shown in Fig. 8.8. In Fig. 8.9, the relative integral source error

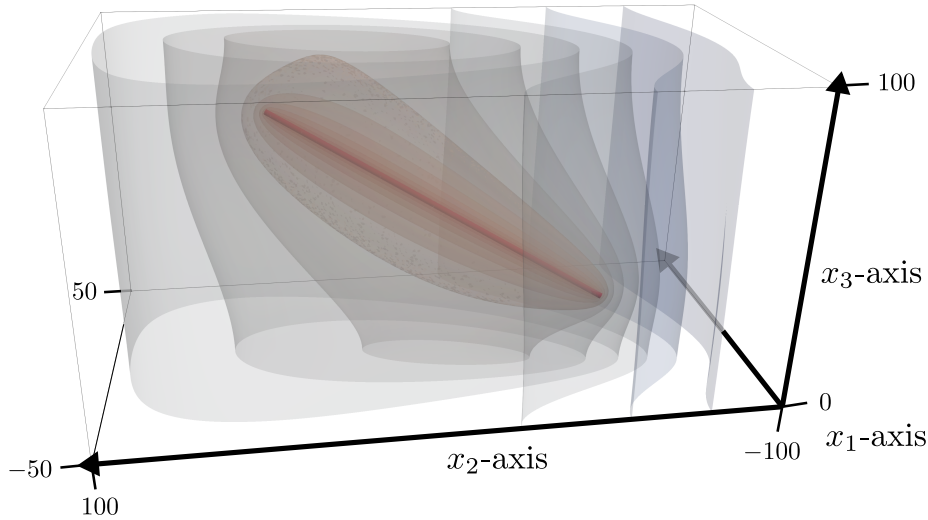


**Figure 8.8 – Reference solution – comparison with Peaceman-type well model.** The well is visualized with a 10-fold increased radius. A selection of pressure iso-surfaces of the reference solution are shown with reduced opacity. The domain extent is given in units of m. Reprinted with permission from Koch et al. (2020c), © 2020 Elsevier Inc.

$$E_Q = \frac{|Q - Q_{\text{ref}}|}{|Q_{\text{ref}}|}, \quad Q = \sum_{K_\Omega \in \Omega_b} Q_{K_\Omega}, \quad (8.31)$$

with respect to the reference solution  $Q_{\text{ref}}$  is shown for grids with different refinement. In a variant of the distributed source model (DS), the extent of the kernel support is adapted to the grid size. This is to keep the regularization effect of the kernel function minimal in order to get, in addition to a good approximation of the source term, a better approximation of the pressure solution close to the well. For  $\varrho_o/r_\omega = 100$ , the extent of the kernel ellipse  $E_{\Phi,x}$  is given by its major and minor axes, 16.12 m and 12.54 m. For the reference solution this extent is kept constant with grid refinement. While this ensures a very good approximation of the source term, the pressure solution is regularized in a larger neighborhood of the well. In the variant, the kernel support is adapted proportional to  $h_{\max}$ , so that for the finest grid

shown in Fig. 8.9 ( $80 \times 160 \times 80$  cells,  $h_{\max} \approx 2.17$  m), the  $E_{\Phi,x}$  major and minor axes measure 2.01 m and 1.57 m. It is evident that the numerical solution for the distributed source model

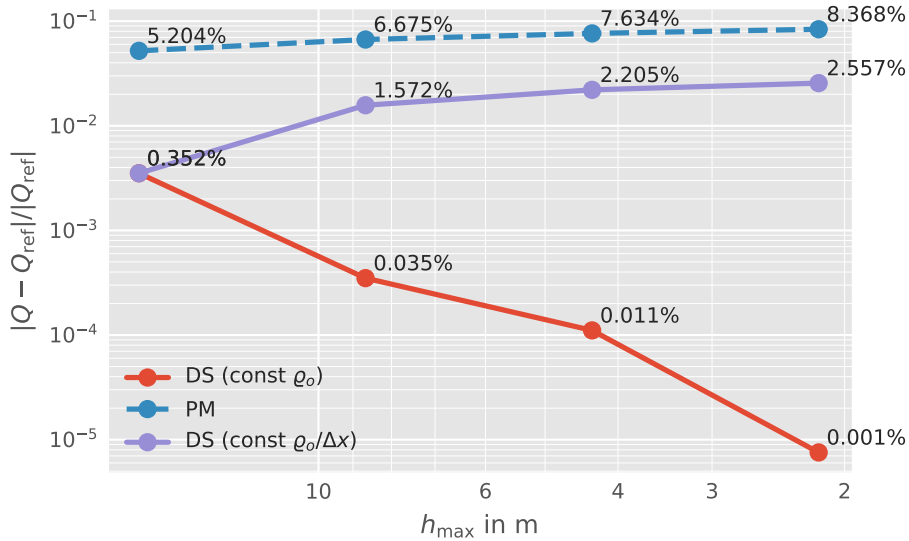


**Figure 8.9 – Differences between PM and DS model.** Comparison of the relative integral source error between a Peaceman-type model (PM) and the new model (DS) for various grid refinements. The error is computed with respect to a reference solution  $Q_{\text{ref}}$ . Both axes are logarithmic. Reprinted with permission from Koch et al. (2020c), © 2020 Elsevier Inc.

converges to the reference solution. More importantly, the relative error is small ( $< 0.5\%$ ) even for the coarsest grid. In comparison, the difference to the Peaceman-type model is large ( $> 5\%$ ). In particular, the error grows with grid refinement (to  $> 8\%$ ), signifying that the generalization of Peaceman's model to arbitrarily-oriented wells is not consistent. The result is comparable with the observations in (Aavatsmark and Klausen, 2003, Table 2), where Alvestad's well indices are compared to a new numerically computed well index, and it is shown that the difference between those two well indices grow, the higher the  $r_w/\Delta x$  ratio. In the variant of the DS model, the error in the source term with respect to the reference solution also grows with larger  $r_w/\Delta x$  ratio. However, the error is consistently smaller (by a factor  $> 3$ ) than for the PM well model. Figure 8.10 shows the numerical pressure solutions along the  $x_1$  and the  $x_2$ -axis, for the reference grid resolution. It can be clearly seen that for the reference solution (DS) the pressure solution is regularized. For the variant of DS, the regularization is minimized, however in the far field the solution matches the reference solution better than the PM well model, which is due to the better approximation of the source term (see Fig. 8.9). We also note that the regularized solution leads to an altered

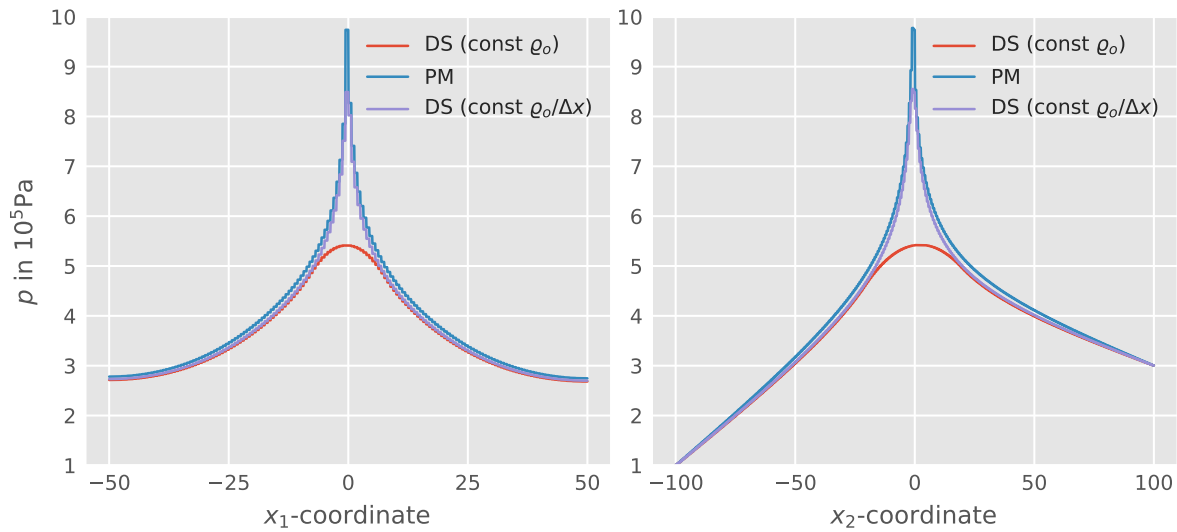


**Figure 8.10 – Numerical pressure solutions.** Plotted along the  $x_1$  and the  $x_2$ -axis for a Peaceman-type model (PM) and the new model (DS) for a grid resolution of  $160 \times 320 \times 160$  cells. Reprinted with permission from Koch et al. (2020c), © 2020 Elsevier Inc.

solution in the near-field of the well but to a better approximation of the source term and thus the far field pressure (outside the kernel support), whereas the poor approximation of the source term in the PM method leads to a globally poor pressure solution.

## 8.5 Summary

A new well model was presented for which the mass exchange between a well and an embedding porous medium is modeled with a source term spatially distributed by a local kernel function. In the spirit of well-index-based well models the source term for a well with given bottom hole pressure is computed based on the numerical pressure in cells intersecting the well. However, the presented derivation of the new model is independent of the discretization method and the type of computational grid. The new model was shown to be consistent in a numerical experiment and exhibited grid convergence with the expected rates. In the same experiment it is shown that the absolute error with respect to an analytical solution is relatively small, even for coarse computational grids and small kernel support. It was shown, that the error in the source term can be decreased by increasing the region over which the source term is distributed. However, coincidentally, the pressure

profile close to the well (inside the kernel support) becomes increasingly regularized. A comparison with a Peaceman-type well model generalized for arbitrarily oriented wells, suggested that even if the region is chosen to be very small (only covering the neighboring cells of cells with well intersection), thus minimizing the regularization effect, the source term can be approximated with good accuracy ( $< 2\%$  error with respect to a reference solution), whereas the Peaceman-type well model for the same case showed larger differences ( $> 8\%$ ) which also had a negative global effect on the pressure solution. The example showed that the new model gives the choice between a more accurate representation of the near-well pressure and a more accurate representation of the source term. Additionally, it was shown that if the source term is accurately approximated, the far-field pressure (outside kernel support) is equally well-approximated while the regularization of the pressure profile only happens locally in the well neighborhood. On the other hand, a bad approximation of the source term leads to global errors in the pressure profile. Finally, the new model was shown to be robust with respect to well rotation, as well as robust with respect to rotations of the anisotropic permeability tensor.

In this work, the well model derivation is restricted to one-phase flow and possible modifications for multi-phase flow are yet to be explored. An extension of the well model for wells with casing is easily conceivable, combining the findings with the derivations presented in Chapter 7. Moreover, the herein presented cases considered a given constant bottom hole pressure. However, the presented model may be extended to the coupled 1D-3D case where the well pressure solves an additional one-dimensional partial differential equation in the well domain. Finally, using the superposition principle, which equally applies for the case of anisotropic permeabilities, the presented well model is also expected to provide good approximations when multiple wells are present in the domain.

The code to reproduce the simulations in this chapter can be found at <https://git.iws.uni-stuttgart.de/dumux-pub/Koch2019c>.



# 9 A multi-scale sub-voxel perfusion model for perfusion MRI\*

This chapter presents an embedded mixed-dimension sub-voxel perfusion model to estimate diffusive capillary wall conductivity in multiple sclerosis lesions from perfusion MRI data.

Multiple sclerosis (MS) is characterized by a cascade of inflammatory reactions that result in the formation of acute demyelinating lesions (MS plaques). Acute lesions are associated with an impaired blood-brain barrier (BBB) (Kermode et al., 1990). In healthy brain tissue, the tight junctions between endothelial cells forming the blood vessel walls, are an efficient barrier for most molecules in the brain capillaries. In active MS lesions tight junctions have been found to be damaged or open (Plumb et al., 2002). Due to an auto-immune reaction, immunological cells can pass the BBB and attack the myelin sheath covering the electrical pulse conducting axons, leading to dysfunctions of the central nervous system (Minagar and Alexander, 2003). Magnetic resonance (MR) enhancement, using contrast agents such as Gadolinium-based molecules, corresponds to areas of inflammation and contrast agent leakage into the extra-vascular space. Furthermore, it is related to the histologic age of the plaques (Absinta et al., 2015). Advanced imaging techniques, such as perfusion MR imaging (perfusion MRI), aim at the characterization of the temporal evolution of enhancing lesion formation in relapsing-remitting MS (Verma et al., 2017). Perfusion MRI is sensitive to inflammatory activity and can depict active lesions previous to Gadolinium enhancement and even after its disappearance (Wuerfel et al., 2004). Furthermore, it has been shown that perfusion in lesions is highly dynamic and related to the activity and temporal evolution of the lesions (Ge et al., 2005; Ingrisich et al., 2012). Cross-sectional studies in normal appearing white matter (NAWM) have also demonstrated abnormal perfusion behavior in patients with MS compared with healthy controls (for review, see Lapointe et al. (2018)). To examine MS lesions in-vivo, magnetic resonance (MR) contrast enhancing agents, typically Gadolinium-based molecules, can be administered to patients. While the contrast agent cannot pass the capillary wall in normal brain tissue, it leaks into the extra-vascular, extra-cellular space in MS lesions with impaired BBB, altering the tissue's magnetic response (Forslin et al., 2017).

---

\*This chapter is based on Koch, Flemisch, Helmig, Wiest, and Obrist (2020a).

This effect is used to characterize lesions in a perfusion MR sequence known as dynamic susceptibility contrast MRI (DSC-MRI) (Verma et al., 2013, 2017).

Dynamic susceptibility contrast MRI (DSC-MRI) has proven to be informative when assessing the integrity of the BBB (Calamante, 2010; Shiroishi et al., 2015). In a typical DSC-MRI study, contrast agent is administered intravenously (bolus injection) and whole brain MR image sequences are recorded with a repetition time of about two seconds over a few minutes (Shiroishi et al., 2015). Normal appearing white matter is distinguished from inflammatory plaques by image contrast and differences in intensity-time curves. Using adequate post-processing techniques, qualitative assessment of leakage coefficients allows identifying contrast-enhancing lesions in an automated way (Boxerman et al., 2006). Although today, perfusion MRI is not considered a standard procedure in the neuro-imaging workup of MS, it enables a classification of lesions according to parenchymal leakage of an MR contrast agent due to differences in perfusion behavior (Verma et al., 2013). Perfusion imaging, both DSC and dynamic contrast enhanced (DCE), may provide information about the leakiness of the tissue under investigation. In this work, we investigate DSC-MRI. However, the extension of the method to DCE-MRI is conceivable.

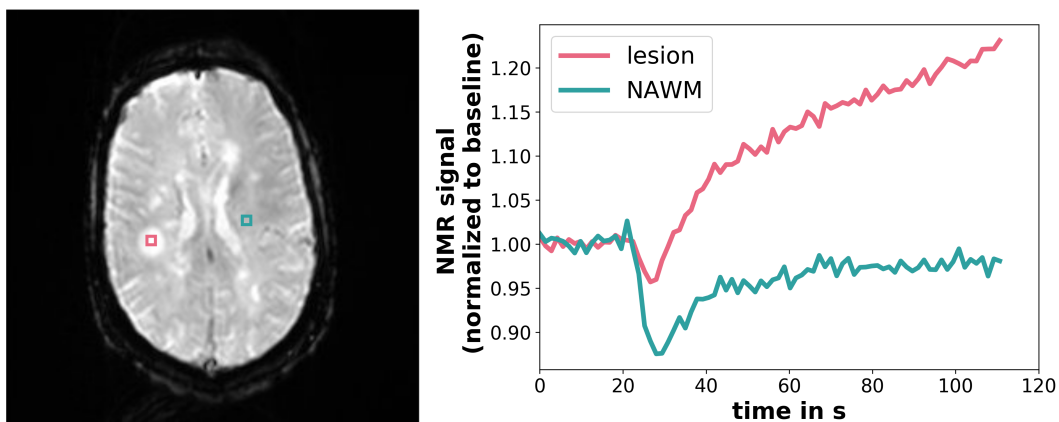


**Figure 9.1 – Signal intensity-time curves for lesion and NAWM tissue.** Lesion tissue (red) and NAWM tissue curves (blue) and the respective sampling locations in the brain. Signal values are normalized to pre-contrast signal. Data obtained by gradient echo - echo planar imaging (GRE-EPI), at magnetic field strength 3 T, repetition time  $T_R = 1400$  ms, echo time  $T_E = 29$  ms, flip angle  $\alpha = 90^\circ$ , voxel size  $1.8 \times 1.8 \times 5$  mm, and an image resolution of  $256 \times 256$  pixels per slice. Reprinted from Koch et al. (2020a).

For the interpretation of images obtained in a DSC-MRI study, the gray scale image sequence is post-processed to provide indicators within regions of interest to the radiologist. Two typical signal intensity-time curves from the brain white matter, with the characteristic first

---

pass signal dip, are shown in Fig. 9.1. Mathematical models (forward model) for contrast agent perfusion in the brain tissue can help to understand the underlying reasons for a particular intensity-time curve of a voxel, by identifying and analyzing the model parameters which are able to reproduce the MRI data. This process is also known as solving the inverse problem. To this end, the model parameters are tuned by using parameter estimation techniques. Forward models are typically based on a two-compartment pharmacokinetic tracer model and are parameterized by a small number of parameters (Sourbron and Buckley, 2013, 2012; Heye et al., 2016) and simple ordinary differential balance equations. A routinely used state-of-the-art post-processing procedure and model is described by Boxerman et al. (2006). Such models have to reflect two processes: (1) the perfusion process governed mainly by bio-fluid-mechanical principles, and (2) the physical process of nuclear magnetic resonance (NMR) exploited to acquire the MR image. There have been many suggestions for improving the modeling of the latter process (Kiselev, 2001; Pathak et al., 2008; Quarles et al., 2009; Semmineh et al., 2014). Kiselev and Novikov (2002); Kiselev (2005) show that the local, sub-voxel tissue structure has a significant effect on the NMR signal. However, all previous studies, including the recent study by Semmineh et al. (2014), rely on state-of-the-art two-compartment models for the perfusion process providing only average concentrations in two tissue compartments within a voxel.

To overcome the limitations of two-compartment models, we present a perfusion model on a sub-voxel scale, including the capillary network structure. Fully, three-dimensionally resolved fluid-mechanical models of brain tissue perfusion imply prohibitively complex and computationally expensive simulations due to the large number of vessels, their non-trivial geometrical embedding, and the complex geometry of the extra-vascular, extra-cellular space (Syková and Nicholson, 2008). To reduce complexity, we use a mixed-dimension embedded model description.

The fluid-mechanical model is coupled to an NMR signal model. We propose that the local distribution of the contrast agent and resulting local susceptibility effects obtained by a sub-voxel scale model may better explain the NMR signal response of the tissue. The application of this new perfusion model is demonstrated for the example of MS lesions.

In the following, we refer to the sub-voxel spatial scale, ranging from a few micrometers to several hundreds of micrometers, as *meso-scale*. We call the scale below the meso-scale, which includes the molecular scale, *micro-scale*, and refer to the scale above as *macro-scale*.

## 9.1 Flow and transport model and model parameters

We use the flow and transport model described in Chapter 3, in particular Eqs. (3.22) and (3.23). We assume constant density and viscosity,  $\rho_1 = 1030 \text{ kg m}^{-3}$ ,  $\mu_1 = 1.32 \text{ Pa s}$ , given that contrast agent concentrations in the extra-vascular compartment are even smaller than in the blood stream, and we consider perfusion an isothermal process. Furthermore, we choose an isotropic intrinsic permeability  $k = 8.3 \cdot 10^{-18} \text{ m}^2$  (Baxter and Jain, 1989) for the extra-vascular compartment. We consider the Gadolinium-based contrast agent Gadobutrol. It is assumed that Gadobutrol will not enter cells, and its effective diffusion coefficient in the extra-vascular domain is  $D_e \approx 1.5 \cdot 10^{-11} \text{ m}^2 \text{ s}^{-1}$ , cf. Eqs. (2.7) and (3.12).

In a perfusion MRI (magnetic resonance imaging) sequence, Gadobutrol is administered intravenously in solution, typically with a concentration of  $1 \text{ mol l}^{-1}$ . Gadobutrol has the chemical formula  $\text{C}_{18}\text{H}_{31}\text{GdN}_4\text{O}_9$ , corresponding to a molar mass of  $M^c = 604.715 \text{ g mol}^{-1}$  (PubChem, 2018). In high concentrations, Gadobutrol has a significant influence on fluid density and viscosity. However, the concentrations arriving in the brain tissue sample are strongly diluted by diffusion and dispersion along the tortuous path through the vascular network, so that the influence on blood density and viscosity can be neglected in this work.

The vascular model is based on a small network of capillaries from the superficial cortex of the rat (Motti et al., 1986; Secomb et al., 2000), which we consider a sufficient approximation of the actual capillary network geometry for type of model analysis presented in this work. The network has the dimensions  $150 \mu\text{m} \times 160 \mu\text{m} \times 140 \mu\text{m}$ , and is shown in Fig. 7.13 (the network used here is slightly smaller because it does not use artificial vessel extensions). The location of inflow and outflow boundaries are given in this data set. For the inflow boundaries, Secomb et al. (2000) provide velocity estimates based on the vessel radius, which are applied as Neumann boundary conditions. The inflow velocities range from  $0.5$  to  $3.5 \text{ mm s}^{-1}$ , depending on the vessel radius. At the outflow boundaries, we enforce Dirichlet boundary conditions for the pressure,  $p_{v,\text{out}} = 1.025 \cdot 10^5 \text{ Pa}$ . The vessel radii are constant for each segment defined in the grid but vary from segment to segment.

The domain initially contains no contrast agent. During the perfusion MR study,  $10 \text{ ml}$  contrast agent ( $0.1 \text{ mmol}$  per  $\text{kg}$  body weight) is administered intravenously as a solution at  $5 \text{ ml s}^{-1}$  and a concentration of  $1 \text{ mol l}^{-1}$ . The injected fluid thus forms a sharp bolus. However, the bolus disperses significantly before it reaches the brain capillaries. Therefore,

the concentration inflow profile to the capillary network has to be estimated from the parameters of the bolus injection. To this end, we use an ansatz from Quarles et al. (2009)

$$c_{v,\text{in}}(t) = at_p^{-2}t e^{-t/t_p} + b(1 - e^{-t/t_p}), \quad (9.1)$$

which describes a concentration profile starting at  $c_{v,\text{in}}(0) = 0 \text{ mol m}^{-3}$  and approaching an equilibrium concentration  $b$  ( $\text{mol m}^{-3}$ , contrast agent is equally distributed in the whole body blood volume), with a single peak after the arrival of the bolus. The parameters  $a$  ( $\text{mol s m}^{-3}$ ) and  $t_p$  (s) are shape parameters of the capillary input function, and can be interpreted as the scaling parameter for the area under the curve, and the time to peak, respectively, in the absence of re-circulation ( $b = 0$ ). The parameter values are patient-specific and also depend on the location in the brain. Values for  $a$ ,  $b$ , and  $t_p$  are discussed below, in the context of parameter estimation.

At the inflow boundary, contrast agent influx is enforced by a Neumann boundary condition. At the outflow boundary, the normal mole fraction gradient is set to zero and the advective component flux is computed by a first-order upwind scheme. For the extra-cellular compartment, we enforce symmetry boundary conditions everywhere, assuming that the modeled domain is surrounded by domains with similar properties.

Our fluid model stands in contrast to the often employed two-compartment kinetic modeling approaches, because it resolves meso-scale flow phenomena. Furthermore, it is based on parameters with a clear physical interpretation.

## 9.2 NMR signal model

A model linking concentration fields with the NMR signal response is required to connect the results of the fluid mechanical model to clinical MRI data. To this end, we develop a model of NMR on the meso-scale. In the following, we describe a gradient echo, echo planar sequence (GRE-EPI) commonly used in DSC-MRI. This fast imaging technique allows acquisition of an entire brain image stack in less than two seconds. Thus, after the injection of a contrast agent, a time series of such images can be acquired, where the characteristic signal-time curve for every voxel is dependent on the evolution of the contrast agent concentration distribution on the meso-scale.

During MRI acquisition, the brain tissue is exposed to a strong magnetic field,  $\mathbf{B}_0$ , that induces oriented magnetic dipole moments of the hydrogen nuclei in the tissue. The magnetic moments originate from the hydrogen nuclei spin. The magnetization can be viewed as a vector field,  $\mathbf{M}$ , describing the magnetic moment per unit volume. The GRE-EPI sequence starts with a radio frequency (RF) pulse, which reorients the magnetic moments in the tissue sample, with the flip angle  $\alpha$  to the main magnetic field  $\mathbf{B}_0$ . The RF pulse causes the magnetic moments to precess, rotating around the axis aligned with  $\mathbf{B}_0$ , with the Larmor frequency of the hydrogen nuclei. The Larmor frequency is a function of the magnetic field magnitude and the gyromagnetic ratio of the hydrogen nuclei,  $\omega = -\gamma|\mathbf{B}|$ . Energy dissipation relaxes the magnetization into the initial state aligned with  $\mathbf{B}_0$ , eventually.

This relaxation process can be split into two processes, longitudinal and transversal relaxation. Longitudinal or  $T_1$  relaxation, describes how the magnetization recovers its component in direction of  $\mathbf{B}_0$ . It can be described by

$$\mathbf{M}_z = \mathbf{M}_{z0}(1 - e^{-t/T_1}), \quad (9.2)$$

where the subscript  $z$  denotes the projection of  $\mathbf{M}$  in the direction of  $\mathbf{B}_0$ . The material constant  $T_1$ , determines the time scale of the longitudinal relaxation. Transversal or  $T_2^*$  relaxation, describes the decay of the transversal magnetization component  $\mathbf{M}_{xy}$ , i.e. the projection of the net magnetization vector into the plane perpendicular to  $\mathbf{B}_0$ . The decay is a result of dephasing. Every precessing dipole also induces small magnetic fields that affect the precession frequencies of other dipoles. Thus, the magnetic moments dephase, decreasing the net transversal magnetization. This effect is known as  $T_2$  relaxation (without asterisk). Furthermore, local static inhomogeneities of the magnetic field  $\mathbf{B}_0$  within a tissue voxel cause dephasing as well. Gadolinium-based contrast agents are para-magnetic substances that additionally cause local magnetic fields accelerating the dephasing process, leading to a shortening of  $T_2^*$ . The sinusoidal evolution of the  $\mathbf{M}_{xy}$  magnetization, also called free induction decay, induces a current in the MR coils and is effectively what is detected as MR signal. The amplitude of  $\mathbf{M}_{xy}$  for a voxel right after the RF pulse can be described by

$$\mathbf{M}_{xy} = \mathbf{M}_{xy0} e^{-t/T_2^*}. \quad (9.3)$$

The time constant of the decay,  $T_2^*$ , includes all aforementioned effects. Eqs. (9.2) and (9.3) are a simplified solution of the Bloch equations (Bloch, 1946) for the signal evolution following the RF pulse, neglecting the effect of slice selection, phase and frequency encoding

gradients in the GRE-EPI sequence. According to Quarles et al. (2009), the GRE-EPI voxel signal during a DSC-MRI perfusion sequence can be modeled as

$$S(t) = \frac{S_0 \left(1 - e^{-T_R/T_1(c(x,t))}\right) e^{-T_E/T_2^*(c(x,t))} \cdot \sin(\alpha)}{1 - e^{-T_R/T_1(c(x,t))} \cdot \cos(\alpha)}, \quad (9.4)$$

where the repetition time  $T_R$ , is the time between two RF pulses, and the effective echo time,  $T_E$ , is the time between RF pulse and signal readout. The base signal  $S_0 > 0$  depends, i.a., on tissue proton density and the MR scanner hardware. In the following, we look only at the normalized signal  $S_n(t) = S(t)S_{\text{pre}}^{-1}$ , where  $S_{\text{pre}}$  is the signal before the contrast agent bolus arrives in the tissue sample. The pre-contrast signal,  $S_{\text{pre}}$ , contains all constant factors in Eq. (9.4), including  $S_0$ . It follows from Eq. (9.4) that a shortening of  $T_2^*$  results in a decrease of NMR signal strength, while a shortening of  $T_1$  results in signal enhancement.

The following two sections introduce the models for the relaxation rates  $R_1(c_v, c_t) = T_1^{-1}(c_v, c_t)$  and  $R_2^*(c_v, c_t) = T_2^{*-1}(c_v, c_t)$ , which are both functions of the contrast agent concentrations  $c_v$  and  $c_t$  computed by the fluid-mechanical model. Semmineh et al. (2014) developed a model including an artificial microstructure using a combination of a finite perturbator method (Pathak et al., 2008) and a finite-difference solution of the Bloch-Torrey equations. However, their model is coupled to a two-compartment tracer perfusion model, only providing voxel-averaged concentrations. In contrast, the presented perfusion model computes the sub-voxel distribution of the contrast agent concentration. We follow Quarles et al. (2009), to develop a model considering the spatial and temporal distribution of the contrast agent.

**Transversal relaxation** The transversal relaxation rate,  $R_2^*$ , depends on the complex local microstructure of the tissue (Kiselev and Novikov, 2002) and is altered by the presence of the contrast agent. We are only interested in the signal change relative to the baseline. Hence, the relaxation rate can be split in a static pre-contrast contribution,  $R_{2,\text{pre}}^*$ , and a time-dependent contribution depending on the contrast agent concentration. The pre-contrast transversal relaxation rate  $R_{2,\text{pre}}^*$  can be measured with dedicated MR sequences. However, for the data set used in this work, such measurements are unavailable, so that  $R_{2,\text{pre}}^*$  has to be estimated from literature values or inferred from available data.

In general, the relaxation rate for a sub-voxel control volume is described by contributions of three compartments, the vascular compartment (v), the extra-cellular, extra-vascular

space (t), and the cellular compartment (s), weighted by their volume fractions,  $\phi_v$ ,  $\phi_t$ ,  $\phi_s$  (Quarles et al., 2009),

$$R_2^* = \phi_v R_{2,v}^* + \phi_t R_{2,t}^* + \phi_s R_{2,s}^*. \quad (9.5)$$

According to Kiselev (2005), the rate in each compartment  $\beta \in \{v, t, s\}$ , comprises contributions on three spatial scales

$$R_{2,\beta}^* = R_{2,\beta,\text{micro}}^* + R_{2,\beta,\text{meso}}^* + R_{2,\beta,\text{macro}}^*. \quad (9.6)$$

The rate  $R_{2,\beta,\text{macro}}^*$  describes effects of static local inhomogeneities of the magnetic field  $B_0$ , which are time-independent. Since the static effects do not depend on the contrast agent concentration, they are included in the pre-contrast relaxation rate,  $R_{2,\text{pre}}^*$ . The rate  $R_{2,\beta,\text{micro}}^*$  depends on the local chemical composition. The effects are independent of the pulse sequence. Gadolinium-based contrast agent molecules increase the relaxation rate, which can be described by a linear relationship (Kiselev, 2005),

$$R_{2,\beta,\text{micro}}^* = r_2 c_\beta + R_{2,\beta,\text{pre,micro}}^*, \quad (9.7)$$

where  $r_2$  is the molar relaxivity, and  $c_\beta$  the local molar contrast agent concentration in compartment  $\beta$ . The molar  $T_2$  relaxivity,  $r_2$ , of Gadobutrol at 3 T and 37 °C is approximately  $3.9 \text{ m}^3 \text{ mol}^{-1} \text{ s}$  (Rohrer et al., 2005). Here, we assume that the contrast agent cannot enter the cells,  $c_s = 0$ , hence  $R_{2,s,\text{micro}}^* = 0$ . The term  $R_{2,\beta,\text{meso}}^*$  stems from a meso-scale effect. The magnetic field perturbations induced by the difference in magnetic susceptibility in the blood vessel and the extra-vascular space, increase the relaxation rate of the extra-vascular space in proximity of a blood vessel. The generated magnetic field perturbations are several orders of magnitude smaller than  $B_0$ . Furthermore, the influence decays rapidly with distance to the vessel surface. Therefore, we consider each segment of the vessel network to cause a perturbation independent of the other segments. The increase in  $R_2^*$  for a given tissue sample caused by mesoscopic magnetic field perturbation will then be the superposition of all  $n$  segment perturbations

$$R_{2,t,\text{meso}}^* = \kappa_B \sum_{i=0}^n \varphi_i |\tilde{c}_v - \tilde{c}_t|_i, \quad (9.8)$$



where  $|\tilde{c}_v - \tilde{c}_t|$  is the difference of the average vessel surface concentrations, given by the average over the entire vessel surface contained in this sample. The factor  $\kappa_B \geq 0$  is an ad-hoc parameter, scaling the strength of these perturbations. The proportionality factor  $\varphi_i$  models the decay of the influence of the with distance from the vessel wall. We set  $\varphi_i = r_v^2/r^2$ , assuming a quadratic decay, where  $r$  is the distance to the vessel center line and  $r_v$  the radius of the vessel segment. The susceptibility contrast likewise increases the transversal relaxation rate, which we model by

$$R_{2,v,\text{meso}}^* = \kappa_B |\tilde{c}_v - \tilde{c}_t|. \quad (9.9)$$

The same effect occurs at the cell surfaces, induced by the difference in magnetic susceptibility between interstitial space and cells. Note that we consider cells not to be invaded by contrast agent. We include this effect by adding a term to Eq. (9.8),

$$R_{2,t,\text{meso}}^* = \kappa_B \sum_{i=0}^n \varphi_i |\tilde{c}_v - \tilde{c}_t|_i + \kappa_T |\tilde{c}_{t,s}|, \quad (9.10)$$

and to the relaxation rate of the cell compartment,

$$R_{2,s,\text{meso}}^* = \kappa_T |\tilde{c}_{t,s}|, \quad (9.11)$$

where  $\kappa_T \geq 0$  is a second ad-hoc parameter, determining the strength of these perturbations, and  $\tilde{c}_{t,s}$  is the average molar concentration on all cell surfaces contained in a tissue sample. Furthermore, we assume that there is no direct interface between the cells and the vascular compartment. Combining Eqs. (9.5), (9.7) and (9.9) to (9.11), we obtain a formulation for the transversal relaxation rate dependent on the concentration fields and the volume fractions of the three compartments:

$$\begin{aligned} R_2^* = & R_{2,\text{pre}}^* + r_2(\phi_v c_v + \phi_t c_t) + \phi_v(\kappa_B |\tilde{c}_v - \tilde{c}_t|) \\ & + \phi_t(\kappa_B \sum_{i=0}^n \varphi_i |\tilde{c}_v - \tilde{c}_t|_i + \kappa_T |\tilde{c}_{t,s}|) \\ & + \phi_s(\kappa_T |\tilde{c}_{t,s}|). \end{aligned} \quad (9.12)$$

**Longitudinal relaxation** Similar to  $T_2^*$ , the contrast agent also shortens  $T_1$ . However, the effects occur merely on the micro-scale. Thus, we can model the relaxation rate  $R_1 = 1/T_1$

of the tissue sample by

$$R_1 = r_1(\phi_v c_v + \phi_t c_t) + R_{1,\text{pre}}, \quad (9.13)$$

where we implicitly assumed that contrast agent does not enter cells,  $c_s(\mathbf{x}, t) = 0$ . The molar  $T_1$  relaxivity,  $r_1$ , of Gadobutrol at 3 T and 37 °C is approximately  $3.2 \text{ m}^3 \text{ mol}^{-1} \text{ s}$  (Rohrer et al., 2005). The pre-contrast longitudinal relaxation rate  $R_{1,\text{pre}}$  can be measured. However, for the given data set in this work such measurements are unavailable, so that  $R_{1,\text{pre}}$  has to be estimated from literature values or inferred from available data.

**Voxel signal** The relaxation rates,  $R_2^*$  and  $R_1$ , Eqs. (9.12) and (9.13), are computed for each control volume (cell) in the three-dimensional domain  $\Omega$ . The volume fraction of the vascular domain,  $\phi_v$ , is computed by integrating over the volume of all vessels within a control volume and dividing this number by the volume of the control volume. The average values  $\tilde{c}_{t,s}$  and  $\tilde{c}_t$  are approximated by the discrete cell values. The average  $\tilde{c}_v$  is computed by intersecting the vessel center-line mesh with the mesh discretizing  $\Omega$  and attributing the surface of the intersecting vessels to the intersected control volume. A local NMR signal can then be computed for each control volume by using Eq. (9.4). The voxel signal is determined by the volume average of all control volume signals. To this end, we assume that the size of our domain is large enough to be representative for an entire voxel, which is commonly about 10 to 20 times larger in diameter than the given domain.

### 9.3 Numerical treatment

The equations of the fluid flow equation system (Eq. (3.22)), and the contrast agent transport system (Eq. (3.23)), are discretized with a cell-centered finite volume method with a two-point flux approximation in space, and an implicit Euler method in time. The two systems are only coupled in one direction, such that Eq. (3.23) depends on the pressure field computed in Eq. (3.22), but Eq. (3.22) can be solved independently of Eq. (3.23). Furthermore, Eq. (3.22) is stationary, so that the pressure field only has to be computed once per perfusion experiment. The linear equation systems resulting from the discretization of Eqs. (3.22) and (3.23) are solved as described in Chapter 11. We assume that the influence of the sub-voxel contrast agent evolution during a single image acquisition on the NMR signal is

negligible, and thus, Eq. (9.4) is solved as a post-processing step after each time step of the perfusion model.

The model converges in time and space to a reference solution computed on a very fine grid and a very small time step size. The convergence study is described in detail in Appendix A.11. As a result of the convergence study, we choose our computational grids such that the largest grid cell does not exceed  $8\ \mu\text{m}$ . This results in a run-time of a few seconds on a normal laptop for a single forward model run. For the kernel function and the definition of the transmural exchange in Eqs. (3.22) and (3.23), we use the method of D'Angelo (2007) (see Chapter 6). The new method presented in Chapter 7 has been developed after running the simulations in this chapter. Since the simulations are very time-consuming, they have not been rerun with the new method. The choice of the numerical method is not expected to alter the results and conclusion drawn from the numerical experiments in this chapter.

## 9.4 Inverse modeling using clinical MRI data

We use clinical MRI data to evaluate the presented model. We choose a patient with relapsing-remitting MS from a clinical study with 12 MS patients, diagnosed according to the revised McDonald criteria (Polman et al., 2011), and showing at least one contrast enhancing lesion on MRI. The data is selected from a previous study that has been published elsewhere (Verma et al., 2016), and fully anonymized for further analysis. For the employed GRE-EPI protocol, 19 parallel images with a slice thickness of 5 mm are taken 80 times during an acquisition time of 119 s. The sequence parameters are given in the caption of Fig. 9.1. From these images, a clinical expert annotated a voxel within a Gadolinium enhancing MS lesion (sample L) and a corresponding voxel in NAWM (sample N). Fig. 9.1 shows the samples L and N, together with the respective voxel locations in the MRI slice.

Several model parameters can be assigned a fixed value, either because the parameter assumes a well-known fixed value given in the literature, or because the parameter is not expected to significantly affect the results of this particular study and an approximate value can be obtained from the literature. However, there are also parameters that are inherently patient-specific and cannot be directly measured, or parameters for which the measurement data is not available for the given patient. These parameters are  $a$ ,  $b$ ,  $t_p$ ,  $\kappa_B$ ,  $\kappa_T$ ,  $T_{1,\text{pre}}$ ,  $T_{2,\text{pre}}^*$ ,  $L_p$ ,  $D_\omega$ . Determining these parameters for a given signal-time curve constitutes an inverse

problem. In particular, we aim to determine  $D_\omega$ , which may quantify contrast agent leakage, and thus, has direct clinical relevance.

In the following, we briefly discuss typical values or value ranges for these parameters. The shape parameters,  $a$ ,  $b$ ,  $t_p$ , determine the inflow profile of the bolus arriving at the voxel under study. They are generally varying from voxel to voxel. In particular,  $a$  and  $t_p$  depend on the voxel location and vessel network structure, as well as the resulting bolus dilution during transport through the vessel tree. The equilibrium contrast agent concentration,  $b$ , depends on the patient's blood volume. Neglecting the filtration of contrast agent in the kidney, and contrast agent leakage, the upper bound for  $b$  is the administered amount of contrast agent divided by the total blood volume. However,  $b$ , can become lower in regions of contrast agent leakage and is dependent on the severity of the leakage and the size of the affected region in the brain. Here, we choose values for  $a$ ,  $b$ , and  $t_p$  within large enough bounds to ensure physically meaningful inflow profiles. The parameters  $\kappa_B$  and  $\kappa_T$  are dimensionless scaling factors for the effect of meso-scale  $T_2^*$ -shortening due to the magnetic susceptibility contrast at the interface of the vascular and the extra-vascular, extra-cellular compartment and the interface of the extra-vascular, extra-cellular and the cell compartment, respectively. Because these values depend on the tissue architecture,  $\kappa_B$  and  $\kappa_T$  can also mitigate errors in the NMR signal prediction caused by patient-specific variations in vessel geometry. The pre-contrast relaxation times  $T_{1,\text{pre}}$  and  $T_{2,\text{pre}}^*$  vary from voxel to voxel. From Eq. (9.4), it is clear that  $T_{2,\text{pre}}^*$  cancels when  $S(t)$  is normalized. Therefore, the value of  $T_{2,\text{pre}}^*$  is not critical for the present study. Thaler et al. (2017) measured  $T_{1,\text{pre}}$  in patients with relapsing-remitting MS for several lesion types. They reported values between 1.9 s for black holes, and 0.8 s for NAWM, at 3 T. The filtration coefficient  $L_p$  characterizes the fluid mass exchange between the vascular and the extra-vascular compartment. Baxter and Jain (1989) suggest  $L_p = 2.7 \cdot 10^{-12} \text{ mPa}^{-1} \text{ s}$  for normal subcutaneous and  $L_p = 2.1 \cdot 10^{-11} \text{ mPa}^{-1} \text{ s}$  for tumor tissue. While in normal brain tissue the contrast agent stays in the blood stream, it leaves the vascular compartment over the vessel wall in regions where the BBB is impaired. Therefore, the filtration coefficient  $L_p$  is likely to be elevated in such tissue, due to opened tight junctions. The diffusive capillary wall conductivity,  $D_\omega$ , characterizes the diffusive transport of contrast agent between the vascular and the extra-vascular compartment. It depends, i.a., on the molecular diffusion coefficient of the contrast agent, the wall thickness, porosity and the tortuosity of the transmural pathway.

### 9.4.1 Parameter estimation

In a preliminary model investigation, we use the parameter estimation toolbox PEST (Doherty, 2016) to find the parameter set that minimizes the sum of squared differences,  $\|E_{\text{opt}}\|_2^2$ , between the simulated signal-time curve and the MRI data. For the parameter estimation, we employ the truncated singular value decomposition algorithm, available in PEST. The estimated parameter values for the best fit against the curves N and L, cf. Fig. 9.1, as well as the corresponding  $\|E_{\text{opt}}\|_2$ , are given in Table 9.1.

A comparison of the simulated and measured NMR signals, Fig. 9.2, indicates that the model can reproduce the measured curves well. Table 9.1 shows that the diffusive wall conductivity,  $D_\omega$ , is estimated to be low for the NAWM sample (N), and high for the lesion sample (L), with a difference of three orders of magnitude, while the other parameters are within the same order of magnitude. To better understand the influence of the diffusive

**Table 9.1 – Best fit parameter values from global optimization algorithm.** Best fit parameter set minimizes  $\|E_{\text{opt}}\|_2$ . Second column shows parameters for the lesion sample (L). Third column lists parameters for the NAWM sample (N).

parameter	Best fit (L)	Best fit (N)
$a$	30.08 mol s m <sup>-3</sup>	30.03 mol s m <sup>-3</sup>
$b$	1.20 mol m <sup>-3</sup>	0.61 mol m <sup>-3</sup>
$t_p$	4.75 s	6.03 s
$L_p$	$7.20 \cdot 10^{-12}$ m Pa <sup>-1</sup> s <sup>-1</sup>	$1.00 \cdot 10^{-12}$ m Pa <sup>-1</sup> s <sup>-1</sup>
$D_\omega$	$8.20 \cdot 10^{-8}$ m s <sup>-1</sup>	$1.01 \cdot 10^{-10}$ m s <sup>-1</sup>
$\kappa_B$	14.19	35.59
$\kappa_T$	0.73	1.00
$T_{1,\text{pre}}$	1.76 s	2.00 s
$\ E_{\text{opt}}\ _2$	0.055	0.082

wall conductivity on the computed NMR signal, we compute the mass of contrast agent in the extra-vascular space

$$m_t^c = \int_{\Omega} \phi M^c c_t dx, \quad (9.14)$$

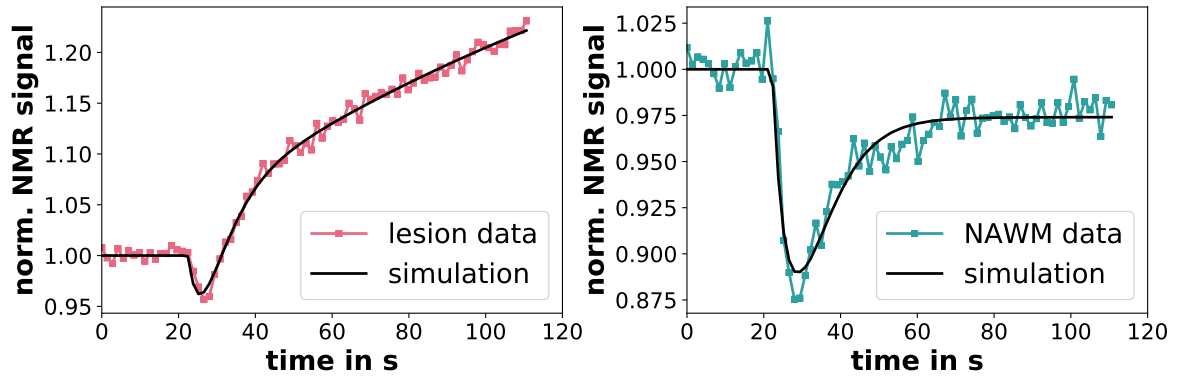


**Figure 9.2 – Simulated NMR signals compared with clinical MRI data.** Signals are normalized with pre-contrast signal. Parameters from Table 9.1. Left, result for the lesion sample (L). Right, the result for the NAWM sample (N). Reprinted from Koch et al. (2020a).

at the end of the simulation,  $t_{\text{end}} = 112$  s. Additionally, we compute the total mass of contrast agent going into the domain over the entire time of the simulation,

$$m_{\text{inj}} = \int_0^{t_{\text{end}}} \int_{\partial\Lambda_{\text{in}}} A_v v_v M^c c_v da dt. \quad (9.15)$$

The results are shown in Fig. 9.3 for different wall diffusivities. The other parameters were chosen as in Table 9.1, sample L. It can be seen that for  $D_\omega < 1.0 \cdot 10^{-9} \text{ m s}^{-1}$ , there is almost no leakage into the extra-vascular space, i.e. the BBB is intact. For  $D_\omega > 3.0 \cdot 10^{-6} \text{ m s}^{-1}$ , the leakage of contrast agent into the extra-vascular space has reached a plateau and does not increase further with  $D_\omega$ . For such high wall diffusivities, the contrast agent mole fractions in vascular and extra-vascular space reach an equilibrium. This situation would lead to a flat NMR signal (as seen, for instance, in the uppermost curve in Fig. 9.4 for  $D_\omega$ ), which is not observed in any of the clinical data. Therefore, such high values of  $D_\omega$  are unlikely to be physiologically sensible. For the values of  $D_\omega$  in Table 9.1, this means that there is little to no contrast agent leakage for sample N, while there is significant leakage for sample L. This is in accordance with the present understanding of the pathology, which assumes leaky vessel walls in MS lesions.

However, the problem of finding best fit parameters is typically ill-conditioned, or even ill-posed as the solution may be non-unique, such that the employed parameter estimation method may not be reliably applied. Therefore, we discuss other methods to further analyze the model parameters in the subsequent sections.

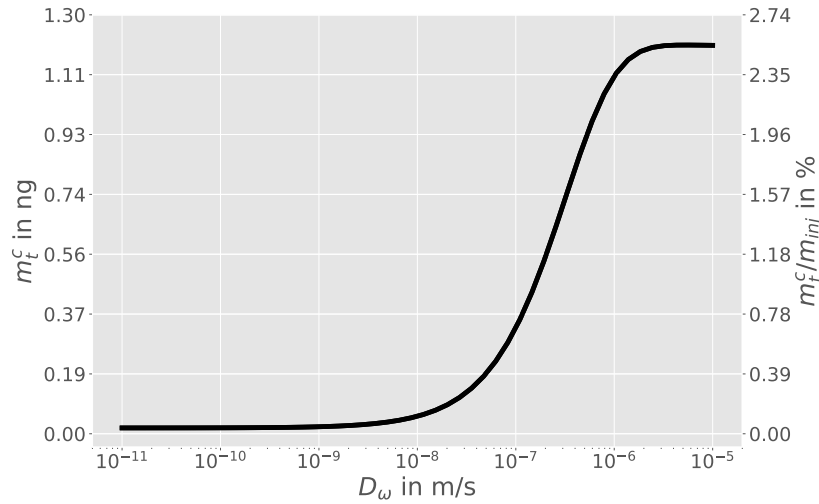


**Figure 9.3 – Contrast agent leakage for different  $D_\omega$ .** The mass of contrast agent in the extra-vascular space at  $t_{\text{end}} = 112$  s for different wall diffusivities  $D_\omega$ . Left axis shows the contrast agent mass in the extra-vascular space,  $m_t^c$ . Right axis shows the ratio of  $m_t^c$  to the total injected contrast agent mass  $m_{\text{inj}}$  in percent. Reprinted from Koch et al. (2020a).

## 9.4.2 Parameter sensitivity

For a better understanding of the influence of the patient-specific parameters on the signal-time curve, as well as the sensitivity of the model output to the model input parameters, we perform a simple sensitivity analysis, where parameters are individually varied, while all other parameters are kept constant at the values listed in Table 9.1. The results of this study are shown in Fig. 9.4 for sample L, and in Fig. 9.5 for sample N. It can be seen that the parameter sensitivity is different for L and N (which correspond to different locations in the parameter space). Such behavior is characteristic for a nonlinear model response.

**Capillary input function** The shape parameters  $a$  and  $t_p$  of the capillary input function have a strong influence on the first pass dip of the NMR signal. The influence is directly related to the  $T_2^*$ -shortening caused by the contrast agent in the blood vessels. Comparing the respective curves in Figs. 9.4 and 9.5, shows that contrast agent leakage dampens the influence of  $a$  and  $t_p$ . The difference in concentration between the vascular and extra-vascular space decreases in the presence of leakage, attenuating the  $T_2^*$ -shortening meso-scale effects. For sample L,  $a$  also influences the signal in later times in the presence of leakage. A higher  $a$  indicates a larger contrast agent bolus, which will also result in a higher amount of leakage

leading to a signal increase at later times, due to the  $T_1$ -shortening effect of the contrast agent in the extra-vascular space. In the absence of leakage (sample N), the late signal is only affected significantly by the equilibrium concentration  $b$ . For sample L,  $b$  has a significant influence on the late signal slope. In that case, the signal slope is directly related to the leakage rate. With a higher  $b$ , the gradient of the contrast agent concentration over the vessel wall is higher, leading to a higher leakage rate. For  $b = 0$ , the slope is negative, indicating that leaked contrast agent flows back into the vascular compartment.

**NMR parameters** The NMR parameters,  $\kappa_B$ ,  $\kappa_T$ ,  $T_{1,\text{pre}}$ , have an equally strong but different effect on the NMR signal. The scaling parameter  $\kappa_B$  for the meso-scale  $T_2^*$ -effects from the vascular wall, affects the signal strength almost linearly throughout the entire simulation. For  $\kappa_B = 0$ , i.e. if meso-scale effects on  $T_2^*$ -relaxation are neglected, the early time signal enhancement due to  $T_1$ -shortening becomes even stronger than the signal decrease due to  $T_2^*$ -shortening, as clearly seen in Fig. 9.5. This illustrates that it is essential for the NMR signal model to include meso-scale effects. The scaling parameter  $\kappa_T$  for the meso-scale  $T_2^*$ -effects from the cell walls, only influences the signal in the presence of leakage (sample L). This is evident, since the difference between the contrast agent concentration in the cells and the extra-vascular, extra-cellular compartment is zero, in the absence of leakage. Fig. 9.4 shows that signal decrease due to  $T_2^*$ -shortening in the extra-vascular compartment exceeds signal enhancement due to  $T_1$ -shortening, if  $\kappa_T$  is chosen too large. Because this is not seen in any of the clinical data,  $\kappa_T$  is likely to be small ( $\kappa_T < 10$ ). The pre-contrast longitudinal relaxation time,  $T_{1,\text{pre}}$ , shows a direct influence on the signal-enhancing effect of  $T_1$ -shortening. If  $T_1$  is already elevated before the administration of contrast agent, the  $T_1$ -shortening has a strong signal-enhancing effect. If  $T_{1,\text{pre}}$  is closer to  $T_1$  values measured for NAWM (Thaler et al., 2017), the signal-enhancing effects are significantly weaker. Fig. 9.4 suggests that signal enhancement is small if  $T_{1,\text{pre}}$  is not elevated, even in the presence of leakage.

**Leakage coefficients** The leakage coefficients for advective and diffusive transmural transport,  $L_p$  and  $D_\omega$ , show a very similar qualitative influence on the NMR signal. However, the sensitivity of the NMR signal with respect to changes in  $L_p$  is significantly lower than the sensitivity with respect to changes in  $D_\omega$ . This suggests that the main mechanism for transmural contrast agent leakage is of diffusive nature. Furthermore, note that changing  $D_\omega$ , while keeping the other parameters constant, can change the signal-time curve from



the shape of sample N to the shape of sample L, and vice versa. This further emphasizes that diffusive wall conductivity plays a dominant role in characterizing curve shapes.

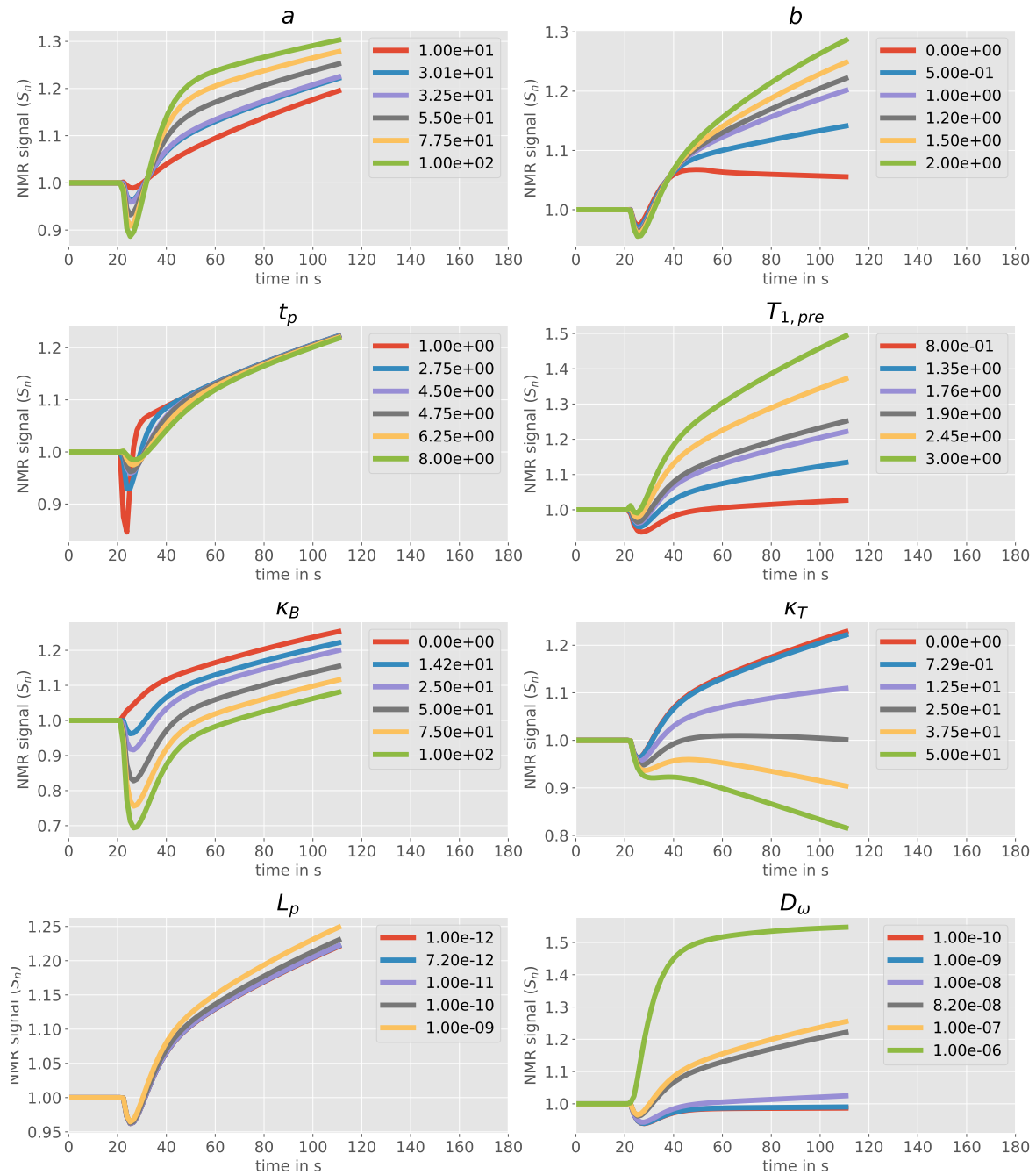


**Figure 9.4 – Parameter sensitivity for lesion tissue.** Influence of different flow, transport, and NMR parameters on the signal-time curve. The parameters are individually varied, while the other parameters are chosen as in Table 9.1 (sample L). Reprinted from Koch et al. (2020a).

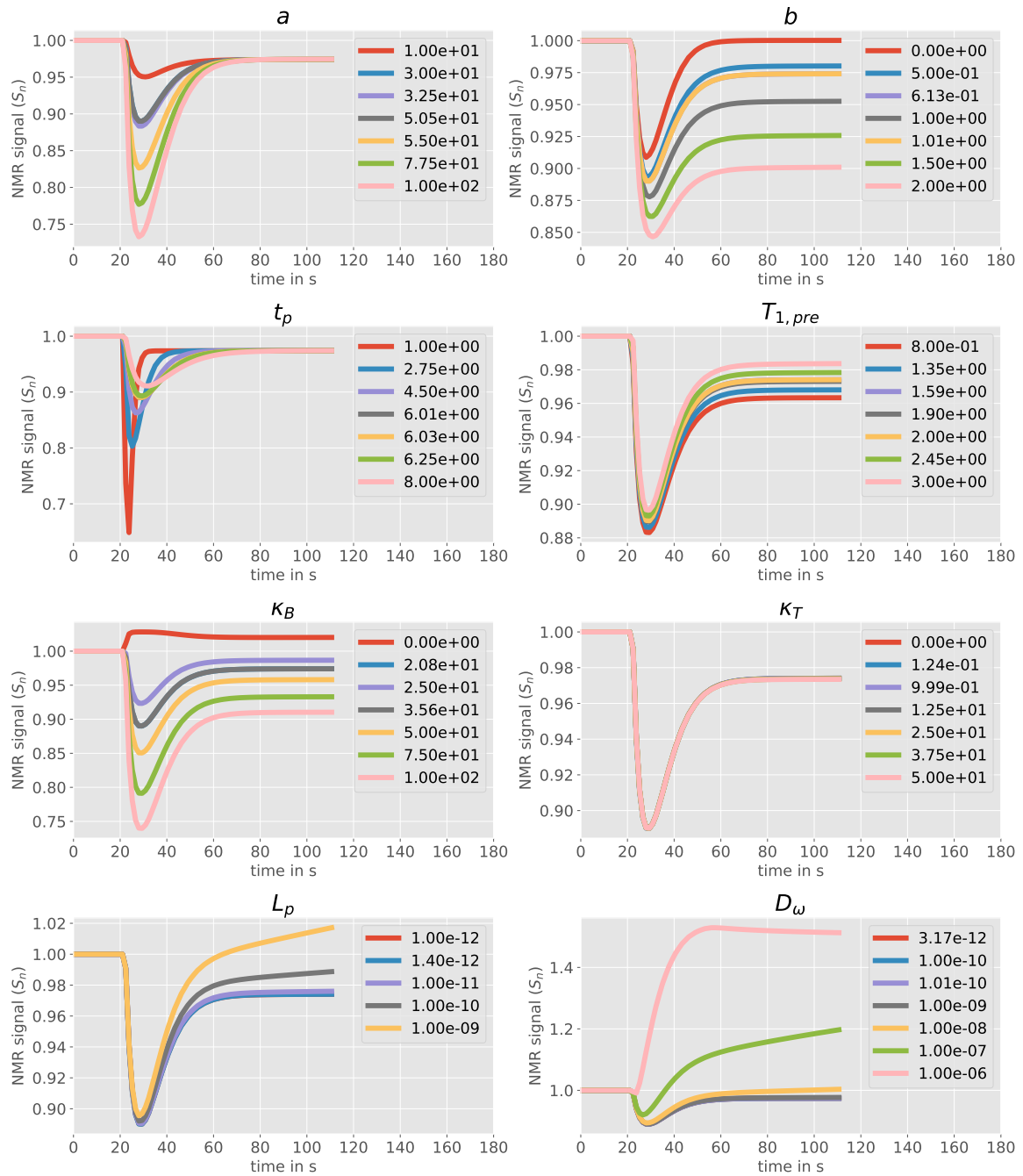


**Figure 9.5 – Parameter sensitivity for NAWM tissue.** Influence of different flow, transport, and NMR parameters on the signal-time curve. The parameters are individually varied, while the other parameters are chosen as in Table 9.1 (sample N). Reprinted from Koch et al. (2020a).

### 9.4.3 Bayesian parameter inference

To complete our critical assessment of the proposed model, we ask and attempt to answer the question: *What can we learn about the model parameters, given the MRI data?* Bayesian parameter inference is a method to estimate unknown parameters of a model, given some prior knowledge about the parameters, and observations, while quantifying the uncertainty that is inherent to such a parameter estimation. Let  $\theta$  denote the parameters of the model  $\mathcal{M}$ , and  $X$  the vector of observed values. Bayes' theorem, applied to the problem of parameter inference, states that

$$p(\theta|X) = \frac{p(X|\theta)p(\theta)}{p(X)}, \quad (9.16)$$

where  $p(\theta|X)$  is the posterior distribution, i.e. the probability of  $\theta$  given the observation data  $X$ .  $p(X|\theta)$  is the likelihood function, i.e. the probability of the  $X$  being from the same population as the model prediction, given  $\theta$ .  $p(\theta)$  is the prior distribution reflecting prior knowledge about the parameters  $\theta$ , before knowing the observations.  $p(X)$  is the marginal likelihood, a normalization constant, not depending on  $\theta$ . Now, let  $Y = \mathcal{M}(\theta)$  be the model prediction given the parameters  $\theta$ . We assume that we can write

$$X = Y + \epsilon, \quad \epsilon \sim \mathcal{N}(0, \sigma^2), \quad (9.17)$$

where  $\epsilon$  is the combination of measurement error and unbiased model error and  $\sigma$  its standard deviation. The likelihood that any model answer,  $Y$ , comes from the same population as the measurement,  $X$ , is a Gaussian likelihood

$$p(X|\theta) \propto \exp\left(-\frac{\sum_i (X_i - Y_i)^2}{2\sigma^2}\right), \quad (9.18)$$

if the errors of all observations are assumed to be uncorrelated. The standard deviation,  $\sigma$ , has to be estimated for the given MRI data and the proposed model. The measurement error is estimated from the MRI data obtained before the contrast agent bolus reaches the tissue sample, where the measurement is assumed to fluctuate around a constant baseline signal. To this end, we take 100 random signal samples from the brain slice shown in Fig. 9.1, normalize the signal to the mean of the first 10 sample data points, and compute the standard deviation of all such baseline data points across all samples, yielding  $\sigma = 0.009$ . Furthermore, we assume that our mathematical model captures the most significant physical processes. The model error is assumed to be sufficiently estimated using, in total, a standard deviation of

$\sigma = 0.009$ . We are aware that this assumption may be too restrictive, in which case the estimated model parameters may additionally include modeling uncertainties that may compromise their physical interpretability for the underlying physical process. However, the estimated standard deviation of  $\sigma = 0.009$  represents a rather large uncertainty given relative signal changes in the order of 0.1, see Fig. 9.2. To estimate the effect of assuming a larger model uncertainty, we run a second numerical experiment with a 10-fold increase of the standard deviation.

Markov chain Monte Carlo (MCMC) methods are methods to sample from the posterior distribution  $p(\theta|X)$  without the need to compute marginal likelihood, which is generally expensive. MCMC draws samples on a random walk through the parameter space, creating a representative set of samples from the posterior distribution, after a sufficient number of iterations. These samples form a Markov chain such that the parameters with which the sample is generated in one step only depend on the parameters in the previous step. Herein, we use the ensemble sampler proposed by Goodman and Weare (2010), which is implemented in the Python module `emcee` (Foreman-Mackey et al., 2013). Its algorithm features an ensemble of interdependent Markov chains (so called walkers), enabling multiple parallel forward model runs within one step. For a brief description of the algorithm, see Appendix A.13. We refer to Goodman and Weare (2010); Foreman-Mackey et al. (2013) for a comprehensive discussion.

In the following, Bayesian parameter inference is used to compute the probability distribution of the patient-specific model parameters, under physical parameter constraints, given a signal-time curve from a voxel of a perfusion MRI sequence. To this end, we choose the prior distributions of the parameters to be uniform distributions within the bounds given in Table A.4 in Appendix A.12. The parameter vector is  $\theta = [a, b, t_p, \log_{10} D_\omega, T_{1,\text{pre}}, \kappa_B, \kappa_T]^T$ . The parameter  $L_p$  remains fixed to reduce the dimension of the parameter space. Its influence on the NMR signal has been shown in the previous section to be significantly weaker than the influence of  $D_\omega$  (see Fig. 9.4).

The resulting histograms from the MCMC for each parameter and their covariance with respect to the other parameters is visualized in Fig. 9.6 for sample L and Fig. 9.7 for sample N (cf. Fig. 9.1). The plots show the results for  $\sigma = 0.009$ . The results with a 10 times larger  $\sigma$  are given in Appendix A.14. The solid black lines in Figs. 9.6 and 9.7 show the parameter values of Table 9.1 that were obtained previously with PEST.

To interpret the results, we recall the original question: *What can we learn about the model parameters, given the MRI data?* If the posterior distribution of a parameter is close to uniform, i.e. close to the prior distribution, the data did not provide any additional information about this parameter. This is, for example, the case for  $a$ ,  $b$ , and  $\kappa_T$  in Fig. 9.7, for which the 90 % credible interval is wide. In contrast, if the posterior distribution differs significantly from the prior distribution, the data provides significant information on this parameter. This is the case for the parameters  $D_\omega$  and  $\kappa_T$  in Fig. 9.6, which is consistent with the observation in Figs. 9.4 and 9.5 that the sensitivity of the NMR curve with respect to those parameters is high, such that only a small range of values for those parameters is likely to match the model results with the clinical MRI data. Furthermore, there seem to be correlations between several parameters. For instance, the inflow curve parameters  $a$  and  $b$  show a strong and nonlinear correlation with MR model parameter  $\kappa_B$  for both samples, L and N. For high values of  $a$  and  $b$ , which corresponds to an increase in the amount of contrast agent entering the tissue sample, it is more likely that  $\kappa_B$  is low, which decreases the effect of contrast-induced signal reduction. Conversely, a high  $\kappa_B$  is more likely if  $a$  and  $b$  are low. This effect is expected, since high concentration values correspond to a higher signal reduction in the vascular compartment, see Eqs. (9.7) and (9.13).

Most interestingly, the distribution of  $D_\omega$  in Fig. 9.6 differs significantly from the distribution of  $D_\omega$  in Fig. 9.7. Both distributions are shown as histograms in Fig. 9.8 for the experiment with  $\sigma = 0.009$ , as well as for the experiment with an increased model and measurement error uncertainty. For sample L, the inferred posterior distribution of the diffusive wall conductivity has a distinct peak around  $D_\omega = 9 \cdot 10^{-8} \text{ ms}^{-1}$  ( $3 \cdot 10^{-7} \text{ ms}^{-1}$  for high  $\sigma$ ). Furthermore, it shows that values below  $D_\omega = 3 \cdot 10^{-8} \text{ ms}^{-1}$  are unlikely, suggesting significant transmural contrast agent leakage with a high probability. For sample N, the inferred diffusive wall conductivity is likely low ( $< 5 \cdot 10^{-9} \text{ ms}^{-1}$ ), suggesting little to no leakage; see Fig. 9.3. For low  $\sigma$ , the results suggest that  $D_\omega$  values between  $3 \cdot 10^{-9} \text{ ms}^{-1}$  and  $3 \cdot 10^{-8} \text{ ms}^{-1}$  are more likely than respective lower values. This could indicate that there may be a small amount of contrast agent leakage in the NAWM sample. That this effect may indeed occur, is suggested in several clinical studies (Ingrisch et al., 2012; Cramer et al., 2014). However, this effect can not be seen for the numerical experiment where  $\sigma$  is assumed 10 times higher (Fig. 9.8, right). Here, all values below  $D_\omega = 1 \cdot 10^{-8} \text{ ms}^{-1}$  are equally likely. Consequently, the indication of leakage in the given NAWM sample could also be an artifact resulting from an overconfidence in the accuracy of the measurement or model data. Moreover, more than 50 % (70 % for high  $\sigma$ ) of the  $D_\omega$  sample values fall

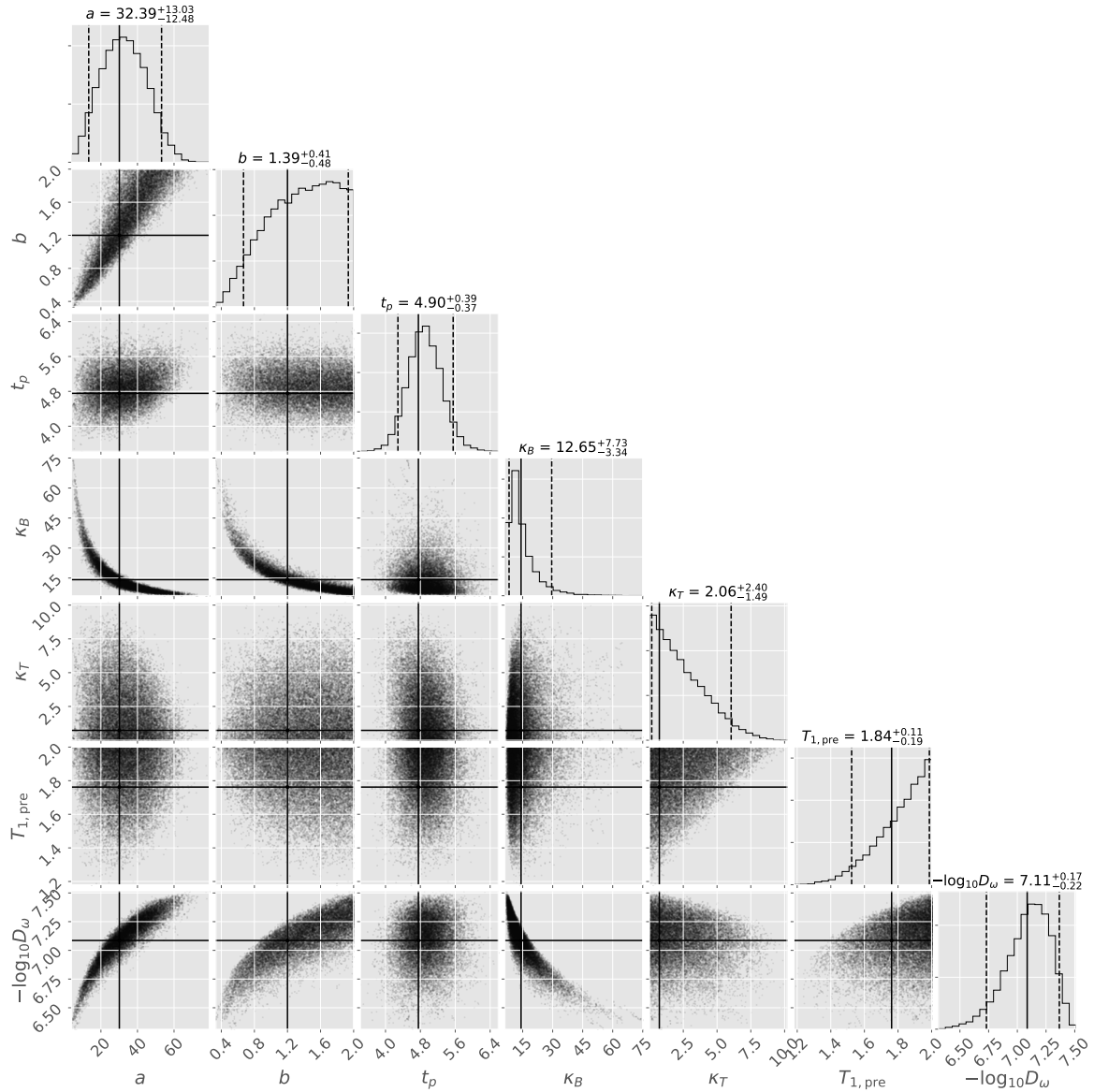


**Figure 9.6 – Parameter distributions for lesion sample ( $\sigma = 0.009$ ).** Histograms on the diagonal show single parameter distributions. Scatter plot in the matrix visualizes covariance of the respective row and column parameters; plot generated with `corner.py` (Foreman-Mackey, 2016). Histogram titles present median, 5<sup>th</sup> and 95<sup>th</sup> percentile (dashed lines). Horizontal and vertical solid black lines show the parameter values for sample L of Table 9.1. Reprinted from Koch et al. (2020a).

below  $3 \cdot 10^{-9} \text{ ms}^{-1}$  (including the value obtained with the optimization approach in the previous section), which corresponds to virtually no contrast agent leakage. Because of the significant difference between the posterior distributions for  $D_{\omega}$  in both samples (L and N), in particular the observation that low  $D_{\omega}$  are likely for sample N, while they are unlikely

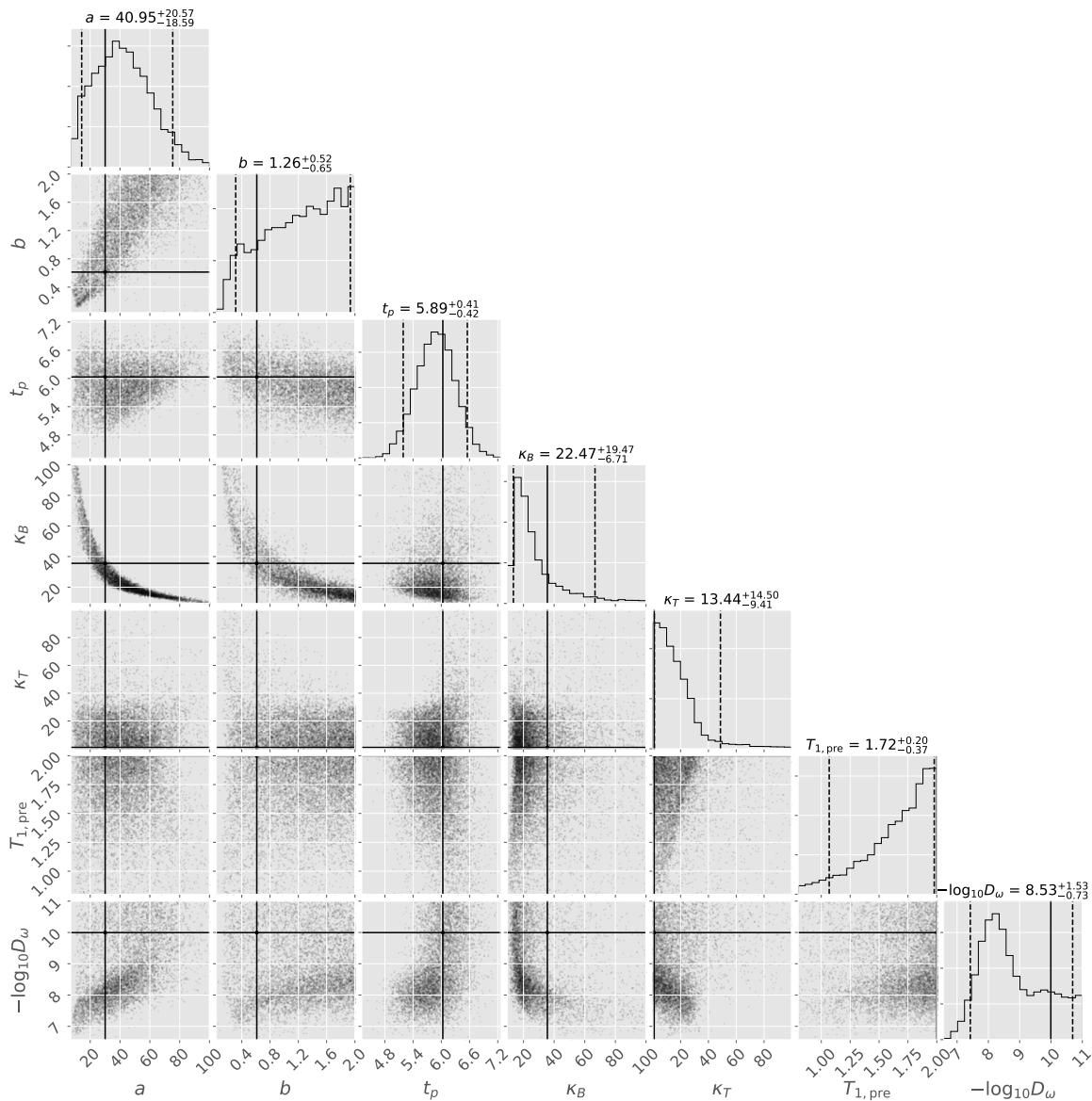


**Figure 9.7 – Parameter distributions for NAWM sample ( $\sigma = 0.009$ ).** Histograms on the diagonal show single parameter distributions. Scatter plot in the matrix visualizes covariance of the respective row and column parameters; plot generated with `corner.py` (Foreman-Mackey, 2016). Histogram titles present median, 5<sup>th</sup> and 95<sup>th</sup> percentile (dashed lines). Horizontal and vertical solid black lines show the parameter values for sample N of Table 9.1. Reprinted from Koch et al. (2020a).

for sample L, we conclude that the two samples can be distinguished just on the basis of  $D_{\omega}$ , without looking at the estimates for the other parameters. The uncertainty in  $D_{\omega}$  reflects the fact that all other parameters are uncertain as well. Consequently, the estimate of  $D_{\omega}$  may be improved with additional information about other parameters. Such information

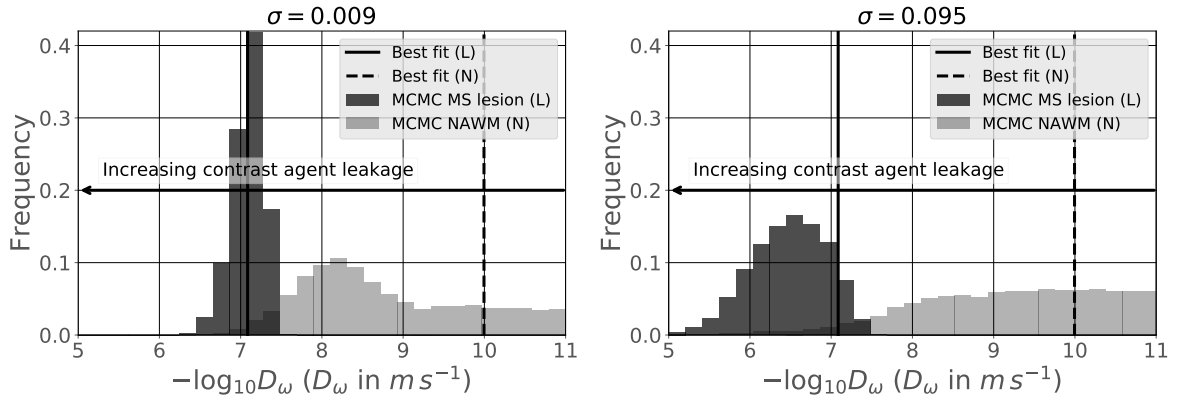


**Figure 9.8** –  $D_\omega$  distributions after learning from clinical MRI data. A low diffusion coefficient is most likely for the NAWM data (N), while a high diffusion coefficient is most likely for the contrast-enhancing lesion data (L). Reprinted from Koch et al. (2020a).

might be, for instance, a direct measurement of  $T_{1,\text{pre}}$ , estimations of the so-called arterial input function (AIF), or data from other MR sequences of the same patient. Furthermore, knowledge that a parameter is expected to be similar in a certain region of the brain, could enable learning from other voxel data of the same sequence. In the Bayesian framework, such information can be included incrementally, where the posterior distributions of the previous Bayesian update are the prior distributions of the next Bayesian update.

The values estimated for  $D_\omega$  cannot be compared to values from two-compartment models straightforwardly. These models are formulated on the macro-scale using averaging techniques. The relation of fluid-mechanical models on the meso-scale (as considered in this work) and models formulated on the macro-scale is yet to be better understood and is addressed in some recent studies (El-Bouri and Payne, 2018; Vidotto et al., 2019; Peyrounette et al., 2018; Shipley et al., 2019). However, values for the diffusive wall permeabilities have been estimated from direct measurements with single or multiple capillaries from different tissues (Crone, 1963; Curry, 1979; Curry et al., 1983; Renkin, 1988). The values and methods are reviewed by Jain (1987) and Michel and Curry (1999). We are not aware of such measurements for Gadobutrol. Nevertheless,  $D_\omega$  values can be assumed to be similar for molecules with similar properties as Gadobutrol (hydrophilic,  $M = 604.715 \text{ g mol}^{-1}$  (PubChem, 2018),  $r_{\text{hy}} \approx 0.8 \text{ nm}$  (Guthausen et al., 2015)). For example, for sucrose (hydrophilic,  $M = 342.30 \text{ g mol}^{-1}$ ,  $r_{\text{hy}} \approx 0.45 \text{ nm}$  (Price et al., 2016)) values in the order of  $1.4 \cdot 10^{-6}$  to  $1.4 \cdot 10^{-7} \text{ m s}^{-1}$  are reported for frog mesentery (Jain, 1987) and skeletal muscle tissue (Michel and Curry, 1999), depending on the measurement method. For (normal) brain tissue in dogs,



no significant permeability is reported (Crone, 1963), meaning that the pathway through the endothelial tight junctions of the BBB is impermeable for sucrose. The filter mechanisms and anatomy of the capillary wall are assumed to be similar in different species (Arkill et al., 2011). Michel and Curry (1999) and Curry et al. (1983) suggest a strong dependence on molecule size, so that for the Gadobutrol molecule with twice the size of the sucrose molecule the expected value for skeletal muscle tissue would be one order of magnitude lower than that of sucrose, see Michel and Curry (1999, Fig. 1). Hence, the  $D_{\omega}$  values for the lesion sample compare to physiological values of other tissues where capillary walls are known to be more permeable to small molecules (Rippe and Haraldsson, 1994) than in the brain. In comparison with our estimated value for sample L, this suggests significant leakage and a strong increase in transmural permeability in comparison with NAWM. The values for NAWM, with two orders of magnitude lower  $D_{\omega}$  values, signify impermeable capillary walls and are in good agreement with the common assumption that the BBB is impermeable for Gadobutrol.

## 9.5 Model limitations and outlook

The current model relies on a single exemplary vessel geometry. Today, patient-specific sub-voxel vessel geometries cannot be routinely measured. Hence, the influence of different vessel geometries on the presented results has to be investigated.

Furthermore, the used model of the inflow curve, Eq. (9.1), neglects re-circulation in the form of a second or third pass of the contrast agent. In particular, the effect of the second pass of the bolus cannot be captured and might lead to more uncertainty in the estimation of other model parameters. In a future step, the inflow curve model can be improved to include re-circulation and to be derived from arterial input function measurements. Including such measurements adds information about the inflow parameters and may thus lead to narrower estimates of other model parameters. Moreover, we used a rather simple approach for the estimation of the model error. In future work, the model error can be more rigorously analyzed, for example, by including the standard deviation of the error model as a random variable. In this way, Bayesian parameter inference provides an estimate for the model error alongside the estimates of the other model parameters. This may increase the uncertainty of the provided parameter estimations.

The presented model considers processes in a sub-voxel tissue sample that is surrounded by tissue with the same properties. However, contrast-enhancing lesions in the brain typically span over several voxels, see Fig. 9.1. Furthermore, patterns such as ring-like shapes have been observed for MS (Llufriu et al., 2010), suggesting processes on a larger scale, or possible inter-voxel dependencies. Such effects can not be included in the model in its current state, since simulation of several voxels are prohibitively expensive due to the large number of blood vessels.

The applicability of the presented model has yet to be confirmed in a clinical environment. This would be of special relevance for monitoring of pharmacologic effects and drug efficacy, e.g. in drugs that are targeted against immune cell trafficking. It is to be analyzed how reliable the method predicts diffusive capillary wall conductivities over a wider range of patient-specific data.

A current drawback of the method is the computational time required to infer diffusive capillary wall conductivities and contrast agent leakage. However, the computational cost can most likely be improved by applying model reduction techniques and machine learning algorithms. Likewise, homogenization techniques can be used for model reduction (El-Bouri and Payne, 2018; Vidotto et al., 2019). However, such techniques are difficult to apply, due to the hierarchical structure of the micro-circulation. For all approaches, the presented model can be used as theoretical basis and as validation tool.

## 9.6 Summary and conclusion

We presented a mixed-dimension fluid-mechanical model for contrast agent brain tissue perfusion on the sub-voxel scale. The blood vessels are considered as a network of cylindrical tubes. The extra-vascular compartment is modeled as a porous medium. The presented discretization results in a coupled system of partial differential equations of three-dimensional and one-dimensional equations. The fluid-mechanical model can describe the three-dimensional evolution of the contrast agent concentration on the sub-voxel scale. We further proposed an NMR signal model, describing the influence of the contrast agent on the NMR voxel signal, including meso-scale effects. A convergence study suggests that the combined model is consistent and converges to a unique solution on grid and time step refinement. Using parameter estimation, it was shown that the model can describe two characteristic NMR

signal curves from clinical data obtained by DSC-MRI for a patient with MS lesions, and that the estimated model parameters provide a meaningful physical interpretation. Bayesian parameter inference, with the given model and clinical DSC-MRI data, showed that the two given NMR signal curves can be distinguished and characterized, only on the basis of the estimated diffusive capillary wall conductivity distributions. The study suggests that the NMR signal curve, given the model, is informative about some patient-specific model parameters, such as the diffusive capillary wall conductivity, and less informative about others, such as the tissue's  $T_1$  relaxation time before contrast agent administration. Furthermore, the uncertainty of the diffusive capillary wall conductivity predictions could be quantified in the Bayesian framework. For a sample from within an MS plaque in the brain white matter, a value of  $D_\omega = 8.2 \cdot 10^{-8} \text{ m s}^{-1}$  was estimated using optimization. This value corresponds to significant contrast agent leakage into the extra-vascular space. With Bayesian parameter inference, we obtained a median value of  $D_\omega = 7.8 \cdot 10^{-8} \text{ m s}^{-1}$  and an equal-tailed 90% credible interval with lower bound  $4.7 \cdot 10^{-8} \text{ m s}^{-1}$  and upper bound  $1.1 \cdot 10^{-7} \text{ m s}^{-1}$ , which contains the value obtained with optimization. With a 10-fold increase of the standard deviation of the assumed modeling and measurement error, slightly higher values for  $D_\omega$  were estimated to be more likely, and the uncertainty increased (median:  $3.2 \cdot 10^{-7} \text{ m s}^{-1}$ ; 90% credible interval:  $6.3 \cdot 10^{-8} \text{ m s}^{-1}$  to  $9.1 \cdot 10^{-7} \text{ m s}^{-1}$ ). However, the values are still clearly distinguishable from those estimated for a NAWM sample, where no significant leakage is observed. The values are comparable to the diffusive wall conductivity estimated from experiments with hydrodynamically similar substances in skeletal muscle tissue. The results agree with the observation that endothelial tight junctions are opened in MS lesions (Plumb et al., 2002). In summary, the presented model constitutes a useful tool to study contrast agent perfusion on a sub-voxel scale, and may lead to an improved understanding of the sub-voxel processes beyond the scope of this work.

The code to reproduce the simulations in this chapter can be found at <https://git.iws.uni-stuttgart.de/dumux-pub/Koch2019a>.



# 10 Simulation of root water uptake and root growth

The following chapter discusses different aspects of root-soil interaction simulations. The simulations are based on the mixed-dimension embedded model developed in Chapters 4 and 6. In Section 10.1, root water uptake is simulated for a small lupin root system. The case is from a recently published benchmark problem (Schnepf et al., 2020), where a reference solution with a method explicitly resolving the root-soil interface with the computational mesh is given. The predicted transpiration rates are shown to depend on the local soil grid resolution due to the development of large local gradients. Sections 10.2 to 10.4 showcase three applications demonstrating the importance of mixed-dimension embedded models for understanding the water management in the vadose zone. The simulations in this chapter motivate several open questions concerning the application of mixed-dimension embedded methods for nonlinear equations, such as the two-phase flow equations. These aspects are briefly discussed in Section 10.5.

## 10.1 Root water uptake benchmark

In this section, we simulate a benchmark case contributed to Schnepf et al. (2020) (case C1.2a). An 8-day-old lupin (see Fig. 6.3) is embedded in a soil box ( $8 \times 8 \times 15$  cm) filled with loamy soil (soil parameters:  $k = 5.89912 \cdot 10^{-13} \text{ m}^2$ ,  $\phi_s = 0.43$ ,  $\alpha_{\text{vG}} = 4.077 \text{ Pa}^{-1}$ ,  $n_{\text{vG}} = 1.6$ ,  $l_{\text{vG}} = 0.5$ ,  $S_{\text{wr}} = 0.186$ ). The initial soil water saturation at the soil surface is 0.3. The water pressure profile is initially purely hydrostatic. All soil boundaries are closed. The potential transpiration rate is given as

$$r_{\text{T,pot}}(t) = \bar{r}_{\text{T}} \left[ 1 + \sin \left( 2\pi t - \frac{\pi}{2} \right) \right], \quad (10.1)$$

with the mean transpiration rate  $\bar{r}_{\text{T}} = 6.4 \text{ cm}^3 \text{ d}^{-1}$ . At the root collar, a transpiration rate of  $r_{\text{T}} = \min\{r_{\text{T,pot}}, r_{\text{T,c}}\}$  is prescribed, where  $r_{\text{T,c}}$  is the transpiration rate for which the root collar pressure is  $p_{\text{r,c}} = -1.4 \text{ MPa}$  (wilting point pressure). The transpiration rate is enforced

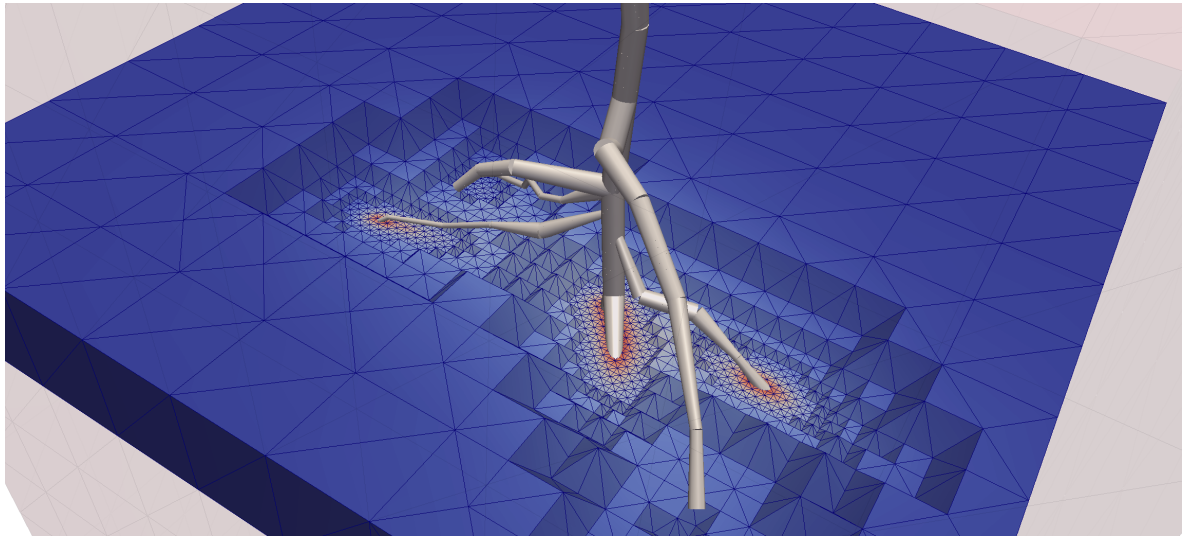


**Figure 10.1 – Locally refined tetrahedral grid.** The root is visualized by tubes scaled with the actual root radius. The smallest tetrahedral cell in the soil grid has a diameter of 0.5 mm, while the root radius ranges from 0.12 mm to 1.2 mm (cf. Fig. 6.3). The grid needs to be significantly refined towards the root to resolve local pressure gradients in drying soil.

as a Robin boundary condition. The root hydraulic properties are constant for the entire root system ( $k_{ax} = 5.07 \cdot 10^{-17} \text{ m}^4 \text{ Pa}^{-1} \text{ s}^{-1}$ ,  $k_{rad} = 2.04 \cdot 10^{-13} \text{ m Pa}^{-1} \text{ s}^{-1}$ ).

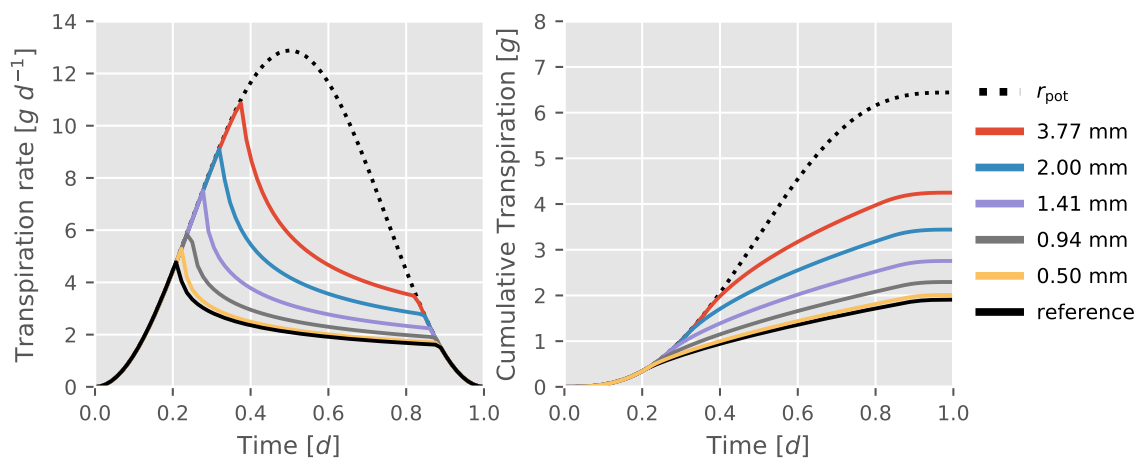


**Figure 10.2 – Benchmark: simulated transpiration rates for drying soil.** Grid convergence study against a reference solution. The reference (solid black line) is given in Koch (2019). The dotted lines show the diurnal sinusoidal potential transpiration rate (left) and the cumulative potential transpiration rate (right). The other lines result from simulations with the mixed-dimension embedded method (Chapter 4) for locally refined tetrahedral grids. The legend shows the smallest cell diameter in the soil grid (the longest distance between two vertices of a cell).

A reference solution (Koch, 2019) has been produced with a method where the interface is explicitly resolved by the soil grid cell faces. For a description of the method, see Schnepf et al. (2020). The benchmark case is designed to investigate the effect of different grid resolutions for mixed-dimension embedded models in the case of drying low-permeable soil (large local pressure gradients, cf. Section 6.2.2). We simulate the first day of the benchmark problem with different soil grid resolutions using the model presented in Chapter 4. The kernel function is chosen to obtain the method of Köppl et al. (2018). The water balance is discretized in space using the BOX method (Huber and Helmig, 1999) in the soil domain and a TPFA cell-centered finite volume method (see Section 7.2) in the root domain. In time, we discretize with a backward Euler method and limit the maximum time step size to 1200 s. The tetrahedral soil grid is locally refined to resolve the pressure gradients at the root soil interface (Fig. 10.1).

The resulting transpiration rates are shown in Fig. 10.2. Transpiration rates decline when the critical pressure is assumed at the root collar. The solution with the mixed-dimension model converges to the reference solution with repeated (local) grid refinement. For moderately fine grids (the smallest cell diameter is 3 times larger as the largest root radius), the transpiration rate is significantly overestimated. The relative difference with respect to the reference solution amounts to over 100% of the transpired water mass after one day. With strong local refinement, this difference is reduced to 5%. However, for the finest grid, the number of grid cells ( $0.5 \cdot 10^6$ ) is as large as the number of grid cells for the reference solution. We conclude that the presented model seems suitable for the simulation of drying soils around small root systems. However, for relatively low permeable soil and dry conditions, it is not more efficient and less accurate than a method which resolves the root-soil interface. If the soil is moderately wet (not close to the residual saturation), or more permeable (e.g. most sandy soils), local pressure profiles are significantly more shallow. In this aspect, the benchmark case is a particularly difficult case for mixed-dimension embedded models.

## 10.2 Application I: Root water uptake with tracer

We simulate root-water uptake and tracer transport in the soil. The tracer is assumed to not enter the root. Such a tracer could be used in an experiment to expose the location of the highest root water uptake rate. The tracer is expected to accumulate at the root-soil

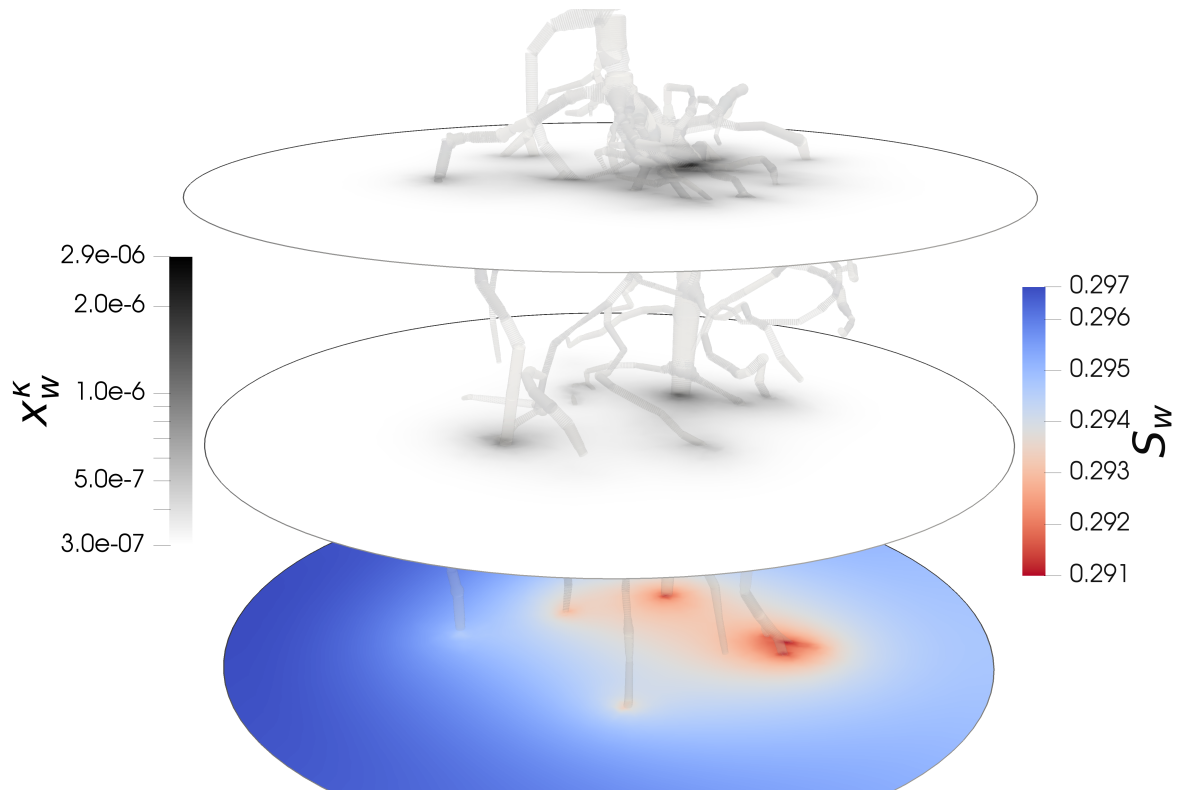


**Figure 10.3 – Simulation result for root-water uptake and simultaneous tracer transport.** The root system is a white lupin, shown at  $t = 3$  d. Three horizontal cuts through the soil domain are shown. The first two slices visualize the mole fraction of the tracer  $\kappa$  in water. The bottom slice displays the water saturation  $S_w$ . Water saturation slightly decreases towards the roots. Its spatial gradient depends on the flow resistances in soil and root, the current water distribution, and the prescribed transpiration rate  $r_T$ . Figure from Koch et al. (2020b).

interface. The example has been presented in a different context in Koch et al. (2020b). We use the model described in Chapter 4.

The soil domain is a closed cylindrical pot (radius: 5 cm, height: 10 cm) and contains a 2-week-old white lupin root system reconstructed from MRI data (Schröder, 2014). The soil domain is discretized with an unstructured tetrahedral grid refined around the root system, while the root domain is represented by an independent grid of line segments forming the root center-line network. At the root collar a transpiration rate of  $r_T = \min\{2.15 \cdot 10^{-8} \text{ kg s}^{-1}, r_{T,c}\}$  is prescribed, where  $r_{T,c}$  is defined in Section 10.1. The tracer is initially uniformly distributed in the soil (mole fraction:  $x_w^\kappa = 3 \cdot 10^{-7}$ , diffusion coefficient:  $D_w^\kappa = 2.3 \cdot 10^{-9} \text{ m s}^{-2}$ ). We simulate for a period of 3 d with a maximum time step size of 1 h (backward Euler time discretization). The remaining parameter values are given in Table 10.1.



**Table 10.1 – Parameter values for root water uptake simulation.**

symbol	name	value	unit
$\phi_s$	soil porosity	0.4	-
$\rho_{m,w}$	molar density of water	$5.55 \cdot 10^4$	$\text{mol m}^{-3}$
$\phi_r$	root porosity	0.4	-
$\alpha_{vG}$	van Genuchten parameter	$2.956 \cdot 10^{-4}$	$\text{Pa}^{-1}$
$n_{vG}$	van Genuchten parameter	2.0	-
$S_{wr}$	residual water saturation	0.1	-
$k_{ax}$	axial root conductivity	$5.10 \cdot 10^{-17}$	$\text{m}^4 \text{Pa}^{-1} \text{s}^{-1}$
$k_{rad}$	radial root conductivity	$2.04 \cdot 10^{-11}$	$\text{mPa}^{-1} \text{s}^{-1}$

The resulting spatial distribution of water and the tracer is shown in Fig. 10.3 and tracer accumulation in close vicinity to the roots is evident. Such a simulation is valuable for the interpretation of hypothetical experimental results, as it may enable quantification of root water uptake by observing local tracer accumulation. The result did not significantly change with grid refinement. Firstly, the local flow field is approximated well by using local grid refinement (grid cell diameters at the root-soil interface are of similar order of magnitude as the root radius). Secondly, the local soil water saturation, and thus water mobility, is high enough to maintain relatively moderate local pressure gradients. The code to reproduce this simulation can be found at <https://git.iws.uni-stuttgart.de/dumux-pub/dumux2019>.

## 10.3 Application II: Grid growth

We simulate two growing root systems confined in a plant pot, using the model described in Chapter 4. The example is published in Koch et al. (2018b). The coupling is locally mass conservative and considers the pore space (xylem) created by the growing root in the root domain and the corresponding pore space reduction in the soil. Small segments are avoided by moving root mesh vertices. The soil domain is discretized using an unstructured hexahedral grid for the soil domain. For simplicity, any kind of competition between the two plants, e.g. for space, water, or sunlight, is neglected.

The initial water pressure profile is hydrostatic with a fixed water saturation of  $S_w = 0.3$  at the soil surface. We neglect soil evaporation and diurnal changes of the boundary conditions

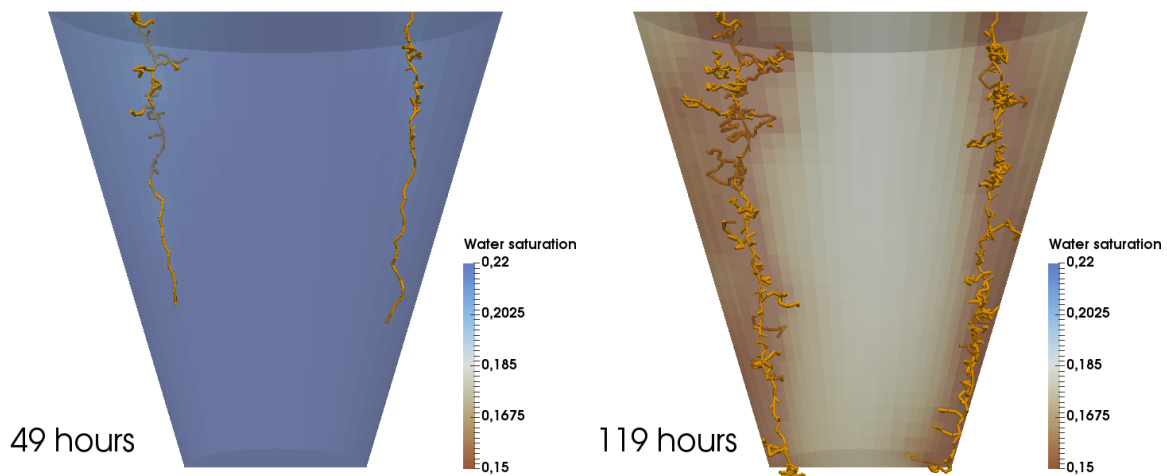


**Figure 10.4 – Root water uptake of two growing root systems.** Uptake is driven by transpiration at the plants’ leaves (prescribed as Neumann boundary condition at the root collar) and modeled as a function of root volume. Vertical cut through a plant pot with the shape of a truncated cone. Root segments are visualized as tubes scaled with the segment radius. The soil color visualizes the water saturation. The domain is 10 cm high with an upper radius of 5 cm and a lower radius of 2 cm. Figure from Koch et al. (2018b).

for simplicity. The tap root initially consists of a single segment of length  $l = 1$  mm without daughter branches. Root growth is parameterized using stochastic parameters fit to a white lupin due to Leitner et al. (2014a).

The root systems are grown at the beginning of each time step, followed by an update of the flow field in the soil. The change in porosity in root and soil is explicitly considered in the storage terms of Eq. (4.8). In this example, root growth is not dependent on soil parameters. The coupled water flow problem is nonlinear in the primary variable water pressure. The discrete system is solved by Newton’s method. In case the Newton method fails to achieve the prescribed residual tolerance within 10 steps, the time step size is cut in half. The root systems are first reset to the previous time step and then regrown for the smaller time step.

At the root collar, we prescribe the transpiration rate  $r_T$  as Neumann boundary condition. We compute the transpiration rate as a function of the root volume using Eq. (4.9) with the values given in Chapter 4. Figure 10.4 shows the resulting root architecture at  $t_1 = 49$  h and  $t_2 = 119$  h. Furthermore, root growth is confined by the domain boundaries, as prescribed by the model.

Errors in the global water mass balance stayed within the range of the numerical precision ( $\approx 1 \cdot 10^{-12} \text{ g d}^{-1}$ ). In contrast, the global mass balance error without considering the porosity change in root and soil, is on average  $0.015 \text{ g d}^{-1}$  on the first day and rises to  $0.075 \text{ g d}^{-1}$  at the end of one week (determined by a second modified simulation with constant porosity per time step). To better understand the magnitude of the error, we can express it as a percentage of the transpiration rate (an indicator of the magnitude of mass flow rates of interest). The error is 17 % and 2 % of the average transpiration rate on the first day and at the end of one week, respectively. The relative error reduces over time, since the transpiration rate is a function of root volume, while the error depends on the newly created root tip volume and the growth rate. The code to reproduce the simulations can be found at <https://git.iws.uni-stuttgart.de/dumux-pub/Koch2017a>.

## 10.4 Application III: Evapotranspiration

We simulate root water uptake and evaporation from soil with a non-isothermal miscible two-phase two-component model. The example is published in Koch et al. (2018b). Transpiration is prescribed by boundary conditions as in Section 10.2. The same root system as in Section 10.2 is embedded in an acrylic glass cube (side length: 10 cm) filled homogeneously with a laboratory sand. Moreover, there is a thin layer of compacted low-permeable sand at a depth of 3 to 3.5 cm to emphasize the role of the root system as a water transport system from deeper soil layers to the surface.

The soil is initially saturated ( $S_w = 0.99$ ) and has a temperature of  $T = 285.15 \text{ K}$ . The evaporation model is described in Section 4.6. The atmospheric conditions above the soil are controlled by a wind tunnel, so that the air has an approximately constant relative humidity of 55 % at  $20 \text{ }^\circ\text{C}$ . The atmospheric temperature varies between  $10 \text{ }^\circ\text{C}$  during night and  $20 \text{ }^\circ\text{C}$  during day in a sinusoidal diurnal cycle. We assume a stable laminar boundary layer of thickness  $\delta_{\text{BL}} = 0.0016 \text{ m}$ . The acrylic glass cube has a thermal conductivity of  $\lambda_{\text{pg}} = 0.184 \text{ W m}^{-1} \text{ K}^{-1}$ , a wall thickness of 5 mm, and exchanges energy with the atmosphere and the soil system through heat conduction. Values for the thermal conductivity ( $\lambda_r = 0.5 \text{ W m}^{-1} \text{ K}^{-1}$ ) and heat capacity ( $c_{p,r} = 1637 \text{ J kg}^{-1} \text{ K}^{-1}$ ) of the roots are taken from Jayalakshmy and Philip (2010). For more details, we refer to Koch et al. (2018b).

To investigate the influence of evaporation from soil and plant transpiration on the evapotranspiration rate (total water flux from soil cube into the atmosphere), we define three scenarios in Table 10.2. The resulting water fluxes are shown in Fig. 10.5. The two stages

**Table 10.2 – Different scenarios for the evapotranspiration simulation.**

scenario	transpiration	evaporation	description
A	✓	✓	evapotranspiration
B	✗	✓	no root (only evaporation)
C	✓	✗	sealed soil (only transpiration)

of evaporation (see Section 4.6) can be identified. For the given setup, it can be seen by comparison of the evapotranspiration rates for case A and B that evaporation from soil exceeds plant transpiration in stage I, while the opposite is the case for diffusion-limited evaporation (stage II). The evaporation rate in a given time interval is slightly higher in the absence of a plant (case B). This is since the water content in the soil decreases more slowly in the absence of transpiration, and evaporation decreases with decreasing water content close to the soil surface (increasing diffusion distance). Furthermore, the plant reduces the

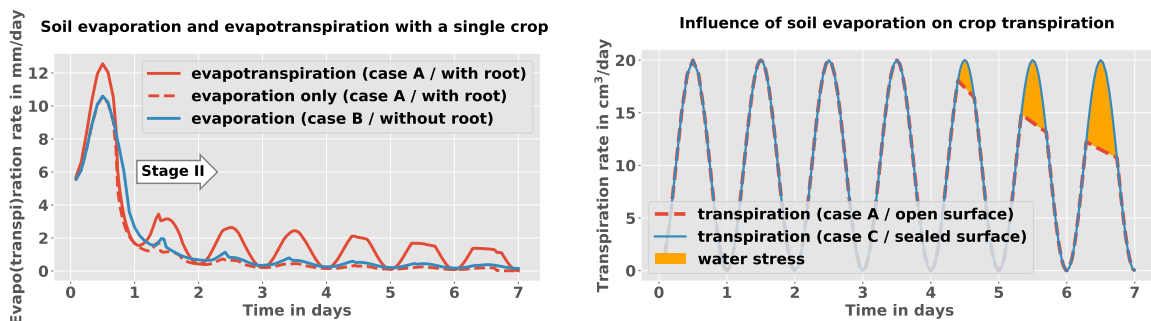


**Figure 10.5 – Influence of transpiration and evaporation on evapotranspiration.** Left, evaporation and evapotranspiration rates for the cases A and B. Right, transpiration rates for the cases A and C, i.e. with and without the influence of evaporation from the soil. Figure from Koch et al. (2018b).

transpiration rate due to water stress significantly later in time, if the soil surface is sealed (case C). Hence, in particular for small root systems, evaporation cannot be neglected when estimating the onset of water stress.

Figure 10.6 shows the simulated soil water distribution at different times. During the beginning of the simulation, the soil is fully saturated. The root water uptake is highest for root segments with higher surface area and lower pressure (closer to the root collar in the

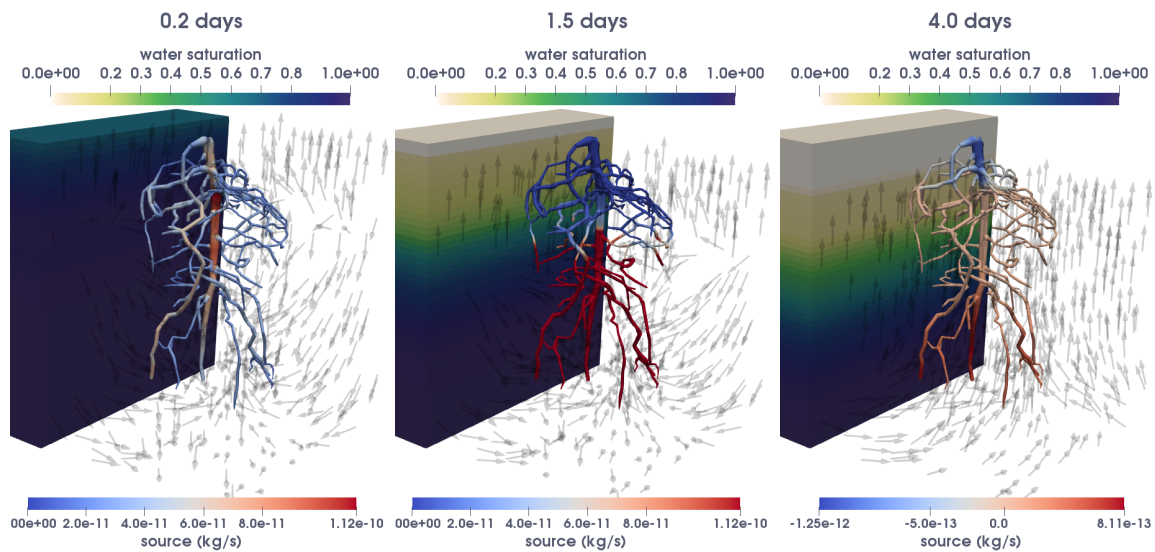


**Figure 10.6 – Root water uptake and hydraulic redistribution.** Source terms and saturation at the beginning of the simulation (after midnight) after 1.5 days (noon) and at midnight after 4 days. The hydraulic redistribution through the root can be seen on the upper dry soil layer as negative source terms in the root (rightmost figure). Figure from Koch et al. (2018b).

hierarchy). However, the soil towards the root surface already starts drying, so that the root water uptake for segments closer to the surface is reduced. At noon on the second day (high transpiration rate), uptake predominantly happens in wet soil (below the compacted soil layer), while no significant uptake is observed in the drier soil. During night after 4 days, the root is observed to take up water from lower (wet) soil layers, and releases water in the upper (dry) soil layers. The hydraulic lift at night (zero transpiration) is only driven by local pressure gradients in the soil. The mass fluxes across the root cortex are about two orders of magnitude lower than during the day. Because of the high permeability of the soil in this experiment, local pressure gradients in the soil are dominated by evaporation and gravitational forces (vertical gradients) rather than by local root water uptake. The code to reproduce the simulations can be found at <https://git.iws.uni-stuttgart.de/dumux-pub/Koch2017a>.

## 10.5 Conclusion and outlook

**Water uptake and dry soils** In comparison with the single phase flow applications in Chapters 3 and 5, modeling two-phase flow in the unsaturated zone around roots is more

challenging for the mixed-dimension embedded model approach. Due to root water uptake, there is a hydraulic pressure drop towards the root. Water saturation is a nonlinear monotone function of the capillary pressure. With increasing capillary pressure (decreasing water pressure) saturation decreases. The local saturation drop at the root-soil interface leads to local drop in relative permeability (over-proportional to the saturation drop, see Eq. (2.6)). A decrease in relative permeability additionally increases the local pressure drop for a given root water uptake rate. In summary, these nonlinear dependencies lead to larger gradients towards the roots than for the single flow systems. For certain parameter combinations, as in the benchmark case presented in Section 10.1, these local gradients lead to systems which can only be solved accurately with strong local grid refinement in the soil domain. Consequently, alternative methods, for example methods based on local analytical reconstructions, are necessary to simulate larger root systems efficiently. However, in contrast to the method presented in Chapter 7 for the linear case, exact reconstructions cannot be found for the nonlinear two-phase flow model. Approximate local pressure or concentration reconstructions have been suggested by Schröder et al. (2009a); Beudez et al. (2013), using simplified analytical solutions, or Mai et al. (2019), solving local radially symmetric problems numerically. However, these methods are constructed in a discrete setting and therefore depend on the discretization method and the discretization length.

**Water stress model** In consequence of the above observations, simulations with very dry soils where the root collar pressure is close to the wilting point pressure, have to be carefully evaluated with respect to local grid refinement and the given model parameters. Grid cell diameters in the soil domain of about 1 cm (one to two orders of magnitude larger than the root diameter) are common in root-soil simulations (Schröder et al., 2008; Schröder, 2014; Leitner et al., 2014b). As demonstrated in Section 10.1, such under-resolved soil domains may lead to significant errors in the predicted transpiration rate during water stress. The presented water uptake model has several limitations. We recall that we do not consider active adaption of plants to drought, such as the reduction in axial and radial conductance, wilting, or stomata closure (Bartlett et al., 2016). Moreover, we note that the applicability of the Van Genuchten-Mualem soil parameter model and the standard two-phase flow porous medium model (e.g. inter-connected water phase) have been questioned for very dry soils (Gray and Hassanizadeh, 1991; Webb, 2000). Finally, we use a linear model for the transmural transport. However, it has been suggested that the radial root conductivity

---

nonlinearly depends on pressure and water content, supported by detailed simulations on root cross-sections (Heymans et al., 2020).

**Root system size** In particular for the investigation of the local water distribution, it is important to sufficiently refine computational grids around roots. Unfortunately, this restricts the applicability of the presented model to small root systems only (young plants). This problem can be partially solved by enabling the code for modern high performance computing architectures. Furthermore, algorithmic improvement similar to the method presented in Chapter 7 may be suitable to improve efficiency.

**Root growth** The presented mixed-dimension embedded methods are well-suited for growth simulations, since complicated re-meshing of the root geometry is avoided. In the case of drying soil, locally adaptive grids may be necessary. However, efficient strategies, e.g. based on octree data structures (Burstedde et al., 2011), can be employed since the computational grids for root and soil are independent. The presented locally mass-conservative continuous growth model is also suitable for the inclusion of feedback from soil properties on root growth.

**Competing effects in the vadose zone** The presented model has been used to qualitatively analyze competing water transport mechanism in the vadose zone (see Fig. 4.1) in Section 10.4. The detailed model may be used to provide improved relations for larger scale models for soil-atmosphere water transport.





# 11 Software and implementation\*

The following chapter discusses implementation aspects and software abstractions for solving embedded mixed-dimension problems. For the implementation of mixed-dimension problems in this work, we developed, in collaboration with Dennis Gläser, Kilian Weishaupt and others, a general software framework for multi-domain simulations. The software module is part of the open-source porous media simulator DuMu<sup>x</sup> since version 3.

DuMu<sup>x</sup> is an open-source simulator for flow and transport processes in porous media (Flemisch et al., 2011; Koch et al., 2020b). It provides a sustainable, consistent and modular framework for the implementation of linear and non-linear flow and transport models and constitutive relations. DuMu<sup>x</sup> has a focus on multi-component multi-phase flow in porous media, and model coupling. It is based on the Distributed Unified Numerics Environment (DUNE) (Bastian et al., 2008b,a; Bastian et al.), an open-source scientific numerical software framework for solving partial differential equations. DUNE and DuMu<sup>x</sup> are written using modern C++ programming techniques and C++ template meta programming for efficiency and description of generic interfaces. The DUNE core modules provide, for example, multiple grid managers implementing a versatile common grid interface (see also Section 11.1), linear algebra abstractions, the iterative solver template library (Blatt and Bastian, 2007), and abstractions facilitating parallel computing.

In DuMu<sup>x</sup>, embedded mixed-dimension problems, as understood in the context of this work, are considered a special category of multi-domain simulations, where several PDE systems, formulated for two or more domains, discretized with different discretization schemes, or considering different physical processes, are coupled, for example by the exchange of mass, momentum, or energy. Different types of such coupled systems are depicted in Fig. 11.1. In contrast to software that couples different solvers for the simulations of the processes in the individual domains (Gaston et al., 2009; Bungartz et al., 2016), implementing a multi-domain module in a single framework allows us to achieve simpler interfaces (no need to write adapter to different application programming interfaces (APIs)) and efficient and easy access to subdomain data. Consequently, this permits, for example, the efficient assembly of the full Jacobian of the coupled system, and the use of monolithic solvers. For

---

\*This chapter is based on Koch et al. (2020b).

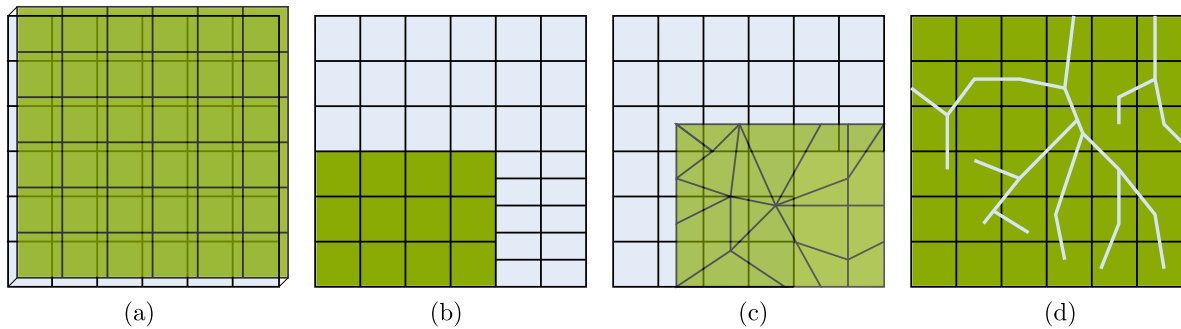


**Figure 11.1 – Different types of model coupling in DuMu<sup>x</sup> multi-domain simulations.** (a) multi-physics models (on the same grid), (b) multiple non-overlapping domains with sharp conforming or non-conforming interface, (c) multiple overlapping domains with different discretizations, (d) conforming and non-conforming (embedded) mixed-dimensional domains (1D-2D, 1D-3D, 2D-3D). The different coupling modes can also be combined. Typical mixed-dimensional simulations also solve multi-physics problems, or use different discretization schemes in the subdomains. The number of subdomains is not limited to two. Figure from Koch et al. (2020b).

many of the considered applications and problem sizes, such solvers have been found both more accurate and faster than iterative coupling methods in preliminary investigations, see, for example, the work by Beck (2019) on the comparison of iterative and monolithic solvers in the context of coupling flow and geomechanical processes in porous media. In comparison with writing a single-purpose code, developing a framework requires more initial effort to implement, produces possibly less efficient code for specific cases (depending on the abilities of the implementer), and results in more abstract code that maybe harder to understand the details to some people. However, there are some striking advantages. Abstract interfaces and generic programming reduce code duplication, making code easier to test and maintain. Furthermore, the implementation behind the interface maybe exchanged for more efficient versions in the future without changing the user code. Once a feature is implemented, it often becomes directly available to all user codes. An example from the multi-domain module is the time discretization scheme. The assembly routine for the explicit Euler scheme in time has been implemented once and is since available in all multi-domain codes which communicate with a generic assembler interface. Finally, the generic coupling interface briefly presented in Section 11.2, allows user code to couple any existing DuMu<sup>x</sup> model to other DuMu<sup>x</sup> models. Hence, although the implementation initially caused more development than a single-purpose code, we are convinced that it saved more time in the subsequent code development.

## 11.1 Network grids<sup>†</sup>

The tubular networks discussed in this work have to be discretized in form of a computational grid. However, the grid is somewhat non-standard as the element dimension is two dimensions less than the coordinate dimension. Furthermore, the grid does not have a manifold structure, that is, an element can have more than one neighbor element with identical geometry of the intersection between the elements. For reasons of efficiency, these properties might not be supported by every grid implementation. While the implementation is not very challenging, additional data structures and logic are required, resulting in memory and run-time overhead for users not interested in this feature. To solve this problem, DUNE provides a generic grid interface where the actual implementation is easily swapped for another. For instance, there is YaspGrid, an efficient (low memory and run-time overhead) implementation of structured grids, or UGGrid, providing a flexible unstructured grid implementation with local conforming and non-conforming refinement, and adaptive vertical and horizontal load balancing. The grid module `dune-foamgrid` is an implementation specialized on surface and network grids. Within the scope of this thesis, `dune-foamgrid` has been extended to support one- and two-dimensional simplex grids embedded in a physical Euclidean space of arbitrary dimension. Furthermore, its interface has been augmented by functions to grow and shrink the grid at run-time (add and remove elements). `dune-foamgrid` is open source and licensed under the LGPLv3+, or the GPLv2 with a linking exception clause. The git repository is currently hosted at <https://gitlab.dune-project.org/extensions/dune-foamgrid.git> and it is described in Sander et al. (2017). The following brief description is adapted from this publication.

The `FoamGrid` class is parameterized with a grid and a coordinate dimension. It can, for example, be constructed from a mesh file in the Gmsh format (Geuzaine and Remacle, 2009):

```
1 using namespace Dune;
2 using Grid = FoamGrid<1,3>;
3 auto grid = std::shared_ptr<Grid>(
    GmshReader<Grid>::read("filename.msh") );
```

Using the DUNE grid interface it can conveniently be written into a VTK file (without additional implementation from the `dune-foamgrid` side):

---

<sup>†</sup>This section is based on Sander, Koch, Schröder, and Flemisch (2017).

```

1 VTKWriter<Grid::LeafGridView> vtkWriter(grid->leafGridView());
2 vtkWriter.write("grid");

```

The file can be visualized, for example, with ParaView (Ahrens et al., 2005). User data is separate from the grid. In order to associate data with grid elements (entities of codimension 0) or vertices (entities of codimension  $d$  in a  $d$ -dimensional grid), the grid implementation provides indices (zero-based consecutive integers) for every entity in the grid. Furthermore, each entity is assigned a unique identifier which is persistent with grid adaptation and grid growth.

A specialty of `dune-foamgrid` is the ability to add and remove elements after grid construction. This makes `dune-foamgrid` a good candidate for modeling root growth, angiogenesis (vessel growth), or fracture growth. The user interface combines ideas from DUNE's `GridFactory` and the adaptivity interface. Since data is stored separately from the grid, the interface also contains functions that help a user to manage the data transfer during growth.

The insertion and removal of elements is a two-step process. New elements and vertices passed to the `FoamGrid` object are not directly inserted but queued for later insertion. Moreover, elements can be marked for removal. Once all desired elements and removal markers are known, the actual grid modification takes place in a second step.

Queuing elements for insertion and removal is controlled by three public member function of the `FoamGrid` class. The first,

```

1 unsigned int insertVertex(const FieldVector<ctype, dimworld>& x);

```

queues a new vertex with coordinates `x` for insertion. The return value of the function is an index that can be used to refer to the new vertex when inserting new elements. The index remains fixed until all queued elements are actually inserted in the grid (by the `grow` function), but may change during the execution of that function. Elements are inserted with

```

1 void insertElement(const GeometryType& type,
2                   const std::vector<unsigned int>& vertices);

```

mimicking the corresponding member function of the `GridFactory` class. The argument `type` has to be a simplex type, because (currently) `dune-foamgrid` supports only simplex elements. The array `vertices` must contain the indices of the vertices of the new element

to be inserted. These can be either indices of existing vertices, or new indices obtained as the return values of the `insertVertex` function.

Finally, the function

```
1 void removeElement(const Codim<0>::Entity& element);
```

marks the given element for removal.

After all elements have been inserted (or marked for removal), the grid is modified using the member function

```
1 bool elementsInserted = grid->grow(); // true if at least one
    element was inserted
```

While element removal is guaranteed, queuing elements does not assure that the element will be inserted. New elements are restricted by the fact that DUNE grids are hierarchic objects. The vertices given by the user to form an element are always leaf vertices but may be contained in different hierarchic levels. However, elements can only be constituted by vertices of the same level. Therefore, new elements in `FoamGrid` are always inserted on the lowest possible level substituting the given vertex by its hierarchic descendants or ancestors. Note that it is not generally guaranteed that relatives of the given vertices on the same level can be found. In that case, the element will not be inserted. The function `grow` will return `true` if it was possible to insert at least one element.

After the call to `grow`, it is possible to check whether a given element has been created by the last call to the `grow` function:

```
1 bool isNew = element.isNew(); // true if element was created
    by last growth step
```

where `isNew()` is a member function of the interface class `Entity<0>`, that is `elements`. This function is helpful, for example, when setting initial values or boundary conditions for newly created elements.

The two following functions have been added later (not part of the initial growth interface described by Sander et al. (2017)):

```

1 unsigned int growthInsertionIndex(const Codim<0>::Entity&
    element) const;
2 unsigned int growthInsertionIndex(const Codim<dimgrid>::Entity&
    vertex) const;

```

They return the index, an element or vertex was assigned at insertion time (its index in the insertion queue). This is necessary to attach data to new elements at insertion time. With this feature, data can be stored in a temporary container with the size of the queue during insertion. After calling `grow()`, the data can be mapped to the new element or vertex using its new index in the grid, and the intersection index obtained by the `growthInsertionIndex` function.

Each growth step is completed with the call

```
1 grid->postGrow();
```

removing all `isNew` markers.

Summing up, growing or shrinking the grid and transferring user data attached to the grid consists of the following steps.

1. Mark elements for removal and queue new vertices and elements for insertion,
2. transfer all simulation data attached to the grid into an intermediate container mapping entity identifier to data,
3. call `grow()`,
4. resize data container and copy data from the intermediate container into the data container,
5. set initial data at newly created elements and vertices and boundary conditions at newly formed boundaries,
6. finalize by calling `postGrow()`.

Grid vertices in `dune-foamgrid` can be moved via the grid interface. There is a public member function of the `FoamGrid` class with the definition

```

1 void setPosition(const Traits::Codim<dimgrid>::Entity& vertex,
2                 const FieldVector<ctype, dimworld>& pos);

```

that resets the position of a vertex (`vertex`) to a given position (`pos`). This feature is essential to model continuous grid growth with a given time step size without creating lots of small elements in every step.

The presented features of `dune-foamgrid` are demonstrated at the example of root growth, and blood flow in a capillary network using adaptive grid refinement in Sander et al. (2017). Moreover, `dune-foamgrid` is used for the computational grid of the network domain in all numerical simulations in this work.

## 11.2 Coupling different domains

The idea of DuMu<sup>x</sup> multi-domain simulations is to solve a coupled PDE system, of which a subset (a subdomain model) can be formulated on a different domain, potentially with different dimensionality, and may be discretized using different meshes or different spatial discretization schemes. The framework is designed to minimize software coupling, such that two existing DuMu<sup>x</sup> models can be coupled without modifications in the core components. To be minimally invasive, only the `Problem` class is required to be slightly modified to become a sub-problem. The `Problem` class in DuMu<sup>x</sup> is implemented by the end-user and specifies initial and boundary conditions, and source terms. Sub-problems define their own initial and boundary conditions, source terms, and store a pointer to the coupling manager instance. Boundary and source terms may depend on quantities of other domains, such as in Eqs. (6.7a) and (6.7b). For the data transfer, we introduce the concept of a coupling manager which is represented in the code by classes that implement the `CouplingManager` interface. A coupling manager has to provide the information which degrees of freedom in one domain are coupled to which degrees of freedom in another domain (the coupling stencil). To this end, every coupling manager has to implement the function shown in Listing 11.1.

**Listing 11.1 – Coupling stencil.** The member function `couplingStencil` has to be implemented by all deriving coupling manager implementations. The template arguments `i` and `j` are the indices of one pair of coupled subdomains. They are deduced from the two index objects `domainI` and `domainJ`, passed as arguments to the function. In case two subdomains are not coupled, the function is required to return a reference to an empty stencil vector. For domain `i`, an instance of the element is passed, for which the residual in the element-wise assembly is to be computed. The function returns a vector of all indices of degrees of freedom coupled to one of the degrees of freedom associated with element `elementI`.

---

```

1 // required member function of every CouplingManager class
2 // return the coupling stencil for element elementI (domain i)
3 // with respect to degrees of freedom in domain j
4 template<std::size_t i, std::size_t j>
5 const std::vector<std::size_t>&
6 couplingStencil(Dune::index_constant<i> domainI,
7                const Element<i>& elementI,
8                Dune::index_constant<j> domainJ) const;

```

Moreover, the coupling manager has to transfer data between the sub-problems. This general concept can be used to implement a wide class of coupling schemes. Apart from the simulation in this thesis the multi-domain framework of DuMu<sup>x</sup> has been successfully applied to flow and transport models for fractured rock systems (Gläser et al., 2017b; Gläser et al., 2019), coupled porous medium flow and atmosphere flow (Darcy-Navier-Stokes) at the soil surface (Schneider et al., 2020), and for a model coupling a pore-network model to a Navier-Stokes model (Weishaupt et al., 2019). The implementation of the different mixed-dimension embedded schemes presented in this work, only differ in the implementation of the `CouplingManager` class but share the same code for temporal and spatial discretization and the mathematical models in the sub-domains.

### 11.3 Intersecting grids

Finding the coupling stencils usually involves intersecting two grids. For this purpose, we implemented efficient grid intersection algorithms based on axis-aligned bounding box volume hierarchy data structures (Ericson, 2004; Massing et al., 2013) computed for DUNE grids. Here, we compute this spatial data structure of a given computational grid with elements  $K$  using a top-down algorithm (Ericson, 2004). To this end, we first compute an axis-aligned bounding box (AABB) of each element  $K$ . Using this information, the AABB for the entire grid can be computed (root node). The set of elements is then split in two halves (children nodes) along the longest axis of the root AABB, where the spatial position of each node is determined by the AABB centroid. In a recursive algorithm, the AABB is computed for each child and the set of elements belonging to the child node are treated in the same procedure. The recursion ends whenever an AABB only contains a single element. The different levels of AABBs for a simplex grid are shown in Fig. 11.2.



The result is a binary tree structure of AABBs allowing for efficient intersection detection.

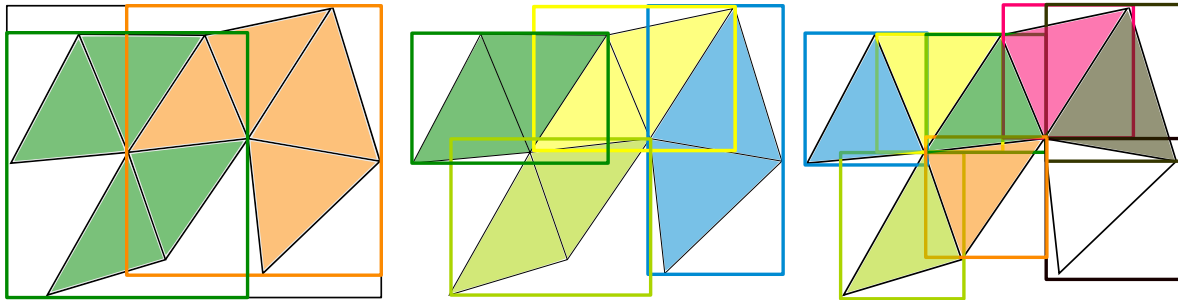


**Figure 11.2 – Axis-aligned bounding box (AABB) volume hierarchy.** Unstructured simplex grid. The individual images show the 0<sup>th</sup> (root) and 1<sup>st</sup> level (left), the 2<sup>nd</sup> level (middle), and the 3<sup>rd</sup> level (right) of the binary tree structure. Bounding boxes containing only one entity are also called the leaf nodes of the AABB tree.

For example, to determine the element(s) intersecting with a given point, we first check if the point intersects the root bounding box (cheap intersection test). If the point intersects, we can step-wise eliminate half of the cells by checking the intersections with the children nodes. If a leaf node AABB intersects, a so-called primitive test (expensive intersection test) has to be performed, where the point is intersected with the actual geometry of the cell. The resulting intersection algorithm has logarithmic complexity. Likewise, two AABB trees can be intersected recursively. Primitive intersections only need to be computed if leaf AABBs intersect. The implementation of the AABB tree data structure in the DuMu<sup>x</sup> class `BoundingBoxTree`<sup>‡</sup> is based on the implementation in FEniCS (Massing et al., 2013). Most of the primitive intersection algorithms are based on the suggestions by Ericson (2004). We can currently intersect 1D and 2D grids with 1D, 2D, and 3D grids, where the coordinate dimension is determined by the grid with the highest dimension. The grid intersection user interface is that of the `MultidomainGlue` class. The interface is similar to that of the `dune-grid-glue` (Bastian et al., 2010) module which implements an advancing front algorithm instead of an AABB-tree-based algorithm. In a comparison between the two implementations, we found that the AABB tree was more reliable and efficient for intersecting network grids with embedding background grids. Listing 11.2 shows how to intersect two grids for a DuMu<sup>x</sup> multi-domain simulation, and how to iterate over the intersection objects.

<sup>‡</sup>see `dumux/common/geometry/boundingboxtree.hh` in the DuMu<sup>x</sup> git repository hosted at <https://git.iws.uni-stuttgart.de/dumux-repositories/dumux.git>

**Listing 11.2 – Intersection of two grid geometries.** A grid geometry is a DuMu<sup>x</sup>-specific wrapper class around DUNE grids, see Koch et al. (2020b). Here, we intersect the grid geometries (`lowDimGridGeometry` and `bulkGridGeometry`) The intersection objects (simplices) can be iterated over using a range-based for loop. Each intersection has geometry information and connectivity information (which elements in grid A and B do I belong to).

```

1
2 // intersect two grid geometries
3 // we choose domain (first argument) = lowDim and target (second argument) = bulk
4 // see <dumux/multidomain/glue.hh>
5 // constructs AABB trees if not constructed yet
6 // intersects AABB trees and computes intersection objects
7 const auto glue = makeGlue(lowDimGridGeometry, bulkGridGeometry);
8
9 // iterate over all intersections
10 for (const auto& is : intersections(glue))
11 {
12     // the element index of the lowDim grid element of this intersection
13     // there is only one such element
14     const auto& domainEntity = is.domainEntity(0);
15     const auto domainIdx = lowDimGridGeometry.elementMapper().index(domainEntity);
16     std::cout << "Element of network grid with index " << domainIdx
17               << " intersects with bulk grid elements:";
18     // there might be multiple bulk elements associated with this intersection
19     for (unsigned int i = 0; i < is.numTargetNeighbors(); ++i)
20     {
21         // the element index of the bulk element of this intersection
22         const auto targetIdx =
23             bulkGridGeometry.elementMapper().index(is.targetEntity(i));
24         std::cout << " " << targetIdx;
25     }
26     // get the geometry of the intersection
27     auto isGeo = is.geometry();
28     std::cout << '\n' << "The intersection volume is " << isGeo.volume()
29               << " The intersection is a " << isGeo.type()
30               << " with " << isGeo.corners() << " corners" << '\n';
31 }

```

Finally, we note that there are other types of bounding geometries, as well as other types of spatial data structures for fast intersection detection, that may be faster for a specific setting. For an overview, we refer to Ericson (2004). However, in the numerical experiments in this work, the computational time and the memory spent on the grid intersection calculation is negligibly small in comparison with other parts of the simulation such as assembly and linear solver execution. This is even true for simulations with growing roots, where the grid intersection is recomputed in every time step.

## 11.4 Assembly and linear solver

DuMu<sup>x</sup> provides an assembler class for multi-domain models, which assembles the discrete PDE system in residual form

$$A\Delta u = \begin{bmatrix} A_1 & C_{12} & \dots & C_{1n} \\ C_{21} & A_2 & & \\ \vdots & & \ddots & \\ C_{n1} & & & A_n \end{bmatrix} \begin{bmatrix} \Delta u_1 \\ \Delta u_2 \\ \vdots \\ \Delta u_n \end{bmatrix} = \begin{bmatrix} r_1 \\ r_2 \\ \vdots \\ r_n \end{bmatrix} = r, \quad (11.1)$$

where  $A_i$  is the Jacobian of the discrete PDE system for subdomain  $i$ , and  $C_{ij}$  is the coupling Jacobian with derivatives of residuals of domain  $i$  with respect to degrees of freedom of domain  $j$ ,  $C_{ij} = \frac{\partial r_i}{\partial u_j}$ . The assembler class and the matrix class are generic, so that the sub-vectors  $u_i$  and sub-matrices  $A_i$  can themselves have a block structure, and support an arbitrary number of subdomains. The block structure can be exploited, for example, for constructing preconditioners for a monolithic system, or to implement schemes based on algebraic decomposition, where the subdomain systems are solved successively in an iterative algorithm. For the numerical examples in this thesis, two preconditioned iterative solvers have been implemented using the generic solver interfaces of `dune-istl` (Blatt and Bastian, 2007). A left-preconditioned version of the system in Eq. (11.1) is given by

$$P^{-1}Ax = P^{-1}r, \quad (11.2)$$

where  $P^{-1}$  is an approximation of  $A^{-1}$ , for which a matrix-vector product,  $P^{-1}v$ , is cheap to compute. In the applications in this work, we use a left-preconditioned stabilized bi-conjugate gradient solver (Saad, 2003, Chapter 7) with block-diagonal preconditioners of the form

$$P^{-1} = \begin{bmatrix} P_1^{-1}(A_1) & & & \\ & P_2^{-1}(A_2) & & \\ & & \ddots & \\ & & & P_n^{-1}(A_n) \end{bmatrix}, \quad (11.3)$$

where  $P_i^{-1}(A_i)$  is an approximation of the  $A_i^{-1}$ , constructed either by an incomplete LU-factorization of the matrix  $A_i$  using  $A_i$ 's sparsity pattern (zero fill-in) (Saad, 2003, Chapter 10), or the algebraic multigrid (AMG) preconditioner implemented in `dune-istl`. Other

preconditioned solvers for mixed-dimension embedded systems are described by Kuchta et al. (2019); Cattaneo and Zunino (2014).

## 11.5 Sustainable development and quality assurance<sup>§</sup>

We close this chapter with a comment on sustainable software development and quality assurance in research software. Together with D. Kempf, we assembled typical quality characteristics expected from scientific software and software frameworks in Kempf and Koch (2017):

- **Correctly implemented code:** the code is expected to be implemented correctly with respect to syntax and functionality of features. It includes e.g. that the source code compiles with all compilers satisfying the communicated minimum requirements. Implementation correctness also includes run-time criteria like the absence of memory leaks and race conditions and proper error handling (e.g. through the use of exceptions).
- **Numerically correct algorithms:** the implemented algorithms should function as intended, namely reproduce results expected from theory. Often, there are well-known mathematical properties of an implemented algorithm that have to be satisfied.
- **Trustworthy results:** models and simulations built with the numerical software framework should produce trustworthy results, in the sense of correctly modeling what experiments or experts predict. Note that this is not solely a task for the framework but also for the scientist to use it as intended.
- **Good documentation, maintainability, testability:** a high coverage of code documentation facilitates code re-usage and also testing.
- **Flexibility:** in order to have many possibilities of combining features, the implementation and interfaces need to be designed with a certain level of abstraction. This is a key competence of numerical software frameworks.
- **Sufficient performance and scalability.**

---

<sup>§</sup>This section is based on Kempf and Koch (2017).

When writing research code, such as for this thesis, it is often difficult to write software satisfying all criteria, given the limited scope of a thesis project. However, we advocate implementing such code by using and contributing missing features to existing research software frameworks. The scientist usually profits from already implemented features (direct reuse) or examples for similar examples (reuse after adaptation), which are already tested for quality criteria. Moreover, the software is often more easily understood by others (using abstractions and conventions of the framework), in particular those peers already working with the same framework. This increases the chance of re-usage by others which also always means testing by others. Additionally, frameworks with larger communities often feature some type of support (mailing list, issue tracker) and a transparent development process. That means that contributions will be discussed, vetted, and tested by others decreasing the chance of possible software bugs. Frameworks often contain a type of testing infrastructure and software testing support for assessing quality continuously. These testing capabilities can be used to set up tests for user software as well. Finally, if software is written in a flexible and more abstract way, it is much easier to adapt certain aspects of the simulations in the research. For example, in Koch et al. (2018b) we demonstrate that by the use of the DuMu<sup>x</sup> framework it is simple to change the governing equations for the flow simulation in the soil. Through the abstractions of the new multi-domain framework, we were able to run simulations with different coupling methods in Chapter 7, by only changing the coupling manager class described in Section 11.2. Likewise, a first prototype implementation for the new numerical method described in Chapter 7 could be realized in a single day, by implementing a different coupling manager.

On the other hand, the flexibility of research software frameworks makes testing challenging. This is mostly due to the high number of feature combinations possible. The number of possible parameter combinations, model coupling possibilities, and possible PDEs is infinite. That is why typical approaches from the software engineering community such as variability models in Software Product Line Engineering (Pohl et al., 2005) are especially difficult to apply in the context of numerical research software (Rommel et al., 2011, 2012; Rommel, 2014; Kempf and Koch, 2017). In Kempf and Koch (2017), as an alternative approach, we design a (system-)testing module at the example of DUNE with the following characteristics:

- testing infrastructure integrated in the existing development workflow of DUNE
- writing a new system test is as simple as writing a unit test
- the possible combinations are reduced by expert knowledge of the developer

- high coverage is realized by the combination of many system tests
- testing infrastructure is also available in user modules (such as DuMu<sup>x</sup>)

The efforts resulted in the DUNE module `dune-testtools`, which is as such part of the DUNE environment.

Finally, we note that the code for most of the numerical examples in this work are publicly available as so-called DuMu<sup>x</sup>-pub modules. These modules are separate DUNE modules which can be installed in the same way as DuMu<sup>x</sup>. Installation instructions are given in the git repository of every module. The hyperlinks to these git repositories can be either found at the end of Chapters 7 to 9 and after each examples in Chapter 10. Additionally, an example for a root water uptake simulation, and the tissue perfusion case with an analytic solution from Chapter 7 are included in the test suite of DuMu<sup>x</sup>, since version 3.0 (Koch et al., 2018a), and are continuously tested against reference solutions in nightly builds.

# 12 Summary and outlook

## 12.1 Summary

In this work, we have investigated numerical aspects and applications of mixed-dimension embedded models for porous media systems with embedded tubular network systems. A mathematical model for biological tissue perfusion with discretely resolved microvasculature has been presented in Chapter 3. A model describing root water uptake and growth and other fluid-mechanical processes in the vadose zone has been developed in Chapter 4. Finally, well modeling has been discussed in Chapter 5. All models are based on a spatial model reduction technique describing flow in the network system by cross-section averaged quantities with a single spatial dimension per segment. The straight segments are coupled at bends and bifurcation by applying physical constraints such as mass conservation. In each application, mass transport from the network domain into the embedding porous domain is an essential process. In Chapter 6, several existing coupling methods have been summarized in a general mathematical form by introducing smoothing kernels to handle the dimensional gap. A new method for linear and elliptic mixed-dimension embedded models has been developed in Chapter 7. We can show numerically, that the method exhibits improved approximation qualities of the exchange fluxes between porous and network compartment for coarse grid resolutions. The robustness and numerical accuracy has been investigated in a series of numerical experiments for isotropic and anisotropic, homogeneous porous media. The extension of the method for anisotropic porous media has been presented for the case of well modeling in Chapter 8. Furthermore, the method has been compared to several existing approaches. In Chapter 9, we have developed an MRI model on the capillary scale. Being formulated on the same scale, the MRI model and the mixed-dimension embedded tissue perfusion model could be combined to model the magnetic resonance of a small brain tissue sample. The integral MR signal from this sample has been shown to match clinical MRI data from multiple sclerosis patients. To this end, the model has been parameterized using Bayesian parameter inference and classical optimization techniques. It has been shown that the diffusive permeability of a contrast agent through the capillary wall is essential to distinguish between active and inactive lesions. In Chapter 10, we showed simulations of root water uptake and growth. Furthermore, we argue that the presented mixed-dimension

embedded model only produces reliable results for high permeable and wet soils, due to the large local pressure gradients occurring in dry soils. However, it remains unclear whether such large gradients occur in real systems or result from shortcomings in the state-of-the-art uptake model. All simulations have been performed using a unified software framework integrated in the open-source simulator DuMu<sup>x</sup>. Software aspects of mixed-dimension embedded models have been discussed in Chapter 11. The software components are generic, so that the framework is useful beyond the applications presented in this work. Finally, we have briefly discussed aspects of sustainable research software development.

## 12.2 Outlook

**Nonlinear mixed-dimension problems** Mixed-dimension embedded problems, as presented in this work (1D-3D), often lead to large local gradients for relevant physical quantities. Consequently, these gradients in vicinity of the embedded networks require fine grid resolutions in the porous domain. Methods to mitigate this problem, including the methods developed in this work, exploit the fact that the involved equations are linear or can be linearized. However, such methods might not be suitable for nonlinear problems. For example, the soil permeability model for the root water uptake problem is strongly nonlinear. To simulate dry soils efficiently (with coarse computational grids), suitable flux correction methods have to be developed and analyzed.

**Bifurcations** Both the models for flow and transport in the network domain and the models for mass and energy exchange between network and porous medium are commonly developed for straight line segments. However, bifurcation regions, depending on their size relative to the distance between bifurcations, may significantly alter the flow field for some applications. Moreover, the analysis in Chapter 7 showed that the predicted exchange flux differs at bifurcations for different numerical methods. The local differences did not show a strong effect on the global mass balance for the presented scenarios. However, it is still to be investigated, whether this holds true for all applications.

**MRI scale dependence** The interpretation of MRI data is resolution dependent, which is of particular importance due to the availability of higher magnetic field strength (Ladd et al.,



2018). One aspect of this problem could be the heterogeneity of the vascular network. In this work, only a small tissue sample with a single vascular network geometry was investigated. However, it remains unclear if the estimated parameter values are independent of the spatial scale. Therefore, the study needs to be repeated for different vascular geometries and tissue sample sizes. Furthermore, the comparison with clinical data acquired with differently parameterize MR sequences is necessary to evaluate the robustness of the model.

**Root mass balance and growth** The root growth algorithm does currently not consider the nutrient demand of growth. Hence, root growth is not affected, if no nutrients are present or water and nutrient uptake is difficult due to dry soil conditions. Therefore, the current model is restricted to growth under optimal supply conditions. Moreover, fine local grid resolutions in the case of growing root systems require locally adaptive grids. This is a straightforward extension of the presented model by using the adaptive grid capabilities of the DUNE grid interface, and a mass-conserving interpolation strategy between different grid levels.

**Parallelization** The analysis of many mixed-dimension problems demands large computational domains. For example, to investigate the scale dependence of the developed MRI model, time-dependent simulations with millions of degrees of freedom become necessary. Other examples include root water uptake for mature root systems, and the interaction of several competing root systems in a field. While parallel algorithms were used in the parameter inference problem in Chapter 9, the mixed-dimension solver developed in this work is purely sequential. To leverage the computing power of modern high performance computing infrastructure, the code has to be parallelized. Parallelization is non-trivial since two or more non-matching computational grids are involved. For example, the distributed memory parallelization model in DUNE (DuMu<sup>x</sup>) is grid-based. Communication patterns via intersections of multiple grids are yet to be implemented\* and it may be difficult to achieve good load balance.

---

\*First steps have been undertaken with the DUNE module `dune-grid-glue` (<https://gitlab.dune-project.org/extensions/dune-grid-glue>)



# A Appendices

## A.1 Dimensional analysis of a simplified tissue system

We want to analyze which tissue compartment is limiting for fluid flow across the vessel membrane and in the extra-vascular space. To this end, consider the dimensionless equation

$$-\nabla^* \cdot (\Theta_m \nabla^* p_m^*) = \Theta_\omega \Delta p^* \delta_\Lambda^*, \quad (\text{A.1})$$

cf. Eq. (6.8) with a given constant pressure drop across the capillary wall,  $\Delta p^* = 1$ . We consider a circular cross-section perpendicular to a single vessel with radius  $r_v$  in a cylinder of radius  $l_m$ . A dimensionless radius is given by  $r^* = l_m^{-1} r$ . Then,  $p^*$  admits a radially symmetric analytical solution of the form

$$p^*(r^*) = p_{m,\mathbb{W}}^* - \frac{\Theta_m}{\Theta_\omega} \frac{1}{2\pi} \ln\left(\frac{l_m}{r_v}\right), \quad (\text{A.2})$$

where we assumed that the flow rate over the vessel cross-section wall is equal to the flow rate over the circle with radius  $l_m$  (e.g. an fluid emitting arterial capillary vessel is symmetrically surrounded by venous capillary vessels that absorb the emitted fluid), and the dimensionless pressure on the vessel surface is  $p_{m,\mathbb{W}}^*$ . The ratio of the pressure drop in the extra-vascular space to the pressure drop across the capillary wall is given by

$$\frac{p_{m,\mathbb{W}}^* - p^*(1)}{\Delta p^*} = \frac{\Theta_\omega}{\Theta_m} \frac{1}{2\pi} \ln\left(\frac{l_m}{r_v}\right). \quad (\text{A.3})$$

For the parameter values given in Section 6.2.1, we obtain values between 0.1 (continuous capillaries) and 100 (fenestrated capillaries). Hence, in healthy brain tissue the capillary wall is limiting the fluid exchange, while for tumor tissue the interstitium is limiting. Finally, we note that due to the logarithmic pressure profile, the flow velocities  $v$  close to the vessel are much higher than velocities at some distance. For example,

$$\frac{v(r_v l_m^{-1})}{v(1)} = \frac{\nabla p_m^*(r_v l_m^{-1})}{\nabla p_m^*(1)} = \frac{l_m}{r_v} \approx 17. \quad (\text{A.4})$$

## A.2 Dimensional analysis of a simplified root system

We analyze the ratio of the axial pressure drop along the root xylem to the pressure drop across the root cortex for different ratios  $\Theta_\omega \Theta_v^{-1}$ . To this end, we consider the dimensionless equation

$$\frac{\partial^2 p_v^*}{\partial s^{*2}} = \frac{\Theta_\omega}{\Theta_v} \Delta p^*, \quad (\text{A.5})$$

cf. Eq. (6.8), with the dimensionless pressure drop across the root cortex  $\Delta p^* = (p_v^* - p_m^*)$ , for a given dimensionless soil pressure  $p_m^*$ . We assume that we have a single straight vertical root with the length  $l_v$  such that the dimensionless coordinate  $s^* \in [0, 1]$ , and prescribe  $\partial p_v^* / \partial s^* = \gamma$  with constant  $\gamma$  at the root collar ( $s^* = 1$ ) and  $\partial p_v^* / \partial s^* = 0$  at the root tip ( $s^* = 0$ ) as boundary conditions.

### Case 1: Constant pressure drop across the root cortex

We assume that  $\Theta_\omega \Theta_v^{-1} \Delta p^*$  is constant. Then, Eq. (A.5) admits the analytical solution

$$p_v^* = \frac{1}{2} \gamma s^{*2} \quad \text{and} \quad \gamma = \frac{\Theta_\omega}{\Theta_v} \Delta p^*. \quad (\text{A.6})$$

We can relate the mean pressure gradient along the root to the mean pressure drop across the root cortex

$$\frac{\overline{\frac{\partial p_v^*}{\partial s^*}}}{\Delta p^*} = \frac{\int_0^1 \frac{\partial p_v^*}{\partial s^*} ds^*}{\Delta p^*} = \frac{1}{2} \frac{\Theta_\omega}{\Theta_v}. \quad (\text{A.7})$$

Consequently, for large  $\Theta_\omega \Theta_v^{-1}$  the pressure drop in the root is much larger than the pressure drop across the root cortex. For small  $\Theta_\omega \Theta_v^{-1}$  the largest pressure drop is across the root cortex.

### Case 2: Constant soil pressure

A second scenario can be constructed if the dimensionless soil pressure  $p_m^*$  is assumed constant (e.g. for highly permeable soils). Then,  $\Delta p^* = (p_v^* - p_m^*)$  is a linear function of

the dimensionless root (xylem) pressure, and Eq. (A.5) admits the analytical solution

$$p_v^* = C (\exp(\beta s^*) + \exp(-\beta s^*)) + p_m^*, \quad (\text{A.8})$$

with some constant  $C$  (which could be determined using the root collar boundary condition) and  $\beta = \sqrt{\Theta_\omega \Theta_v^{-1}}$ . Then, the ratio of the mean pressure gradient along the root to the mean pressure drop across the root cortex is

$$\frac{\overline{\frac{\partial p_v^*}{\partial s^*}}}{\overline{\Delta p^*}} = \frac{\int_0^1 \frac{\partial p_v^*}{\partial s^*} ds^*}{\int_0^1 \Delta p^* ds^*} = \beta \frac{\exp(\beta) + \exp(-\beta) - 2}{\exp(\beta) - \exp(-\beta)} = \beta \tanh\left(\frac{\beta}{2}\right) := f(\beta). \quad (\text{A.9})$$

Note that

$$f(\beta) \approx \begin{cases} \beta & \text{for } \beta > 10 \\ \frac{1}{2}\beta^2 & \text{for } \beta < 0.1 \end{cases} \quad \text{and} \quad \lim_{\beta \rightarrow 0} = 0, \quad (\text{A.10})$$

so that for small  $\Theta_\omega \Theta_v^{-1}$  the result is the same as for Case 1 Eq. (A.7). This result is sensible, since for small  $\Theta_\omega \Theta_v^{-1}$  the root pressure barely changes with  $s^*$ , so that  $\Delta p^*$  can be considered constant.

### A.3 Additional vessel network data

The vessel network used in Section 7.3.4 is described in Table A.1.

**Table A.1 – Vessel network data.** Specifications for the numerical experiment in Section 7.3.4. First two columns list vertex indices and coordinates in  $\mu\text{m}$ . Boundary conditions are supplied, if the vertex is a boundary vertex. 4th and 5th columns list the segment connectivity and the corresponding segment radius in  $\mu\text{m}$ .

index	coordinates ( $\mu\text{m}$ )	boundary condition	segment	radius ( $\mu\text{m}$ )
0	(20, 20, -10)	$v = 1.0 \text{ mm s}^{-1}$	(0, 1)	3.5
1	(20, 20, 50)	-	(1, 2)	3.5
2	(20, 20, 110)	$\tilde{p}_{v,\text{out}} = 2300 \text{ Pa}$	(3, 4)	3.0
3	(60, -10, 20)	$v = 0.8 \text{ mm s}^{-1}$	(4, 5)	3.0
4	(60, 20, 20)	-	(5, 6)	3.0
5	(70, 40, 20)	-	(6, 7)	3.0
6	(80, 60, 20)	-	(8, 9)	3.0
7	(110, 60, 20)	$\tilde{p}_{v,\text{out}} = 3400 \text{ Pa}$	(9, 10)	3.0
8	(80, 110, 80)	$v = 0.8 \text{ mm s}^{-1}$	(10, 11)	3.0
9	(80, 80, 80)	-	(11, 12)	3.0
10	(80, 70, 60)	-	(13, 14)	3.0
11	(20, 80, 20)	-	(14, 15)	3.0
12	(20, 80, -10)	$\tilde{p}_{v,\text{out}} = 2300 \text{ Pa}$	(15, 16)	3.0
13	(60, -10, 80)	$\tilde{p}_{v,\text{out}} = 3400 \text{ Pa}$	(16, 17)	3.0
14	(60, 20, 80)	-		
15	(40, 70, 80)	-		
16	(20, 80, 80)	-		
17	(-10, 80, 80)	$v = 0.8 \text{ mm s}^{-1}$		

#### A.4 Rotation of coordinates in well-bore ellipse axes

In this section, we derive a rotation operation such that the first and second coordinate are aligned with the major and minor axis of the well-bore ellipse and third axis is a normal vector on the ellipse plane. To determine the corresponding rotation matrix  $\tilde{R}$ , we need to characterize this well-bore ellipse. The well cylinder in  $x$ -coordinates is given by

$$\mathbf{x}^T \Psi \mathbf{x} = r_\omega^2, \quad \Psi = I - \phi \phi^T. \quad (\text{A.11})$$

After stretching, the coordinate system can be rotated with the rotation matrix  $R$  so that the third axis is aligned with the well direction. Then, projecting into the plane perpendicular

to the well direction yields the well-bore ellipse equation

$$\hat{v}^T E \hat{v} = \hat{v}^T P^T R \tilde{S}^{-1} \Psi \tilde{S}^{-1} R^T P \hat{v} = r_\omega^2, \quad \tilde{S}^{-1} R^T P \hat{v} = \mathbf{x} \quad (\text{A.12})$$

in  $\hat{v}$ -coordinates, where

$$R = 2 \frac{(\mathbf{e}_3 + \psi')(\mathbf{e}_3 + \psi')^T}{(\mathbf{e}_3 + \psi')^T(\mathbf{e}_3 + \psi')} - I, \quad \mathbf{e}_3 = \begin{bmatrix} 0 \\ 0 \\ 1 \end{bmatrix}, \quad P = \begin{bmatrix} 1 & 0 \\ 0 & 1 \\ 0 & 0 \end{bmatrix}. \quad (\text{A.13})$$

The rotation matrix  $R$  can be derived using Rodrigues' rotation formula as shown in Appendix A.5. The length of the major and minor ellipse axis are found as  $a = r_\omega \gamma_1^{-1/2}$  and  $b = r_\omega \gamma_2^{-1/2}$ , where  $\gamma_i$  are the eigenvalues of  $E$ , and the axis orientations are given by  $\mathbf{v}_1 = P \hat{v}_{E,1}$ ,  $\mathbf{v}_2 = P \hat{v}_{E,2}$ , where  $\hat{v}_{E,i}$  denote the corresponding eigenvectors of  $E$ . We assume that the eigenvalues and eigenvectors are sorted such that  $a \geq b$ , and oriented such that  $\psi' = \mathbf{v}_1 \times \mathbf{v}_2$ . Finally the desired rotation is given by

$$V : \mathbb{R}^3 \rightarrow \mathbb{R}^3, \mathbf{u} \mapsto \mathbf{v} = \tilde{R} \mathbf{u} = \hat{R}^T R^T \mathbf{u}, \quad (\text{A.14})$$

where

$$\hat{R} = \left[ \mathbf{v}_1 \mid \mathbf{v}_2 \mid \psi' \right] \quad (\text{A.15})$$

is rotating about the well direction axis such that the coordinate system is aligned with the principal ellipse axes.

## A.5 Rodrigues' rotation formula

We want to rotate a given basis  $\mathcal{B} = \{\mathbf{e}_1, \mathbf{e}_2, \mathbf{e}_3\}$  such that  $\mathbf{e}_3$  is aligned with a vector  $\psi$ . The Rodrigues' rotation formula (Dai, 2015) describes a rotated vector  $\mathbf{x}_{\text{rot}}$  obtained by rotating a vector  $\mathbf{x}$  by the angle  $\theta$  about an axis given by the unit normal vector  $\mathbf{k}$

$$\mathbf{x}_{\text{rot}} = \mathbf{x} \cos \theta + (\mathbf{k} \times \mathbf{x}) \sin \theta + \mathbf{k}(\mathbf{k} \cdot \mathbf{x})(1 - \cos \theta). \quad (\text{A.16})$$

The desired rotation can be described by a rotation by an angle  $\theta = \pi$  about the axis  $\mathbf{k} = \frac{(\mathbf{e}_3 + \psi)}{2|\mathbf{e}_3 + \psi|}$ ,

$$\mathbf{x}_{\text{rot},\pi} = 2\mathbf{k}(\mathbf{k} \cdot \mathbf{x}) - \mathbf{x}. \quad (\text{A.17})$$

Equation (A.17) can be expressed in matrix notation as  $\mathbf{x}_{\text{rot},\pi} = R\mathbf{x}$  with

$$R = (2\mathbf{k}\mathbf{k}^T - I), \quad R = R^T = R^{-1}, \quad \det(R) = 1. \quad (\text{A.18})$$

## A.6 Properties of the conformal mapping

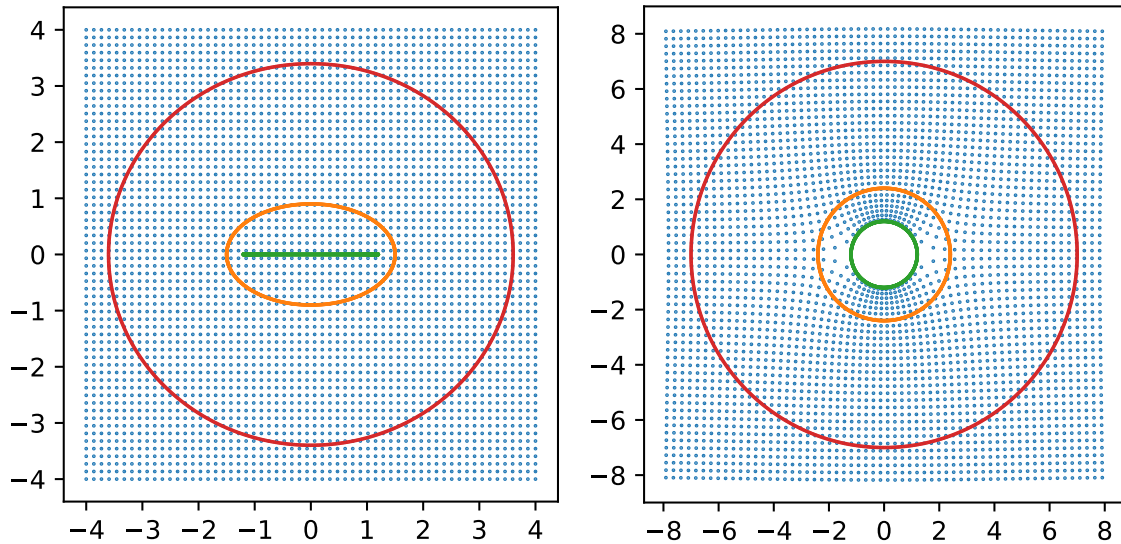


**Figure A.1 - Visualization of the (inverse) Joukowski transformation.** Exemplarily, for  $a = 1.5$ ,  $b = 0.9$ , and thus  $f = 1.2$ . The points on the left are shown on the complex  $z$ -plane, the points on the right are shown in the complex  $w$ -plane, and  $w = T(z)$ . The inner circle on the right image has radius  $f$ . The other circles have radii of  $r_o = a + b$  and  $3r_o$ . Reprinted with permission from Koch et al. (2020c), © 2020 Elsevier Inc.

To motivate a suitable kernel function for anisotropic problems, we first have a closer look at the properties of the employed Joukowski transformation. The effect of the mapping  $T$ , Eq. (8.9), is shown in Fig. A.1. Points on the exterior of a line on the real axis between  $f$  and  $-f$  are mapped onto the exterior of a circle with radius  $f$ . The ellipse with major axis  $a$  and minor axis  $b$  is mapped onto a circle with radius  $r_o = a + b$ . Going further away from the well, the deformation due to the mapping is less and less pronounced. This matches the



expectations for the physical flow problem, since isobars at large distance from an elliptical well-bore become increasingly circular in isotropic media.

The inverse transformation is given by

$$T^{-1} : \mathbb{C} \rightarrow \mathbb{C}, w \mapsto z = \frac{1}{2} \left( w + \frac{f^2}{w} \right), \quad |w| > f, \quad (\text{A.19})$$

where the restriction on  $|w|$  is necessary to obtain a one-to-one mapping. The transformation  $T^{-1}$  can equally be interpreted as an  $\mathbb{R}^2 \rightarrow \mathbb{R}^2$  mapping. The Jacobian of the transformation  $T^{-1}$  for  $z = x + iy$  and  $w = u + iv$  has the form

$$J_{T^{-1}} = \begin{bmatrix} \frac{\partial x}{\partial u} & \frac{\partial x}{\partial v} \\ \frac{\partial y}{\partial u} & \frac{\partial y}{\partial v} \end{bmatrix} = \begin{bmatrix} \eta & \epsilon \\ -\epsilon & \eta \end{bmatrix}, \quad (\text{A.20})$$

which follows from the Cauchy–Riemann equations (Rudin, 1987). Since the transformation can be viewed as the composition of a scaling and a rotation, it is angle-preserving. The transformation is associated with a spatially dependent volume deformation characterized by the determinant of  $J_{T^{-1}}$ . Furthermore, it can be shown that the Laplace operator behaves as follows under the transformation  $z = T^{-1}(w)$ ,

$$\Delta_w p = \frac{\partial^2 p}{\partial u^2} + \frac{\partial^2 p}{\partial v^2} = \left| \frac{\partial T^{-1}}{\partial w} \right|^2 \Delta_z p = |\det(J_{T^{-1}})| \Delta_z p \quad (\text{A.21})$$

by computing the derivative of the real and the imaginary part of  $p$  separately, applying the chain rule and the Cauchy–Riemann equations, as shown for completeness in Appendix A.7. From Eq. (A.21) follows that

$$|\det(J_{T^{-1}})|^{-1} \Delta_w p = \Delta_z p, \quad (\text{A.22})$$

for the transformation  $w = T(z)$ . The determinant can be explicitly computed, using Eq. (A.21) and complex differentiation (shown in Appendix A.9) as

$$|\det(J_{T^{-1}})(w)| = \left| \frac{\partial T^{-1}}{\partial w} \right|^2 = \left| \frac{\partial z}{\partial w} \right|^2 = \frac{1}{4} \left( 1 + \frac{f^4 - 2f^2 \Re(w^2)}{|w|^4} \right) := \Phi_J^{-1}, \quad (\text{A.23})$$

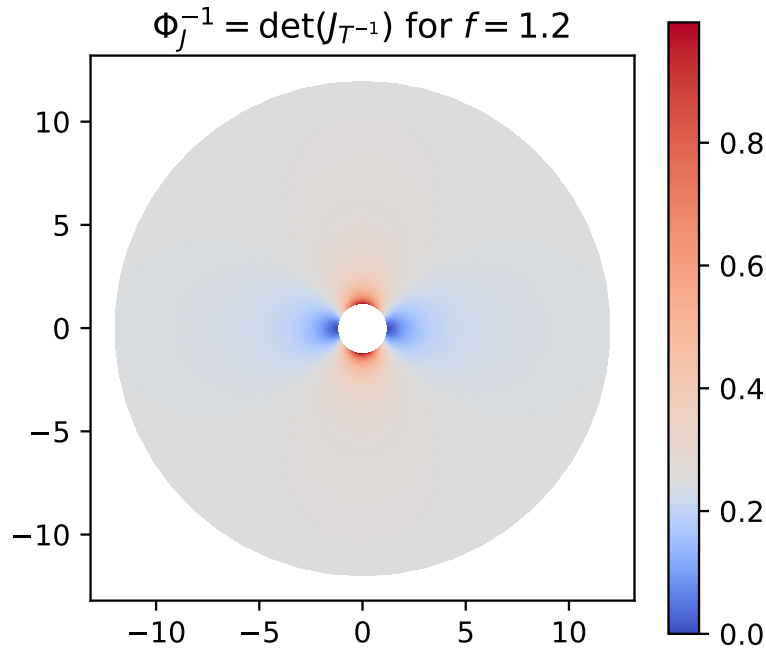


**Figure A.2 – Determinant of the Jacobian.** For the transformation  $z = T^{-1}(w)$  for  $|w| > f$  where  $f^2 = a^2 - b^2$  and  $a > b$ . Larger volume deformations only occur very locally in vicinity of the well radius  $r_o = a + b$  and quickly converge to 0.25 with larger distance to the well. Reprinted with permission from Koch et al. (2020c), © 2020 Elsevier Inc.

where  $\Re(w^2)$  is real part of  $w^2$ , and  $|w|$  the absolute value of  $w$ . We note that  $\Phi_J$  quickly converges to the value 4 with increasing  $|w|$ , that is with increasing distance from the well. The function  $\Phi_J^{-1}$  is plotted in Fig. A.2 exemplarily for  $f = 1.2$ .

## A.7 Transformation of the Laplace operator

The Joukowski transformation is a complex function  $z = T^{-1}(w)$  that can be decomposed in its real and imaginary parts,  $x = \Re(z)$  and  $y = \Im(z)$ . Furthermore, let  $u = \Re(w)$  and  $v = \Im(w)$ . As a conformal mapping,  $z$  satisfies the Cauchy Riemann equations (Nehari, 1975)

$$\frac{\partial x}{\partial u} = \frac{\partial y}{\partial v} \quad \text{and} \quad \frac{\partial x}{\partial v} = -\frac{\partial y}{\partial u}. \quad (\text{A.24})$$

The Jacobian of the transformation  $J_{T^{-1}}$  is given by Eq. (A.20). We investigate the effect of the transformation on the Laplace operator

$$\Delta_w p = \frac{\partial^2 p}{\partial u^2} + \frac{\partial^2 p}{\partial v^2}, \quad (\text{A.25})$$

where  $p$  is analytic in  $\Omega_w$ . Applying the chain rule yields

$$\frac{\partial p}{\partial u} = \frac{\partial p}{\partial x} \frac{\partial x}{\partial u} + \frac{\partial p}{\partial y} \frac{\partial y}{\partial u}, \quad (\text{A.26})$$

$$\begin{aligned} \frac{\partial^2 p}{\partial u^2} &= \frac{\partial p}{\partial x} \frac{\partial^2 x}{\partial u^2} + \frac{\partial p}{\partial y} \frac{\partial^2 y}{\partial u^2} + \frac{\partial}{\partial x} \left( \frac{\partial p}{\partial u} \right) \frac{\partial x}{\partial u} + \frac{\partial}{\partial y} \left( \frac{\partial p}{\partial u} \right) \frac{\partial y}{\partial u} \\ &= \frac{\partial p}{\partial x} \frac{\partial^2 x}{\partial u^2} + \frac{\partial p}{\partial y} \frac{\partial^2 y}{\partial u^2} + \frac{\partial^2 p}{\partial x^2} \left( \frac{\partial x}{\partial u} \right)^2 + 2 \frac{\partial^2 p}{\partial x \partial y} \frac{\partial x}{\partial u} \frac{\partial y}{\partial u} + \frac{\partial^2 p}{\partial y^2} \left( \frac{\partial y}{\partial u} \right)^2. \end{aligned} \quad (\text{A.27})$$

Analogously, we arrive at a similar expression for  $\partial^2 p / \partial v^2$ . Using Eq. (A.24) and

$$\frac{\partial^2 y}{\partial v^2} = \frac{\partial}{\partial v} \left( \frac{\partial y}{\partial v} \right) \stackrel{(\text{B.1})}{=} \frac{\partial}{\partial v} \left( \frac{\partial x}{\partial u} \right) = \frac{\partial}{\partial u} \left( \frac{\partial x}{\partial v} \right) \stackrel{(\text{B.1})}{=} -\frac{\partial y^2}{\partial u^2}, \quad \frac{\partial^2 x}{\partial v^2} = -\frac{\partial^2 x}{\partial u^2}, \quad (\text{A.28})$$

we find that

$$\frac{\partial^2 p}{\partial u^2} + \frac{\partial^2 p}{\partial v^2} = \left[ \left( \frac{\partial x}{\partial u} \right)^2 + \left( \frac{\partial y}{\partial u} \right)^2 \right] \left[ \frac{\partial^2 p}{\partial x^2} + \frac{\partial^2 p}{\partial y^2} \right]. \quad (\text{A.29})$$

With the complex derivative of  $T^{-1}$  (Rudin, 1987),

$$\frac{\partial T^{-1}}{\partial w} = \frac{\partial T^{-1}}{\partial u} = \frac{\partial x}{\partial u} + i \frac{\partial y}{\partial u} \quad \text{and} \quad \left| \frac{\partial T^{-1}}{\partial w} \right| = \sqrt{\left( \frac{\partial x}{\partial u} \right)^2 + \left( \frac{\partial y}{\partial u} \right)^2}. \quad (\text{A.30})$$

From the determinant of the Jacobian of the transformation, we find

$$\det(J_{T^{-1}}) = \frac{\partial x}{\partial u} \frac{\partial y}{\partial v} - \frac{\partial x}{\partial u} \frac{\partial y}{\partial v} = \left( \frac{\partial x}{\partial u} \right)^2 + \left( \frac{\partial y}{\partial u} \right)^2 = \left| \frac{\partial T^{-1}}{\partial w} \right|^2, \quad (\text{A.31})$$

using Eq. (A.24). Hence,

$$\Delta_w p = \left| \frac{\partial T^{-1}}{\partial w} \right|^2 \Delta_z p = |\det(J_{T^{-1}})| \Delta_z p, \quad (\text{A.32})$$

which also proves that any harmonic function ( $\Delta f = 0$ ) yields another harmonic function after a coordinate transformation with a conformal mapping.  $\square$

## A.8 Source scaling factor in $w$ -coordinates

We want to construct a pressure solution in  $w$ -coordinates such that the total mass flux over the well boundary matches the specified boundary condition in  $x$ -coordinates. Hence, the total mass flux over the boundary of a well segment with length  $\hat{L}$  in  $w$ -coordinates needs to match the total mass flux over the boundary of a well segment with length  $L$  in  $x$ -coordinates. A  $\hat{q}$  has to be chosen such that  $qL = \hat{q}\hat{L}$ . A relation between  $L$  and  $\hat{L}$  can be derived by looking at two related volume integrals. The Joukowski transformation only affects the two-dimensional well-bore plane such that length  $\hat{L}$  of a well segment is not affected. The volume of that well segment in  $v$ -coordinates (an elliptic cylinder) is given by

$$V_v = \pi ab\hat{L}. \quad (\text{A.33})$$

The volume of the same well segment in  $x$ -coordinates (a circular cylinder with slanted parallel planar elliptic caps) is given by

$$V_x = |\psi^T \tilde{S} \tilde{R}^T \mathbf{e}_3| |E_{\omega,x}| L = \pi r_\omega^2 L, \quad (\text{A.34})$$

where  $|E_{\omega,x}|$  is the area of the well-bore ellipse described by Eq. (A.12) transformed to  $x$ -coordinates (as shown in Fig. 8.3) and the last equality uses the fact that the integral can be transformed to an integral over a regular cylinder with radius  $r_\omega$  and length  $L$ . From the transformation theorem, we know that  $V_x = V_v \det(\tilde{S})$ . As the parameter  $k_l$  is chosen such that  $\det(\tilde{S}) = 1$ ,

$$\hat{L} = L \frac{r_\omega^2}{ab}, \quad (\text{A.35})$$

and if the source term is chosen as

$$\hat{q} = q \frac{ab}{r_\omega^2} := q\zeta, \quad (\text{A.36})$$

then  $qL = \hat{q}\hat{L}$ . □

## A.9 Determinant of the Joukowski transformation

In Appendix A.7, we show that  $|\det(J_{T^{-1}})| = \left| \frac{\partial z}{\partial w} \right|^2$ . Using complex differentiation,

$$\frac{\partial z}{\partial w} = \frac{\partial z}{\partial u} = \frac{\partial}{\partial u} \left[ \frac{1}{2} \left( w + \frac{f^2}{w} \right) \right] = \frac{1}{2} \left( 1 - \frac{f^2}{w^2} \right) = \frac{1}{2} \left( 1 - \frac{f^2 \bar{w}^2}{|w|^4} \right), \quad (\text{A.37})$$

where we used the identities  $w^{-1} = \bar{w}|w|^{-2}$ ,  $\bar{w}$  denoting the complex conjugate of  $w$ , and  $\overline{w^2} = \bar{w}^2$ . Furthermore,

$$\Re \left( \frac{\partial z}{\partial w} \right)^2 = \frac{1}{4} \left( 1 - \frac{2f^2 \Re(w^2)}{|w|^4} + \frac{f^4 \Re(w^2)^2}{|w|^8} \right), \quad (\text{A.38})$$

$$\Im \left( \frac{\partial z}{\partial w} \right)^2 = \frac{1}{4} \left( \frac{f^4 \Im(w^2)^2}{|w|^8} \right), \quad \Re(w^2)^2 + \Im(w^2)^2 = |w|^4, \quad (\text{A.39})$$

such that

$$\left| \frac{\partial z}{\partial w} \right|^2 = \Re \left( \frac{\partial z}{\partial w} \right)^2 + \Im \left( \frac{\partial z}{\partial w} \right)^2 = \frac{1}{4} \left( 1 + \frac{f^4 - 2f^2 \Re(w^2)}{|w|^4} \right). \quad (\text{A.40})$$

□

## A.10 Convergence rates for different anisotropy ratios

The following table contains the convergence rate data corresponding to Fig. 8.5 in Chapter 8.

**Table A.2 – Convergence rates for  $E_q$  for different anisotropy ratios  $\alpha$ .**

$\alpha$	$h_{\max}$			
	17.32 m	8.66 m	4.33 m	2.17 m
1	2.0545	2.0724	1.9454	-
10	1.7715	2.0184	2.0763	-
50	1.5904	1.9747	2.0925	-
100	1.5970	1.9666	2.1218	-

## A.11 Convergence study in space and time

We present a numerical converge study in space and time for the model presented in Chapter 9. As there is no analytical solution to the problem, we use the solution computed with a very fine resolution in space and time as a reference for a grid convergence study. We compute errors with respect to the fine scale solution by mapping the coarse scale solution to the finest grid. Let  $\mathbb{R}^{|\mathcal{M}_n|}$  be the solution space on grid  $\mathcal{M}_n$ , where  $|\mathcal{M}_n|$  is the number of cells on grid level  $n$ , and  $\mathcal{M}_n$  is a set of hexahedra,  $K_i$ , such that  $\mathcal{M}_n = \bigcup_i K_i$  is a discrete representation of  $\Omega$ . The levels are constructed by dividing each hexahedron on level  $n$  into 8 hexahedrons on level  $n + 1$ , such that  $\forall L \in \mathcal{M}_{\text{ref}}$ , there exists exactly one  $K \in \mathcal{M}_n$  such that  $L \subset K$ , where  $\mathcal{M}_{\text{ref}}$  denotes the reference grid. The mapping from coarse to fine scale,  $\mathcal{I}$ , can be defined as

$$\mathcal{I} := \{\mathcal{I}_L\}_{L \in \mathcal{M}_{\text{ref}}}, \quad \text{with } \mathcal{I}_L : \mathbb{R}^{|\mathcal{M}_n|} \mapsto \mathbb{R}, \mathcal{I}_L(u) = u_K. \quad (\text{A.41})$$

The relative error of the physical quantity  $u \in \{p_t, x_t\}$ , between reference and a solution on a coarser grid,  $u_{\text{ref}}$ ,  $u$ , respectively, is defined as

$$e_u = \frac{\sqrt{\sum_{L \in \mathcal{M}_{\text{ref}}} |L| (\mathcal{I}_L(u) - u_{\text{ref},L})^2}}{\sqrt{\sum_{L \in \mathcal{M}_{\text{ref}}} |L| u_{\text{ref},L}^2}}. \quad (\text{A.42})$$

In time, we define the maximum relative error over all time steps  $t^i$ ,  $i \in \{0, \dots, \tau\}$ , where  $\tau$  is the number of time steps, as

$$e_{u,\infty} = \max(e_u^i). \quad (\text{A.43})$$

Finally, we measure the difference of the signal-time curve,  $S$ , to the reference curve,  $S_{\text{ref}}$ , computed with the finest spatial and temporal discretization, in the following norm

$$e_S = \|S - S_{\text{ref}}\|_{\infty} = \max |S^i - S_{\text{ref}}^i| \quad (\text{A.44})$$

The convergence rates for a given error  $e$  are computed from one refinement level  $n$  to the next as

$$\text{rate} = \frac{\ln e^{n+1} - \ln e^n}{\ln v_{\text{max}}^{n+1} - \ln v_{\text{max}}^n}, \quad (\text{A.45})$$

where  $\nu_{\max}$  is the respective maximum discretization length. In space,  $\nu_{\max}$  is defined as the maximum edge length of all elements,  $h_{\max}$ . When refining, the vessel domain grid is also refined by bisecting large elements until the maximum element length is smaller than  $h_{\max}$ . In time,  $\nu_{\max}$  is defined as the maximum time step size. The time step size,  $\Delta t$ , is chosen to be small around the time when the contrast agent front reaches the domain, and increasingly larger as the process becomes slower, following the heuristic

$$\Delta t = \theta \ln(t + 1.05), \quad (\text{A.46})$$

where  $\theta > 0$  is a factor controlling the time step size in the refinement study.

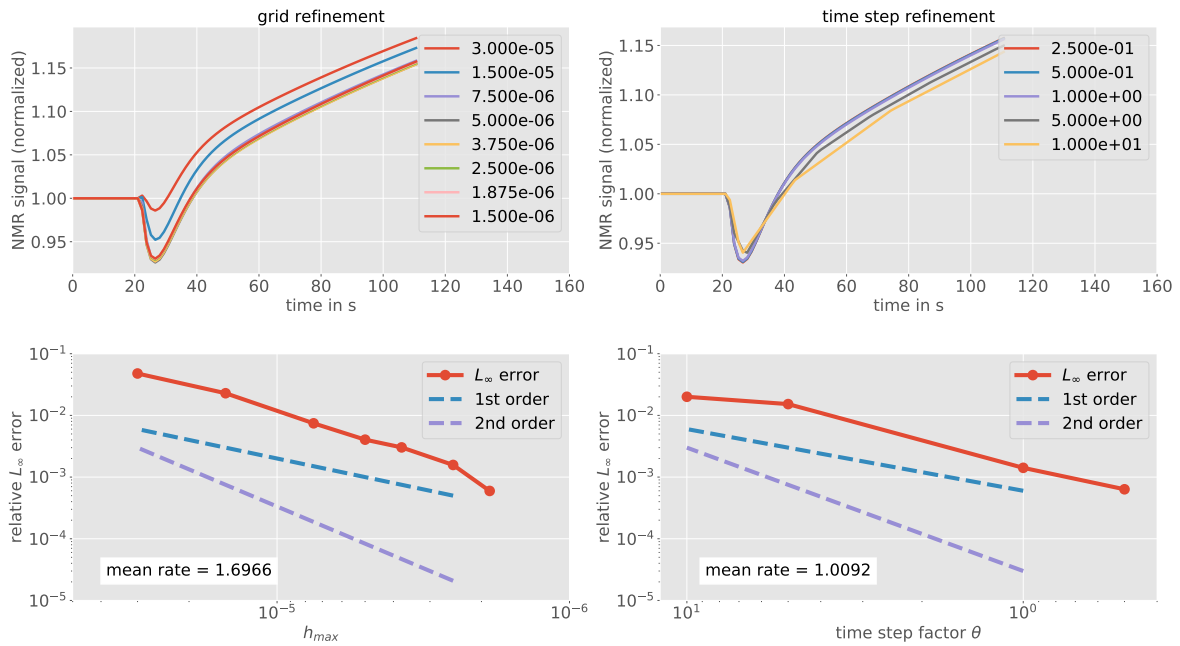
The reference solution is obtained with  $h_{\max} = 1 \mu\text{m}$  and  $\theta = 0.125$ . The parameters are chosen to be the optimal parameter set computed by an optimization algorithm described in Section 9.4.1 and Table 9.1, minimizing the signal difference to the MRI data from an MS lesion shown in Fig. 9.1 (in red).

Table A.3 show the errors and convergence rates of the extra-vascular fluid pressure,  $p_t$ , and the contrast agent mole fraction,  $x_t$ . Fig. A.3 shows the NMR signal curves and errors with respect to the reference solution when refining in space and time.

**Table A.3 – Errors and convergence rates in space.** Errors are given for pressure,  $p_t$ , and contrast agent mole fraction,  $x_t$ , in the extra-vascular domain.

$h_{\max}$	$e_{p_t}$	rate	$e_{x_t, \infty}$	rate
32 $\mu\text{m}$	0.000414833	-	0.028418	-
16 $\mu\text{m}$	0.000210479	0.978853	0.0152967	0.893589
8 $\mu\text{m}$	0.000107219	0.973115	0.00874756	0.806266
4 $\mu\text{m}$	5.31281e-05	1.01302	0.00471859	0.890526
2 $\mu\text{m}$	2.54764e-05	1.06032	0.00228896	1.04366

It can be seen that all quantities converge to the reference solution. We obtain convergence rates close to 1 for the pressure and the mole fraction of the contrast agent. The signal curve converges with first order in time and a slightly higher order in space. The higher convergence may be explained by the computation of the signal involving the integration of the concentration over the entire domain. The relative error with respect to the reference solution, is smaller than 1% for a moderate spatial and temporal refinement. In conclusion, we consider a spatial resolution of  $h_{\max} = 8 \mu\text{m}$ , and a temporal resolution  $\theta = 1$  as sufficient



**Figure A.3 – Convergence study in space and time.** The NMR signal curves and errors to reference solutions when refining in time, while keeping the same fine resolution in space (left), and in space, while keeping the same fine resolution in time (right). The top left legend indicates the grid cell size in m, the top right legend indicates the time step factor  $\theta$  from Eq. (A.46). The bottom left error plot shows convergence with a mean rate of 1.6966 with grid refinement. The bottom right error plot shows convergence with a mean rate of 1.0092 with time step refinement.

for the subsequent analysis. We justify this with the assumption that the errors resulting from model parameter uncertainty, as well as the errors in the measurement data, are larger than the discretization error. This is also evident, when looking at the results of the parameter study and comparing the variability with that of the signal–time curves shown in Fig. A.3 for different spatial and temporal discretizations. In order to verify that the discretization error is small also for other parameter configurations, we ran the above analysis for various parameter configurations and confirmed that the analysis looks similar for those other cases. The results are omitted for brevity.



## A.12 Prior distributions for MCMC

The following table gives an overview over the prior distributions used for the MCMC in Chapter 9.

Table A.4 – Prior parameter distributions for Bayesian parameter inference.

parameter	prior distribution	unit
$a$	uniform in $[0, 200]$	$\text{mol s l}^{-1}$
$b$	uniform in $[0, 2.0]$	$\text{mol l}^{-1}$
$t_p$	uniform in $(0, 15]$	s
$-\log_{10} D_\omega$	uniform in $[5, 12]$	$\text{m s}^{-1}$
$L_p$	fixed at $1 \cdot 10^{-12}$	$\text{m Pa}^{-1} \text{s}^{-1}$
$T_{1,\text{pre}}$	uniform in $[0.8, 2.0]$	s
$\kappa_B$	uniform in $[0, 100]$	-
$\kappa_T$	uniform in $[0, 100]$	-

## A.13 Ensemble sampler for MCMC

This is a brief description of the ensemble sampler used in Chapter 9. We refer to Goodman and Weare (2010) and Foreman-Mackey et al. (2013) for a comprehensive discussion. The employed ensemble sampler of Goodman and Weare (2010) considers two sets of  $k/2$  random walkers,  $S_0 = \{\omega_i\}_{i=1, \dots, k/2}$ ,  $S_1 = \{\omega_i\}_{i=k/2+1, \dots, k}$ , where the position of walker  $\omega_i$  in step  $n$  is a position in the parameter space (a vector of parameters), denoted as  $\theta_n^i$ . After each step the walkers in  $S_m$  are moved such that

$$\theta_{n+1}^i = \theta_{n+m}^j + \zeta (\theta_n^j - \theta_{n+m}^i), \quad (\text{A.47})$$

where  $\theta^j$  is a walker position randomly drawn from the positions of the other set of walkers,  $S_{1-m}$ , and  $\zeta$  is a random variable drawn from a proposal distribution  $g(\zeta)$ ,

$$g(\zeta) \propto \begin{cases} 1/\sqrt{\zeta} & \text{if } \zeta \in (\frac{1}{2}, 2) \\ 0 & \text{otherwise} \end{cases} \quad (\text{A.48})$$

Note that this means moving the walkers in  $S_0$  first, then the walkers in  $S_1$ . At each walker position, a sample is proposed. The sample is accepted with the probability (Foreman-Mackey et al., 2013)

$$z = \min\left(1, \zeta^{N-1} \frac{p(X|\theta_{n+1}^i)p(\theta_{n+1}^i)}{p(X|\theta_n^i)p(\theta_n^i)}\right), \quad (\text{A.49})$$

where  $N = \dim(\theta)$  is the dimension of the parameter space. If the sample is not accepted, the walker remains at the position  $\theta_n^i$ , increasing the number of samples at this position by one. Each step requires a run of the forward model for every walker, which is computationally the most expensive part. Fortunately, advancing the walkers within a set of walkers can be done in parallel.

The ensemble sampler is configured with  $k = 100$  walkers and  $N = 7$ . The sampler convergence is estimated using the integrated auto-correlation time,  $\tau_f$  (Goodman and Weare, 2010),

$$\tau_f = \sum_{t=-\infty}^{\infty} \frac{C_f(t)}{C_f(0)}, \quad \text{with} \quad C_f(t) = \frac{1}{M-t} \sum_{k=1}^{M-t} (f_k - \mu_f)(f_{k+t} - \mu_f), \quad (\text{A.50})$$

where  $f = \{f_i\}_{i=1}^M$  is a finite chain of length  $M$ , e.g. the value of parameter  $a$  for each sample in the Markov chain, and  $\mu_f$  its arithmetic mean. We use an estimate of the integrated auto-correlation,  $\tau_{f,e}$ , using the Python module *acor* (dfm; Goodman). We compute this estimate for the chain of each parameter,  $\theta_i$ , and use the maximum and minimum values,  $\tau_{\max} = \max_{0 \leq i < N} \tau_{\theta_i,e}$ ,  $\tau_{\min} = \min_{0 \leq i < N} \tau_{\theta_i,e}$ . The sampler is run until the sample size,  $j > 100 \cdot \tau_{\max}$ , and the change in the auto-correlation time estimate from sample  $j - \tau_{\max}$  to sample  $j$  is less than 1%. To eliminate artifacts from the burn-in phase of the MCMC algorithm, the first  $10 \cdot \tau_{\max}$  samples are discarded. To have only independent samples, every  $\tau_{\min}$  sample of the remaining samples is chosen (Goodman and Weare, 2010), while the others are discarded.

## A.14 MCMC results for $\sigma = 0.095$

The MCMC (Markov Chain Monte Carlo) algorithm described in Chapter 9 approximates the posterior distributions of all parameters in the parameter vector simultaneously. The

resulting histograms for each parameter and their covariance with respect to the other parameters is visualized in Fig. A.4 for sample L and Fig. A.5 for sample N (cf. Fig. 9.1). The plots show the results for  $\sigma = 0.095$ . The results with a 10 times smaller  $\sigma$  are given in Figs. 9.6 and 9.7, see Chapter 9.

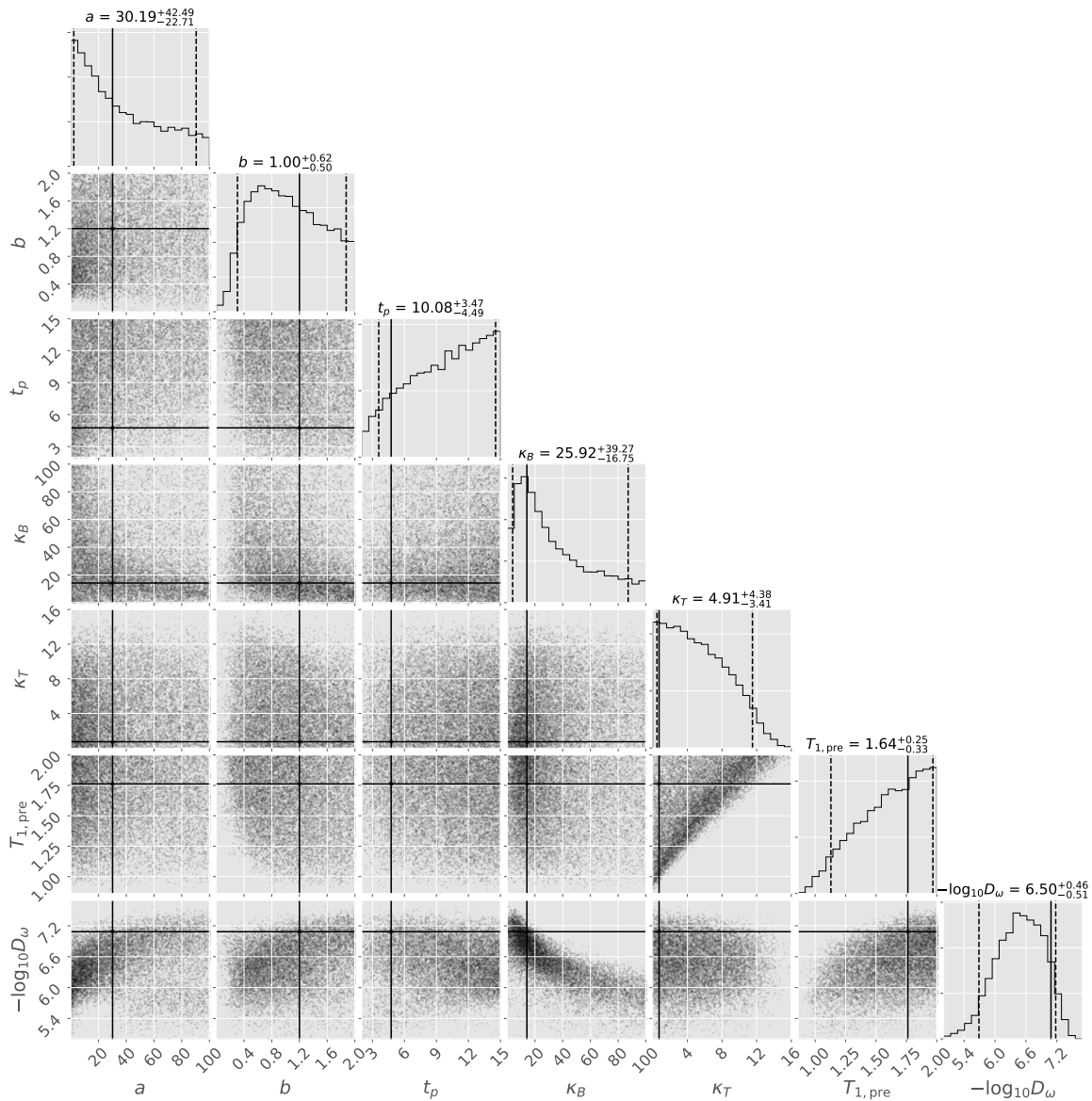


**Figure A.4 – Parameter distributions for lesion sample ( $\sigma = 0.095$ ).** The standard deviation for the measurement and model error is increased to  $\sigma = 0.095$  in comparison with the results in Fig. 9.6 ( $\sigma = 0.009$ ). The horizontal and vertical solid black lines show the parameter values for sample L of Table 9.1.

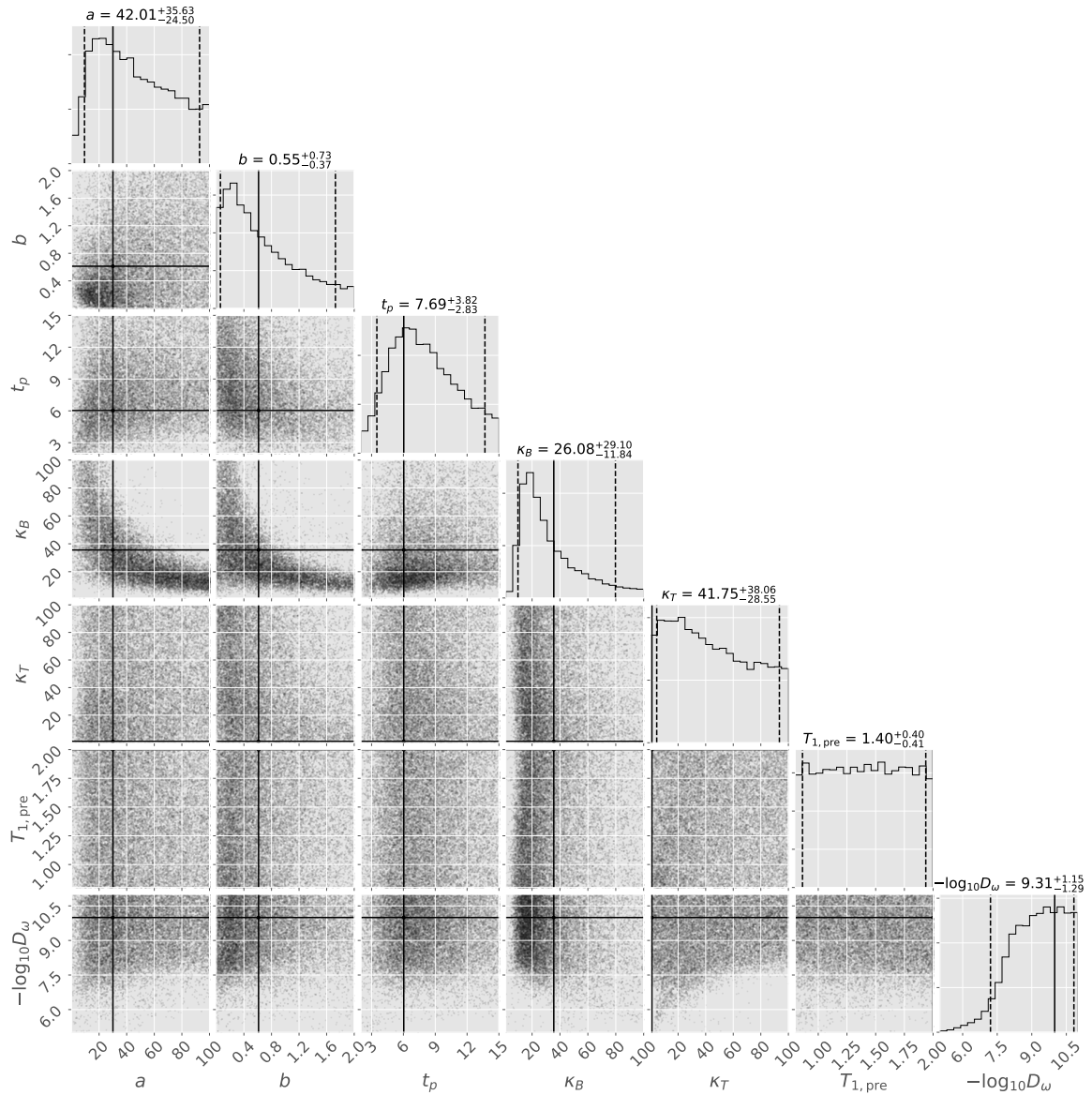


**Figure A.5 – Parameter distributions for lesion sample ( $\sigma = 0.095$ ).** The standard deviation for the measurement and model error is increased to  $\sigma = 0.095$  in comparison with the results in Fig. 9.7 ( $\sigma = 0.009$ ). The horizontal and vertical solid black lines show the parameter values for sample N of Table 9.1.

# Bibliography

- Python module acor. <https://github.com/dfm/acor>. Last accessed: 18 Oct 2018.
- I. Aavatsmark. An introduction to multipoint flux approximations for quadrilateral grids. *Computational Geosciences*, 6(3):405–432, 2002. doi:10.1023/A:1021291114475.
- I. Aavatsmark. Equivalent well-cell radius for hexagonal k-orthogonal grids in numerical reservoir simulation. *Applied Mathematics Letters*, 61:122–128, 2016. doi:10.1016/j.aml.2016.05.013.
- I. Aavatsmark and R. A. Klausen. Well index in reservoir simulation for slanted and slightly curved wells in 3d grids. *SPE Journal*, 8(01):41–48, 2003. doi:10.2118/75275-PA.
- M. Absinta, G. Nair, P. Sati, I. C. Cortese, M. Filippi, and D. S. Reich. Direct MRI detection of impending plaque development in multiple sclerosis. *Neurology - Neuroimmunology Neuroinflammation*, 2(5), 2015. doi:10.1212/NXI.0000000000000145.
- R. Ahmed, M. Edwards, S. Lamine, B. Huisman, and M. Pal. Control-volume distributed multi-point flux approximation coupled with a lower-dimensional fracture model. *Journal of Computational Physics*, 284:462–489, 2015. doi:10.1016/j.jcp.2014.12.047.
- J. Ahrens, B. Geveci, and C. Law. Paraview: An end-user tool for large-data visualization. In C. D. Hansen and C. R. Johnson, editors, *Visualization Handbook*, pages 717–731. Butterworth-Heinemann, Burlington, 2005. ISBN 978-0-12-387582-2. doi:10.1016/B978-012387582-2/50038-1.
- J. Alvestad, K. Holing, K. Christoffersen, and O. Stava. *SPE-27577-MS*, chapter Interactive Modelling of Multiphase Inflow Performance of Horizontal and Highly Deviated Wells, page 16. Society of Petroleum Engineers, Aberdeen, United Kingdom, 1994. ISBN 978-1-55563-474-2. doi:10.2118/27577-MS.
- K. Arkill, C. Knupp, C. Michel, C. Neal, K. Qvortrup, J. Rostgaard, and J. Squire. Similar endothelial glycocalyx structures in microvessels from a range of mammalian tissues: Evidence for a common filtering mechanism? *Biophysical Journal*, 101(5):1046 – 1056, 2011. doi:10.1016/j.bpj.2011.07.036.
- S. Axler, P. Bourdon, and W. Ramey. *Harmonic Function Theory*. Springer, New York, NY, 1992. ISBN 978-0-387-21527-3. doi:10.1007/b97238.
- K. Baber. *Coupling free flow and flow in porous media in biological and technical applications: from a simple to a complex interface description*. Phd thesis, University of Stuttgart, 2014.

- D. K. Babu and A. S. Odeh. Productivity of a horizontal well. *SPE Reservoir Engineering*, 4(04): 417–421, 1989. doi:10.2118/18298-PA.
- D. K. Babu, A. S. Odeh, A. J. Al-Khalifa, and R. C. McCann. The relation between wellblock and wellbore pressures in numerical simulation of horizontal wells. *SPE Reservoir Engineering*, 6(03): 324–328, 1991. doi:10.2118/20161-PA.
- M. K. Bartlett, T. Klein, S. Jansen, B. Choat, and L. Sack. The correlations and sequence of plant stomatal, hydraulic, and wilting responses to drought. *Proceedings of the National Academy of Sciences*, 113(46):13098–13103, 2016. doi:10.1073/pnas.1604088113.
- P. Bastian, M. Blatt, A. Dedner, C. Engwer, J. Fahlke, C. Gersbacher, C. Gräser, C. Grüniger, D. Kempf, R. Klöfkorn, S. Müthing, M. Nolte, M. Ohlberger, and O. Sander. DUNE Webpage. URL <http://www.dune-project.org>. Last accessed 23 Sep 2019.
- P. Bastian, M. Blatt, A. Dedner, C. Engwer, R. Klöfkorn, R. Kornhuber, M. Ohlberger, and O. Sander. A Generic Grid Interface for Parallel and Adaptive Scientific Computing. Part II: Implementation and Tests in DUNE. *Computing*, 82(2-3):121–138, 2008a. doi:10.1007/s00607-008-0004-9.
- P. Bastian, M. Blatt, A. Dedner, C. Engwer, R. Klöfkorn, M. Ohlberger, and O. Sander. A Generic Grid Interface for Parallel and Adaptive Scientific Computing. Part I: Abstract Framework. *Computing*, 82(2-3):103–119, 2008b. doi:10.1007/s00607-008-0003-x.
- P. Bastian, G. Buse, and O. Sander. Infrastructure for the coupling of dune grids. In G. Kreiss, P. Lötstedt, A. Målqvist, and M. Neytcheva, editors, *Numerical Mathematics and Advanced Applications 2009*, pages 107–114, Berlin, Heidelberg, 2010. Springer Berlin Heidelberg. ISBN 978-3-642-11795-4. doi:10.1007/978-3-642-11795-4\_10.
- L. T. Baxter and R. K. Jain. Transport of fluid and macromolecules in tumors. i. role of interstitial pressure and convection. *Microvascular Research*, 37(1):77 – 104, 1989. doi:10.1016/0026-2862(89)90074-5.
- J. Bear. *Dynamics of fluids in porous media*. Courier Corporation, 2013.
- J. Bear and G. Dagan. The relationship between solutions of flow problems in isotropic and anisotropic soils. *Journal of Hydrology*, 3(2):88–96, 1965. doi:10.1016/0022-1694(65)90002-8.
- D. A. Beard and J. B. Bassingthwaite. Modeling advection and diffusion of oxygen in complex vascular networks. *Annals of Biomedical Engineering*, 29(4):298–310, 2001. doi:10.1114/1.1359450.
- M. Beck. *Conceptual approaches for the analysis of coupled hydraulic and geomechanical processes*. Phd thesis, University of Stuttgart, 2019.

- B. Beckers and P. Beckers. A general rule for disk and hemisphere partition into equal-area cells. *Computational Geometry*, 45(7):275–283, 2012. doi:10.1016/j.comgeo.2012.01.011.
- M. Bertossi, D. Virgintino, E. Maiorano, M. Occhiogrosso, and L. Roncali. Ultrastructural and morphometric investigation of human brain capillaries in normal and peritumoral tissues. *Ultrastructural Pathology*, 21(1):41–49, 1997. doi:10.3109/01913129709023246.
- N. Beudez, C. Doussan, G. Lefeuvre-Mesgouez, and A. Mesgouez. Influence of three root spatial arrangement on soil water flow and uptake. results from an explicit and an equivalent, upscaled, model. *Procedia Environmental Sciences*, 19:37–46, 2013. doi:10.1016/j.proenv.2013.06.005. Four Decades of Progress in Monitoring and Modeling of Processes in the Soil-Plant-Atmosphere System: Applications and Challenges.
- J. Bierhuizen and R. Slatyer. Effect of atmospheric concentration of water vapour and co<sub>2</sub> in determining transpiration-photosynthesis relationships of cotton leaves. *Agricultural Meteorology*, 2(4):259 – 270, 1965. doi:10.1016/0002-1571(65)90012-9.
- P. J. Blanco, S. M. Watanabe, M. A. R. F. Passos, P. A. Lemos, and R. A. Feijóo. An anatomically detailed arterial network model for one-dimensional computational hemodynamics. *IEEE Transactions on Biomedical Engineering*, 62(2):736–753, 2015. doi:10.1109/TBME.2014.2364522.
- M. Blatt and P. Bastian. The iterative solver template library. In B. Kågström, E. Elmroth, J. Dongarra, and J. Waśniewski, editors, *Applied Parallel Computing. State of the Art in Scientific Computing: 8th International Workshop, PARA 2006, Umeå, Sweden, June 18-21, 2006, Revised Selected Papers*, pages 666–675, Berlin, Heidelberg, 2007. Springer Berlin Heidelberg. ISBN 978-3-540-75755-9. doi:10.1007/978-3-540-75755-9\_82.
- P. Blinder, P. S. Tsai, J. P. Kaufhold, P. M. Knutsen, H. Suhl, and D. Kleinfeld. The cortical angiome: an interconnected vascular network with noncolumnar patterns of blood flow. *Nature Neuroscience*, 16(7):889–897, 2013. ISSN 1546-1726. doi:10.1038/nn.3426.
- F. Bloch. Nuclear induction. *Phys. Rev.*, 70:460–474, 1946. doi:10.1103/PhysRev.70.460.
- J. Boxerman, K. Schmainda, and R. Weisskoff. Relative cerebral blood volume maps corrected for contrast agent extravasation significantly correlate with glioma tumor grade, whereas uncorrected maps do not. *American Journal of Neuroradiology*, 27(4):859–867, 2006.
- G. O. Brown. *The History of the Darcy-Weisbach Equation for Pipe Flow Resistance*, pages 34–43. 2003. doi:10.1061/40650(2003)4.

- H.-J. Bungartz, F. Lindner, B. Gatzhammer, M. Mehl, K. Scheufele, A. Shukaev, and B. Uekermann. preCICE – a fully parallel library for multi-physics surface coupling. *Computers and Fluids*, 141: 250–258, 2016. doi:10.1016/j.compfluid.2016.04.003. Advances in Fluid-Structure Interaction.
- C. Burstedde, L. C. Wilcox, and O. Ghattas. p4est: Scalable algorithms for parallel adaptive mesh refinement on forests of octrees. *SIAM Journal on Scientific Computing*, 33(3):1103–1133, 2011. doi:10.1137/100791634.
- J. Buysse, E. Smolders, and R. Merckx. Modelling the uptake of nitrate by a growing plant with an adjustable root nitrate uptake capacity. *Plant and Soil*, 181(1):19–23, 1996. doi:10.1007/BF00011287.
- F. Calamante. Perfusion MRI using dynamic-susceptibility contrast MRI: quantification issues in patient studies. *Topics in Magnetic Resonance Imaging*, 21(2):75–85, 2010. doi:10.1097/RMR.0b013e31821e53f5.
- M. M. Caldwell and J. H. Richards. Hydraulic lift: water efflux from upper roots improves effectiveness of water uptake by deep roots. *Oecologia*, 79(1):1–5, 1989. doi:10.1007/BF00378231.
- M. M. Caldwell, T. E. Dawson, and J. H. Richards. Hydraulic lift: consequences of water efflux from the roots of plants. *Oecologia*, 113(2):151–161, 1998. doi:10.1007/s004420050363.
- A. Carminati, A. B. Moradi, D. Vetterlein, P. Vontobel, E. Lehmann, U. Weller, H.-J. Vogel, and S. E. Oswald. Dynamics of soil water content in the rhizosphere. *Plant and Soil*, 332(1):163–176, 2010. doi:10.1007/s11104-010-0283-8.
- L. Cattaneo and P. Zunino. Computational models for fluid exchange between microcirculation and tissue interstitium. *Networks & Heterogeneous Media*, 9(1), 2014. doi:10.3934/nhm.2014.9.135.
- D. Cerroni, F. Laurino, and P. Zunino. Mathematical analysis, finite element approximation and numerical solvers for the interaction of 3d reservoirs with 1d wells. *GEM - International Journal on Geomathematics*, 10(1):4, 2019. doi:10.1007/s13137-019-0115-9.
- S. Chapman, R. Shipley, and R. Jawad. Multiscale modeling of fluid transport in tumors. *Bulletin of Mathematical Biology*, 70(8):2334–2357, 2008. doi:10.1007/s11538-008-9349-7.
- Z. Chen and Y. Zhang. Well flow models for various numerical methods. *International Journal of Numerical Analysis & Modeling*, 6(3), 2009.
- H. Class. *Models for non-isothermal compositional gas-liquid flow and transport in porous media*. PhD thesis, University of Stuttgart, 2007.
- H. Class, R. Helmig, and P. Bastian. Numerical simulation of non-isothermal multiphase multicomponent processes in porous media.: 1. an efficient solution technique. *Advances in Water Resources*, 25(5):533 – 550, 2002. doi:10.1016/S0309-1708(02)00014-3.



- V. Clausnitzer and J. W. Hopmans. Simultaneous modeling of transient three-dimensional root growth and soil water flow. *Plant and Soil*, 164(2):299–314, 1994. doi:10.1007/BF00010082.
- S. Cramer, H. Simonsen, J. Frederiksen, E. Rostrup, and H. Larsson. Abnormal blood–brain barrier permeability in normal appearing white matter in multiple sclerosis investigated by mri. *NeuroImage: Clinical*, 4:182–189, 2014. doi:10.1016/j.nicl.2013.12.001.
- C. Crone. The permeability of capillaries in various organs as determined by use of the ‘indicator diffusion’ method. *Acta Physiologica Scandinavica*, 58(4):292–305, 1963. doi:10.1111/j.1748-1716.1963.tb02652.x.
- F. Curry. Permeability coefficients of the capillary wall to low molecular weight hydrophilic solutes measured in single perfused capillaries of frog mesentery. *Microvascular Research*, 17(3):290 – 308, 1979. doi:10.1016/S0026-2862(79)80005-9.
- F. E. Curry, V. H. Huxley, and R. H. Adamson. Permeability of single capillaries to intermediate-sized colored solutes. *American Journal of Physiology-Heart and Circulatory Physiology*, 245(3): H495–H505, 1983. doi:10.1152/ajpheart.1983.245.3.H495.
- J. S. Dai. Euler–Rodrigues formula variations, quaternion conjugation and intrinsic connections. *Mechanism and Machine Theory*, 92:144–152, 2015. doi:10.1016/j.mechmachtheory.2015.03.004.
- Q. A. Dang and M. Ehrhardt. On dirac delta sequences and their generating functions. *Applied Mathematics Letters*, 25(12):2385 – 2390, 2012. doi:10.1016/j.aml.2012.07.009.
- C. D’Angelo. Multiscale modelling of metabolism and transport phenomena in living tissues. *Bibliothèque de l’EPFL, Lausanne*, 2007.
- C. D’Angelo. Finite element approximation of elliptic problems with dirac measure terms in weighted spaces: Applications to one- and three-dimensional coupled problems. *SIAM Journal on Numerical Analysis*, 50(1):194–215, 2012. doi:10.1137/100813853.
- H. Darcy. *Les fontaines publiques de la ville de Dijon: exposition et application...* Victor Dalmont, 1856.
- A. d’Esposito, P. W. Sweeney, M. Ali, M. Saleh, R. Ramasawmy, T. A. Roberts, G. Agliardi, A. Desjardins, M. F. Lythgoe, R. B. Pedley, R. Shipley, and S. Walker-Samuel. Computational fluid dynamics with imaging of cleared tissue and of in vivo perfusion predicts drug uptake and treatment responses in tumours. *Nature Biomedical Engineering*, 2(10):773–787, 2018. doi:10.1038/s41551-018-0306-y.
- A. J. Diggle. ROOTMAP—a model in three-dimensional coordinates of the growth and structure of fibrous root systems. *Plant and Soil*, 105(2):169–178, 1988. doi:10.1007/BF02376780.

- M. O. Dogan. *Coupling of porous media flow with pipe flow*. PhD thesis, University of Stuttgart, 2011.
- J. Doherty. Pest, model-independent parameter estimation — user manual (6th ed.), 2016. URL <http://www.pesthomepage.org/>.
- C. Doussan, L. Pages, and G. Vercambre. Modelling of the Hydraulic Architecture of Root Systems: An Integrated Approach to Water Absorption—Model Description. *Annals of Botany*, 81(2): 213–223, 1998. doi:10.1006/anbo.1997.0540.
- P. M. Doyen. Permeability, conductivity, and pore geometry of sandstone. *Journal of Geophysical Research: Solid Earth*, 93(B7):7729–7740, 1988. doi:10.1029/JB093iB07p07729.
- V. M. Dunbabin, M. Airey, A. Diggle, M. Renton, Z. Rengel, R. Armstrong, Y. Chen, and K. Siddique. Simulating the interaction between plant roots, soil water and nutrient flows, and barriers and objects in soil using rootmap. In *Proceedings 19th International Congress on Modelling and Simulation (MODSIM2011)*, pages 12–16, 2011.
- V. M. Dunbabin, J. a. Postma, A. Schnepf, L. Pagès, M. Javaux, L. Wu, D. Leitner, Y. L. Chen, Z. Rengel, and A. J. Diggle. Modelling root-soil interactions using three-dimensional models of root growth, architecture and function. *Plant and Soil*, 372:93–124, 2013. doi:10.1007/s11104-013-1769-y.
- ECLIPSE, 2014. ECLIPSE Technical Description, 2014. Schlumberger N.V.
- N. E. Edlefsen and A. B. C. Anderson. Thermodynamics of soil moisture. *Hilgardia*, 15(2):31–298, 1943. doi:10.3733/hilg.v15n02p031.
- W. Ehlers and J. Blum. *Porous media: theory, experiments and numerical applications*, chapter Foundations of multiphase and porous materials, pages 3–86. Berlin: Springer-Verlag, 2002.
- W. Ehlers and A. Wagner. Multi-component modelling of human brain tissue: a contribution to the constitutive and computational description of deformation, flow and diffusion processes with application to the invasive drug-delivery problem. *Computer Methods in Biomechanics and Biomedical Engineering*, 18(8):861–879, 2015. doi:10.1080/10255842.2013.853754.
- W. El-Bouri and S. Payne. Multi-scale homogenization of blood flow in 3-dimensional human cerebral microvascular networks. *Journal of theoretical biology*, 380:40–47, 2015. doi:10.1016/j.jtbi.2015.05.011.
- W. El-Bouri and S. Payne. Investigating the effects of a penetrating vessel occlusion with a multi-scale microvasculature model of the human cerebral cortex. *NeuroImage*, 172:94–106, 2018. doi:10.1016/j.neuroimage.2018.01.049.

- 
- C. Engwer, J. Vorwerk, J. Ludewig, and C. Wolters. A discontinuous galerkin method to solve the eeg forward problem using the subtraction approach. *SIAM Journal on Scientific Computing*, 39(1): B138–B164, 2017. doi:10.1137/15M1048392.
- C. Ericson. *Real-time collision detection*. CRC Press, 2004.
- L. C. Evans. *Partial differential equations*, chapter 2.2. American Mathematical Society, Providence, R.I., 2010.
- R. E. Ewing, R. D. Lazarov, S. L. Lyons, D. V. Papavassiliou, J. Pasciak, and G. Qin. Numerical well model for non-darcy flow through isotropic porous media. *Computational Geosciences*, 3(3): 185–204, 1999. doi:10.1023/A:1011543412675.
- Q. Fang, S. Sakadžić, L. Ruvinskaya, A. Devor, A. M. Dale, and D. A. Boas. Oxygen advection and diffusion in a three dimensional vascular anatomical network. *Optics express*, 16(22):17530–17541, 2008. doi:10.1364/oe.16.17530.
- S. Fatichi, C. Pappas, and V. Y. Ivanov. Modeling plant–water interactions: an ecohydrological overview from the cell to the global scale. *Wiley Interdisciplinary Reviews: Water*, 3(3):327–368, 2016. doi:10.1002/wat2.1125.
- T. Fetzer, K. M. Smits, and R. Helmig. Effect of turbulence and roughness on coupled porous-medium/free-flow exchange processes. *Transport in Porous Media*, 114(2):395–424, 2016. doi:10.1007/s11242-016-0654-6.
- T. Fetzer, J. Vanderborght, K. Mosthaf, K. M. Smits, and R. Helmig. Heat and water transport in soils and across the soil-atmosphere interface: 2. numerical analysis. *Water Resources Research*, 53(2):1080–1100, 2017. doi:10.1002/2016WR019983.
- C. R. Fitts. Exact solution for two-dimensional flow to a well in an anisotropic domain. *Groundwater*, 44(1):99–101, 2006. doi:10.1111/j.1745-6584.2005.00082.x.
- B. Flemisch, M. Darcis, K. Erbertseder, B. Faigle, A. Lauser, K. Mosthaf, S. Müthing, P. Nuske, A. Tatomir, M. Wolff, and R. Helmig. DuMu<sup>x</sup>: DUNE for multi-{phase, component, scale, physics,...} flow and transport in porous media. *Advances in Water Resources*, 34(9):1102–1112, 2011. doi:10.1016/j.advwatres.2011.03.007.
- P. Forchheimer. *Wasserbewegung durch Boden*, volume 45. Zeitschrift des Vereins deutscher Ingenieure, Düsseldorf, 1901.
- D. Foreman-Mackey. corner.py: Scatterplot matrices in python. *The Journal of Open Source Software*, 24, 2016. doi:10.21105/joss.00024.

- D. Foreman-Mackey, D. W. Hogg, D. Lang, and J. Goodman. emcee : The mcmc hammer. *Publications of the Astronomical Society of the Pacific*, 125(925):306, 2013. doi:10.1086/670067.
- L. Formaggia, D. Lamponi, and A. Quarteroni. One-dimensional models for blood flow in arteries. *Journal of engineering mathematics*, 47(3-4):251–276, 2003.
- L. Formaggia, A. M. Quarteroni, and A. Veneziani. *Cardiovascular mathematics*. Springer, 2009.
- Y. Forslin, S. Shams, F. Hashim, P. Aspelin, G. Bergendal, J. Martola, S. Fredrikson, M. Kristoffersen-Wiberg, and T. Granberg. Retention of gadolinium-based contrast agents in multiple sclerosis: Retrospective analysis of an 18-year longitudinal study. *American Journal of Neuroradiology*, 38(7): 1311–1316, 2017. doi:10.3174/ajnr.A5211.
- P. A. Forsyth. Comparison of the single-phase and two-phase numerical model formulation for saturated-unsaturated groundwater flow. *Computer Methods in Applied Mechanics and Engineering*, 69(2):243 – 259, 1988. doi:10.1016/0045-7825(88)90190-9.
- K. O. Friedrichs. The identity of weak and strong extensions of differential operators. *Transactions of the American Mathematical Society*, 55(1):132–151, 1944. doi:10.1090/S0002-9947-1944-0009701-0.
- K. O. Friedrichs. On the differentiability of the solutions of linear elliptic differential equations. *Communications on Pure and Applied Mathematics*, 6(3):299–326, 1953. doi:10.1002/cpa.3160060301.
- Y. Fung and B. Zweifach. Microcirculation: mechanics of blood flow in capillaries. *Annual Review of Fluid Mechanics*, 3(1):189–210, 1971. doi:10.1146/annurev.fl.03.010171.001201.
- Y.-C. Fung. Stochastic flow in capillary blood vessels. *Microvascular Research*, 5(1):34 – 48, 1973. doi:10.1016/S0026-2862(73)80005-6.
- L. Gagnon, S. Sakadžić, F. Lesage, J. J. Musacchia, J. Lefebvre, Q. Fang, M. A. Yücel, K. C. Evans, E. T. Mandeville, J. Cohen-Adad, J. R. Polimeni, M. A. Yaseen, E. H. Lo, D. N. Greve, R. B. Buxton, A. M. Dale, A. Devor, and D. A. Boas. Quantifying the microvascular origin of BOLD-fMRI from first principles with two-photon microscopy and an oxygen-sensitive nanoprobe. *Journal of Neuroscience*, 35(8):3663–3675, 2015. doi:10.1523/JNEUROSCI.3555-14.2015.
- E. Garrigues, C. Doussan, and A. Pierret. Water uptake by plant roots: I – formation and propagation of a water extraction front in mature root systems as evidenced by 2d light transmission imaging. *Plant and Soil*, 283(1):83, 2006. doi:10.1007/s11104-004-7903-0.
- D. Gaston, C. Newman, G. Hansen, and D. Lebrun-Grandié. Moose: A parallel computational framework for coupled systems of nonlinear equations. *Nuclear Engineering and Design*, 239(10): 1768–1778, 2009. doi:10.1016/j.nucengdes.2009.05.021.

- Y. Ge, M. Law, G. Johnson, J. Herbert, J. S. Babb, L. J. Mannon, and R. I. Grossman. Dynamic susceptibility contrast perfusion MR imaging of multiple sclerosis lesions: Characterizing hemodynamic impairment and inflammatory activity. *American Journal of Neuroradiology*, 26(6): 1539–1547, 2005. URL <http://www.ajnr.org/content/26/6/1539>.
- C. Geuzaine and J.-F. Remacle. Gmsh: A 3-D finite element mesh generator with built-in pre- and post-processing facilities. *International Journal for Numerical Methods in Engineering*, 79(11): 1309–1331, 2009. doi:10.1002/nme.2579.
- I. G. Gjerde, K. Kumar, J. M. Nordbotten, and B. Wohlmuth. Splitting method for elliptic equations with line sources. *ESAIM: Mathematical Modelling and Numerical Analysis*, 53(5):1715–1739, 2019. doi:10.1051/m2an/2019027.
- D. Gläser, B. Flemisch, R. Helmig, and H. Class. A hybrid-dimensional discrete fracture model for non-isothermal two-phase flow in fractured porous media. *GEM - International Journal on Geomathematics*, 10(1):5, 2019. doi:10.1007/s13137-019-0116-8.
- D. Gläser, R. Helmig, B. Flemisch, and H. Class. A discrete fracture model for two-phase flow in fractured porous media. *Advances in Water Resources*, 110:335 – 348, 2017a. doi:10.1016/j.advwatres.2017.10.031.
- D. Gläser, R. Helmig, B. Flemisch, and H. Class. A discrete fracture model for two-phase flow in fractured porous media. *Advances in Water Resources*, 110:335–348, 2017b. doi:10.1016/j.advwatres.2017.10.031.
- D. Goldman. Theoretical models of microvascular oxygen transport to tissue. *Microcirculation*, 15(8):795–811, 2008. doi:10.1080/10739680801938289.
- J. Goodman. Acor, statistical analysis of a time series. <https://www.math.nyu.edu/faculty/goodman/software/acor/>. Last accessed: 18 Oct 2018.
- J. Goodman and J. Weare. Ensemble samplers with affine invariance. *Communications in applied mathematics and computational science*, 5(1):65–80, 2010. doi:10.2140/camcos.2010.5.65.
- W. G. Gray and S. M. Hassanizadeh. Paradoxes and realities in unsaturated flow theory. *Water Resour. Res.*, 27(8):1847–1854, 1991. doi:10.1029/91WR01259.
- R. Guibert, C. Fonta, and F. Plouraboué. Cerebral blood flow modeling in primate cortex. *Journal of Cerebral Blood Flow & Metabolism*, 30(11):1860–1873, 2010. doi:10.1038/jcbfm.2010.105.
- R. Guibert, C. Fonta, L. Risser, and F. Plouraboué. Coupling and robustness of intra-cortical vascular territories. *NeuroImage*, 62(1):408–417, 2012. doi:10.1016/j.neuroimage.2012.04.030.

- G. Guthausen, J. R. Machado, B. Luy, A. Baniodeh, A. K. Powell, S. Krämer, F. Ranzinger, M. P. Herrling, S. Lackner, and H. Horn. Characterisation and application of ultra-high spin clusters as magnetic resonance relaxation agents. *Dalton Transactions*, 44(11):5032–5040, 2015. doi:10.1039/C4DT02916J.
- E. Haghighi, E. Shahraeeni, P. Lehmann, and D. Or. Evaporation rates across a convective air boundary layer are dominated by diffusion. *Water Resources Research*, 49(3):1602–1610, 2013. doi:10.1002/wrcr.20166.
- H. B. Hales. *SPE-39065-MS*, chapter An Improved Method for Simulating Reservoir Pressures Through the Incorporation of Analytical Well Functions, page 6. Society of Petroleum Engineers, Rio de Janeiro, Brazil, 1997. ISBN 978-1-55563-401-8. doi:10.2118/39065-MS.
- D. Hanahan and R. Weinberg. Hallmarks of cancer: The next generation. *Cell*, 144(5):646 – 674, 2011. doi:10.1016/j.cell.2011.02.013.
- R. Helmig. *Multiphase flow and transport processes in the subsurface: a contribution to the modeling of hydrosystems*. Springer-Verlag, 1997.
- A. Hewitt. Soil properties for plant growth. *Landcare Research Science Series*, 2004.
- A. K. Heye, M. J. Thrippleton, P. A. Armitage, M. d. C. V. Hernández, S. D. Makin, A. Glatz, E. Sakka, and J. M. Wardlaw. Tracer kinetic modelling for DCE-MRI quantification of subtle blood–brain barrier permeability. *NeuroImage*, 125:446–455, 2016. doi:10.1016/j.neuroimage.2015.10.018.
- A. Heymans, V. Couvreur, T. LaRue, A. Paez-Garcia, and G. Lobet. Granar, a computational tool to better understand the functional importance of monocotyledon root anatomy. *Plant Physiology*, 182(2):707–720, 2020. ISSN 0032-0889. doi:10.1104/pp.19.00617.
- R. Hill. Elastic properties of reinforced solids: Some theoretical principles. *Journal of the Mechanics and Physics of Solids*, 11(5):357 – 372, 1963. doi:doi.org/10.1016/0022-5096(63)90036-X.
- K. E. Holter, M. Kuchta, and K.-A. Mardal. Sub-voxel perfusion modeling in terms of coupled 3d-1d problem. In F. A. Radu, K. Kumar, I. Berre, J. M. Nordbotten, and I. S. Pop, editors, *Numerical Mathematics and Advanced Applications ENUMATH 2017*, pages 35–47, Cham, 2019. Springer International Publishing. ISBN 978-3-319-96415-7.
- R. Hsu and T. W. Secomb. A green’s function method for analysis of oxygen delivery to tissue by microvascular networks. *Mathematical Biosciences*, 96(1):61–78, 1989. doi:10.1016/0025-5564(89)90083-7.

- R. Huber and R. Helmig. Multiphase flow in heterogeneous porous media: A classical finite element method versus an implicit pressure-explicit saturation-based mixed finite element-finite volume approach. *International Journal for Numerical Methods in Fluids*, 29(8):899–920, 1999. doi:10.1002/(SICI)1097-0363(19990430)29:8 < 899::AID-FLD715 > 3.0.CO;2-W.
- E. R. Hyde, C. Michler, J. Lee, A. N. Cookson, R. Chabiniok, D. A. Nordsletten, and N. P. Smith. Parameterisation of multi-scale continuum perfusion models from discrete vascular networks. *Medical & Biological Engineering & Computing*, 51(5):557–570, 2013. doi:10.1007/s11517-012-1025-2.
- IMEX, 2014. IMEX User’s Guide, 2014. Computer Modelling Group Ltd.
- M. Ingrisch, S. P. Sourbron, D. Morhard, B. Ertl-Wagner, T. Kümpfel, R. Hohlfeld, M. Reiser, and C. Glaser. Quantification of perfusion and permeability in multiple sclerosis: Dynamic contrast-enhanced MRI in 3D at 3T. *Investigative Radiology*, 47(4), 2012. doi:10.1097/RLI.0b013e31823bfc97.
- R. Jain. Transport of molecules across tumor vasculature. *Cancer and Metastasis Reviews*, 6(4): 559–593, 1987. doi:10.1007/BF00047468.
- B. Jakobsen and A. Dexter. Effect of soil structure on wheat root growth, water uptake and grain yield. a computer simulation model. *Soil and Tillage Research*, 10(4):331–345, 1987. doi:10.1016/0167-1987(87)90022-5.
- P. Jarvis and K. McNaughton. Stomatal control of transpiration: Scaling up from leaf to region. *Advances in Ecological Research*, 15:1 – 49, 1986. doi:10.1016/S0065-2504(08)60119-1.
- M. Javaux, T. Schröder, J. Vanderborght, and H. Vereecken. Use of a Three-Dimensional Detailed Modeling Approach for Predicting Root Water Uptake. *Vadose Zone Journal*, 7(3):1079, 2008. doi:10.2136/vzj2007.0115.
- M. S. Jayalakshmy and J. Philip. Thermophysical properties of plant leaves and their influence on the environment temperature. *International Journal of Thermophysics*, 31(11-12):2295–2304, 2010. doi:10.1007/s10765-010-0877-7.
- N. Joukowsky. Über die Konturen der Tragflächen der Drachenflieger. *Zeitschrift für Flugtechnik und Motorluftschiffahrt*, 1:281–284, 1910.
- L. C. Junqueira, J. Carneiro, and R. O. Kelley. *Histologie*, volume 5, pages 163–187. Springer, Heidelberg, 2002. ISBN 9783540418580.
- D. Karvounis and P. Jenny. Adaptive hierarchical fracture model for enhanced geothermal systems. *Multiscale Modeling & Simulation*, 14(1):207–231, 2016. doi:10.1137/140983987.

- O. Kedem and A. Katchalsky. Thermodynamic analysis of the permeability of biological membranes to non-electrolytes. *Biochimica et Biophysica Acta*, 27:229–246, 1958. doi:10.1016/0006-3002(58)90330-5.
- D. Kempf and T. Koch. System testing in scientific numerical software frameworks using the example of dune. *Archive of Numerical Software*, 5(1):151–168, 2017. doi:10.11588/ans.2017.1.27447.
- A. Kermode, A. Thompson, P. Tofts, D. MacManus, B. Kendall, D. Kingsley, I. Moseley, P. Rudge, and W. McDonald. Breakdown of the blood-brain barrier precedes symptoms and other MRI signs of new lesions in multiple sclerosis. *Brain*, 113(5):1477–1489, 1990.
- V. G. Kiselev. On the theoretical basis of perfusion measurements by dynamic susceptibility contrast MRI. *Magnetic Resonance in Medicine*, 46(6):1113–1122, 2001. doi:10.1002/mrm.1307.
- V. G. Kiselev. Transverse relaxation effect of MRI contrast agents: A crucial issue for quantitative measurements of cerebral perfusion. *Journal of Magnetic Resonance Imaging*, 22(6):693–696, 2005. doi:10.1002/jmri.20452.
- V. G. Kiselev and D. S. Novikov. Transverse NMR relaxation as a probe of mesoscopic structure. *Phys. Rev. Lett.*, 89:278101, 2002. doi:10.1103/PhysRevLett.89.278101.
- T. Koch. Benchmark C1.2 Data Set - Numerical results reference solution, 2019. doi:10.18419/darus-471.
- T. Koch, D. Gläser, K. Weishaupt, S. Ackermann, M. Beck, B. Becker, S. Burbulla, H. Class, E. Coltman, T. Fetzer, B. Flemisch, C. Grüninger, K. Heck, J. Hommel, T. Kurz, M. Lipp, F. Mohammadi, M. Schneider, G. Seitz, S. Scholz, and F. Weinhardt. Dumux 3.0.0, 2018a. doi:10.5281/zenodo.2479595.
- T. Koch, K. Heck, N. Schröder, H. Class, and R. Helmig. A new simulation framework for soil-root interaction, evaporation, root growth, and solute transport. *Vadose Zone Journal*, 17, 2018b. doi:10.2136/vzj2017.12.0210.
- T. Koch, B. Flemisch, R. Helmig, R. Wiest, and D. Obrist. A multiscale subvoxel perfusion model to estimate diffusive capillary wall conductivity in multiple sclerosis lesions from perfusion mri data. *International Journal for Numerical Methods in Biomedical Engineering*, 36(2):e3298, 2020a. doi:10.1002/cnm.3298.
- T. Koch, D. Gläser, K. Weishaupt, S. Ackermann, M. Beck, B. Becker, S. Burbulla, H. Class, E. Coltman, S. Emmert, T. Fetzer, C. Grüninger, K. Heck, J. Hommel, T. Kurz, M. Lipp, F. Mohammadi, S. Scherrer, M. Schneider, G. Seitz, L. Stadler, M. Utz, F. Weinhardt, and B. Flemisch. Dumu<sup>x</sup> 3 – an open-source simulator for solving flow and transport problems in



- porous media with a focus on model coupling. *Computers & Mathematics with Applications*, 2020b. ISSN 0898-1221. doi:10.1016/j.camwa.2020.02.012.
- T. Koch, R. Helmig, and M. Schneider. A new and consistent well model for one-phase flow in anisotropic porous media using a distributed source model. *Journal of Computational Physics*, 410:109369, 2020c. ISSN 0021-9991. doi:10.1016/j.jcp.2020.109369.
- T. Koch, M. Schneider, R. Helmig, and P. Jenny. Modeling tissue perfusion in terms of 1d-3d embedded mixed-dimension coupled problems with distributed sources. *Journal of Computational Physics*, 410:109370, 2020d. ISSN 0021-9991. doi:10.1016/j.jcp.2020.109370.
- M. Kuchta, K.-A. Mardal, and M. Mortensen. Preconditioning trace coupled 3d-1d systems using fractional laplacian. *Numerical Methods for Partial Differential Equations*, 35(1):375–393, 2019. doi:10.1002/num.22304.
- T. Köppl. *Multi-scale modeling of flow and transport processes in arterial networks and tissue*. Phd thesis, Technical University of Munich, 2015.
- T. Köppl, E. Vidotto, and B. Wohlmuth. A local error estimate for the poisson equation with a line source term. In B. Karasözen, M. Manguoğlu, M. Tezer-Sezgin, S. Göktepe, and Ö. Uğur, editors, *Numerical Mathematics and Advanced Applications ENUMATH 2015*, pages 421–429, Cham, 2016. Springer International Publishing. ISBN 978-3-319-39929-4.
- T. Köppl, E. Vidotto, B. Wohlmuth, and P. Zunino. Mathematical modeling, analysis and numerical approximation of second-order elliptic problems with inclusions. *Mathematical Models and Methods in Applied Sciences*, 28(05):953–978, 2018. doi:10.1142/S0218202518500252.
- M. E. Ladd, P. Bachert, M. Meyerspeer, E. Moser, A. M. Nagel, D. G. Norris, S. Schmitter, O. Speck, S. Straub, and M. Zaiss. Pros and cons of ultra-high-field mri/mrs for human application. *Progress in Nuclear Magnetic Resonance Spectroscopy*, 109:1–50, 2018. doi:10.1016/j.pnmrs.2018.06.001.
- E. Lapointe, D. Li, A. Trabouise, and A. Rauscher. What have we learned from perfusion MRI in multiple sclerosis? *American Journal of Neuroradiology*, 39(6):994–1000, 2018. doi:10.3174/ajnr.A5504.
- T.-R. Lee, M. Choi, A. M. Kopacz, S.-H. Yun, W. K. Liu, and P. Decuzzi. On the near-wall accumulation of injectable particles in the microcirculation: smaller is not better. *Scientific Reports*, 3, 2013. doi:10.1038/srep02079.
- P. Lehmann, S. Assouline, and D. Or. Characteristic lengths affecting evaporative drying of porous media. *Phys. Rev. E*, 77:056309, 2008. doi:10.1103/PhysRevE.77.056309.
- D. Leitner and A. Schnepf. CRootBox, 2016.

- D. Leitner, S. Klepsch, G. Bodner, and A. Schnepf. A dynamic root system growth model based on l-systems. *Plant and Soil*, 332(1):177–192, 2010. doi:10.1007/s11104-010-0284-7.
- D. Leitner, B. Felderer, P. Vontobel, and A. Schnepf. Recovering root system traits using image analysis exemplified by two-dimensional neutron radiography images of lupine. *Plant Physiology*, 164(1):24–35, 2014a. doi:10.1104/pp.113.227892.
- D. Leitner, F. Meunier, G. Bodner, M. Javaux, and A. Schnepf. Impact of contrasted maize root traits at flowering on water stress tolerance – a simulation study. *Field Crops Research*, 165:125 – 137, 2014b. doi:10.1016/j.fcr.2014.05.009. Crop root system behaviour and yield.
- J. Levick. Capillary filtration-absorption balance reconsidered in light of dynamic extravascular factors. *Experimental Physiology*, 76(6):825–857, 1991. doi:10.1113/expphysiol.1991.sp003549.
- M. Libault, L. Brechenmacher, J. Cheng, D. Xu, and G. Stacey. Root hair systems biology. *Trends in Plant Science*, 15(11):641 – 650, 2010. doi:10.1016/j.tplants.2010.08.010.
- A. A. Linninger, I. G. Gould, T. Marinnan, C.-Y. Hsu, M. Chojecki, and A. Alaraj. Cerebral microcirculation and oxygen tension in the human secondary cortex. *Annals of Biomedical Engineering*, 41(11):2264–2284, 2013. doi:10.1007/s10439-013-0828-0.
- S. Llufriu, T. Pujol, Y. Blanco, K. Hankiewicz, M. Squarcia, J. Berenguer, P. Villoslada, F. Graus, and A. Saiz. T2 hypointense rims and ring-enhancing lesions in ms. *Multiple Sclerosis Journal*, 16(11):1317–1325, 2010. doi:10.1177/1352458510377905.
- S. Lorthois, F. Cassot, and F. Lauwers. Simulation study of brain blood flow regulation by intracortical arterioles in an anatomically accurate large human vascular network: Part i: Methodology and baseline flow. *NeuroImage*, 54(2):1031–1042, 2011. doi:10.1016/j.neuroimage.2010.09.032.
- C. Lovisolo and A. Schubert. Effects of water stress on vessel size and xylem hydraulic conductivity in *vitis vinifera* l. *Journal of Experimental Botany*, 49(321):693–700, 1998. doi:10.1093/jxb/49.321.693.
- L. Luckner, M. T. Van Genuchten, and D. Nielsen. A consistent set of parametric models for the two-phase flow of immiscible fluids in the subsurface. *Water Resources Research*, 25(10):2187–2193, 1989. doi:10.1029/WR025i010p02187.
- J. Lynch. Root architecture and plant productivity. *Plant physiology*, 109(1):7, 1995.
- J. P. Lynch, K. L. Nielsen, R. D. Davis, and A. G. Jabllokow. Simroot: Modelling and visualization of root systems. *Plant and Soil*, 188(1):139–151, 1997. doi:10.1023/A:1004276724310.
- A. Lücker. *Computational Modeling of Oxygen Transport in the Microcirculation. From an Experiment-Based Model to Theoretical Analyses*. PhD thesis, ETH Zurich, Zurich, 2017.

- T. H. Mai, A. Schnepf, H. Vereecken, and J. Vanderborght. Continuum multiscale model of root water and nutrient uptake from soil with explicit consideration of the 3d root architecture and the rhizosphere gradients. *Plant and Soil*, 439(1):273–292, 2019. doi:10.1007/s11104-018-3890-4.
- E. Malézieux, Y. Crozat, C. Dupraz, M. Laurans, D. Makowski, B. Rapidel, and S. D. Tourdonnet. Mixing Plant Species in Cropping Systems : Concepts , Tools and Models : A Review. *Agronomy Journal*, 29:43–62, 2009. doi:10.1051/agro.
- G. Manoli, C.-W. Huang, S. Bonetti, J.-C. Domec, M. Marani, and G. Katul. Competition for light and water in a coupled soil-plant system. *Advances in Water Resources*, 108:216–230, 2017. doi:10.1016/j.advwatres.2017.08.004.
- B. S. Massey and J. Ward-Smith. *Mechanics of Fluids*. CRC Press, 8 edition, 2005. doi:10.4324/9780203012314.
- A. Massing, M. Larson, and A. Logg. Efficient implementation of finite element methods on nonmatching and overlapping meshes in three dimensions. *SIAM Journal on Scientific Computing*, 35(1):C23–C47, 2013. doi:10.1137/11085949X.
- C. C. Michel and F. E. Curry. Microvascular permeability. *Physiological Reviews*, 79(3):703–761, 1999. doi:10.1152/physrev.1999.79.3.703.
- C. Michler, A. N. Cookson, R. Chabiniok, E. Hyde, J. Lee, M. Sinclair, T. Sochi, A. Goyal, G. Viguera, D. A. Nordsletten, and N. P. Smith. A computationally efficient framework for the simulation of cardiac perfusion using a multi-compartment darcy porous-media flow model. *International Journal for Numerical Methods in Biomedical Engineering*, 29(2):217–232, 2013. doi:10.1002/cnm.2520.
- A. Minagar and J. S. Alexander. Blood-brain barrier disruption in multiple sclerosis. *Multiple Sclerosis Journal*, 9(6):540–549, 2003.
- J. Misra, M. Patra, and S. Misra. A non-newtonian fluid model for blood flow through arteries under stenotic conditions. *Journal of Biomechanics*, 26(9):1129–1141, 1993. doi:10.1016/S0021-9290(05)80011-9.
- K. Mosthaf, K. Baber, B. Flemisch, R. Helmig, A. Leijnse, I. Rybak, and B. Wohlmuth. A coupling concept for two-phase compositional porous-medium and single-phase compositional free flow. *Water Resources Research*, 47(10), 2011. doi:10.1029/2011WR010685. W10522.
- K. Mosthaf, R. Helmig, and D. Or. Modeling and analysis of evaporation processes from porous media on the rev scale. *Water Resources Research*, 50(2):1059–1079, 2014. doi:10.1002/2013WR014442.

- E. D. F. Motti, H.-G. Imhof, and M. G. Yaşargil. The terminal vascular bed in the superficial cortex of the rat. *Journal of Neurosurgery*, 65(6):834–846, 1986. doi:10.3171/jns.1986.65.6.0834.
- Y. Mualem. A new model for predicting the hydraulic conductivity of unsaturated porous media. *Water Resources Research*, 12(3):513–522, 1976. doi:10.1029/WR012i003p00513.
- M. Nabil, P. Decuzzi, and P. Zunino. Modelling mass and heat transfer in nano-based cancer hyperthermia. *Open Science*, 2(10), 2015. doi:10.1098/rsos.150447.
- Z. Nehari. *Conformal mapping*. Dover Publications, Inc., New York, 1975. Reprinting of the 1952 edition.
- R. B. Neumann and Z. G. Cardon. The magnitude of hydraulic redistribution by plant roots: a review and synthesis of empirical and modeling studies. *New Phytologist*, 194(2):337–352, 2012. doi:10.1111/j.1469-8137.2012.04088.x.
- C. E. Neuzil. How permeable are clays and shales? *Water Resources Research*, 30(2):145–150, 1994. doi:10.1029/93WR02930.
- D. A. Nield and A. Bejan. *Convection in Porous Media*. Springer, New York, NY, 2013. doi:10.1007/978-1-4614-5541-7.
- D. Obrist, B. Weber, A. Buck, and P. Jenny. Red blood cell distribution in simplified capillary networks. *Philosophical Transactions of the Royal Society A: Mathematical, Physical and Engineering Sciences*, 368(1921):2897–2918, 2010. doi:10.1098/rsta.2010.0045.
- M. S. Olufsen, C. S. Peskin, W. Y. Kim, E. M. Pedersen, A. Nadim, and J. Larsen. Numerical simulation and experimental validation of blood flow in arteries with structured-tree outflow conditions. *Annals of Biomedical Engineering*, 28(11):1281–1299, 2000. doi:10.1114/1.1326031.
- L. Pagès, G. Vercambre, J.-L. Drouet, F. Lecompte, C. Collet, and J. Le Bot. Root typ: a generic model to depict and analyse the root system architecture. *Plant and Soil*, 258(1):103–119, 2004. doi:10.1023/B:PLSO.0000016540.47134.03.
- A. P. Pathak, B. D. Ward, and K. M. Schmainda. A novel technique for modeling susceptibility-based contrast mechanisms for arbitrary microvascular geometries: the finite perturber method. *Neuroimage*, 40(3):1130–1143, 2008. doi:10.1016/j.neuroimage.2008.01.022.
- D. W. Peaceman. Interpretation of well-block pressures in numerical reservoir simulation. *Society of Petroleum Engineers Journal*, 18(03):183–194, 1978.
- D. W. Peaceman. Interpretation of well-block pressures in numerical reservoir simulation with nonsquare grid blocks and anisotropic permeability. *Society of Petroleum Engineers Journal*, 23(03): 531–543, 1983. doi:10.2118/10528-PA.

- L. Pedersen, E. B. Nielsen, M. K. Christensen, M. Buchwald, and M. Nybo. Measurement of plasma viscosity by free oscillation rheometry: imprecision, sample stability and establishment of a new reference range. *Annals of Clinical Biochemistry*, 51(4):495–498, 2014. doi:10.1177/0004563213504550.
- R. Penta, D. Ambrosi, and A. Quarteroni. Multiscale homogenization for fluid and drug transport in vascularized malignant tissues. *Mathematical Models and Methods in Applied Sciences*, 25(01):79–108, 2015. doi:10.1142/S0218202515500037.
- P. Perdikaris, L. Grinberg, and G. E. Karniadakis. Multiscale modeling and simulation of brain blood flow. *Physics of Fluids*, 28(2):021304, 2016. doi:10.1063/1.4941315.
- M. Peyrounette, Y. Davit, M. Quintard, and S. Lorthois. Multiscale modelling of blood flow in cerebral microcirculation: Details at capillary scale control accuracy at the level of the cortex. *PLoS one*, 13(1):e0189474, 2018.
- J. Plumb, S. McQuaid, M. Mirakhur, and J. Kirk. Abnormal endothelial tight junctions in active lesions and normal-appearing white matter in multiple sclerosis. *Brain Pathology*, 12(2):154–169, 2002. doi:10.1111/j.1750-3639.2002.tb00430.x.
- K. Pohl, G. Böckle, and F. van der Linden. *Software Product Line Engineering - Foundations, Principles, and Techniques*. Springer, 2005. ISBN 978-3-540-24372-4. doi:10.1007/3-540-28901-1.
- C. H. Polman, S. C. Reingold, B. Banwell, M. Clanet, J. A. Cohen, M. Filippi, K. Fujihara, E. Havrdova, M. Hutchinson, L. Kappos, F. D. Lublin, X. Montalban, P. O’Connor, M. Sandberg-Wollheim, A. J. Thompson, E. Waubant, B. Weinshenker, and J. S. Wolinsky. Diagnostic criteria for multiple sclerosis: 2010 revisions to the mcdonald criteria. *Ann Neurol*, 69(2):292–302, 2011. doi:10.1002/ana.22366.
- A. S. Popel and P. C. Johnson. Microcirculation and hemorheology. *Annual Review of Fluid Mechanics*, 37(1):43–69, 2005. doi:10.1146/annurev.fluid.37.042604.133933.
- L. Possenti, S. di Gregorio, F. M. Gerosa, G. Raimondi, G. Casagrande, M. L. Costantino, and P. Zunino. A computational model for microcirculation including fahraeus-lindqvist effect, plasma skimming and fluid exchange with the tissue interstitium. *International Journal for Numerical Methods in Biomedical Engineering*, 35(3):e3165, 2019. doi:10.1002/cnm.3165.
- J. A. Postma, C. Kuppe, M. R. Owen, N. Mellor, M. Griffiths, M. J. Bennett, J. P. Lynch, and M. Watt. Opensimroot: widening the scope and application of root architectural models. *New Phytologist*, 215(3):1274–1286, 2017. doi:10.1111/nph.14641. 2017-24197.
- H. C. Price, J. Mattsson, and B. J. Murray. Sucrose diffusion in aqueous solution. *Phys. Chem. Chem. Phys.*, 18:19207–19216, 2016. doi:10.1039/C6CP03238A.

- A. Pries, K. Ley, M. Claassen, and P. Gaetgens. Red cell distribution at microvascular bifurcations. *Microvascular Research*, 38(1):81 – 101, 1989. doi:10.1016/0026-2862(89)90018-6.
- A. R. Pries and W. M. Kuebler. *Normal Endothelium*, chapter 1, pages 1–40. Springer Berlin Heidelberg, Berlin, Heidelberg, 2006. ISBN 978-3-540-32967-1. doi:10.1007/3-540-32967-6\_1.
- A. R. Pries, T. W. Secomb, and P. Gaetgens. Biophysical aspects of blood flow in the microvasculature1. *Cardiovascular Research*, 32(4):654–667, 1996. doi:10.1016/S0008-6363(96)00065-X.
- P. Prusinkiewicz. Modeling plant growth and development. *Current opinion in plant biology*, 7(1):79–83, 2004. doi:10.1016/j.pbi.2003.11.007.
- PubChem. Gadobutrol. <https://pubchem.ncbi.nlm.nih.gov/compound/15814656>, 2018. last accessed, 4 Sep 2018.
- C. Quarles, D. Gochberg, J. Gore, and T. Yankeelov. A theoretical framework to model DSC-MRI data acquired in the presence of contrast agent extravasation. *Physics in medicine and biology*, 54(19):5749, 2009. doi:10.1088/0031-9155/54/19/006.
- A. Quarteroni and L. Formaggia. Mathematical modelling and numerical simulation of the cardiovascular system. *Handbook of numerical analysis*, 12:3–127, 2004.
- A. Quarteroni, A. Manzoni, and C. Vergara. The cardiovascular system: mathematical modelling, numerical algorithms and clinical applications. *Acta Numerica*, 26:365–590, 2017. doi:10.1017/S0962492917000046.
- J. Reichold, M. Stampanoni, A. L. Keller, A. Buck, P. Jenny, and B. Weber. Vascular graph model to simulate the cerebral blood flow in realistic vascular networks. *Journal of Cerebral Blood Flow & Metabolism*, 29(8):1429–1443, 2009. doi:10.1038/jcbfm.2009.58.
- H. Rimmel. *Supporting the Quality Assurance of a Scientific Framework*. PhD thesis, University of Heidelberg, 2014.
- H. Rimmel, B. Paech, C. Engwer, and P. Bastian. Supporting the Testing of Scientific Frameworks with Software Product Line Engineering: A Proposed Approach. In *Proceedings of the 4th International Workshop on Software Engineering for Computational Science and Engineering*, SECSE ’11, pages 10–18, New York, NY, USA, 2011. ACM. ISBN 978-1-4503-0598-3. doi:10.1145/1985782.1985785.
- H. Rimmel, B. Paech, P. Bastian, and C. Engwer. System Testing a Scientific Framework Using a Regression-Test Environment. *Computing in Science & Engineering*, 14(2):38–45, 2012. doi:10.1109/MCSE.2011.115.

- E. M. Renkin. *Transport Pathways and Processes*, pages 51–68. Springer US, Boston, MA, 1988. ISBN 978-1-4613-0937-6. doi:10.1007/978-1-4613-0937-6\_3.
- J. H. Richards and M. M. Caldwell. Hydraulic lift: Substantial nocturnal water transport between soil layers by artemisia tridentata roots. *Oecologia*, 73(4):486–489, 1987. doi:10.1007/BF00379405.
- L. A. Richards. Capillary conduction of liquids through porous mediums. *Physics*, 1(5):318–333, 1931. doi:10.1063/1.1745010.
- B. Rippe and B. Haraldsson. Transport of macromolecules across microvascular walls: the two-pore theory. *Physiological Reviews*, 74(1):163–219, 1994. doi:10.1152/physrev.1994.74.1.163.
- G. D. Robert, K. Pavitra, W. D. R., M. Bostjan, B. Russell, M. Ruth, and P. Mike. Estimating oxygen distribution from vasculature in three-dimensional tumour tissue. *Journal of The Royal Society Interface*, 13(116):20160070, 2016. doi:10.1098/rsif.2016.0070.
- M. Rohrer, H. Bauer, J. Mintorovitch, M. Requardt, and H.-J. Weinmann. Comparison of magnetic properties of MRI contrast media solutions at different magnetic field strengths. *Investigative radiology*, 40(11):715–724, 2005. doi:10.1097/01.rli.0000184756.66360.d3.
- T. Roose and A. Schnepf. Mathematical models of plant–soil interaction. *Philosophical Transactions of the Royal Society of London A: Mathematical, Physical and Engineering Sciences*, 366(1885):4597–4611, 2008. doi:10.1098/rsta.2008.0198.
- T. Roose and M. A. Swartz. Multiscale modeling of lymphatic drainage from tissues using homogenization theory. *Journal of biomechanics*, 45(1):107–115, 2012. doi:10.1016/j.jbiomech.2011.09.015.
- W. Rudin. *Real and Complex Analysis, 3rd Ed.* McGraw-Hill, Inc., New York, NY, USA, 1987. ISBN 0070542341.
- D. Ruth and H. Ma. On the derivation of the forchheimer equation by means of the averaging theorem. *Transport in Porous Media*, 7(3):255–264, 1992. doi:10.1007/BF01063962.
- Y. Saad. *Iterative Methods for Sparse Linear Systems*. Society for Industrial and Applied Mathematics, Philadelphia, PA, USA, 2nd edition, 2003. ISBN 0898715342.
- S. Sakadzic, E. T. Mandeville, L. Gagnon, J. J. Musacchia, M. A. Yaseen, M. A. Yucel, J. Lefebvre, F. Lesage, A. M. Dale, K. Eikermann-Haerter, C. Ayata, V. J. Srinivasan, E. H. Lo, A. Devor, and D. A. Boas. Large arteriolar component of oxygen delivery implies a safe margin of oxygen supply to cerebral tissue. *Nature Communications*, 5(1):5734, 2014. doi:10.1038/ncomms6734.
- O. Sander, T. Koch, N. Schröder, and B. Flemisch. The dune foamgrid implementation for surface and network grids. *Archive of Numerical Software*, 5(1):217–244, 2017. doi:10.11588/ans.2017.1.28490.

- G. W. Scherer. Theory of drying. *Journal of the American Ceramic Society*, 73(1):3–14, 1990. doi:10.1111/j.1151-2916.1990.tb05082.x.
- F. Schmid. *Cerebral Blood Flow Modeling with Discrete Red Blood Cell Tracking. Analyzing Microvascular Networks and their Perfusion*. PhD thesis, ETH Zurich, 2017.
- F. Schmid, J. Reichold, B. Weber, and P. Jenny. The impact of capillary dilation on the distribution of red blood cells in artificial networks. *American Journal of Physiology-Heart and Circulatory Physiology*, 308(7):H733–H742, 2015. doi:10.1152/ajpheart.00335.2014.
- F. Schmid, P. S. Tsai, D. Kleinfeld, P. Jenny, and B. Weber. Depth-dependent flow and pressure characteristics in cortical microvascular networks. *PLOS Computational Biology*, 13(2):1–22, 2017. doi:10.1371/journal.pcbi.1005392.
- C. L. Schneider, S. Attinger, J.-O. Delfs, and A. Hildebrandt. Implementing small scale processes at the soil-plant interface - the role of root architectures for calculating root water uptake profiles. *Hydrology and Earth System Sciences*, 14(2):279–289, 2010. doi:10.5194/hess-14-279-2010.
- M. Schneider. *Nonlinear finite volume schemes for complex flow processes and challenging grids*. PhD thesis, University of Stuttgart, 2018.
- M. Schneider, D. Gläser, B. Flemisch, and R. Helmig. Comparison of finite-volume schemes for diffusion problems. *Oil Gas Sci. Technol. - Rev. IFP Energies nouvelles*, 73:82, 2018. doi:10.2516/ogst/2018064.
- M. Schneider, K. Weishaupt, D. Gläser, W. M. Boon, and R. Helmig. Coupling staggered-grid and mpfa finite volume methods for free flow/porous-medium flow problems. *Journal of Computational Physics*, 401:109012, 2020. doi:10.1016/j.jcp.2019.109012.
- A. Schnepf, D. Leitner, M. Landl, G. Lobet, T. H. Mai, S. Morandage, C. Sheng, M. Zörner, J. Vanderborght, and H. Vereecken. CRootBox: a structural–functional modelling framework for root systems. *Annals of Botany*, page mcx221, 2018. doi:10.1093/aob/mcx221.
- A. Schnepf, C. K. Black, V. Couvreur, B. M. Delory, C. Doussan, A. Koch, T. Koch, M. Javaux, M. Landl, D. Leitner, G. Lobet, T. H. Mai, F. Meunier, L. Petrich, J. A. Postma, E. Priesack, V. Schmidt, J. Vanderborght, H. Vereecken, and M. Weber. Call for participation: Collaborative benchmarking of functional-structural root architecture models. the case of root water uptake. *Frontiers in Plant Science*, 11:316, 2020. ISSN 1664-462X. doi:10.3389/fpls.2020.00316.
- N. Schröder. *Three-dimensional Solute Transport Modeling in Coupled Soil and Plant Root Systems*. Dr., Université catholique de Louvain (UCL), Louvain-La-Neuve, Jülich, 2014. URL [http:](http://)



- //juser.fz-juelich.de/record/151172. Université catholique de Louvain (UCL), Louvain-La-Neuve, Diss., 2013.
- P. Schröder, A. Wagner, D. Stöhr, M. Rehm, A. Jensch, N. Radde, and W. Ehlers. Modelling of lung-metastases apoptosis within brain tissue. *Proc. Appl. Math. Mech.*, 18(1):e201800323, 2018. doi:10.1002/pamm.201800323.
- T. Schröder, M. Javaux, J. Vanderborght, B. Körfgen, and H. Vereecken. Effect of local soil hydraulic conductivity drop using a three-dimensional root water uptake model. 7:1089–1098, 2008. doi:10.2136/vzj2007.0114. 3.
- T. Schröder, M. Javaux, J. Vanderborght, B. Körfgen, and H. Vereecken. Implementation of a Microscopic Soil–Root Hydraulic Conductivity Drop Function in a Three-Dimensional Soil–Root Architecture Water Transfer Model. *Vadose Zone Journal*, 8(3):783–792, 2009a. doi:10.2136/vzj2008.0116.
- T. Schröder, L. Tang, M. Javaux, J. Vanderborght, B. Körfgen, and H. Vereecken. A grid refinement approach for a three-dimensional soil-root water transfer model. *Water Resources Research*, 45(10), 2009b. doi:10.1029/2009WR007873. W10412.
- T. W. Secomb, R. Hsu, M. W. Dewhirst, B. Klitzman, and J. F. Gross. Analysis of oxygen transport to tumor tissue by microvascular networks. *International Journal of Radiation Oncology\*Biophysics*, 25(3):481–489, 1993. doi:10.1016/0360-3016(93)90070-C.
- T. W. Secomb, R. Hsu, N. Beamer, and B. Coull. Theoretical simulation of oxygen transport to brain by networks of microvessels: Effects of oxygen supply and demand on tissue hypoxia. *Microcirculation*, 7(4):237–247, 2000. doi:10.1111/j.1549-8719.2000.tb00124.x.
- T. W. Secomb, R. Hsu, E. Y. Park, and M. W. Dewhirst. Green’s function methods for analysis of oxygen delivery to tissue by microvascular networks. *Annals of Biomedical Engineering*, 32(11): 1519–1529, 2004. doi:10.1114/B:ABME.0000049036.08817.44.
- T. W. Secomb, J. P. Alberding, R. Hsu, M. W. Dewhirst, and A. R. Pries. Angiogenesis: An adaptive dynamic biological patterning problem. *PLOS Computational Biology*, 9(3):1–12, 2013. doi:10.1371/journal.pcbi.1002983.
- N. B. Semmineh, J. Xu, J. L. Boxerman, G. W. Delaney, P. W. Cleary, J. C. Gore, and C. C. Quarles. An efficient computational approach to characterize DSC-MRI signals arising from three-dimensional heterogeneous tissue structures. *PloS one*, 9(1):e84764, 2014. doi:10.1371/journal.pone.0084764.
- U. Shani and A. Ben-Gal. Long-term response of grapevines to salinity: osmotic effects and ion toxicity. *American journal of enology and viticulture*, 52:148–154, 2005. doi:10.1023/A:1004378602378.

- S. Sherwin, V. Franke, J. Peiró, and K. Parker. One-dimensional modelling of a vascular network in space-time variables. *Journal of Engineering Mathematics*, 47(3):217–250, 2003. doi:10.1023/B:ENGI.0000007979.32871.e2.
- R. J. Shipley and S. J. Chapman. Multiscale modelling of fluid and drug transport in vascular tumours. *Bulletin of mathematical biology*, 72(6):1464–1491, 2010. doi:10.1007/s11538-010-9504-9.
- R. J. Shipley, A. F. Smith, P. W. Sweeney, A. R. Pries, and T. W. Secomb. A hybrid discrete–continuum approach for modelling microcirculatory blood flow. *Mathematical Medicine and Biology: A Journal of the IMA*, 2019. doi:10.1093/imammb/dqz006.
- M. S. Shiroishi, G. Castellazzi, J. L. Boxerman, F. D’Amore, M. Essig, T. B. Nguyen, J. M. Provenzale, D. S. Enterline, N. Anzalone, A. Dörfler, A. Rovira, M. Wintermark, and M. Law. Principles of T2\*-weighted dynamic susceptibility contrast MRI technique in brain tumor imaging. *Journal of Magnetic Resonance Imaging*, 41(2):296–313, 2015. doi:10.1002/jmri.24648.
- D. R. Smart, E. Carlisle, M. Goebel, and B. A. Nunez. Transverse hydraulic redistribution by a grapevine. *Plant, Cell & Environment*, 28(2):157–166, 2005. doi:10.1111/j.1365-3040.2004.01254.x.
- K. A. Snyder, J. H. Richards, and L. A. Donovan. Night-time conductance in c3 and c4 species: do plants lose water at night? *Journal of Experimental Botany*, 54(383):861, 2003. doi:10.1093/jxb/erg082.
- W. H. Somerton. *Thermal properties and temperature-related behavior of rock/fluid systems*, volume 37, page 83. Elsevier, 1992.
- W. H. Somerton, J. A. Keese, and S. L. Chu. Thermal behavior of unconsolidated oil sands. *Society of Petroleum Engineers Journal*, 14(05):513–521, 1974. doi:10.2118/4506-PA.
- F. Somma, J. W. Hopmans, and V. Clausnitzer. Transient three-dimensional modeling of soil water and solute transport with simultaneous root growth, root water and nutrient uptake. *Plant and Soil*, 202:281–293, 1998.
- S. P. Sourbron and D. L. Buckley. Tracer kinetic modelling in MRI: estimating perfusion and capillary permeability. *Physics in medicine and biology*, 57(2):R1, 2012. doi:10.1088/0031-9155/57/2/R1.
- S. P. Sourbron and D. L. Buckley. Classic models for dynamic contrast-enhanced MRI. *NMR in Biomedicine*, 26(8):1004–1027, 2013. doi:10.1002/nbm.2940.
- E. H. Starling. On the absorption of fluids from the connective tissue spaces. *J Physiol*, 19(4):312–326, 1896.
- E. Steudle and C. A. Peterson. How does water get through roots? *Journal of Experimental Botany*, 49(322):775–788, 1998. doi:10.1093/jxb/49.322.775.

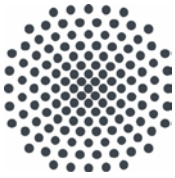
- M. Sugihara-Seki and B. M. Fu. Blood flow and permeability in microvessels. *Fluid Dynamics Research*, 37(1):82 – 132, 2005. doi:10.1016/j.fluiddyn.2004.03.006. Biofluidynamics.
- Q. Sun and G. X. Wu. Coupled finite difference and boundary element methods for fluid flow through a vessel with multibranches in tumours. *International journal for numerical methods in biomedical engineering*, 29(3):309–331, 2013. doi:10.1002/cnm.2502.
- P. W. Sweeney, A. d’Esposito, S. Walker-Samuel, and R. J. Shipley. Modelling the transport of fluid through heterogeneous, whole tumours in silico. *PLOS Computational Biology*, 15(6):1–28, 2019. doi:10.1371/journal.pcbi.1006751.
- E. Syková and C. Nicholson. Diffusion in brain extracellular space. *Physiological reviews*, 88(4): 1277–1340, 2008. doi:10.1152/physrev.00027.2007.
- A. Szymkiewicz. *Mathematical Models of Flow in Porous Media*, pages 9–47. Springer Berlin Heidelberg, Berlin, Heidelberg, 2013. ISBN 978-3-642-23559-7. doi:10.1007/978-3-642-23559-7\_2.
- C. Thaler, T. Faizy, J. Sedlacik, B. Holst, K. Stürner, C. Heesen, J.-P. Stellmann, J. Fiehler, and S. Siemonsen. T1 recovery is predominantly found in black holes and is associated with clinical improvement in patients with multiple sclerosis. *American Journal of Neuroradiology*, 38(2): 264–269, 2017. doi:10.3174/ajnr.A5004.
- S. Tron, G. Bodner, F. Laio, L. Ridolfi, and D. Leitner. Can diversity in root architecture explain plant water use efficiency? a modeling study. *Ecological modelling*, 312:200–210, 2015. doi:10.1016/j.ecolmodel.2015.05.028.
- C. Truesdell. Thermodynamics of diffusion. In *Rational thermodynamics*, pages 219–236. Springer, 1984.
- M. L. Turgeon. *Clinical hematology: theory and procedures*. Lippincott Williams & Wilkins, 2005.
- M. T. Tyree. The cohesion-tension theory of sap ascent: current controversies. *Journal of Experimental Botany*, 48(10):1753, 1997. doi:10.1093/jxb/48.10.1753.
- M. T. Van Genuchten. A closed-form equation for predicting the hydraulic conductivity of unsaturated soils. *Soil science society of America journal*, 44(5):892–898, 1980. doi:10.2136/sssaj1980.03615995004400050002x.
- J. Vanderborght, R. Kasteel, M. Herbst, M. Javaux, D. Thiéry, M. Vanclooster, C. Mouvet, and H. Vereecken. A set of analytical benchmarks to test numerical models of flow and transport in soils. 4:206–221, 2005. doi:10.2136/vzj2005.0206. 1.

- J. Vanderborght, T. Fetzner, K. Mosthaf, K. M. Smits, and R. Helmig. Heat and water transport in soils and across the soil-atmosphere interface: 1. theory and different model concepts. *Water Resources Research*, 53(2):1057–1079, 2017. doi:10.1002/2016WR019982.
- G. Vercambre, C. Doussan, L. Pages, R. Habib, and A. Pierret. Influence of xylem development on axial hydraulic conductance within prunus root systems. *Trees*, 16(7):479–487, 2002. doi:10.1007/s00468-002-0190-6.
- R. K. Verma, J. Slotboom, M. R. Heldner, F. Kellner-Weldon, R. Kottke, C. Ozdoba, C. Weisstanner, C. P. Kamm, and R. Wiest. Characterization of microcirculation in multiple sclerosis lesions by dynamic texture parameter analysis (dtpa). *PloS one*, 8(7):e67610, 2013.
- R. K. Verma, J. Slotboom, C. Locher, M. R. Heldner, C. Weisstanner, E. Abela, F. Kellner-Weldon, M. Zbinden, C. P. Kamm, and R. Wiest. Characterization of enhancing ms lesions by dynamic texture parameter analysis of dynamic susceptibility perfusion imaging. *Biomed Res Int*, 2016, 2016. doi:10.1155/2016/9578139.
- R. K. Verma, R. Wiest, C. Locher, M. R. Heldner, P. Schucht, A. Raabe, J. Gralla, C. P. Kamm, J. Slotboom, and F. Kellner-Weldon. Differentiating enhancing multiple sclerosis lesions, glioblastoma, and lymphoma with dynamic texture parameters analysis (dtpa): A feasibility study. *Medical Physics*, 44(8):4000–4008, 2017. doi:10.1002/mp.12356.
- E. Vidotto, T. Koch, T. Köppl, R. Helmig, and B. Wohlmuth. Hybrid models for simulating blood flow in microvascular networks. *Multiscale Modeling & Simulation*, 17(3):1076–1102, 2019. doi:10.1137/18M1228712.
- A. Wagner and W. Ehlers. Continuum-mechanical analysis of human brain tissue. *Proc. Appl. Math. Mech.*, 10(1):99–100, 2010. doi:10.1002/pamm.201010042.
- A. Wagner, D. Fink, and W. Ehlers. Efficient numerical simulations of drug delivery in multi-component brain tissue. *Proc. Appl. Math. Mech.*, 18(1):e201800127, 2018. doi:10.1002/pamm.201800127.
- X. Wang, F. Thauvin, and K. Mohanty. Non-darcy flow through anisotropic porous media. *Chemical Engineering Science*, 54(12):1859 – 1869, 1999. doi:10.1016/S0009-2509(99)00018-4.
- S. W. Webb. A simple extension of two-phase characteristic curves to include the dry region. *Water Resources Research*, 36(6):1425–1430, 2000. doi:10.1029/2000WR900057.
- K. Weishaupt, V. Joekar-Niasar, and R. Helmig. An efficient coupling of free flow and porous media flow using the pore-network modeling approach. *Journal of Computational Physics: X*, 1:100011, 2019. doi:10.1016/j.jcpX.2019.100011.

- 
- S. Whitaker. The forchheimer equation: A theoretical development. *Transport in Porous Media*, 25 (1):27–61, 1996. doi:10.1007/BF00141261.
- C. Wolfsteiner, L. J. Durlofsky, and K. Aziz. Calculation of well index for nonconventional wells on arbitrary grids. *Computational Geosciences*, 7(1):61–82, 2003. doi:10.1023/A:1022431729275.
- J. H. M. Wösten, G. J. Veerman, W. J. M. de Groot, and J. Stolte. Waterretentie- en doorlatendheidskarakteristieken van boven- en ondergronden in Nederland: De staringreeks. Technical report, Alterra, Wageningen, The Netherlands, 2001.
- J. Wuerfel, J. Bellmann-Strobl, P. Brunecker, O. Aktas, H. McFarland, A. Villringer, and F. Zipp. Changes in cerebral perfusion precede plaque formation in multiple sclerosis: a longitudinal perfusion MRI study. *Brain*, 127(1):111–119, 2004. doi:10.1093/brain/awh007.
- M. Zarebanadkouki, Y. X. Kim, and A. Carminati. Where do roots take up water? Neutron radiography of water flow into the roots of transpiring plants growing in soil. *The New phytologist*, 199(4):1034–44, 2013. doi:10.1111/nph.12330.
- J. Zhang and H. Xing. Numerical modeling of non-darcy flow in near-well region of a geothermal reservoir. *Geothermics*, 42:78 – 86, 2012. doi:10.1016/j.geothermics.2011.11.002.

## List of publications

- O. Sander, T. Koch, N. Schröder, and B. Flemisch. The dune foamgrid implementation for surface and network grids. *Archive of Numerical Software*, 5(1):217–244, 2017. doi:10.11588/ans.2017.1.28490
- D. Kempf and T. Koch. System testing in scientific numerical software frameworks using the example of dune. *Archive of Numerical Software*, 5(1):151–168, 2017. doi:10.11588/ans.2017.1.27447
- T. Koch, K. Heck, N. Schröder, H. Class, and R. Helmig. A new simulation framework for soil-root interaction, evaporation, root growth, and solute transport. *Vadose Zone Journal*, 17, 2018b. doi:10.2136/vzj2017.12.0210
- E. Vidotto, T. Koch, T. Köppl, R. Helmig, and B. Wohlmuth. Hybrid models for simulating blood flow in microvascular networks. *Multiscale Modeling & Simulation*, 17(3):1076–1102, 2019. doi:10.1137/18M1228712
- T. Koch, B. Flemisch, R. Helmig, R. Wiest, and D. Obrist. A multiscale subvoxel perfusion model to estimate diffusive capillary wall conductivity in multiple sclerosis lesions from perfusion mri data. *International Journal for Numerical Methods in Biomedical Engineering*, 36(2):e3298, 2020a. doi:10.1002/cnm.3298
- T. Koch, M. Schneider, R. Helmig, and P. Jenny. Modeling tissue perfusion in terms of 1d-3d embedded mixed-dimension coupled problems with distributed sources. *Journal of Computational Physics*, 410:109370, 2020d. ISSN 0021-9991. doi:10.1016/j.jcp.2020.109370
- T. Koch, R. Helmig, and M. Schneider. A new and consistent well model for one-phase flow in anisotropic porous media using a distributed source model. *Journal of Computational Physics*, 410:109369, 2020c. ISSN 0021-9991. doi:10.1016/j.jcp.2020.109369
- T. Koch, D. Gläser, K. Weishaupt, S. Ackermann, M. Beck, B. Becker, S. Burbulla, H. Class, E. Coltman, S. Emmert, T. Fetzner, C. Grüniger, K. Heck, J. Hommel, T. Kurz, M. Lipp, F. Mohammadi, S. Scherrer, M. Schneider, G. Seitz, L. Stadler, M. Utz, F. Weinhardt, and B. Flemisch. Dumu<sup>x</sup> 3 – an open-source simulator for solving flow and transport problems in porous media with a focus on model coupling. *Computers & Mathematics with Applications*, 2020b. ISSN 0898-1221. doi:10.1016/j.camwa.2020.02.012
- A. Schnepf, C. K. Black, V. Couvreur, B. M. Delory, C. Doussan, A. Koch, T. Koch, M. Javaux, M. Landl, D. Leitner, G. Lobet, T. H. Mai, F. Meunier, L. Petrich, J. A. Postma, E. Priesack, V. Schmidt, J. Vanderborght, H. Vereecken, and M. Weber. Call for participation: Collaborative benchmarking of functional-structural root architecture models. the case of root water uptake. *Frontiers in Plant Science*, 11:316, 2020. ISSN 1664-462X. doi:10.3389/fpls.2020.00316



## Institut für Wasser- und Umweltsystemmodellierung Universität Stuttgart

Pfaffenwaldring 61  
70569 Stuttgart (Vaihingen)  
Telefon (0711) 685 - 60156  
Telefax (0711) 685 - 51073  
E-Mail: [iws@iws.uni-stuttgart.de](mailto:iws@iws.uni-stuttgart.de)  
<http://www.iws.uni-stuttgart.de>

### Direktoren

Prof. Dr. rer. nat. Dr.-Ing. András Bárdossy  
Prof. Dr.-Ing. Rainer Helmig  
Prof. Dr.-Ing. Wolfgang Nowak  
Prof. Dr.-Ing. Silke Wieprecht

### Vorstand (Stand 1.5.2019)

Prof. Dr. rer. nat. Dr.-Ing. A. Bárdossy  
Prof. Dr.-Ing. R. Helmig  
Prof. Dr.-Ing. W. Nowak  
Prof. Dr.-Ing. S. Wieprecht  
Prof. Dr. J.A. Sander Huisman  
Jürgen Braun, PhD  
apl. Prof. Dr.-Ing. H. Class  
PD Dr.-Ing. Claus Haslauer  
Stefan Haun, PhD  
PD Dr.-Ing. habil. Sergey Oladyshkin  
Dr. rer. nat. J. Seidel  
Dr.-Ing. K. Terheiden

### Emeriti

Prof. Dr.-Ing. habil. Dr.-Ing. E.h. Jürgen Giesecke  
Prof. Dr.h.c. Dr.-Ing. E.h. Helmut Kobus, PhD

### Lehrstuhl für Wasserbau und Wassermengenwirtschaft

Leiterin: Prof. Dr.-Ing. Silke Wieprecht  
Stellv.: Dr.-Ing. Kristina Terheiden  
**Versuchsanstalt für Wasserbau**  
Leiter: Stefan Haun, PhD

### Lehrstuhl für Hydromechanik und Hydrosystemmodellierung

Leiter: Prof. Dr.-Ing. Rainer Helmig  
Stellv.: apl. Prof. Dr.-Ing. Holger Class

### Lehrstuhl für Hydrologie und Geohydrologie

Leiter: Prof. Dr. rer. nat. Dr.-Ing. András Bárdossy  
Stellv.: Dr. rer. nat. Jochen Seidel  
**Hydrogeophysik der Vadosen Zone**  
(mit Forschungszentrum Jülich)  
Leiter: Prof. Dr. J.A. Sander Huisman

### Lehrstuhl für Stochastische Simulation und Sicherheitsforschung für Hydrosysteme

Leiter: Prof. Dr.-Ing. Wolfgang Nowak  
Stellv.: PD Dr.-Ing. habil. Sergey Oladyshkin

### VEGAS, Versuchseinrichtung zur Grundwasser- und Altlastensanierung

Leiter: Jürgen Braun, PhD  
PD Dr.-Ing. Claus Haslauer

## Verzeichnis der Mitteilungshefte

- 1 Röhnisch, Arthur: *Die Bemühungen um eine Wasserbauliche Versuchsanstalt an der Technischen Hochschule Stuttgart*, und Fattah Abouleid, Abdel: *Beitrag zur Berechnung einer in lockeren Sand gerammten, zweifach verankerten Spundwand*, 1963
- 2 Marotz, Günter: *Beitrag zur Frage der Standfestigkeit von dichten Asphaltbelägen im Großwasserbau*, 1964
- 3 Gurr, Siegfried: *Beitrag zur Berechnung zusammengesetzter ebener Flächentragwerke unter besonderer Berücksichtigung ebener Stauwände, mit Hilfe von Randwert- und Lastwertmatrizen*, 1965
- 4 Plica, Peter: *Ein Beitrag zur Anwendung von Schalenkonstruktionen im Stahlwasserbau*, und Petrikat, Kurt: *Möglichkeiten und Grenzen des wasserbaulichen Versuchswesens*, 1966

- 5 Plate, Erich: *Beitrag zur Bestimmung der Windgeschwindigkeitsverteilung in der durch eine Wand gestörten bodennahen Luftschicht*, und  
Röhnisch, Arthur; Marotz, Günter: *Neue Baustoffe und Bauausführungen für den Schutz der Böschungen und der Sohle von Kanälen, Flüssen und Häfen; Gestehungskosten und jeweilige Vorteile*, sowie  
Unny, T.E.: *Schwingungsuntersuchungen am Kegelstrahlschieber*, 1967
- 6 Seiler, Erich: *Die Ermittlung des Anlagenwertes der bundeseigenen Binnenschiffahrtsstraßen und Talsperren und des Anteils der Binnenschifffahrt an diesem Wert*, 1967
- 7 *Sonderheft anlässlich des 65. Geburtstages von Prof. Arthur Röhnisch mit Beiträgen von*  
Benk, Dieter; Breitling, J.; Gurr, Siegfried; Haberhauer, Robert; Honekamp, Hermann; Kuz, Klaus Dieter; Marotz, Günter; Mayer-Vorfelder, Hans-Jörg; Miller, Rudolf; Plate, Erich J.; Radomski, Helge; Schwarz, Helmut; Vollmer, Ernst; Wildenhahn, Eberhard; 1967
- 8 Jumikis, Alfred: *Beitrag zur experimentellen Untersuchung des Wassernachschubs in einem gefrierenden Boden und die Beurteilung der Ergebnisse*, 1968
- 9 Marotz, Günter: *Technische Grundlagen einer Wasserspeicherung im natürlichen Untergrund*, 1968
- 10 Radomski, Helge: *Untersuchungen über den Einfluß der Querschnittsform wellenförmiger Spundwände auf die statischen und rammtechnischen Eigenschaften*, 1968
- 11 Schwarz, Helmut: *Die Grenztragfähigkeit des Baugrundes bei Einwirkung vertikal gezogener Ankerplatten als zweidimensionales Bruchproblem*, 1969
- 12 Erbel, Klaus: *Ein Beitrag zur Untersuchung der Metamorphose von Mittelgebirgsschneedecken unter besonderer Berücksichtigung eines Verfahrens zur Bestimmung der thermischen Schneequalität*, 1969
- 13 Westhaus, Karl-Heinz: *Der Strukturwandel in der Binnenschifffahrt und sein Einfluß auf den Ausbau der Binnenschiffskanäle*, 1969
- 14 Mayer-Vorfelder, Hans-Jörg: *Ein Beitrag zur Berechnung des Erdwiderstandes unter Ansatz der logarithmischen Spirale als Gleitflächenfunktion*, 1970
- 15 Schulz, Manfred: *Berechnung des räumlichen Erddruckes auf die Wandung kreiszylindrischer Körper*, 1970
- 16 Mobasseri, Manoutschehr: *Die Rippenstützmauer. Konstruktion und Grenzen ihrer Standicherheit*, 1970
- 17 Benk, Dieter: *Ein Beitrag zum Betrieb und zur Bemessung von Hochwasserrückhaltebecken*, 1970
- 18 Gàl, Attila: *Bestimmung der mitschwingenden Wassermasse bei überströmten Fischbauchklappen mit kreiszylindrischem Staublech*, 1971, vergriffen
- 19 Kuz, Klaus Dieter: *Ein Beitrag zur Frage des Einsetzens von Kavitationserscheinungen in einer Düsenströmung bei Berücksichtigung der im Wasser gelösten Gase*, 1971, vergriffen
- 20 Schaak, Hartmut: *Verteilleitungen von Wasserkraftanlagen*, 1971
- 21 *Sonderheft zur Eröffnung der neuen Versuchsanstalt des Instituts für Wasserbau der Universität Stuttgart mit Beiträgen von*  
Brombach, Hansjörg; Dirksen, Wolfram; Gàl, Attila; Gerlach, Reinhard; Giesecke, Jürgen; Holthoff, Franz-Josef; Kuz, Klaus Dieter; Marotz, Günter; Minor, Hans-Erwin; Petrikat, Kurt; Röhnisch, Arthur; Rueff, Helge; Schwarz, Helmut; Vollmer, Ernst; Wildenhahn, Eberhard; 1972
- 22 Wang, Chung-su: *Ein Beitrag zur Berechnung der Schwingungen an Kegelstrahlschiebern*, 1972
- 23 Mayer-Vorfelder, Hans-Jörg: *Erdwiderstandsbeiwerte nach dem Ohde-Variationsverfahren*, 1972
- 24 Minor, Hans-Erwin: *Beitrag zur Bestimmung der Schwingungsanfachungsfunktionen überströmter Stauklappen*, 1972, vergriffen
- 25 Brombach, Hansjörg: *Untersuchung strömungsmechanischer Elemente (Fluidik) und die Möglichkeit der Anwendung von Wirbelkammerelementen im Wasserbau*, 1972, vergriffen
- 26 Wildenhahn, Eberhard: *Beitrag zur Berechnung von Horizontalfilterbrunnen*, 1972



- 27 Steinlein, Helmut: *Die Eliminierung der Schwebstoffe aus Flußwasser zum Zweck der unterirdischen Wasserspeicherung, gezeigt am Beispiel der Iller*, 1972
- 28 Holthoff, Franz Josef: *Die Überwindung großer Hubhöhen in der Binnenschifffahrt durch Schwimmerhebwerke*, 1973
- 29 Röder, Karl: *Einwirkungen aus Baugrundbewegungen auf trog- und kastenförmige Konstruktionen des Wasser- und Tunnelbaues*, 1973
- 30 Kretschmer, Heinz: *Die Bemessung von Bogenstau mauern in Abhängigkeit von der Talform*, 1973
- 31 Honekamp, Hermann: *Beitrag zur Berechnung der Montage von Unterwasserpipelines*, 1973
- 32 Giesecke, Jürgen: *Die Wirbelkammertriode als neuartiges Steuerorgan im Wasserbau*, und Brombach, Hansjörg: *Entwicklung, Bauformen, Wirkungsweise und Steuereigenschaften von Wirbelkammerverstärkern*, 1974
- 33 Rueff, Helge: *Untersuchung der schwingungserregenden Kräfte an zwei hintereinander angeordneten Tiefschützen unter besonderer Berücksichtigung von Kavitation*, 1974
- 34 Röhnisch, Arthur: *Einpreßversuche mit Zementmörtel für Spannbeton - Vergleich der Ergebnisse von Modellversuchen mit Ausführungen in Hüllwellrohren*, 1975
- 35 *Sonderheft anlässlich des 65. Geburtstages von Prof. Dr.-Ing. Kurt Petrikat mit Beiträgen von:* Brombach, Hansjörg; Erbel, Klaus; Flinspach, Dieter; Fischer jr., Richard; Gál, Attila; Gerlach, Reinhard; Giesecke, Jürgen; Haberhauer, Robert; Hafner Edzard; Hausenblas, Bernhard; Horlacher, Hans-Burkhard; Hutarew, Andreas; Knoll, Manfred; Krummet, Ralph; Marotz, Günter; Merkle, Theodor; Miller, Christoph; Minor, Hans-Erwin; Neumayer, Hans; Rao, Syamala; Rath, Paul; Rueff, Helge; Ruppert, Jürgen; Schwarz, Wolfgang; Topal-Gökceli, Mehmet; Vollmer, Ernst; Wang, Chung-su; Weber, Hans-Georg; 1975
- 36 Berger, Jochum: *Beitrag zur Berechnung des Spannungszustandes in rotationssymmetrisch belasteten Kugelschalen veränderlicher Wandstärke unter Gas- und Flüssigkeitsdruck durch Integration schwach singulärer Differentialgleichungen*, 1975
- 37 Dirksen, Wolfram: *Berechnung instationärer Abflussvorgänge in gestauten Gerinnen mittels Differenzenverfahren und die Anwendung auf Hochwasserrückhaltebecken*, 1976
- 38 Horlacher, Hans-Burkhard: *Berechnung instationärer Temperatur- und Wärmespannungsfelder in langen mehrschichtigen Hohlzylindern*, 1976
- 39 Hafner, Edzard: *Untersuchung der hydrodynamischen Kräfte auf Baukörper im Tiefwasserbereich des Meeres*, 1977, ISBN 3-921694-39-6
- 40 Ruppert, Jürgen: *Über den Axialwirbelkammerverstärker für den Einsatz im Wasserbau*, 1977, ISBN 3-921694-40-X
- 41 Hutarew, Andreas: *Beitrag zur Beeinflussbarkeit des Sauerstoffgehalts in Fließgewässern an Abstürzen und Wehren*, 1977, ISBN 3-921694-41-8, vergriffen
- 42 Miller, Christoph: *Ein Beitrag zur Bestimmung der schwingungserregenden Kräfte an unterströmten Wehren*, 1977, ISBN 3-921694-42-6
- 43 Schwarz, Wolfgang: *Druckstoßberechnung unter Berücksichtigung der Radial- und Längsverschiebungen der Rohrwandung*, 1978, ISBN 3-921694-43-4
- 44 Kinzelbach, Wolfgang: *Numerische Untersuchungen über den optimalen Einsatz variabler Kühlsysteme einer Kraftwerkskette am Beispiel Oberrhein*, 1978, ISBN 3-921694-44-2
- 45 Barczewski, Baldur: *Neue Meßmethoden für Wasser-Luftgemische und deren Anwendung auf zweiphasige Auftriebsstrahlen*, 1979, ISBN 3-921694-45-0
- 46 Neumayer, Hans: *Untersuchung der Strömungsvorgänge in radialen Wirbelkammerverstärkern*, 1979, ISBN 3-921694-46-9
- 47 Elalfy, Youssef-Elhassan: *Untersuchung der Strömungsvorgänge in Wirbelkammerdioden und -drosseln*, 1979, ISBN 3-921694-47-7
- 48 Brombach, Hansjörg: *Automatisierung der Bewirtschaftung von Wasserspeichern*, 1981, ISBN 3-921694-48-5
- 49 Geldner, Peter: *Deterministische und stochastische Methoden zur Bestimmung der Selbstdichtung von Gewässern*, 1981, ISBN 3-921694-49-3, vergriffen

- 50 Mehlhorn, Hans: *Temperaturveränderungen im Grundwasser durch Brauchwassereinleitungen*, 1982, ISBN 3-921694-50-7, vergriffen
- 51 Hafner, Edzard: *Rohrleitungen und Behälter im Meer*, 1983, ISBN 3-921694-51-5
- 52 Rinnert, Bernd: *Hydrodynamische Dispersion in porösen Medien: Einfluß von Dichteunterschieden auf die Vertikalvermischung in horizontaler Strömung*, 1983, ISBN 3-921694-52-3, vergriffen
- 53 Lindner, Wulf: *Steuerung von Grundwasserentnahmen unter Einhaltung ökologischer Kriterien*, 1983, ISBN 3-921694-53-1, vergriffen
- 54 Herr, Michael; Herzer, Jörg; Kinzelbach, Wolfgang; Kobus, Helmut; Rinnert, Bernd: *Methoden zur rechnerischen Erfassung und hydraulischen Sanierung von Grundwasserkontaminationen*, 1983, ISBN 3-921694-54-X
- 55 Schmitt, Paul: *Wege zur Automatisierung der Niederschlagsermittlung*, 1984, ISBN 3-921694-55-8, vergriffen
- 56 Müller, Peter: *Transport und selektive Sedimentation von Schwebstoffen bei gestautem Abfluß*, 1985, ISBN 3-921694-56-6
- 57 El-Qawasmeh, Fuad: *Möglichkeiten und Grenzen der Tropfbewässerung unter besonderer Berücksichtigung der Verstopfungsanfälligkeit der Tropfelemente*, 1985, ISBN 3-921694-57-4, vergriffen
- 58 Kirchenbaur, Klaus: *Mikroprozessorgesteuerte Erfassung instationärer Druckfelder am Beispiel seegangsbelasteter Baukörper*, 1985, ISBN 3-921694-58-2
- 59 Kobus, Helmut (Hrsg.): *Modellierung des großräumigen Wärme- und Schadstofftransports im Grundwasser*, Tätigkeitsbericht 1984/85 (DFG-Forschergruppe an den Universitäten Hohenheim, Karlsruhe und Stuttgart), 1985, ISBN 3-921694-59-0, vergriffen
- 60 Spitz, Karlheinz: *Dispersion in porösen Medien: Einfluß von Inhomogenitäten und Dichteunterschieden*, 1985, ISBN 3-921694-60-4, vergriffen
- 61 Kobus, Helmut: *An Introduction to Air-Water Flows in Hydraulics*, 1985, ISBN 3-921694-61-2
- 62 Kaleris, Vassilios: *Erfassung des Austausches von Oberflächen- und Grundwasser in horizontalebene Grundwassermodellen*, 1986, ISBN 3-921694-62-0
- 63 Herr, Michael: *Grundlagen der hydraulischen Sanierung verunreinigter Porengrundwasserleiter*, 1987, ISBN 3-921694-63-9
- 64 Marx, Walter: *Berechnung von Temperatur und Spannung in Massenbeton infolge Hydratation*, 1987, ISBN 3-921694-64-7
- 65 Koschitzky, Hans-Peter: *Dimensionierungskonzept für Sohlbelüfter in Schußrinnen zur Vermeidung von Kavitationsschäden*, 1987, ISBN 3-921694-65-5
- 66 Kobus, Helmut (Hrsg.): *Modellierung des großräumigen Wärme- und Schadstofftransports im Grundwasser*, Tätigkeitsbericht 1986/87 (DFG-Forschergruppe an den Universitäten Hohenheim, Karlsruhe und Stuttgart) 1987, ISBN 3-921694-66-3
- 67 Söll, Thomas: *Berechnungsverfahren zur Abschätzung anthropogener Temperaturanomalien im Grundwasser*, 1988, ISBN 3-921694-67-1
- 68 Dittrich, Andreas; Westrich, Bernd: *Bodenseeufererosion, Bestandsaufnahme und Bewertung*, 1988, ISBN 3-921694-68-X, vergriffen
- 69 Huwe, Bernd; van der Ploeg, Rienk R.: *Modelle zur Simulation des Stickstoffhaushaltes von Standorten mit unterschiedlicher landwirtschaftlicher Nutzung*, 1988, ISBN 3-921694-69-8, vergriffen
- 70 Stephan, Karl: *Integration elliptischer Funktionen*, 1988, ISBN 3-921694-70-1
- 71 Kobus, Helmut; Zilliox, Lothaire (Hrsg.): *Nitratbelastung des Grundwassers, Auswirkungen der Landwirtschaft auf die Grundwasser- und Rohwasserbeschaffenheit und Maßnahmen zum Schutz des Grundwassers*. Vorträge des deutsch-französischen Kolloquiums am 6. Oktober 1988, Universitäten Stuttgart und Louis Pasteur Strasbourg (Vorträge in deutsch oder französisch, Kurzfassungen zweisprachig), 1988, ISBN 3-921694-71-X

- 72 Soyeaux, Renald: *Unterströmung von Stauanlagen auf klüftigem Untergrund unter Berücksichtigung laminarer und turbulenter Fließzustände*, 1991, ISBN 3-921694-72-8
- 73 Kohane, Roberto: *Berechnungsmethoden für Hochwasserabfluß in Fließgewässern mit überströmten Vorländern*, 1991, ISBN 3-921694-73-6
- 74 Hassinger, Reinhard: *Beitrag zur Hydraulik und Bemessung von Blocksteinrampen in flexibler Bauweise*, 1991, ISBN 3-921694-74-4, vergriffen
- 75 Schäfer, Gerhard: *Einfluß von Schichtenstrukturen und lokalen Einlagerungen auf die Längsdispersion in Porengrundwasserleitern*, 1991, ISBN 3-921694-75-2
- 76 Giesecke, Jürgen: *Vorträge, Wasserwirtschaft in stark besiedelten Regionen; Umweltforschung mit Schwerpunkt Wasserwirtschaft*, 1991, ISBN 3-921694-76-0
- 77 Huwe, Bernd: *Deterministische und stochastische Ansätze zur Modellierung des Stickstoffhaushalts landwirtschaftlich genutzter Flächen auf unterschiedlichem Skalenniveau*, 1992, ISBN 3-921694-77-9, vergriffen
- 78 Rommel, Michael: *Verwendung von Kluftdaten zur realitätsnahen Generierung von Kluftnetzen mit anschließender laminar-turbulenter Strömungsberechnung*, 1993, ISBN 3-92 1694-78-7
- 79 Marschall, Paul: *Die Ermittlung lokaler Stofffrachten im Grundwasser mit Hilfe von Einbohrloch-Meßverfahren*, 1993, ISBN 3-921694-79-5, vergriffen
- 80 Ptak, Thomas: *Stofftransport in heterogenen Porenaquiferen: Felduntersuchungen und stochastische Modellierung*, 1993, ISBN 3-921694-80-9, vergriffen
- 81 Haakh, Frieder: *Transientes Strömungsverhalten in Wirbelkammern*, 1993, ISBN 3-921694-81-7
- 82 Kobus, Helmut; Cirpka, Olaf; Barczewski, Baldur; Koschitzky, Hans-Peter: *Versuchseinrichtung zur Grundwasser- und Altlastensanierung VEGAS, Konzeption und Programmrahmen*, 1993, ISBN 3-921694-82-5
- 83 Zang, Weidong: *Optimaler Echtzeit-Betrieb eines Speichers mit aktueller Abflußregenerierung*, 1994, ISBN 3-921694-83-3, vergriffen
- 84 Franke, Hans-Jörg: *Stochastische Modellierung eines flächenhaften Stoffeintrages und Transports in Grundwasser am Beispiel der Pflanzenschutzmittelproblematik*, 1995, ISBN 3-921694-84-1
- 85 Lang, Ulrich: *Simulation regionaler Strömungs- und Transportvorgänge in Karstaquiferen mit Hilfe des Doppelkontinuum-Ansatzes: Methodenentwicklung und Parameteridentifikation*, 1995, ISBN 3-921694-85-X, vergriffen
- 86 Helmig, Rainer: *Einführung in die Numerischen Methoden der Hydromechanik*, 1996, ISBN 3-921694-86-8, vergriffen
- 87 Cirpka, Olaf: *CONTRACT: A Numerical Tool for Contaminant Transport and Chemical Transformations - Theory and Program Documentation -*, 1996, ISBN 3-921694-87-6
- 88 Haberlandt, Uwe: *Stochastische Synthese und Regionalisierung des Niederschlages für Schmutzfrachtberechnungen*, 1996, ISBN 3-921694-88-4
- 89 Croisé, Jean: *Extraktion von flüchtigen Chemikalien aus natürlichen Lockergesteinen mittels erzwungener Luftströmung*, 1996, ISBN 3-921694-89-2, vergriffen
- 90 Jorde, Klaus: *Ökologisch begründete, dynamische Mindestwasserregelungen bei Ausleitungskraftwerken*, 1997, ISBN 3-921694-90-6, vergriffen
- 91 Helmig, Rainer: *Gekoppelte Strömungs- und Transportprozesse im Untergrund - Ein Beitrag zur Hydrosystemmodellierung-*, 1998, ISBN 3-921694-91-4, vergriffen
- 92 Emmert, Martin: *Numerische Modellierung nichtisothermer Gas-Wasser Systeme in porösen Medien*, 1997, ISBN 3-921694-92-2
- 93 Kern, Ulrich: *Transport von Schweb- und Schadstoffen in staugeregelten Fließgewässern am Beispiel des Neckars*, 1997, ISBN 3-921694-93-0, vergriffen
- 94 Förster, Georg: *Druckstoßdämpfung durch große Luftblasen in Hochpunkten von Rohrleitungen* 1997, ISBN 3-921694-94-9

- 95 Cirpka, Olaf: *Numerische Methoden zur Simulation des reaktiven Mehrkomponententransports im Grundwasser*, 1997, ISBN 3-921694-95-7, vergriffen
- 96 Färber, Arne: *Wärmetransport in der ungesättigten Bodenzone: Entwicklung einer thermischen In-situ-Sanierungstechnologie*, 1997, ISBN 3-921694-96-5
- 97 Betz, Christoph: *Wasserdampfdestillation von Schadstoffen im porösen Medium: Entwicklung einer thermischen In-situ-Sanierungstechnologie*, 1998, SBN 3-921694-97-3
- 98 Xu, Yichun: *Numerical Modeling of Suspended Sediment Transport in Rivers*, 1998, ISBN 3-921694-98-1, vergriffen
- 99 Wüst, Wolfgang: *Geochemische Untersuchungen zur Sanierung CKW-kontaminierter Aquifere mit Fe(0)-Reaktionswänden*, 2000, ISBN 3-933761-02-2
- 100 Sheta, Hussam: *Simulation von Mehrphasenvorgängen in porösen Medien unter Einbeziehung von Hysterese-Effekten*, 2000, ISBN 3-933761-03-4
- 101 Ayros, Edwin: *Regionalisierung extremer Abflüsse auf der Grundlage statistischer Verfahren*, 2000, ISBN 3-933761-04-2, vergriffen
- 102 Huber, Ralf: *Compositional Multiphase Flow and Transport in Heterogeneous Porous Media*, 2000, ISBN 3-933761-05-0
- 103 Braun, Christopherus: *Ein Upscaling-Verfahren für Mehrphasenströmungen in porösen Medien*, 2000, ISBN 3-933761-06-9
- 104 Hofmann, Bernd: *Entwicklung eines rechnergestützten Managementsystems zur Beurteilung von Grundwasserschadensfällen*, 2000, ISBN 3-933761-07-7
- 105 Class, Holger: *Theorie und numerische Modellierung nichtisothermer Mehrphasenprozesse in NAPL-kontaminierten porösen Medien*, 2001, ISBN 3-933761-08-5
- 106 Schmidt, Reinhard: *Wasserdampf- und Heißluftinjektion zur thermischen Sanierung kontaminierter Standorte*, 2001, ISBN 3-933761-09-3
- 107 Josef, Reinhold: *Schadstoffextraktion mit hydraulischen Sanierungsverfahren unter Anwendung von grenzflächenaktiven Stoffen*, 2001, ISBN 3-933761-10-7
- 108 Schneider, Matthias: *Habitat- und Abflussmodellierung für Fließgewässer mit unscharfen Berechnungsansätzen*, 2001, ISBN 3-933761-11-5
- 109 Rathgeb, Andreas: *Hydrodynamische Bemessungsgrundlagen für Lockerdeckwerke an überströmbaren Erddämmen*, 2001, ISBN 3-933761-12-3
- 110 Lang, Stefan: *Parallele numerische Simulation instationärer Probleme mit adaptiven Methoden auf unstrukturierten Gittern*, 2001, ISBN 3-933761-13-1
- 111 Appt, Jochen; Stumpp Simone: *Die Bodensee-Messkampagne 2001, IWS/CWR Lake Constance Measurement Program 2001*, 2002, ISBN 3-933761-14-X
- 112 Heimerl, Stephan: *Systematische Beurteilung von Wasserkraftprojekten*, 2002, ISBN 3-933761-15-8, vergriffen
- 113 Iqbal, Amin: *On the Management and Salinity Control of Drip Irrigation*, 2002, ISBN 3-933761-16-6
- 114 Silberhorn-Hemminger, Annette: *Modellierung von Kluftaquifersystemen: Geostatistische Analyse und deterministisch-stochastische Kluftgenerierung*, 2002, ISBN 3-933761-17-4
- 115 Winkler, Angela: *Prozesse des Wärme- und Stofftransports bei der In-situ-Sanierung mit festen Wärmequellen*, 2003, ISBN 3-933761-18-2
- 116 Marx, Walter: *Wasserkraft, Bewässerung, Umwelt - Planungs- und Bewertungsschwerpunkte der Wasserbewirtschaftung*, 2003, ISBN 3-933761-19-0
- 117 Hinkelmann, Reinhard: *Efficient Numerical Methods and Information-Processing Techniques in Environment Water*, 2003, ISBN 3-933761-20-4
- 118 Samaniego-Eguiguren, Luis Eduardo: *Hydrological Consequences of Land Use / Land Cover and Climatic Changes in Mesoscale Catchments*, 2003, ISBN 3-933761-21-2
- 119 Neunhäuserer, Lina: *Diskretisierungsansätze zur Modellierung von Strömungs- und Transportprozessen in geklüftet-porösen Medien*, 2003, ISBN 3-933761-22-0
- 120 Paul, Maren: *Simulation of Two-Phase Flow in Heterogeneous Poros Media with Adaptive Methods*, 2003, ISBN 3-933761-23-9

- 121 Ehret, Uwe: *Rainfall and Flood Nowcasting in Small Catchments using Weather Radar*, 2003, ISBN 3-933761-24-7
- 122 Haag, Ingo: *Der Sauerstoffhaushalt staugeregelter Flüsse am Beispiel des Neckars - Analysen, Experimente, Simulationen -*, 2003, ISBN 3-933761-25-5
- 123 Appt, Jochen: *Analysis of Basin-Scale Internal Waves in Upper Lake Constance*, 2003, ISBN 3-933761-26-3
- 124 Hrsg.: Schrenk, Volker; Batereau, Katrin; Barczewski, Baldur; Weber, Karolin und Koschitzky, Hans-Peter: *Symposium Ressource Fläche und VEGAS - Statuskolloquium 2003, 30. September und 1. Oktober 2003*, 2003, ISBN 3-933761-27-1
- 125 Omar Khalil Ouda: *Optimisation of Agricultural Water Use: A Decision Support System for the Gaza Strip*, 2003, ISBN 3-933761-28-0
- 126 Batereau, Katrin: *Sensorbasierte Bodenluftmessung zur Vor-Ort-Erkundung von Schadensherden im Untergrund*, 2004, ISBN 3-933761-29-8
- 127 Witt, Oliver: *Erosionsstabilität von Gewässersedimenten mit Auswirkung auf den Stofftransport bei Hochwasser am Beispiel ausgewählter Stauhaltungen des Oberrheins*, 2004, ISBN 3-933761-30-1
- 128 Jakobs, Hartmut: *Simulation nicht-isothermer Gas-Wasser-Prozesse in komplexen Kluft-Matrix-Systemen*, 2004, ISBN 3-933761-31-X
- 129 Li, Chen-Chien: *Deterministisch-stochastisches Berechnungskonzept zur Beurteilung der Auswirkungen erosiver Hochwasserereignisse in Flusstauhaltungen*, 2004, ISBN 3-933761-32-8
- 130 Reichenberger, Volker; Helmig, Rainer; Jakobs, Hartmut; Bastian, Peter; Niessner, Jennifer: *Complex Gas-Water Processes in Discrete Fracture-Matrix Systems: Up-scaling, Mass-Conservative Discretization and Efficient Multilevel Solution*, 2004, ISBN 3-933761-33-6
- 131 Hrsg.: Barczewski, Baldur; Koschitzky, Hans-Peter; Weber, Karolin; Wege, Ralf: *VEGAS - Statuskolloquium 2004*, Tagungsband zur Veranstaltung am 05. Oktober 2004 an der Universität Stuttgart, Campus Stuttgart-Vaihingen, 2004, ISBN 3-933761-34-4
- 132 Asie, Kemal Jabir: *Finite Volume Models for Multiphase Multicomponent Flow through Porous Media*. 2005, ISBN 3-933761-35-2
- 133 Jacoub, George: *Development of a 2-D Numerical Module for Particulate Contaminant Transport in Flood Retention Reservoirs and Impounded Rivers*, 2004, ISBN 3-933761-36-0
- 134 Nowak, Wolfgang: *Geostatistical Methods for the Identification of Flow and Transport Parameters in the Subsurface*, 2005, ISBN 3-933761-37-9
- 135 Süß, Mia: *Analysis of the influence of structures and boundaries on flow and transport processes in fractured porous media*, 2005, ISBN 3-933761-38-7
- 136 Jose, Surabhin Chackiath: *Experimental Investigations on Longitudinal Dispersive Mixing in Heterogeneous Aquifers*, 2005, ISBN: 3-933761-39-5
- 137 Filiz, Fulya: *Linking Large-Scale Meteorological Conditions to Floods in Mesoscale Catchments*, 2005, ISBN 3-933761-40-9
- 138 Qin, Minghao: *Wirklichkeitsnahe und recheneffiziente Ermittlung von Temperatur und Spannungen bei großen RCC-Staumauern*, 2005, ISBN 3-933761-41-7
- 139 Kobayashi, Kenichiro: *Optimization Methods for Multiphase Systems in the Subsurface - Application to Methane Migration in Coal Mining Areas*, 2005, ISBN 3-933761-42-5
- 140 Rahman, Md. Arifur: *Experimental Investigations on Transverse Dispersive Mixing in Heterogeneous Porous Media*, 2005, ISBN 3-933761-43-3
- 141 Schrenk, Volker: *Ökobilanzen zur Bewertung von Altlastensanierungsmaßnahmen*, 2005, ISBN 3-933761-44-1
- 142 Hundecha, Hirpa Yeshewatesfa: *Regionalization of Parameters of a Conceptual Rainfall-Runoff Model*, 2005, ISBN: 3-933761-45-X
- 143 Wege, Ralf: *Untersuchungs- und Überwachungsmethoden für die Beurteilung natürlicher Selbstreinigungsprozesse im Grundwasser*, 2005, ISBN 3-933761-46-8

- 144 Breiting, Thomas: *Techniken und Methoden der Hydroinformatik - Modellierung von komplexen Hydrosystemen im Untergrund*, 2006, ISBN 3-933761-47-6
- 145 Hrsg.: Braun, Jürgen; Koschitzky, Hans-Peter; Müller, Martin: *Ressource Untergrund: 10 Jahre VEGAS: Forschung und Technologieentwicklung zum Schutz von Grundwasser und Boden*, Tagungsband zur Veranstaltung am 28. und 29. September 2005 an der Universität Stuttgart, Campus Stuttgart-Vaihingen, 2005, ISBN 3-933761-48-4
- 146 Rojanschi, Vlad: *Abflusskonzentration in mesoskaligen Einzugsgebieten unter Berücksichtigung des Sickerraumes*, 2006, ISBN 3-933761-49-2
- 147 Winkler, Nina Simone: *Optimierung der Steuerung von Hochwasserrückhaltebeckensystemen*, 2006, ISBN 3-933761-50-6
- 148 Wolf, Jens: *Räumlich differenzierte Modellierung der Grundwasserströmung alluvialer Aquifere für mesoskalige Einzugsgebiete*, 2006, ISBN: 3-933761-51-4
- 149 Kohler, Beate: *Externe Effekte der Laufwasserkraftnutzung*, 2006, ISBN 3-933761-52-2
- 150 Hrsg.: Braun, Jürgen; Koschitzky, Hans-Peter; Stuhmann, Matthias: *VEGAS-Statuskolloquium 2006*, Tagungsband zur Veranstaltung am 28. September 2006 an der Universität Stuttgart, Campus Stuttgart-Vaihingen, 2006, ISBN 3-933761-53-0
- 151 Niessner, Jennifer: *Multi-Scale Modeling of Multi-Phase - Multi-Component Processes in Heterogeneous Porous Media*, 2006, ISBN 3-933761-54-9
- 152 Fischer, Markus: *Beanspruchung eingerdeter Rohrleitungen infolge Austrocknung bindiger Böden*, 2006, ISBN 3-933761-55-7
- 153 Schneck, Alexander: *Optimierung der Grundwasserbewirtschaftung unter Berücksichtigung der Belange der Wasserversorgung, der Landwirtschaft und des Naturschutzes*, 2006, ISBN 3-933761-56-5
- 154 Das, Tapash: *The Impact of Spatial Variability of Precipitation on the Predictive Uncertainty of Hydrological Models*, 2006, ISBN 3-33761-57-3
- 155 Bielinski, Andreas: *Numerical Simulation of CO<sub>2</sub> sequestration in geological formations*, 2007, ISBN 3-933761-58-1
- 156 Mödinger, Jens: *Entwicklung eines Bewertungs- und Entscheidungsunterstützungssystems für eine nachhaltige regionale Grundwasserbewirtschaftung*, 2006, ISBN 3-933761-60-3
- 157 Manthey, Sabine: *Two-phase flow processes with dynamic effects in porous media - parameter estimation and simulation*, 2007, ISBN 3-933761-61-1
- 158 Pozos Estrada, Oscar: *Investigation on the Effects of Entrained Air in Pipelines*, 2007, ISBN 3-933761-62-X
- 159 Ochs, Steffen Oliver: *Steam injection into saturated porous media – process analysis including experimental and numerical investigations*, 2007, ISBN 3-933761-63-8
- 160 Marx, Andreas: *Einsatz gekoppelter Modelle und Wetterradar zur Abschätzung von Niederschlagsintensitäten und zur Abflussvorhersage*, 2007, ISBN 3-933761-64-6
- 161 Hartmann, Gabriele Maria: *Investigation of Evapotranspiration Concepts in Hydrological Modelling for Climate Change Impact Assessment*, 2007, ISBN 3-933761-65-4
- 162 Kebede Gurmessa, Tesfaye: *Numerical Investigation on Flow and Transport Characteristics to Improve Long-Term Simulation of Reservoir Sedimentation*, 2007, ISBN 3-933761-66-2
- 163 Trifković, Aleksandar: *Multi-objective and Risk-based Modelling Methodology for Planning, Design and Operation of Water Supply Systems*, 2007, ISBN 3-933761-67-0
- 164 Göttinger, Jens: *Distributed Conceptual Hydrological Modelling - Simulation of Climate, Land Use Change Impact and Uncertainty Analysis*, 2007, ISBN 3-933761-68-9
- 165 Hrsg.: Braun, Jürgen; Koschitzky, Hans-Peter; Stuhmann, Matthias: *VEGAS – Kolloquium 2007*, Tagungsband zur Veranstaltung am 26. September 2007 an der Universität Stuttgart, Campus Stuttgart-Vaihingen, 2007, ISBN 3-933761-69-7
- 166 Freeman, Beau: *Modernization Criteria Assessment for Water Resources Planning; Klamath Irrigation Project, U.S.*, 2008, ISBN 3-933761-70-0

- 167 Dreher, Thomas: *Selektive Sedimentation von Feinstschwebstoffen in Wechselwirkung mit wandnahen turbulenten Strömungsbedingungen*, 2008, ISBN 3-933761-71-9
- 168 Yang, Wei: *Discrete-Continuous Downscaling Model for Generating Daily Precipitation Time Series*, 2008, ISBN 3-933761-72-7
- 169 Kopecki, Ianina: *Calculational Approach to FST-Hemispheres for Multiparametrical Benthos Habitat Modelling*, 2008, ISBN 3-933761-73-5
- 170 Brommundt, Jürgen: *Stochastische Generierung räumlich zusammenhängender Niederschlagszeitreihen*, 2008, ISBN 3-933761-74-3
- 171 Papafotiou, Alexandros: *Numerical Investigations of the Role of Hysteresis in Heterogeneous Two-Phase Flow Systems*, 2008, ISBN 3-933761-75-1
- 172 He, Yi: *Application of a Non-Parametric Classification Scheme to Catchment Hydrology*, 2008, ISBN 978-3-933761-76-7
- 173 Wagner, Sven: *Water Balance in a Poorly Gauged Basin in West Africa Using Atmospheric Modelling and Remote Sensing Information*, 2008, ISBN 978-3-933761-77-4
- 174 Hrsg.: Braun, Jürgen; Koschitzky, Hans-Peter; Stuhmann, Matthias; Schrenk, Volker: *VEGAS-Kolloquium 2008 Ressource Fläche III*, Tagungsband zur Veranstaltung am 01. Oktober 2008 an der Universität Stuttgart, Campus Stuttgart-Vaihingen, 2008, ISBN 978-3-933761-78-1
- 175 Patil, Sachin: *Regionalization of an Event Based Nash Cascade Model for Flood Predictions in Ungauged Basins*, 2008, ISBN 978-3-933761-79-8
- 176 Assteerawatt, Anongnart: *Flow and Transport Modelling of Fractured Aquifers based on a Geostatistical Approach*, 2008, ISBN 978-3-933761-80-4
- 177 Karnahl, Joachim Alexander: *2D numerische Modellierung von multifraktionalem Schwebstoff- und Schadstofftransport in Flüssen*, 2008, ISBN 978-3-933761-81-1
- 178 Hiester, Uwe: *Technologieentwicklung zur In-situ-Sanierung der ungesättigten Bodenzone mit festen Wärmequellen*, 2009, ISBN 978-3-933761-82-8
- 179 Laux, Patrick: *Statistical Modeling of Precipitation for Agricultural Planning in the Volta Basin of West Africa*, 2009, ISBN 978-3-933761-83-5
- 180 Ehsan, Saqib: *Evaluation of Life Safety Risks Related to Severe Flooding*, 2009, ISBN 978-3-933761-84-2
- 181 Prohaska, Sandra: *Development and Application of a 1D Multi-Strip Fine Sediment Transport Model for Regulated Rivers*, 2009, ISBN 978-3-933761-85-9
- 182 Kopp, Andreas: *Evaluation of CO<sub>2</sub> Injection Processes in Geological Formations for Site Screening*, 2009, ISBN 978-3-933761-86-6
- 183 Ebigbo, Anozie: *Modelling of biofilm growth and its influence on CO<sub>2</sub> and water (two-phase) flow in porous media*, 2009, ISBN 978-3-933761-87-3
- 184 Freiboth, Sandra: *A phenomenological model for the numerical simulation of multiphase multicomponent processes considering structural alterations of porous media*, 2009, ISBN 978-3-933761-88-0
- 185 Zöllner, Frank: *Implementierung und Anwendung netzfreier Methoden im Konstruktiven Wasserbau und in der Hydromechanik*, 2009, ISBN 978-3-933761-89-7
- 186 Vasin, Milos: *Influence of the soil structure and property contrast on flow and transport in the unsaturated zone*, 2010, ISBN 978-3-933761-90-3
- 187 Li, Jing: *Application of Copulas as a New Geostatistical Tool*, 2010, ISBN 978-3-933761-91-0
- 188 AghaKouchak, Amir: *Simulation of Remotely Sensed Rainfall Fields Using Copulas*, 2010, ISBN 978-3-933761-92-7
- 189 Thapa, Pawan Kumar: *Physically-based spatially distributed rainfall runoff modelling for soil erosion estimation*, 2010, ISBN 978-3-933761-93-4
- 190 Wurms, Sven: *Numerische Modellierung der Sedimentationsprozesse in Retentionsanlagen zur Steuerung von Stoffströmen bei extremen Hochwasserabflussereignissen*, 2011, ISBN 978-3-933761-94-1

- 191 Merkel, Uwe: *Unsicherheitsanalyse hydraulischer Einwirkungen auf Hochwasserschutzdeiche und Steigerung der Leistungsfähigkeit durch adaptive Strömungsmodellierung*, 2011, ISBN 978-3-933761-95-8
- 192 Fritz, Jochen: *A Decoupled Model for Compositional Non-Isothermal Multiphase Flow in Porous Media and Multiphysics Approaches for Two-Phase Flow*, 2010, ISBN 978-3-933761-96-5
- 193 Weber, Karolin (Hrsg.): *12. Treffen junger WissenschaftlerInnen an Wasserbauinstituten*, 2010, ISBN 978-3-933761-97-2
- 194 Bliedernicht, Jan-Geert: *Probability Forecasts of Daily Areal Precipitation for Small River Basins*, 2011, ISBN 978-3-933761-98-9
- 195 Hrsg.: Koschitzky, Hans-Peter; Braun, Jürgen: *VEGAS-Kolloquium 2010 In-situ-Sanierung - Stand und Entwicklung Nano und ISCO -*, Tagungsband zur Veranstaltung am 07. Oktober 2010 an der Universität Stuttgart, Campus Stuttgart-Vaihingen, 2010, ISBN 978-3-933761-99-6
- 196 Gafurov, Abror: *Water Balance Modeling Using Remote Sensing Information - Focus on Central Asia*, 2010, ISBN 978-3-942036-00-9
- 197 Mackenberg, Sylvia: *Die Quellstärke in der Sickerwasserprognose: Möglichkeiten und Grenzen von Labor- und Freilanduntersuchungen*, 2010, ISBN 978-3-942036-01-6
- 198 Singh, Shailesh Kumar: *Robust Parameter Estimation in Gauged and Ungauged Basins*, 2010, ISBN 978-3-942036-02-3
- 199 Doğan, Mehmet Onur: *Coupling of porous media flow with pipe flow*, 2011, ISBN 978-3-942036-03-0
- 200 Liu, Min: *Study of Topographic Effects on Hydrological Patterns and the Implication on Hydrological Modeling and Data Interpolation*, 2011, ISBN 978-3-942036-04-7
- 201 Geleta, Habtamu Itefa: *Watershed Sediment Yield Modeling for Data Scarce Areas*, 2011, ISBN 978-3-942036-05-4
- 202 Franke, Jörg: *Einfluss der Überwachung auf die Versagenswahrscheinlichkeit von Staustufen*, 2011, ISBN 978-3-942036-06-1
- 203 Bakimchandra, Oinam: *Integrated Fuzzy-GIS approach for assessing regional soil erosion risks*, 2011, ISBN 978-3-942036-07-8
- 204 Alam, Muhammad Mahboob: *Statistical Downscaling of Extremes of Precipitation in Mesoscale Catchments from Different RCMs and Their Effects on Local Hydrology*, 2011, ISBN 978-3-942036-08-5
- 205 Hrsg.: Koschitzky, Hans-Peter; Braun, Jürgen: *VEGAS-Kolloquium 2011 Flache Geothermie - Perspektiven und Risiken*, Tagungsband zur Veranstaltung am 06. Oktober 2011 an der Universität Stuttgart, Campus Stuttgart-Vaihingen, 2011, ISBN 978-3-933761-09-2
- 206 Haslauer, Claus: *Analysis of Real-World Spatial Dependence of Subsurface Hydraulic Properties Using Copulas with a Focus on Solute Transport Behaviour*, 2011, ISBN 978-3-942036-10-8
- 207 Dung, Nguyen Viet: *Multi-objective automatic calibration of hydrodynamic models – development of the concept and an application in the Mekong Delta*, 2011, ISBN 978-3-942036-11-5
- 208 Hung, Nguyen Nghia: *Sediment dynamics in the floodplain of the Mekong Delta, Vietnam*, 2011, ISBN 978-3-942036-12-2
- 209 Kuhlmann, Anna: *Influence of soil structure and root water uptake on flow in the unsaturated zone*, 2012, ISBN 978-3-942036-13-9
- 210 Tuhtan, Jeffrey Andrew: *Including the Second Law Inequality in Aquatic Ecodynamics: A Modeling Approach for Alpine Rivers Impacted by Hydropeaking*, 2012, ISBN 978-3-942036-14-6
- 211 Tolossa, Habtamu: *Sediment Transport Computation Using a Data-Driven Adaptive Neuro-Fuzzy Modelling Approach*, 2012, ISBN 978-3-942036-15-3
- 212 Tatomir, Alexandru-Bodgan: *From Discrete to Continuum Concepts of Flow in Fractured Porous Media*, 2012, ISBN 978-3-942036-16-0



- 213 Erbertseder, Karin: *A Multi-Scale Model for Describing Cancer-Therapeutic Transport in the Human Lung*, 2012, ISBN 978-3-942036-17-7
- 214 Noack, Markus: *Modelling Approach for Interstitial Sediment Dynamics and Reproduction of Gravel Spawning Fish*, 2012, ISBN 978-3-942036-18-4
- 215 De Boer, Cjestrir Volkert: *Transport of Nano Sized Zero Valent Iron Colloids during Injection into the Subsurface*, 2012, ISBN 978-3-942036-19-1
- 216 Pfaff, Thomas: *Processing and Analysis of Weather Radar Data for Use in Hydrology*, 2013, ISBN 978-3-942036-20-7
- 217 Lebreuz, Hans-Henning: *Addressing the Input Uncertainty for Hydrological Modeling by a New Geostatistical Method*, 2013, ISBN 978-3-942036-21-4
- 218 Darcis, Melanie Yvonne: *Coupling Models of Different Complexity for the Simulation of CO<sub>2</sub> Storage in Deep Saline Aquifers*, 2013, ISBN 978-3-942036-22-1
- 219 Beck, Ferdinand: *Generation of Spatially Correlated Synthetic Rainfall Time Series in High Temporal Resolution - A Data Driven Approach*, 2013, ISBN 978-3-942036-23-8
- 220 Guthke, Philipp: *Non-multi-Gaussian spatial structures: Process-driven natural genesis, manifestation, modeling approaches, and influences on dependent processes*, 2013, ISBN 978-3-942036-24-5
- 221 Walter, Lena: *Uncertainty studies and risk assessment for CO<sub>2</sub> storage in geological formations*, 2013, ISBN 978-3-942036-25-2
- 222 Wolff, Markus: *Multi-scale modeling of two-phase flow in porous media including capillary pressure effects*, 2013, ISBN 978-3-942036-26-9
- 223 Mosthaf, Klaus Roland: *Modeling and analysis of coupled porous-medium and free flow with application to evaporation processes*, 2014, ISBN 978-3-942036-27-6
- 224 Leube, Philipp Christoph: *Methods for Physically-Based Model Reduction in Time: Analysis, Comparison of Methods and Application*, 2013, ISBN 978-3-942036-28-3
- 225 Rodríguez Fernández, Jhan Ignacio: *High Order Interactions among environmental variables: Diagnostics and initial steps towards modeling*, 2013, ISBN 978-3-942036-29-0
- 226 Eder, Maria Magdalena: *Climate Sensitivity of a Large Lake*, 2013, ISBN 978-3-942036-30-6
- 227 Greiner, Philipp: *Alkoholinjektion zur In-situ-Sanierung von CKW Schadensherden in Grundwasserleitern: Charakterisierung der relevanten Prozesse auf unterschiedlichen Skalen*, 2014, ISBN 978-3-942036-31-3
- 228 Lauser, Andreas: *Theory and Numerical Applications of Compositional Multi-Phase Flow in Porous Media*, 2014, ISBN 978-3-942036-32-0
- 229 Enzenhöfer, Rainer: *Risk Quantification and Management in Water Production and Supply Systems*, 2014, ISBN 978-3-942036-33-7
- 230 Faigle, Benjamin: *Adaptive modelling of compositional multi-phase flow with capillary pressure*, 2014, ISBN 978-3-942036-34-4
- 231 Oladyshkin, Sergey: *Efficient modeling of environmental systems in the face of complexity and uncertainty*, 2014, ISBN 978-3-942036-35-1
- 232 Sugimoto, Takayuki: *Copula based Stochastic Analysis of Discharge Time Series*, 2014, ISBN 978-3-942036-36-8
- 233 Koch, Jonas: *Simulation, Identification and Characterization of Contaminant Source Architectures in the Subsurface*, 2014, ISBN 978-3-942036-37-5
- 234 Zhang, Jin: *Investigations on Urban River Regulation and Ecological Rehabilitation Measures, Case of Shenzhen in China*, 2014, ISBN 978-3-942036-38-2
- 235 Siebel, Rüdiger: *Experimentelle Untersuchungen zur hydrodynamischen Belastung und Standsicherheit von Deckwerken an überströmbaren Erddämmen*, 2014, ISBN 978-3-942036-39-9
- 236 Baber, Katherina: *Coupling free flow and flow in porous media in biological and technical applications: From a simple to a complex interface description*, 2014, ISBN 978-3-942036-40-5

- 237 Nuske, Klaus Philipp: *Beyond Local Equilibrium — Relaxing local equilibrium assumptions in multiphase flow in porous media*, 2014, ISBN 978-3-942036-41-2
- 238 Geiges, Andreas: *Efficient concepts for optimal experimental design in nonlinear environmental systems*, 2014, ISBN 978-3-942036-42-9
- 239 Schwenck, Nicolas: *An XFEM-Based Model for Fluid Flow in Fractured Porous Media*, 2014, ISBN 978-3-942036-43-6
- 240 Chamorro Chávez, Alejandro: *Stochastic and hydrological modelling for climate change prediction in the Lima region, Peru*, 2015, ISBN 978-3-942036-44-3
- 241 Yulizar: *Investigation of Changes in Hydro-Meteorological Time Series Using a Depth-Based Approach*, 2015, ISBN 978-3-942036-45-0
- 242 Kretschmer, Nicole: *Impacts of the existing water allocation scheme on the Limarí watershed – Chile, an integrative approach*, 2015, ISBN 978-3-942036-46-7
- 243 Kramer, Matthias: *Luftbedarf von Freistrahlturbinen im Gegendruckbetrieb*, 2015, ISBN 978-3-942036-47-4
- 244 Hommel, Johannes: *Modeling biogeochemical and mass transport processes in the sub-surface: Investigation of microbially induced calcite precipitation*, 2016, ISBN 978-3-942036-48-1
- 245 Germer, Kai: *Wasserinfiltration in die ungesättigte Zone eines makroporösen Hanges und deren Einfluss auf die Hangstabilität*, 2016, ISBN 978-3-942036-49-8
- 246 Hörning, Sebastian: *Process-oriented modeling of spatial random fields using copulas*, 2016, ISBN 978-3-942036-50-4
- 247 Jambhekar, Vishal: *Numerical modeling and analysis of evaporative salinization in a coupled free-flow porous-media system*, 2016, ISBN 978-3-942036-51-1
- 248 Huang, Yingchun: *Study on the spatial and temporal transferability of conceptual hydrological models*, 2016, ISBN 978-3-942036-52-8
- 249 Kleinknecht, Simon Matthias: *Migration and retention of a heavy NAPL vapor and remediation of the unsaturated zone*, 2016, ISBN 978-3-942036-53-5
- 250 Kwakye, Stephen Oppong: *Study on the effects of climate change on the hydrology of the West African sub-region*, 2016, ISBN 978-3-942036-54-2
- 251 Kissinger, Alexander: *Basin-Scale Site Screening and Investigation of Possible Impacts of CO<sub>2</sub> Storage on Subsurface Hydrosystems*, 2016, ISBN 978-3-942036-55-9
- 252 Müller, Thomas: *Generation of a Realistic Temporal Structure of Synthetic Precipitation Time Series for Sewer Applications*, 2017, ISBN 978-3-942036-56-6
- 253 Grüninger, Christoph: *Numerical Coupling of Navier-Stokes and Darcy Flow for Soil-Water Evaporation*, 2017, ISBN 978-3-942036-57-3
- 254 Suroso: *Asymmetric Dependence Based Spatial Copula Models: Empirical Investigations and Consequences on Precipitation Fields*, 2017, ISBN 978-3-942036-58-0
- 255 Müller, Thomas; Mosthaf, Tobias; Gunzenhauser, Sarah; Seidel, Jochen; Bárdossy, András: *Grundlagenbericht Niederschlags-Simulator (NiedSim3)*, 2017, ISBN 978-3-942036-59-7
- 256 Mosthaf, Tobias: *New Concepts for Regionalizing Temporal Distributions of Precipitation and for its Application in Spatial Rainfall Simulation*, 2017, ISBN 978-3-942036-60-3
- 257 Fenrich, Eva Katrin: *Entwicklung eines ökologisch-ökonomischen Vernetzungsmodells für Wasserkraftanlagen und Mehrzweckspeicher*, 2018, ISBN 978-3-942036-61-0
- 258 Schmidt, Holger: *Microbial stabilization of lotic fine sediments*, 2018, ISBN 978-3-942036-62-7
- 259 Fetzer, Thomas: *Coupled Free and Porous-Medium Flow Processes Affected by Turbulence and Roughness – Models, Concepts and Analysis*, 2018, ISBN 978-3-942036-63-4
- 260 Schröder, Hans Christoph: *Large-scale High Head Pico Hydropower Potential Assessment*, 2018, ISBN 978-3-942036-64-1
- 261 Bode, Felix: *Early-Warning Monitoring Systems for Improved Drinking Water Resource Protection*, 2018, ISBN 978-3-942036-65-8

- 262 Gebler, Tobias: *Statistische Auswertung von simulierten Talsperrenüberwachungsdaten zur Identifikation von Schadensprozessen an Gewichtsstaumauern*, 2018, ISBN 978-3-942036-66-5
- 263 Harten, Matthias von: *Analyse des Zuppinger-Wasserrades – Hydraulische Optimierungen unter Berücksichtigung ökologischer Aspekte*, 2018, ISBN 978-3-942036-67-2
- 264 Yan, Jieru: *Nonlinear estimation of short time precipitation using weather radar and surface observations*, 2018, ISBN 978-3-942036-68-9
- 265 Beck, Martin: *Conceptual approaches for the analysis of coupled hydraulic and geomechanical processes*, 2019, ISBN 978-3-942036-69-6
- 266 Haas, Jannik: *Optimal planning of hydropower and energy storage technologies for fully renewable power systems*, 2019, ISBN 978-3-942036-70-2
- 267 Schneider, Martin: *Nonlinear Finite Volume Schemes for Complex Flow Processes and Challenging Grids*, 2019, ISBN 978-3-942036-71-9
- 268 Most, Sebastian Christopher: *Analysis and Simulation of Anomalous Transport in Porous Media*, 2019, ISBN 978-3-942036-72-6
- 269 Buchta, Rocco: *Entwicklung eines Ziel- und Bewertungssystems zur Schaffung nachhaltiger naturnaher Strukturen in großen sandgeprägten Flüssen des norddeutschen Tieflandes*, 2019, ISBN 978-3-942036-73-3
- 270 Thom, Moritz: *Towards a Better Understanding of the Biostabilization Mechanisms of Sediment Beds*, 2019, ISBN 978-3-942036-74-0
- 271 Stolz, Daniel: *Die Nullspannungstemperatur in Gewichtsstaumauern unter Berücksichtigung der Festigkeitsentwicklung des Betons*, 2019, ISBN 978-3-942036-75-7
- 272 Rodriguez Pretelin, Abelardo: *Integrating transient flow conditions into groundwater well protection*, 2020, ISBN: 978-3-942036-76-4
- 273 Weishaupt, Kilian: *Model Concepts for Coupling Free Flow with Porous Medium Flow at the Pore-Network Scale: From Single-Phase Flow to Compositional Non-Isothermal Two-Phase Flow*, 2020, ISBN: 978-3-942036-77-1
- 274 Koch, Timo: *Mixed-dimension models for flow and transport processes in porous media with embedded tubular network systems*, 2020, ISBN: 978-3-942036-78-8

Die Mitteilungshefte ab der Nr. 134 (Jg. 2005) stehen als pdf-Datei über die Homepage des Instituts: [www.iws.uni-stuttgart.de](http://www.iws.uni-stuttgart.de) zur Verfügung.